UNIVERSITÉ D'ORLÉANS

ÉCOLE DOCTORALE ÉNERGIE MATÉRIAUX SCIENCES DE LA TERRE ET DE L'UNIVERS

THÈSE présentée par :

Euan DUNCAN

Soutenue le : **21 Janvier 2025**

Pour obtenir le grade de : **Docteur de l'Université d'Orléans**

Discipline/ Spécialité : Chimie

New Functional Oxides by Crystallisation of Glass Precursors

Nouveaux oxydes fonctionnels par cristallisation de précurseurs vitreux

THÈSE dirigée par :

M. Michael Pitcher	Chargé de Recherche, CEMHTI CNRS
M. Mathieu Allix	Directeur de Recherche, CEMHTI CNRS

RAPPORTEURS :

M. Olivier Hernandez	Professeur, IMN Nantes / Université de Nantes
Mme Laeticia Petit	Professeur, Tampere University

JURY :

Mme Gaëlle Delaizir	Professor, IRCER / Université de Limoges **Présidente du jury**
M. Alberto Fernandez-Carrion	Maître de Recherche, CSIC/Universidad de Sevilla
M. Olivier Hernandez	Professeur, IMN Nantes / Université de Nantes
Mme Laeticia Petit	Professeur, Tampere University
M. Michael Pitcher	Chargé de Recherche, CEMHTI CNRS
M. Mathieu Allix	Directeur de Recherche, CEMHTI CNRS

"If you want to be a grocer, or a general, or a politician, or a judge, you will invariably become it; that is your punishment. If you never know what you want to be, if you live what some might call the dynamic life, if each day you are unsure of who you are and what you know, you will never become anything, and that is your reward."

Stephen Fry; Oscar Wilde

"Tu vis, et faut vivre à fond"

Rone, Alain Damasio

Acknowledgements

Where to begin in acknowledging everyone who has contributed to the completion of this thesis. I owe a great many things to an even greater number of people. To arrive in a foreign country and be accepted the way I have been, will I'm sure remain one of the greatest pleasures of my life. So, to all those who I have met along the way, who have translated documents, shared a drink, shared a laugh, and put out fires, I would like you to know that you have made these past three years some of the best of my life and I will never forget them.

I must begin, of course, by thanking my two supervisors, Michael Pitcher and Mathieu Allix, your guidance and patience over the past three years has turned me into the researcher I am today. Having the opportunity to learn from you both during my PhD has truly been invaluable. When I arrived at CEMHTI, after completing my masters during covid, I had little of experience of practical lab work and how to conduct research and now I have fired lasers at molten beads of levitating glass, discovered (and patented) new phases, and had my definition of what 'high temperature' means, forever changed. Looking back, I can now appreciate how lucky I was the day that you selected me for this project. Moreover, I would like to thank all the members of the CERAM team, both past and present, who created such a friendly environment to work in that it hardly felt like work at all. Additionally, I must extend my deepest gratitude to the jury members (Mme. Laeticia Petit, M. Olivier Hernandez**,** Mme. Gaelle Delaizir and M. Alberto Fernandez-Carrion) who have kindly agreed to review my thesis. I hope reading my work comes with less stress than writing it. I would also like to thank all of the researchers and collaborators who have contributed to this manuscript, Sandra Ory, Franck Fayon, Cécile Genevois, Emmanuel Veron, Victor Castaing, Ana Isabel Becerro and Patrick Houizot. Your tireless work and insightful explanations were essential to the writing of this thesis.

I am contractually obligated to thank my parents, without whom, I would quite literally not be here today. Your support over the years has truly meant everything to me, and gave me the confidence, or stupidity, to travel to a new country and complete a PhD (I am sorry mum that you will no longer be the only doctor in the family). To Etta (and my other grandparents who are sadly no longer with us) I hope I have made you proud. I also want to thank my brother and sister, who growing up inspired me both creatively and academically and softened the strictness of our parents, enabling me to get away with a lot more im sure. To wee baby Archie, I am blessed to be your uncle and am very much looking to watching you grow up, and I want you to always remember that the completion of this PhD, officially makes me smarter than your father.

To all my friends, both back home in Scotland and in Orléans, you have made my life immeasurably better simply by being in it. To my friends back home, I have missed you incredibly since leaving for France and im very fortunate that you have not forgotten about me. I am even more fortunate for all the times you let me

sleep on your sofas, so that I could come and visit and remember why I left in the first place. To all the friends I've made in Orléans, your friendship has transformed what once felt like a scary foreign city into the best place on Earth. It is simply impossible for me to adequately express the impact each and every one of you have had on me in your own way. You somehow put up with, and perhaps even more amazingly seem to enjoy, the mountains of superfluous inane drivel which forever seems to tumble from my mouth. It would be a sad little life without you all in it, I truly am such a lucky mec.

I would be remiss not to give a special thanks to Renaud Voila, I am 100% certain I would have long been booted from this country had it not been for your help. Your cultural teachings in the ways of La Vie Français - Pastis, Paix Dieu, and Andouillette - (I'm sorry but you will never convince me that Maroilles is not the devils work) were truly an eye-opening experience into the intoxicating and delicious underbelly of this country. Not to mention our numerous and fierce scientific debates that would electrify the walls of our office, I swear, at times, not even Einstein or Oppenheimer would've been able to match wits with us.

Finally, I would like to thank three more people, to whom I owe an unending debt of gratitude, the first is my best friend who has supported me since the very beginning of this thesis. The second is perhaps the smartest person I know, watching you succeed so effortlessly in life is equal parts inspiring and annoying and is a constant source of motivation for me. The third is the love of my life, who's existence never fails to bring me unending joy. Fortunately, all of these people have the same name - Eilidh MacAulay. I can never thank you enough for all you have done for me over the past three years, taking planes, trains, buses, trams and taxis just so we can see each other. The truth is I am a cheap reproduction of all your best qualities, and so whatever reasons you have for sticking by me, can in fact be attributed back to you. I will love you forever.

Abstract

This PhD work aimed to discover new metal-oxide compounds, with potential functional applications, by crystallisation of glass precursors. Such approaches are necessary to address the growing need for new phases with enhanced properties, and in principle can facilitate step changes improvements in performance by replacing current materials. The SrO-Al_2O_3-SiO_2 ternary diagram was focussed on due to its broad glass-forming domain, and the variety of known phases with functional (especially optical) applications already found within it. In the first part of this work, glass crystallisation in different regions of the phase diagram led to the discovery of a new metastable compound, $Sr_{12}Al_{20}Si_{12}O_{66}$. The second part of this work concerns attempts to isolate the new ternary silicate $Sr_2Si_3O_8$ (discovered previously at CEMHTI by a recent computationally-guided approach) as a phase-pure fully-crystallised material, facilitating the exploration of its mechanoluminescence properties for the first time. These compounds were characterised at multiple length scales (unit cell to micron scale) and temperatures, through powder X-ray and neutron diffraction methods and high-resolution transmission electron microscopy using state-of-the-art instruments (for diffraction, atomic-resolution STEM-HAADF, and EELS spectroscopy). This permitted *ab-initio* structure solution of $Sr_{12}Al_{20}Si_{12}O_{66}$. Finally, local atomic arrangements in $Sr_{12}Al_{20}Si_{12}O_{66}$ were studied by ^{27}Al and ^{29}Si MAS-NMR coupled to DFT modelling, which revealed an unusual partial ordering of Al and Si over the tetrahedral framework sites of the crystal structure, which could not be resolved directly by diffraction. The luminescent properties of these materials were explored (in collaboration with the CSIC institute in Seville and the Institut de Physique (IPR) in Rennes). Whilst $Sr_2Si_3O_8$ was found to have a modest mechanoluminescence response, $Sr_{12}Al_{20}Si_{12}O_{66}$ was found to have bright long-lasting blue persistent luminescence emission in addition to an intense mechanoluminescence response, with the performance of both properties comparable to current state-of-the-art materials.

Key words: Oxides, functional oxides, glass-ceramics, metastable, out-of-equilibrium, molten, amorphous, glass-crystallisation, optical properties, persistent luminescence, mechanoluminescence.

Résumé

Ce travail de thèse à découvrir de nouveaux composés fonctionnels à base d'oxydes, en utilisant la cristallisation du verre comme moyen de synthèse original. Ces recherches sont nécessaires pour répondre au besoin croissant de nouvelles phases cristallines à propriétés améliorées, et peut en principe faciliter des évolutions progressives des performances en remplaçant les matériaux actuels. Le diagramme ternaire SrO-Al_2O_3-SiO_2 a été choisi en raison de son large domaine de formation vitreux et de la variété des phases cristallines répertoriées ayant des applications fonctionnelles, en particulier dans le domaine de l'optique. Dans la première partie de ce travail, l'utilisation de la cristallisation de verre provenant de différentes régions du diagramme de phase a conduit à la découverte d'un nouveau composé métastable, $Sr_{12}Al_{20}Si_{12}O_{66}$. La deuxième partie de ce travail concerne les tentatives d'isoler le nouveau silicate $Sr_2Si_3O_8$ (découvert précédemment au CEMHTI par une approche récente utilisant le guidage par calcul prédictif) comme matériau entièrement cristallisé et monophasique, facilitant l'exploration de ses propriétés de mécanoluminescence. Ces composés ont été caractérisés de manière multi-échelle (de la maille unitaire à l'échelle du grain) et en température, par des méthodes de diffraction des rayons X et de neutrons sur poudre et par microscopie électronique en transmission à haute résolution en utilisant des instruments de pointe (résolution atomique STEM-HAADF et spectroscopie EELS). Cette approche a permis de résoudre *ab-initio* la structure du composé $Sr_{12}Al_{20}Si_{12}O_{66}$. Enfin, les arrangements atomiques locaux dans $Sr_{12}Al_{20}Si_{12}O_{66}$ ont été étudiés par spectroscopie RMN du solide à l'angle magique (noyaux ^{27}Al et ^{29}Si) couplée à une modélisation DFT, qui ont révélé un ordre partiel inhabituel entre Al et Si au sein des sites tétraédriques de la structure cristalline, qui n'a pas pu être observé directement par diffraction. Les propriétés de luminescence de ces matériaux ont été explorées (en collaboration avec l'institut CSIC de Séville et l'institut de physique (IPR) de Rennes). Alors que $Sr_2Si_3O_8$ montre une réponse de mécanoluminescence modeste, $Sr_{12}Al_{20}Si_{12}O_{66}$ s'est avéré avoir une émission de luminescence bleue persistante de longue durée, en plus d'une réponse en mécanoluminescence intense. Les performances de ce nouvel aluminosilicate sont comparables à l'état de l'art.

Mots clés : Oxydes, oxydes fonctionnels, vitrocéramiques, métastables, hors équilibre, fondus, amorphes, cristallisation du verre, propriétés optiques, luminescence persistante, mécanoluminescence.

General Contents Page

General Introduction

Functional inorganic oxides are essential in the development of modern technologies.[1] Their applications span a wide range, from electronics (e.g., phones and batteries) to healthcare (e.g., dentistry), construction, consumer goods (e.g. cookware), lasers, and more.[2] Given their diverse uses, the demand for new inorganic materials with enhanced properties—such as improved hardness, durability, and thermal or electrical conductivity—has grown exponentially.[3] At the same time, there is a general push towards greener, more cost-effective synthesis methods. However, conventional synthesis techniques, such as the solid-state method, are increasingly unable to meet this growing demand. New methodologies are therefore needed to discover next-generation inorganic oxides and functionalise them to overcome the property plateaus set by the gradual optimisation of established materials.

Despite the clear motivation for new material discoveries, the process can be fundamentally challenging.[4] What synthesis methods can target the formation of new phases? How can stable and promising compositions be selected from the virtually limitless possibilities within the periodic table? Currently, these questions are mainly addressed by two approaches: (i) **Synthesis-based approaches**, where innovative methods are used to access phases not formed by conventional techniques, which tend to favour thermodynamically stable products,[3,5] and (ii) **Efficiency-based approaches**, which use computational tools (such as the probe structure method and density functional theory (DFT) calculations) to identify compositions with desirable properties.[6,7] Computational tools, in particular, enhance research efficiency by guiding the selection of compositions for synthesis, allowing researchers to focus on the most promising targets. These approaches need not be considered mutually exclusive; in fact, their combination can leverage unique benefits. This thesis proposes an approach that integrates innovative synthesis methods (such as melt and amorphous-assisted synthesis) with computational guidance to target the discovery and functionalisation of new inorganic oxides, thus overcoming the property limitations of established materials.

Specifically, this work focuses on the synthesis of metastable (out-of-equilibrium) glass-ceramics and ceramics in the SrO-$AlO_{1.5}$-SiO_2 ternary diagram. Metastable phases, by their very nature, are often missed by classical high temperature solid-state reactions, which are typically biased towards the synthesis of thermodynamically stable prodcuts.[8] As a result, even in well-studied phase diagrams, numerous metastable phases may remain undiscovered. Glass-ceramics, a class of materials that combines the mechanical properties of glass with the functional benefits of crystalline materials, are of particular interest.[9] These materials have even been shown to rival ceramics in some applications while retaining unique properties, such as transparency, that open the door to optical applications.[10] The untapped potential of metastable phase discovery, coupled with the diverse applications of glass-ceramics and ceramics, presents exciting opportunities for the development of novel materials with enhanced properties.[11]

One of the primary techniques for synthesising metastable glass-ceramics is glass crystallisation (GC).[12,13] By crystallising from glass, an inherently out-of-equilibrium state of matter, this technique favours the formation of non-equilibrium products. The GC approach also aligns with glass-ceramic formation, by providing the initial glassy matrix in which crystallisation can occur. Additionally, by fully crystallising the glass it is possible to synthesise ceramic samples. Crystallising from an out-of-equilibrium state, lowers the kinetic barrier to phase formation, so lower temperatures can be used, when compared to conventional routes. In addition to GC, other out-of-equilibrium synthesis techniques were also explored in this work, such as high energy milling (HEM), aerodynamic levitation (ADL) coupled to two CO_2 lasers.

To complement these synthesis methods, a computational probe structure approach was employed in collaboration with the University of Liverpool.[14–16] This method guided the selection of target compositions by rapidly identifying low energy 'zones of interest' in the SrO-$AlO_{1.5}$-SiO_2 ternary diagram, where new phases were more likely to form. Focusing on these zones allowed for more efficient resource allocation and reduced experimental time. Furthermore, the reduced energy requirements of GC synthesis enabled the exploration of compositions in shallower energy wells.

Literature surveys revealed a number of promising optical materials in the SrO-$AlO_{1.5}$-SiO_2 phase space, such as $SrAl_2O_4$:1%Eu^{2+},2%Dy^{3+}), prompting the focus on optical properties in the functionalisation of any discovered compositions.[17] Specifically, persistent luminescence and mechanoluminescence were targeted, as these properties are valuable in a wide range of industries such as jewellery making, safety signage, and construction.[18] Microstructural engineering techniques were also employed to enhance or permit transparency in discovered phases, thus benefitting from volume effects in luminescence and further expanding the potential applications of these materials.

The combination of innovative synthesis techniques (GC) with computational phase prediction represents a novel approach to materials discovery. This approach led to the identification of three new metastable glass-ceramics in the SrO-$AlO_{1.5}$-SiO_2 diagram, which were then functionalised to exhibit high-performance persistent luminescent and mechanoluminescent properties.

This thesis is organised into four main chapters, summarised as follows:

- Chapter 1: The relevant literature on metastable phases and glass-ceramics is reviewed, with a focus on their functionalisation. It provides an overview of the out-of-equilibrium techniques used in this work, with a particular emphasis on the advantages of GC. The chapter also discusses the challenges of synthesising transparent glass-ceramics and methods for introducing optical properties such as persistent luminescence and mechanoluminescence. Some examples are then given which highlight the uses and limitations of the current SrO-$AlO_{1.5}$-SiO_2 phases which exhibit these properties.
- Chapter 2: A well explored zone of the SrO-$AlO_{1.5}$-SiO_2 ternary diagram is investigated. The first part of this chapter covers the phase-pure synthesis and functionalisation of a previously discovered

metastable ceramic, $SrAl_2SiO_6$. This work leads to the discovery of a second new compound, $Sr_{12}Al_{20}Si_{12}O_{66}$, whose synthesis optimisation, structural determination, and functionalisation forms the main body of the chapter. Microstructural features such as crystallite orientation are investigated as routes to tuning the optical properties in both phases. These properties are then quantitatively analysed before finally, the compositional limits of $Sr_{12}Al_{20}Si_{12}O_{66}$, with respect to substitutions and solid solutions is explored.

- Chapter 3: The new metastable glass-ceramic, $Sr_2Si_3O_8$, is the subject of this chapter. This phase was identified as the crystalline component of a complex compositionally-heterogeneous glass-ceramic, immediately prior to the start of this thesis work, by a combined synthesis and computation approach. The chapter outlines the challenges in optimising the synthesis of this phase by congruent crystallisation of the glass, and the use of substitutions and nucleating agents to optimise its crystallinity and stability. Finally, by analogy with recent publications on the related compound $Ba_4Si_6O_{16}$ partial nitridation of the precursor glass is explored as a means of elucidating highly crystalline $Sr_2Si_3O_8$ with mechanoluminescent properties.
- General conclusion: The manuscript is concluded by summarising the main findings and providing perspectives on future research and potential applications of the newly discovered materials.

Finally, Annexes I, II, and III provide additional details on certain sections of the thesis, and Chapter 4 outlines the various synthesis and characterisation methods used in this work, including the GC method, ADL, HEM, and diffraction-based techniques (XRD, SPD, NPD) for structural determination. Additionally, local and micro-environment analysis techniques such as NMR, TEM, and SEM are discussed, along with methods for quantifying optical properties.

References:

[1] P. Alivisatos, P. F. Barbara, A. W. Castleman, J. Chang, D. A. Dixon, M. L. Klein, G. L. McLendon, J. S. Miller, M. A. Ratner, P. J. Rossky, S. I. Stupp and M. E. Thompson, *Advanced Materials*, 1998, **10**, 1297–1336.

[2] C. Sanchez, L. Rozes, F. Ribot, C. Laberty-Robert, D. Grosso, C. Sassoye, C. Boissiere and L. Nicole, *Comptes Rendus Chimie*, 2010, **13**, 3–39.

[3] U. S. Schubert and N. Hüsing, *Synthesis of inorganic materials*, John Wiley & Sons, 2019.

[4] J. M. Rondinelli, N. A. Benedek, D. E. Freedman, A. Kavner, E. E. Rodriguez, E. S. Toberer and L. W. Martin, *American Ceramic Society Bulletin*, 2013, **92**, 14–22.

[5] R. Xu and Y. Xu, *Modern inorganic synthetic chemistry*, Elsevier, 2010.

[6] E. O. Pyzer-Knapp, J. W. Pitera, P. W. J. Staar, S. Takeda, T. Laino, D. P. Sanders, J. Sexton, J. R. Smith and A. Curioni, *npj Computational Materials*, 2022, **8**, 84.

[7] A. R. Oganov, C. J. Pickard, Q. Zhu and R. J. Needs, *Nature Reviews Materials*, 2019, **4**, 331–348.

[8] M. Jansen, *Angewandte Chemie International Edition*, 2002, **41**, 3746–3766.

[9] M. Allix and L. Cormier, *Techniques de l'Ingénieur*, DOI:10.51257/a-v1-n4802.

[10] O. J. Akinribide, G. N. Mekgwe, S. O. Akinwamide, F. Gamaoun, C. Abeykoon, O. T. Johnson and P. A. Olubambi, *Journal of Materials Research and Technology*, 2022, **21**, 712–738.

[11] W. Sun, S. T. Dacek, S. P. Ong, G. Hautier, A. Jain, W. D. Richards, A. C. Gamst, K. A. Persson and G. Ceder, *Science Advances*, **2**, e1600225.

[12] P. F. James, *Journal of Non-Crystalline Solids*, 1995, **181**, 1–15.

[13] N. Karpukhina, R. Hill and R. Law, *Chemical Society Reviews*, 2014, **43**, 2174–2186.

[14] C. Collins, L. Daniels, Q. Gibson, M. Gaultois, M. Moran, R. Feetham, M. Pitcher, M. Dyer, C. Delacotte, M. Zanella, C. Murray, G. Glodan, O. Perez, D. Pelloquin, T. Manning, J. Alaria, G. Darling, J. Claridge and M. Rosseinsky, *ANGEWANDTE CHEMIE-INTERNATIONAL EDITION*, 2021, **60**, 16457–16465.

[15] C. Collins, G. R. Darling and M. J. Rosseinsky, *Faraday Discuss.*, 2018, **211**, 117–131.

[16] C. Collins, M. S. Dyer, M. J. Pitcher, G. F. S. Whitehead, M. Zanella, P. Mandal, J. B. Claridge, G. R. Darling and M. J. Rosseinsky, *Nature*, 2017, **546**, 280–284.

[17] R. E. Rojas-Hernandez, F. Rubio-Marcos, M. Á. Rodriguez and J. F. Fernandez, *Renewable and Sustainable Energy Reviews*, 2018, **81**, 2759–2770.

[18] E. D. Zanotto, *American Ceramics Society Bulletin*, 2010, **89**, 19–27.

Chapter 1: State-of-the-Art

Contents Page

1.1. The Role of Non-Equilibrium Synthesis Techniques in the Synthesis of Functional Inorganic Oxides

1.1.1. Introduction & Aims

Materials science is one of the fastest-growing fields of research, fuelled by demand from industry, government, and the public for materials with enhanced properties and greener synthesis methods.[1,2,3] Currently, the approach to satisfying this demand is mostly through the incremental improvement of existing materials and their properties.[4,5] However, this method alone can no longer keep pace with the rate of technological advancement in modern society.[6] Alternative approaches, specifically targeting novel phase synthesis, are needed to overcome property plateaus set by the current 'best in class' materials and to enable step-change improvements in their functionality. A pertinent example of this is the recent discovery of hybrid lead halide perovskite solar absorbers, which led to the development of highly efficient 'tandem' photovoltaic cells.[7] These cells outperformed traditional silicon-based cells, a technology that has been optimised over several decades, and marked a new frontier in photovoltaic research.[8]

Materials discovery is the branch of materials science which aims to uncover these next-generation inorganic materials and thus permit the necessary step-change improvements in property ceilings. Currently, there are two main approaches to this field, (i) the development of innovative synthesis methods, capable of accessing phases commonly missed by conventional methods, and (ii) increasing researcher efficiency through the use of computational aids.[9] Examples of some relevant innovative synthesis methods are shown in Fig. 1.1.

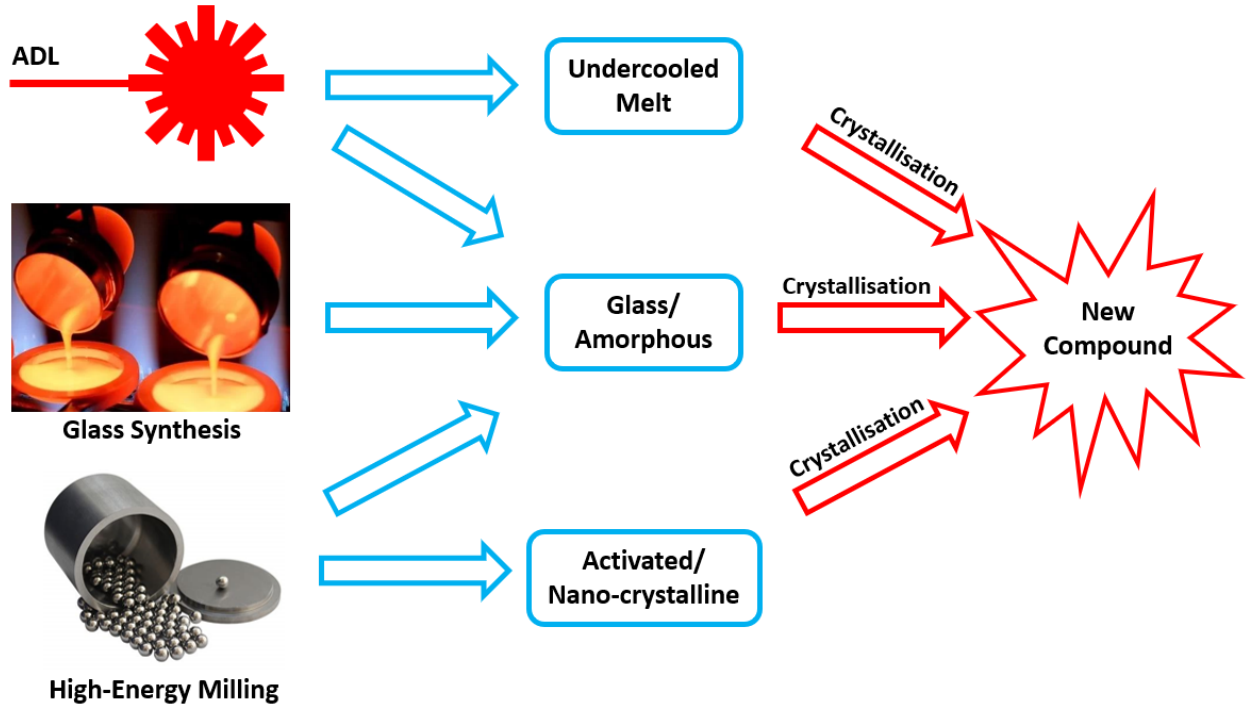

Fig. 1.1. Examples of the innovative synthesis methods employed in this work to target non-equilibrium intermediates, which were then used as 'stepping stones' to novel phase discovery. (ADL - aerodynamic levitation coupled to two CO_2 lasers).

In this work, a synthetic approach is presented, wherein the primary aim is to combine the advantages of both current methods. This approach proposes a novel route for the targeted discovery of novel metastable glass-ceramics and ceramics in the SrO-$AlO_{1.5}$-SiO_2 ternary diagram. Which has long been studied for its glass forming ability and host of interesting functional materials.[10–12] By integrating the advantages of innovative synthesis methods with exploratory computational prediction, this project has the potential to advance the field of inorganic materials discovery. Metastable glass-ceramics and ceramics were targeted, as they are known to exhibit diverse, highly tuneable structures with properties such as transparency, optical luminescence, and structural polarity.[13–15] The metastable phase space itself offers exciting opportunities for out-of-equilibrium structural motifs with unique chemical bonding, and therefore, the potential for novel functionalities.[16]

Traditionally, the synthesis of metastable compositions has been hindered by two main challenges:

1. Conventional solid-state synthesis routes, which predominantly lead to the formation of thermodynamically stable products.[17]
2. The identification of potentially stable target compositions from the vast possibilities within the periodic table.[18]

These challenges may be addressed through the combination of the aforementioned innovative synthesis techniques based on activated precursors (Fig. 1.1.) and by computational methods to focus synthesis efforts close to compositions that are likely to give stable compounds. Using glass crystallisation (GC) as the principal synthesis tool, this may provide a route to the discovery of new, complex glass-ceramics or ceramics, with the potential for functionalisation. This functionalisation could manifest at the unit cell scale (for example by doping to introduce optical properties), since the discovery of new phases inherently offers the possibility of new properties. Additionally, control over micro- and nanoscale structural features could be leveraged to elicit or enhance properties that would otherwise be absent, for example the realisation of a new transparent ceramic.

In this chapter, the current state-of-the-art in out-of-equilibrium synthesis techniques is reviewed, with particular emphasis on GC, due to its prominent use in this work. Subsequent sections provide examples of materials that either utilise GC or exhibit transparent and luminescent properties, these properties were focussed on due to their relevance to the SrO-$AlO_{1.5}$-SiO_2 diagram and their real-world usefulness.[19–21]

1.2. Innovative Synthesis Techniques Combined with Computational Prediction

1.2.1. Targeting Metastability

A metastable oxide can be described as an ambiently stable state of matter whose free energy lies at a local energy minimum rather than a global one, as shown in Fig. 1.2.[22,23] A key characteristic of these materials therefore, is their decomposition when energetically disturbed, for example by further heating. Due to this trait, they are commonly missed by conventional approaches (such as the solid-state one described in Section 1.2.2.), meaning that a whole host of undiscovered metastable phases could exist, even in well explored diagrams, such as the SrO-$AlO_{1.5}$-SiO_2 one.

The metastability of these materials marks the biggest obstable in their synthesis. Which techniques provide sufficient energy to yield metastable products, without decomposing them?

Solutions to this problem were found by considering the schematic reaction coordinate diagram in Fig. 1.2. The figure demonstrates that by lowering the activation energy (△E) of reactions, the synthesis and isolation of non-equilibrium (metastable) products can be more readily facilitated.

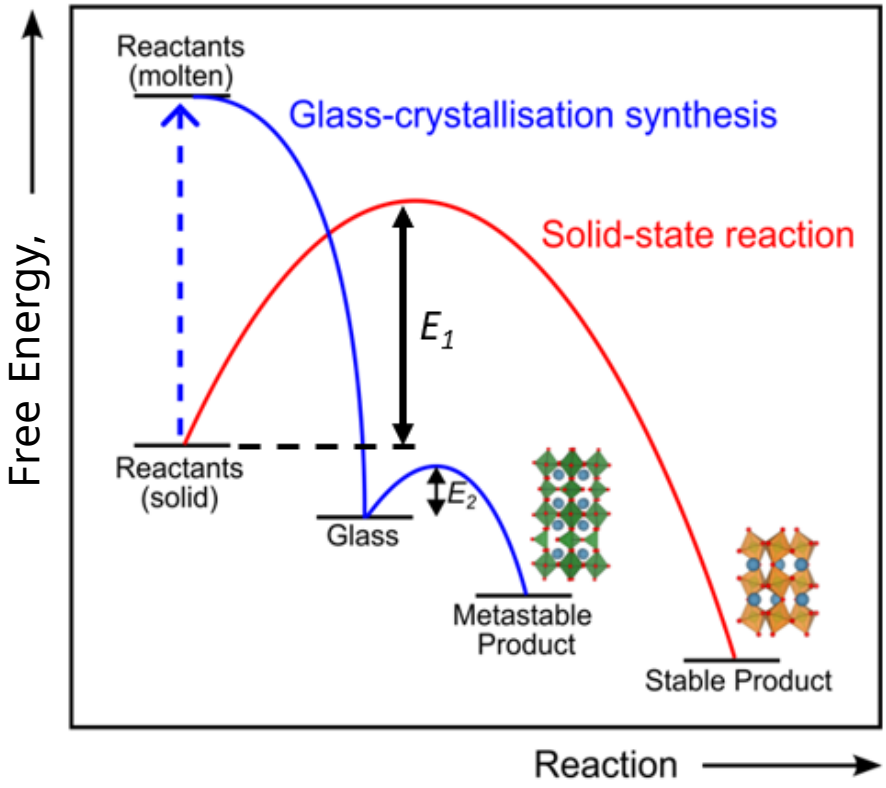

Fig. 1.2. Diagram showing the reaction pathways of different products and possible synthesis techniques to access them. Inspired by [24].

1.2.2. Limitations of the Solid-State Method

The solid-state method is the most commonly used technique for the synthesis of metal oxides, its simplicity, scalability, and universality has made it highly valuable in both industry and research.[17] It is an approach which has led to the discovery of many notable phases, over the years, with highly desirable properties.[25,26] The first step of the method is the manual grinding of precursors, which shortens diffusion pathways and reduces grain sizes to the micron scale. The prepared reaction mixture is then sintered, as either a loose or pelletised powder, for 12–48 hours at high temperatures, typically 900–1600°C.[27]

Due to reactions only occurring at grain interfaces, multiple repetitions can be required to ensure a complete reaction. This problem is further exasperated by inhomogeneities in the reaction mixture and the relatively low surface area of the micron sized grains. These disadvantages, explain why high temperatures and long reaction times are required to overcome activation energies and allow atoms to diffuse across the grain boundaries. They also explain why this approach commonly favours the formation of thermodynamically stable products rather than metastable ones.

Clearly, to target metastable glass-ceramics, alternative synthesis techniques must be considered, particularly those that can 'activate' precursors (i.e. lowering $\triangle E$ for the product formation step, as shown schematically in Fig. 1.2.). In this context, the term 'activated precursors' refers to precursors whose barriers to product formation (grain boundaries, micron-scale diffusion etc.) have been reduced through their preparation method (e.g. melting, glass formation, or ball-milling).

1.2.3. Out-of-equilibrium Synthesis Methods

A non-exhaustive list of commonly used synthesis methods in materials science is shown in Fig. 1.3. The bottom two branches (soft chemistry and melt/amorphous-assisted) were identified as out-of-equilibrium methods for targeting metastable glass-ceramics or ceramics. Solution-based processes (e.g. the sol-gel method) in particular, have been demonstrated as effective for bypassing the slow diffusion rates typical of the solid-state method.[28,29] However, in this work, the focus was placed on melt/amorphous-assisted methods (the green branch of Fig. 1.3.), as they were identified as an efficient route to 'activated' precursors.[26] Like solution-based processes, melt/amorphous-assisted routes also circumvent the limitations of the solid-state method, promoting the formation of metastable glass-ceramics.

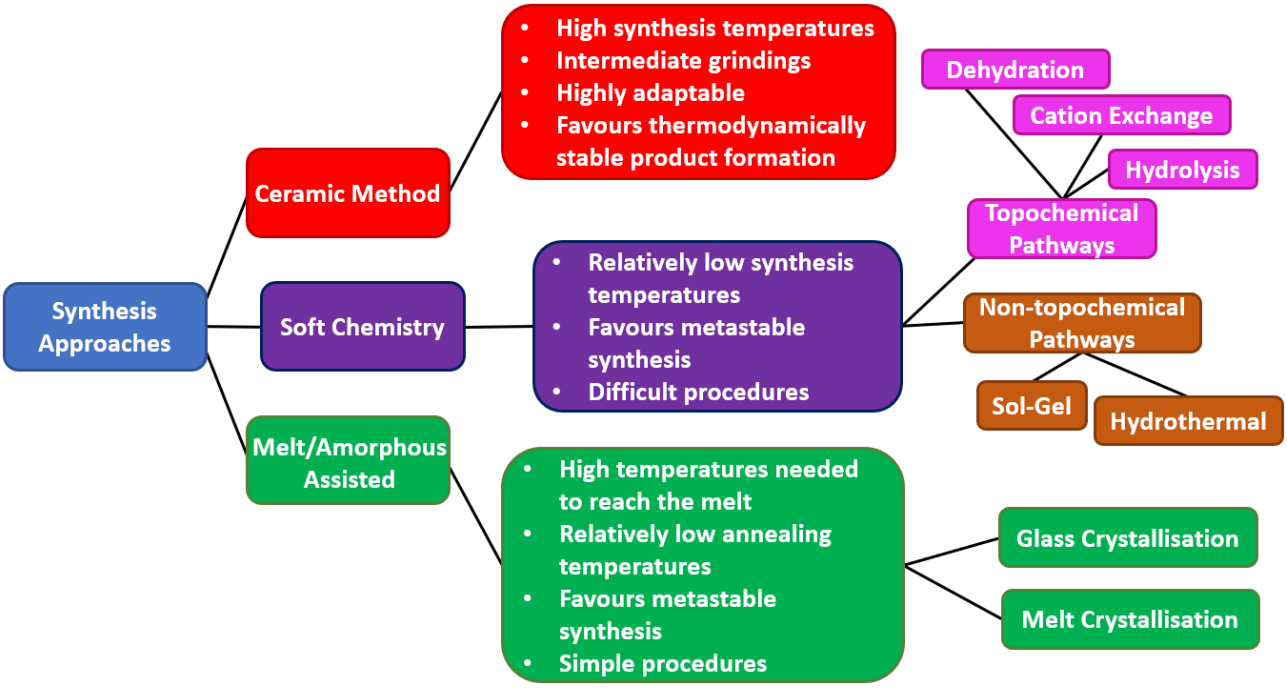

Fig. 1.3. A non-exhaustive list of synthesis techniques commonly used in materials science. Their advantages and disadvantages are compared with respect to the synthesis of metastable phases. Adapted from [26].

1.2.4. Glass Crystallisation - Step 1. Glass Formation

The main synthesis technique used in this project was GC, its relatively simple procedure made it an attractive choice in the search for new metastable phases. GC, as a synthesis technique, involves two key steps: first, the formation of glass, followed by its crystallisation. In this work, the first step was achieved by the classic melt-quenching of molten precursor (contained Pt crucibles) in a water bath. This step of GC, logically, favoured the formation of glass-ceramics by providing the glassy matrix within which crystallisation could occur.[15] Using glass as a starting point for crystallisation also explained why the SrO-$AlO_{1.5}$-SiO_2 ternary diagram was chosen, with much of the diagram being vitrifiable.[30]

Additionally, to understand the choice of GC, it is also important to consider the definition of glass, as this state of matter provides numerous advantages in the targeting of metastable phases. However, defining glass remains a challenging task with the topic still being heavily debated.[31] In this work, the most recent definition by E. D. Zanotto and J. C. Mauro was accepted "*Glass is a nonequilibrium, non-crystalline condensed state of matter that exhibits a glass transition. The structure of glasses is similar to that of their parent supercooled liquids (SCL), and they spontaneously relax toward the SCL state. Their ultimate fate, in the limit of infinite time, is to crystallize*".[32]

1.2.5. Glass as an 'Activated Precursor'

In the context of solid-state synthesis, glass, as a non-equilibrium state of matter provokes a direct comparison to the role of 'activated' precursors: a relatively modest heating step can accelerate the crystallisation of glass into the desired phase. Given the appropriate system, this reaction can be directed towards metastable crystalline phases. Glass synthesis also facilitated the functionalisation of discovered materials by enabling the preparation of both powdered and bulk samples, depending on the glass treatment step used, and by introducing transparency into bulk samples through the full and congruent crystallisation of glass technique discussed in Section 1.4.2.

The similarities between glass and its parent supercooled liquid, along with the lack of long-range ordering, was crucial. These characteristics reduced the energy required for atomic diffusion into an ordered crystalline network (Fig. 1.4.). Additionally, the typically random and atomically mixed structure of glasses helped prevent inhomogeneities in the reaction mixtures, which thereby increased the likelihood of achieving phase-pure synthesis.

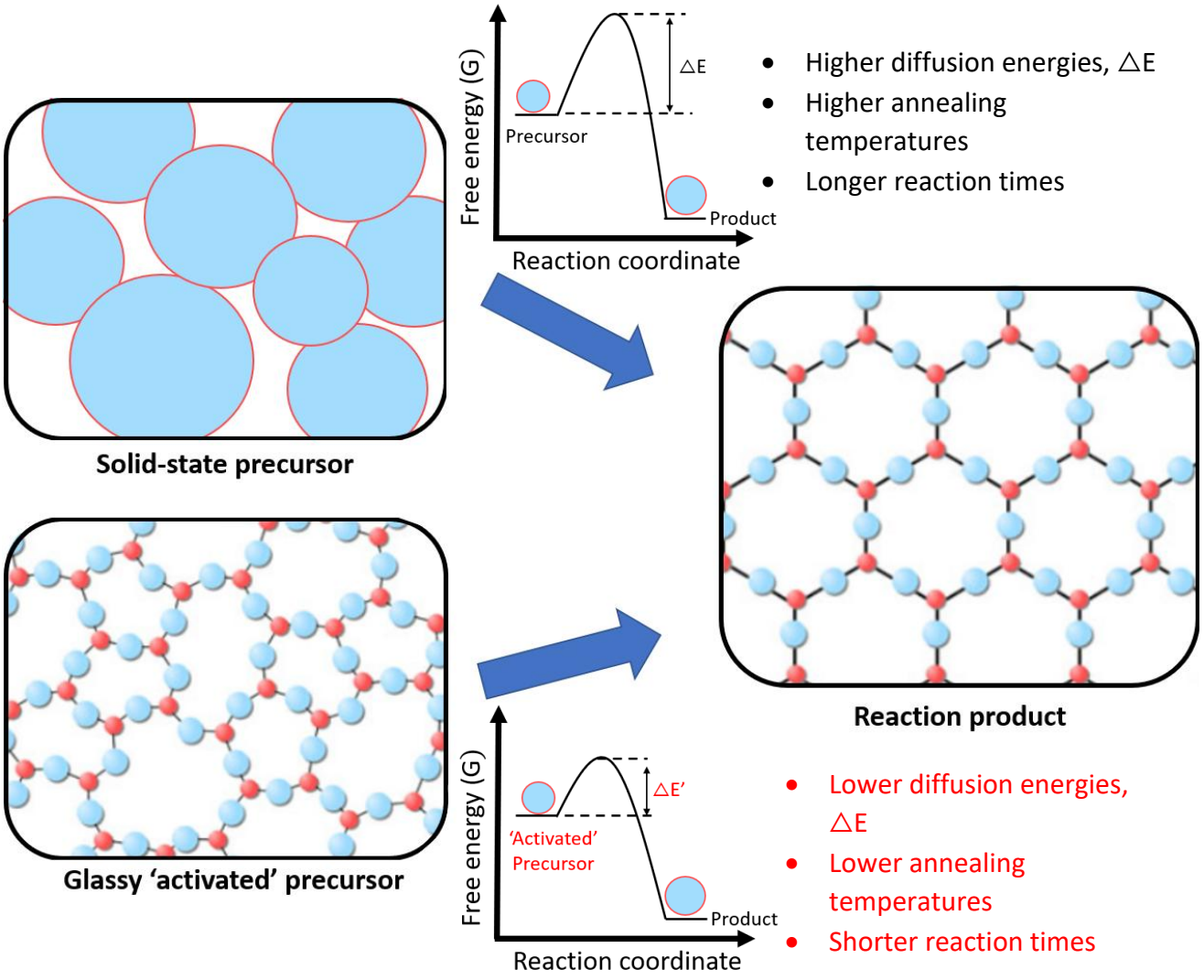

Fig. 1.4. Comparison of reaction pathways when starting from conventional solid-state precursors vs. glassy 'activated' precursors.

Using glass as a starting point for crystalline phase synthesis simplified the number of targetable compositions. As a key factor in a composition's glass-forming ability is whether it can form a covalently bonded network.[33] Specifically, the composition must contain a network former, such as Si^{4+} (SiO_2), which ensures the formation of long, strongly bonded chains essential for glass formation.[34] A network intermediate (e.g. Al^{3+}, Ge^{4+}, Ga^{3+}… etc.) then links the network former to a network modifier (e.g. Sr^{2+}) which is added to impart properties such as hardness and strength.[35] These glass-forming conditions, again, highlighted why the SrO-$AlO_{1.5}$-SiO_2 diagram was selected for investigation, as it incorporates all of these factors. It also explains why ADL was considered as a synthesis route, as its ability to reach high temperatures and rapidly quench samples, expands the investigable regions within the SrO-$AlO_{1.5}$-SiO_2 phase space. Additionally, the substitution of the network modifier (Ba^{2+}, Ca^{2+}, La^{2+}) and the network intermediate (Ge^{4+}, Ga^{3+}) to enhance or modify specific properties of the synthesised phases was also explored in this work.

1.2.6. Glass Crystallisation - Step 2. Crystallisation

In the second step of GC, synthesised glass is sintered as either a bulk sample or pelletised powder to form a glass-ceramic, or, if fully crystallised, a ceramic. In industry, a commonly added pre-annealing step for bulk samples is to relax the glass at 100°C below its glass transition temperature (T_g), which releases internal constraints in the samples.[36]

Glass-ceramics were first discovered by D. Stookey at Corning in 1953 and have most recently been described as: "*inorganic, non-metallic materials prepared by controlled crystallisation of glasses via different processing methods. They contain at least one type of functional crystalline phase and a residual glass. The volume fraction crystallized may vary from ppm to almost 100%*".[15,37] The ability of this class of material to combine the versatile properties of glass with the strength and stability of crystals has led to numerous improvements in both consumer and specialised products.[38]

While the exact mechanism of crystallisation processes is still debated, the classical nucleation theory (CNT) theory is widely used, due to its simplicity.[39] This theory assumes that crystallisation occurs as a two steps process: (i) initial nucleation of the glass (homogeneously or heterogeneously), where seed crystals appear, (ii) growth of the seed crystals into ordered crystalline domains (Fig. 1.5.).[40] Step (i) occurs at temperatures slightly above the T_g, whereas step (ii) occurs above the crystallisation temperature (T_c). For metastable phases a second exothermic event is also commonly observed, which represents the decomposition of the phase and is annotated as T_d in this work.

Control of the crystallisation process is crucial for the formation of metastable glass-ceramics or ceramics, not only to prevent phase decomposition but also to optimise properties.[41] The size, shape, quality, and orientation of the crystals within the glass or fully crystallised matrix have all been found to influence the final properties of a material.[42,43]

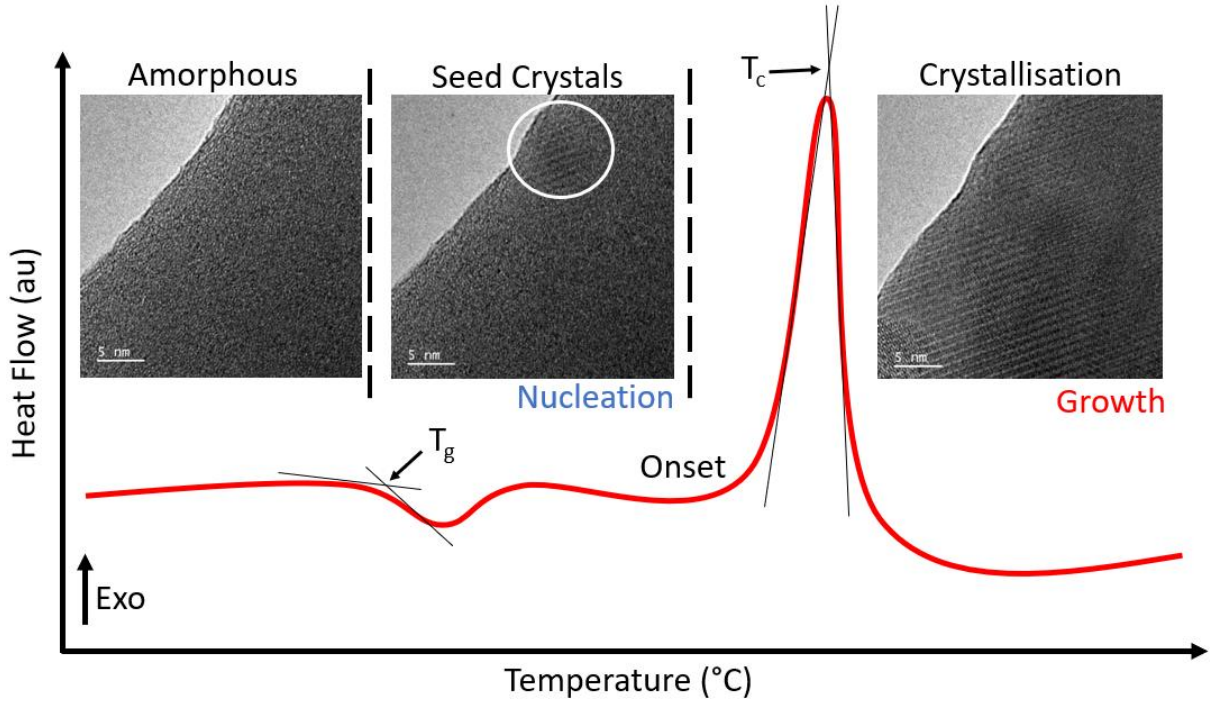

Fig 1.5. Diagram of a crystallisation process following the CNT mechanism, a typical DSC trace is used to show the temperature dependence of crystal nucleation and growth. The insets show *in-situ* transmission electron microscopy (TEM) images of the crystallisation of yttrium aluminium garnet (YAG). The first (amorphous) was taken at room temperature, while the second and third (seed crystals & crystallisation) were taken just below and above 810°C. The TEM images were recorded by Dr. J. Rezkallah.

Homogeneous nucleation is, typically, the desired mechanism of crystallisation as it leads to volume crystallisation, i.e. instantaneous crystallisation of the sample in the absence of nucleation points.[44] This results in homogeneous properties being observed across the sample. However, in reality this is rarely observed due to nucleation centres (sample surface, crucible, impurities etc…) causing heterogenous crystallisation to occur, i.e. different nucleating points inducing crystallisation throughout the sample. This type of crystallisation, presents the opportunity for unique benefits however. If microstructural features of the crystallites, such as their size, shape, and orientation, can be controlled then specific properties (e.g. transparency) can be targeted.[43,45,46] Studies have identified nucleating agents as the primary method for controlling crystallisation, with respect to properties.[41,47] However, full and congruent crystallisation induced from the surface of bulk glass is another approach explored in this work, aimed at enhancing the properties of the discovered phases.[48]

Crystallisation of phase-pure metastable glass-ceramics or ceramics was targeted by careful optimisation of the sintering step and the samples composition. In certain cases, nucleating agents, such as ZrO_2, $ZrTiO_4$, and Al_2O_3 were also added to the 'activated' glass, as they have been shown to improve or even induce crystallisation in glass by increasing the number of nucleating sites.[49–51] An increase in nucleation sites lowers the activation energy of the reaction, helping to favour metastable synthesis.[52] Other factors such as particle

size and the addition of dopants or substitutions, were also investigated as ways of targeting metastable phase synthesis and tuning properties.

1.2.7. Mechanical Activation of Glass by High Energy Milling

While the advantages of GC are numerous, it has one main drawback. It is only effective on compositions or systems where glass formation is possible. In such cases where it isn't, high energy milling (HEM) can be used as an alternative route to amorphous precursors without going through the T_g. Use of this technique can therefore expand the range of investigable compositions from an 'activated precursor' starting point.

In this work however, as the highly vitrifiable $SrO\text{-}AlO_{1.5}\text{-}SiO_2$ diagram was being explored, HEM was used to achieve 'mechanical activation' of the glass. This technique (specifically employed in Chapter 3) increased surface area by reducing particle size (nm scale), and was motivated by the need to promote surface-based crystallisation. Through this reduction in particle size, HEM lowers a reactions activation energy by increasing the surface contact between reactant grains. As shown in Fig. 1.6., a decrease in a reactions activation energy by HEM, coincides with an increase in its free energy.[24] This effect can therefore be harnessed to promote the favourability of metastable product formation, and is especially prominent in systems where surface nucleation is the dominant crystallisation mechanism.

The metastable phase, WO_3, exemplifies HEM, as it is the only solventless technique capable of accessing it, when followed by a post-annealing step.[53] Homogenisation of the powder mixtures promotes phase-pure synthesis by preventing concentrated areas of any one precursor.

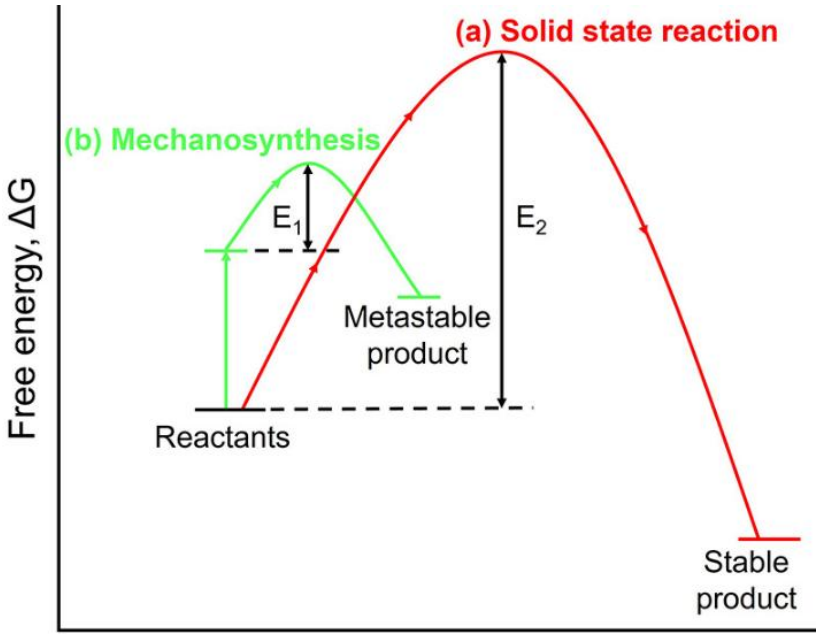

Fig. 1.6. Free energy reaction profile of two reactions using the same initial precursors. **(a)** solid-state reaction (red line) and **(b)** 'mechanical activation' through HEM (green line). Figure taken from [24].

In some cases, it has been shown that the energy imparted into the system from milling is sufficient to induce crystallisation, allowing it to also be considered as a synthesis method. Finally, on the lab scale, this method can be used to scale up synthesis, as up to 10g of powder can be prepared at any one time.

1.2.8. Glass Formation by Aerodynamic Levitation Coupled to Two CO_2 Lasers

The final method used to complement furnace-based glass formation, was aerodynamic levitation coupled to laser heating, (ADL).[54,55] This technique permitted higher melting temperatures (up to 3000°C) and quenching times (~1000°C/s) to be achieved. This approach extends the glass-forming limits of phase diagrams (SrO-$AlO_{1.5}$-SiO_2) by enabling the vitrification of compositions that would otherwise be impossible by classic melt-quenching methods. This is achieved through the use of a container-less levitation approach which prevents nucleation sites occurring from the crucible. The absence of a crucible also allows for rapid cooling rates, as heat loss occurs through radiative processes from the sample itself.

Control of the cooling rate and mass of the reactants was found to play a major role in the phases synthesised by ADL. As demonstrated by the work of W. Cao *et al.* who found that three different phases were synthesisable from the same starting composition, by varying the cooling rate and mass of the bead used, (Fig. 1.7.). It was found that, from the same parent YAG precursor, it was possible to synthesise glass, when a high cooling rate was used, a mixture of perovskite $YAlO_3$ and corundum Al_2O_3, when a slower cooling rate was used, and a single garnet phase when a medium cooling rate, which matched a classical approach, was used.[56]

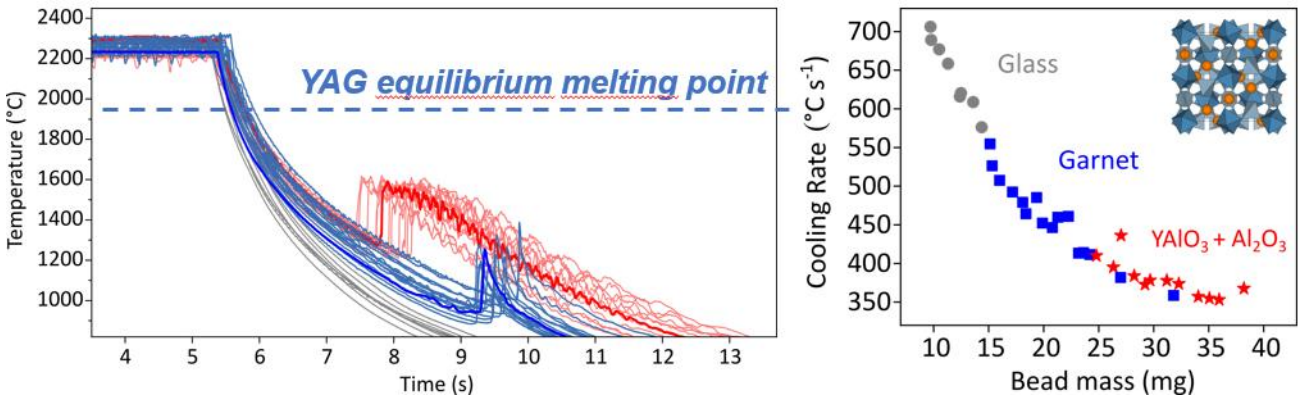

Fig. 1.7. *In-situ* cooling curves obtained in the YAG system when different masses of precursor were fired by ADL and the products achieved at these rates and mass. Figure taken from [56].

1.2.9. Phase Space Exploration by Computational Predication

Complementary to the synthesis work in this project, a state-of-the-art computational prediction tool, developed by M. Dyer and C. Collins at the university of Liverpool, was employed.[18] This collaboration had already been established at the start of this project. Specifically, the "probe structure" method, using the MC-EMMA and FUSE structure-prediction codes, was applied to calculate the formation energies of known

and theoretical structures within the SrO-$AlO_{1.5}$-SiO_2 ternary diagram.[57] These energies were then ranked by a second DFT relaxation step, to create an energy map of the diagram, which subsequently guided its exploration. This technique permits efficient identification of 'zones of interest' (lighter coloured areas of Fig. 1.8.), with the most potential to yield stable (new) crystalline phases. Fig. 1.8. illustrates the systematic exploratory pathway employed in this work, demonstrating the adaptability of this approach. The pathway can be repeated until the diagram is fully exhausted, (zones A, B, and C etc.), after which the compositional precursors can be modified, (e.g. CaO, La_2O_3, Ga_2O_3, GeO_2 etc…) and the energy map recalculated. Computational prediction played a crucial role in isolating the phase discussed in Chapter 3, $Sr_2Si_3O_8$, as the crystalline component of a complex glass-ceramic.

The SrO-$AlO_{1.5}$-SiO_2 ternary diagram was selected for computational exploration for two main reasons. Historically, it is a well explored diagram, meaning any new phase discovery would demonstrate the effectiveness of this approach. Additionally, known aluminosilicates such as $LaAlSiO_5$, $SrAl_2O_4$, and $SrAl_2Si_2O_8$, have already shown the diverse, tuneable properties and structural types within this diagram.[19,20,58] Finally, as already discussed, Si^{4+} and Al^{3+} are prominent glass formers, meaning that almost the entire phase diagram can be explored by GC.[59,60] A technique that is most effective for exploratory synthesis when a broad region of the diagram being investigated is accessible in glass form. Compared to solid-state reactions, use of GC also enabled shallower energy regions of the diagram to be investigated by reducing energy requirements for reaction.

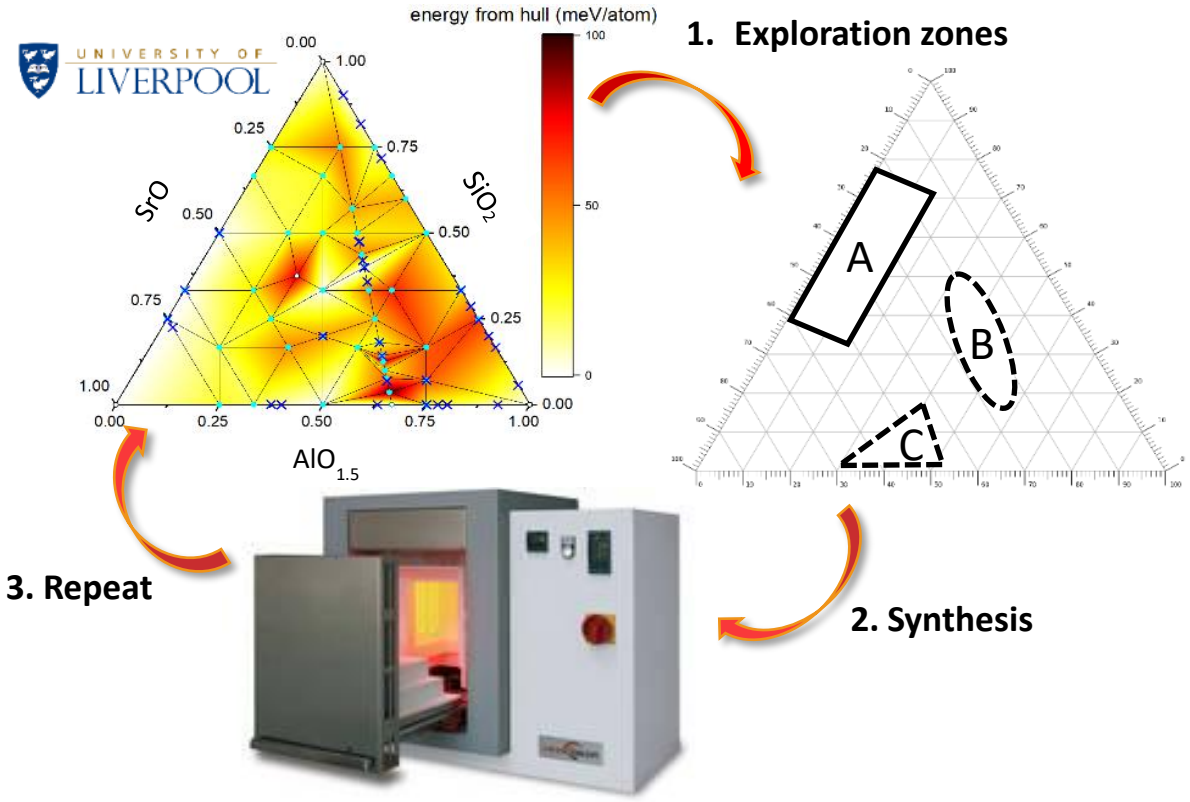

Fig. 1.8. Schematic showing the general methodology used in this work. The energy map of the SrO-$AlO_{1.5}$-SiO_2 diagram used in this work is shown in the top left [18,61].

1.3. Notable Phases Discovered by Glass Crystallisation

Although GC has been used as a technique for several decades in the field of vitroceramics, there is surprisingly little literature on its application for the targeted discovery of new crystalline phases, highlighting the need for this work. The majority of GC research has focussed on enhancing the existing properties of materials (microstructure engineering, bulk mechanical, and thermomechanical).[62] Below notable phases that have been discovered through GC are presented.

1.3.1. $BaAl_4O_7$ & $BaGa_4O_7$

Through investigation of the BaO-Al_2O_3 pseudo binary system, a new phase, $BaAl_4O_7$, was discovered by M. Allix *et al.*[63] Conventional equilibrium methods proved unsuccessful in the vitrification of this pseudo binary system and so ADL was used instead. Subsequent full crystallisation of $1/3BaO - 2/3Al_2O_3$ glass yielded two metastable polymorphs of $BaAl_4O_7$, shown in Fig. 1.9. The α-form crystallised at 960°C, while the β-form irreversibly formed at 1080°C. *Ab-initio* structural determination revealed the structural uniqueness of both polymorphs, demonstrating the fundamental potential of GC in novel phase discovery, as neither of these polymorphs were accessible by conventional methods.

The crystallographic interest of this phase was matched by its functional potential. Both polymorphs were found to be transparent as fully crystallised ceramic beads, (Fig. 1.9.), enabling their use in a wide range of industries, scintillators in particular.[64]

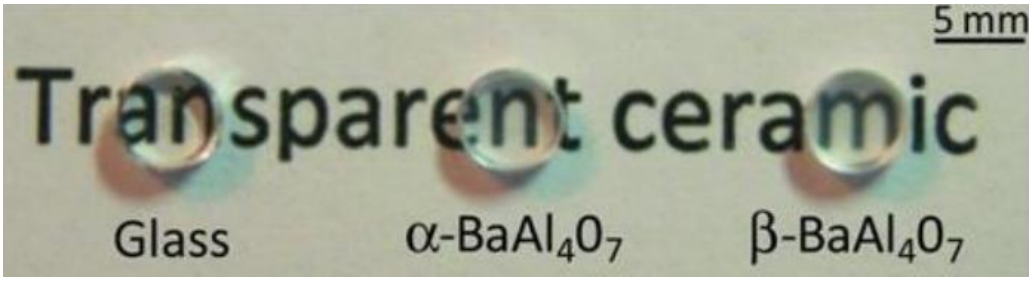

Fig. 1.9. Transparency achieved in the glass of $BaAl_4O_7$ and the fully crystallised α-$BaAl_4O_7$ and β-$BaAl_4O_7$ forms. From [63].

The gallium analogue of $BaAl_4O_7$ (*I*2/*m*) was also found to be synthesisable by ADL, through direct crystallisation of the cooling melt. This phase was found as an original but also atypical member of the $A_3BC_{10}O_{20}$ structural framework due to the exclusive presence of divalent and trivalent cations. The presence of these cations resulted in a disordered defect-type partial substitution of Ga^{2+} and O^{2-} ions onto the Ba^{2+} sites, particularly those in the pentagonal channels of the framework, in order to maintain charge neutrality. However, due to this, a high degree of structural flexibility was observed in the crystalline phase, which enabled $BaGa_4O_7$ to be heavily doped with Eu^{2+}, thus allowing strong orange-luminescence emission to be observed in the 618 nm range when excited with 393 nm light.[65]

1.3.2. $SrREGa_3O_7$ Melilites

Work by Boyer *et al.* reported a series of metastable melilites, SrREGa3O7 (rare-earth, RE = Eu-Yb, Y), which were only synthesisable through the use of GC.[66] When the phase was originally discovered by a solid-state approach, dopants were limited to La-Tb, however, through the use of GC this range was extended to include the smaller RE elements Dy-Yb and Y. When precursor glasses of these compositions were prepared by quenching from 1650°C and then crystallised at 700-765°C, single-phase melilites were obtained. Broyer observed that further heating of these phases, above 850°C, resulted in thermal decomposition of the phase. It was also observed that through full and congruent crystallisation of the glass (discussed further in Section 1.4.2.) large transparent ceramics could be prepared from these compositions (Fig.1.10.) and that white light emission was possible for Dy^{3+} or Tb^{3+}/Eu^{3+} doped samples, after UV excitation.[66] The PhD work of H. Bazzaoui further investigated this phase and found complex cation ordering between Sr and RE (in the metastable regime RE<Tb), which could be controlled by different heating procedures.[67]

Fig. 1.10. The range of small RE melilite samples, SrREGa3O7 (RE = Eu-Yb, Y), which could only be synthesised by a GC approach. The transparency observed in each sample is shown.

1.3.3. Non-Stoichiometric YAG

Stoichiometric YAG is a well-known material for commercial and technological scintillation applications.[68] However, its structural inflexibility constrains the doping of optical elements to a single sublattice. Meaning that the optical properties of YAG are generally dictated by the dopant selected, with very little room for tuning via control of the crystalline lattice. The discovery of non-stoichiometric YAG ($Y_{3+x}Al_{5-x}O_{12}$) by ADL synthesis, in principle, removed this constraint as the excess of Y^{3+} must be incorporated at an alternative site within the structure.[56] This generates a second site for RE dopants to be accommodated and is of particular interest for dopants such as Ce^{3+}, who show emission and absorption properties which are sensitive to the local crystal field splitting. Meaning that the luminescent spectra may be controllable by altering the degree of non-stoichiometry in the host YAG structure. The full range of non-stoichiometric YAG compositions ($0 < x < 0.40$) were only found to be synthesisable by ADL routes (briefly discussed in Section 1.2.8.), with direct melt quenching or classic GC approaches leading to reduced solid-solution ranges.

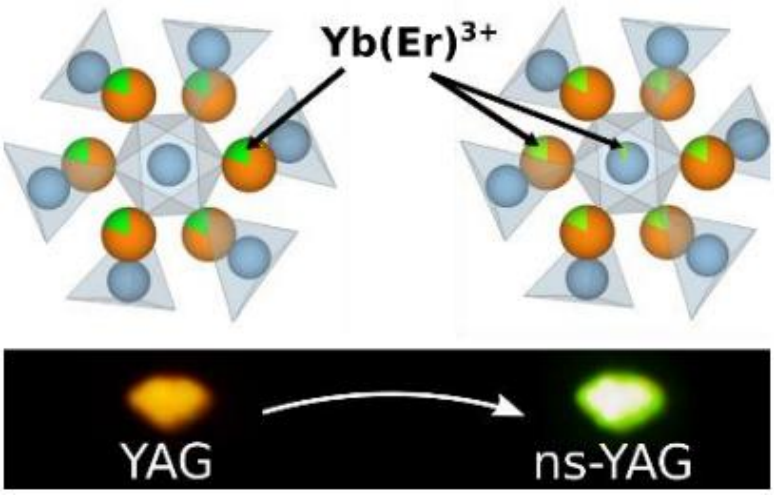

Fig. 1.11. Doping sites and luminescence colour observed in YAG and non-stoichiometric YAG, with Yb^{3+}, Er^{2+} as the dopants. As shown, the change in the host lattice results in a change in the emission colour. From [56].

1.3.4. $Li_2Si_3O_5$ & $Li_2Si_3O_7$

Crystalline lithium silicates are an important class of materials in solid-state chemistry, owing to their wide range of applications in glass-ceramics, CO_2 absorbers, and solid electrolytes for lithium batteries.[69–71] Notably, $Li_2Si_3O_5$ is highly relevant to the field of glass-ceramics, as the first developed glass-ceramic was based on this composition.[72] The high Si content of the system readily enabled exploratory synthesis from a glassy starting point.

Despite $Li_2Si_3O_5$ representing the origins of glass-ceramics, $Li_2Si_3O_7$ combines glass-ceramics and metastable synthesis therefore making it more relevant to the work here.[73] When the binary Li_2CO_3-SiO_2 system was investigated via GC, the metastable phase $Li_2Si_3O_7$ was discovered.[74,75] This underscores the value of GC as a technique, as it enables the discovery of useful phases even in well-explored phase diagrams.

1.3.5. $Pb_5Ge_3O_{11}$

Using GC, a metastable orthorhombic polymorph of $Pb_5Ge_3O_{11}$ was discovered.[76] Crystals of this phase exhibit preferred growth along the polar c-axis, perpendicular to the surface (Fig. 1.12.), making their geometry ideal for use as pyroelectric infrared detectors. More generally, the ferroelectric properties of this phase suggest potential applications in the electronic, thermal, and photovoltaic industries.[77] Although it was discovered in the 1970s, the crystal structure of this phase has yet to be solved, meaning that the full potential of $Pb_5Ge_3O_{11}$ remains untapped. Resolving the structure may reveal methods for tuning its ferroelectric properties.

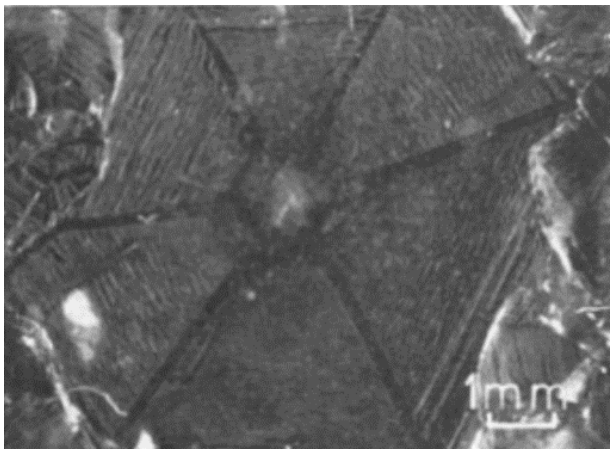

Fig. 1.12. $Pb_5Ge_3O_{11}$ thin film crystals obtained by GC. From [76].

1.4. Applications of Glass-Ceramics & Metastable Phases

So far, new compositions and properties have been discussed at the unit cell scale. However, as mentioned previously, microstructural engineering can also be harnessed to elucidate properties on the nano- or micro-scale. The synthesis of glass-ceramics, facilitates unique microstructural engineering and property tuning possibilities through the combination of glassy and crystalline properties. Additionally, targeting metastable glass-ceramics or ceramics, may facilitate the synthesis of new structure types whose functional potentials are yet to be studied. The polycrystalline nature of glass-ceramics and ceramics makes this microstructure tuning possible, for example through, specific orientation of the crystal domains, non-stoichiometry of the composition and changing porosity. Literature has demonstrated that glass-ceramics, in particular, can be tailored to applications in a wide range of industries (dentistry, medicine, lasers etc…), as shown in Fig. 1.13.[2,78–80]

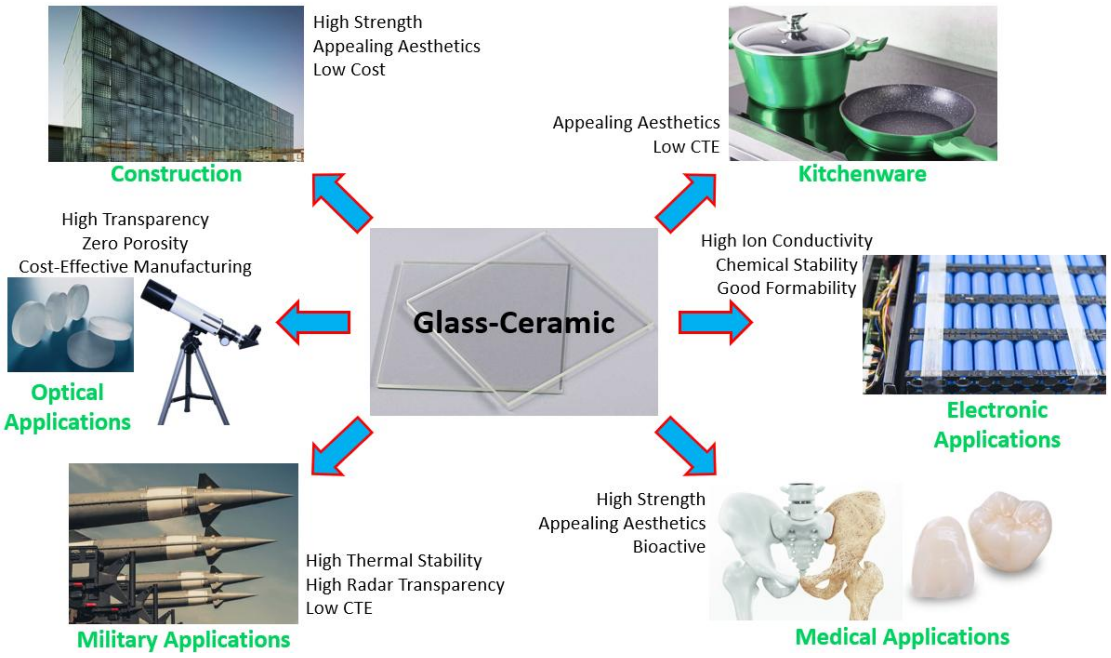

Fig. 1.13. Examples of the wide range of industries that glass-ceramics have been applied. Image inspired by [78].

In this work, the properties of transparency and phosphorescence were targeted based on literature findings that identified notable phases with these properties within the SrO-$AlO_{1.5}$–SiO_2 phase diagram. The SiO_2 component of this diagram meant that glass formation was possible, making transparency an attainable property if the crystallisation process was carefully controlled. The parameters required to achieve these properties will be discussed in the following sections.

1.4.1. Conditions for Transparency

A perfectly transparent glass-ceramic does not show any of the following processes: absorption, scattering, and reflection (surface).[81] For polycrystalline glass-ceramics these conditions are almost impossible to meet due to several factors, with porosity, cracks, grain boundaries and crystallite size being the most common (Fig. 1.14.).[82–85] These inclusions create scattering or birefringent centres which cause the diffusion of incident light, reducing the theoretical maximum transmission.[86] When crystallising from bulk glasses, a fully dense material, it is possible to maintain this density and therefore increase the likelihood of transparency.

In glass-ceramics, Rayleigh-type light scattering is important to consider, as it applies to the majority of transparent examples in this material class.[87] This type of light scattering relates the size of the crystallites and the distance between them to the wavelength of the incident light.[88] Examining this model shows that transparency can be improved by reducing crystallite size (approximately 10x smaller than the incident wavelength) and/or by reducing the variations in refractive indices encountered when passing from one media to another. The dual nature of glass-ceramics, being both glassy and crystalline, means that any differences in the refractive indices of the glass and the crystalline phase will reduce transmission as light passes through the material.[89]

To minimise this effect, as well as the other factors mentioned, careful preparation of the glass and its subsequent crystallisation is essential. The use of high-purity reactants, (>99.99%), can remove impurities. While synthesis methods which permit homogenised reaction products and full phase-pure crystallisation, such as GC, can limit grain boundary, pore and crack scattering effects.

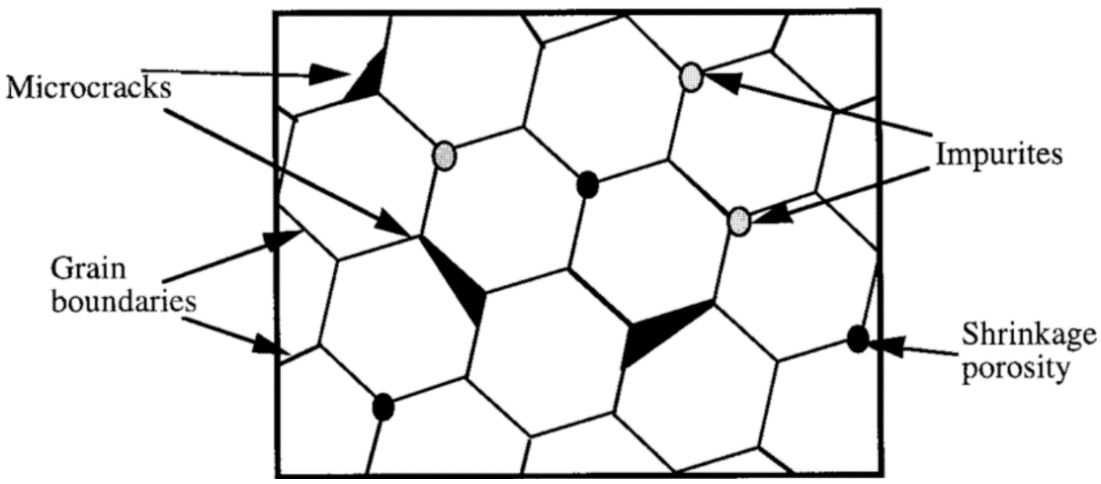

Fig. 1.14. The common defects within glass-ceramics that can limit their transparency.

1.4.2. Transparent Ceramics by Full & Congruent Crystallisation of Bulk Glass

A method for inducing transparency in the glass-ceramics synthesised during this work was to consider crystallisation of the bulk glass.[90] As suggested, this approach enables transparency through the complete crystallisation of parent bulk glasses, resulting in ceramic pieces.[48,91,92] This factor reduces scattering centres by crystallising from a fully dense material and minimises refractive index differences. Careful preparation of the glass, e.g. relaxation of the phase and polishing of the surface, must be adopted to remove bubbles and surface roughness which can impact the level of transparency observed.

This method is advantageous for its ease of use, ability to produce large glass-ceramic pieces and the use of inexpensive equipment. It has already produced a variety of transparent samples, such as the previously discussed $BaAl_4O_7$, (Fig. 1.9), $Sr_3Al_2O_6$, $Sr_3Ga_2O_6$, YAG-Al_2O_3 and the solid solution $Sr_{1-x/2}Al_{2-x}Si_xO_4$ ($0.1 < x \leq 0.5$), (Fig. 1.14.(a)).[63,93–95] This method was also adopted by the IRCER laboratory in Limoges to develop tellurite (TBN) based polycrystalline ceramics of composition $75TeO_2$-$12.5Nb_2O_3$-$12.5Bi_2O_3$, (Fig. 1.14.(b)).[96]

In this work the method was further extended, by considering partial surface crystallisation of the bulk glass. This was effective in systems where crystallisation could be induced from the surface, such as those discussed in Chapter 2, $SrAl_2SiO_6$ & $Sr_{12}Al_{20}Si_{12}O_{66}$. Through a layered 'sandwich-like' crystallisation a combination of transparency from the glass and properties from the crystalline phase was achieved. By controlling the depth of the crystalline layer and orientation of the surface crystallites the transparency could be tuned as desired.[97] This partial crystallisation approach aligned more with the goal of synthesising glass-ceramics rather than fully crystalline ceramics.

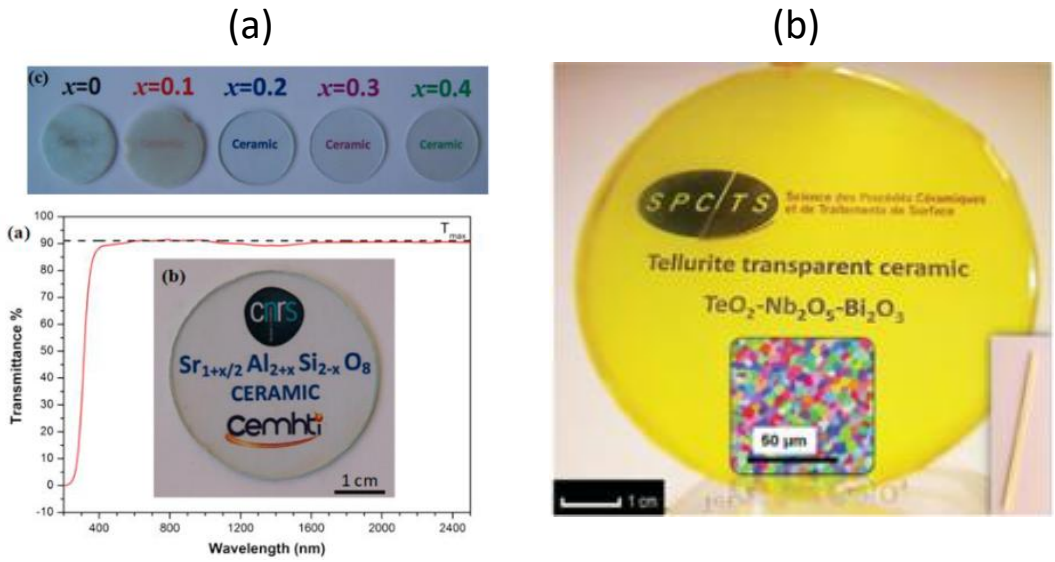

Fig. 1.14. Transparent ceramics achieved by crystallisation of the parent glass. **(a)** $Sr_{1+x/2}Al_{2+x}Si_{2-x}O_8$ ($0 \leq x \leq 0.4$) [48], and **(b)** transparent tellurite (TBN) based polycrystalline ceramic [96].

1.4.3. Optical Properties Combined with Transparency

Photoluminescence (PL) is an active optical property characterised by the instantaneous emission of light from excited electronic states, after their absorption of light (typically UV).[98] Many phases within the SrO-$AlO_{1.5}$-SiO_2 ternary diagram have been found to exhibit optical properties such as PL, when doped with lanthanides.[19–21,95] Consequently, PL and related properties, such as persistent luminescence (PersL) and mechanoluminescence (ML) were targeted in the functionalisation of any discovered phases. When combined with transparency, PL, PersL, and ML properties can be enhanced by facilitating light emission and absorption throughout the sample volume (the volume effect) rather than just the surface.[99] This combination, therefore, serves to expand the applicational limits of any discovered glass-ceramics or ceramics.

In this work, functionalisation by lanthanide doping was targeted for both powdered and bulk samples. Typically, Eu^{2+} and Dy^{3+} were chosen as the doped luminescent centres, as literature had demonstrated their effectiveness in existing aluminosilicate systems such as $SrAl_2O_4$:1%Eu^{2+},2%Dy^{3+}.[19] However, other elements such as Tm^{3+}, Cr^{3+}, and Ho^{3+} were also considered as means of tuning the colour, intensity, storage capacity, and afterglow kinetics of any PL or PersL properties observed. Doping both cation and anion sites was also considered as ways of further tuning the optical properties.

1.4.4. Examination of Persistent Luminescence

PersL is correlated to PL, in that it is characterised by a materials ability to emit light after excitation. However, for PersL materials, the relaxation mechanism can take many hours, enabling the material to continue emitting light long after the excitation source has been removed, (Fig. 1.15.(a)).[100,101] The property was first observed in Bologna stone (baryte) in 1603 and has since been implemented in many industries, e.g. bio-imaging, safety signage, decoration and optical image storage, and become the basis of many studies.[102–104] Particular attention has been paid to the SrO-$AlO_{1.5}$-SiO_2 diagram, as it can be said that, in addition to sulphide based systems, materials within this phase space produce the most efficient afterglow effect in the visible spectrum.[5,19,105]

The current understanding of the PersL mechanism is described in Chapter 4 (4.7.1.), however, the guiding principle is an electron capture and release process (electron trap model).[106] When the material is optically excited, an electron-hole (e-h) pair is created, excited electrons are then trapped at structural defects, usually referred to as electron traps (typically a second doped lanthanide). These electrons are then slowly released, over time, back to the electron holes left in the luminescent centres, by thermal stimulation of the sample. This effect produces the afterglow effect the eye sees as PersL, (Fig. 1.15.(b)). Therefore, common strategies in the designing of these materials is engineering of the electron trap depths, doping concentrations of the

luminescent centres, the luminescent centres themselves, and the band gap energy.[107,108] All of these factors play a role in the colour, lifetime and intensity of the light produced.

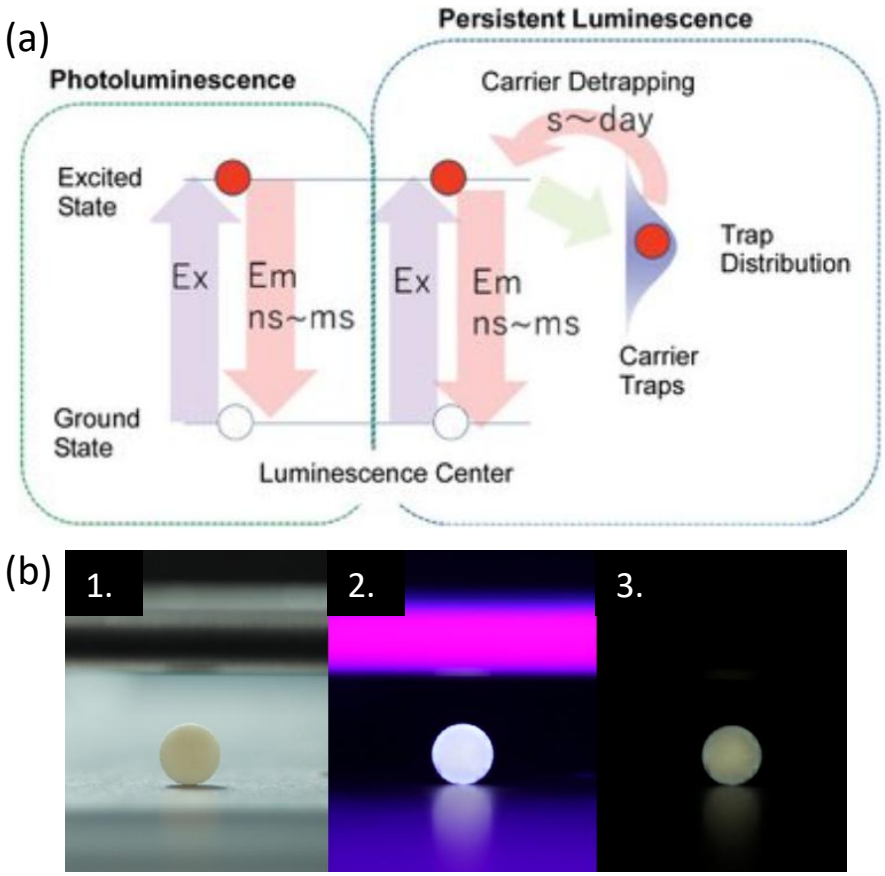

Fig. 1.15. (a) Schematic comparing the PL and PersL mechanisms, from [109]. **(b)** Images of white PersL from Bi^{3+}-doped $ZnGa_2O_4$ ceramics, **(1)** before excitation, **(2)** under excitation, **(3)** after excitation stops, from [110].

1.5. The Current Generation of PL & PersL Phosphors Within the SrO-$AlO_{1.5}$-SiO_2 Diagram

1.5.1. $SrAl_2O_4:Eu^{2+},Dy^{3+}$

A benchmark example of PL and PersL properties, is $SrAl_2O_4$, co-doped with 1%Eu^{2+} and 2%Dy^{3+} ($SrAl_2O_4:Eu^{2+},Dy^{3+}$).[19] It was first reported as a green emitting, PersL phase in 1996 by Matsuzawa *et al.*, with two decades of subsequent research leading to its usage in industries such as jewellery making, road markings and safety signage.[111,112] Initially, studies on the phase saw it solely doped it with Eu^{2+}, due to the identical 2+ oxidation state and the similar ionic radii of Sr^{2+} and Eu^{2+}. However, the afterglow effect was seen to dramatically increase from a few minutes to over 30 hours when the sample was co-doped with Dy^{3+}.[113] The effect of co-doping and substitution has since become the basis of many optical $SrAl_2O_4$ studies, as methods of tuning the intensity and colour of the emitted light. For example, it was found that near infrared

(NIR) PersL emission, with a lifetime of 10 minutes, could be achieved in $SrAl_2O_4:Eu^{2+}$, when co-doped with Er^{3+}.[114]

The substitution of Ca^{2+} in $SrAl_2O_4:Eu^{2+},Dy^{3+}$, was also found to be a way of tuning the green PL emission to blue light, (Fig. 1.16.).[115] In terms of PersL emission, both the Ba and Ca analogue of $SrAl_2O_4$, ($BaAl_2O_4$ & $CaAl_2O_4$), were found to have a blue PersL properties when doped with Tb^{3+} and Eu^{2+}, Nd^{3+} respectively.[116,117] Therefore, the substitution of Ba^{2+}/Ca^{2+} for Sr^{2+} could lead to tailoring of the PersL colour between green and blue. Although, to date not many studies have investigated this effect.[118] Y. Cai *et al.* has reported, however, that the PersL lifetime of $BaAl_2O_4$ is ~3h30 and so colour tuning may come at the cost of lifetime.[116]

Evidently, the lack of options when it comes to tuning of the optical properties in $SrAl_2O_4:Eu^{2+},Dy^{3+}$ remains a major limitation of the phase. New phases must be considered to fill the remaining gaps in the colour wheel left by $SrAl_2O_4:Eu^{2+},Dy^{3+}$. Focus was placed on systems doped with Eu^{2+} as its emission exhibits a strong dependence on the host matrix. Its 4f7–5d0 to 4f6–5d1 electronic transitions are highly sensitive to the crystal field environment, which affects the energy of the 5d orbital.[119] This sensitivity causes the emission wavelength to vary significantly with changes in the host matrix, unlike the shielded 4f electrons in other lanthanides, which are less affected by the surrounding lattice. Another drawback of $SrAl_2O_4$ is its lack of a network-forming element, such as Si, and the propagation of cracks induced by a monoclinic-to-hexagonal phase transition upon cooling from high temperatures during single crystal synthesis. As a result, it is challenging to produce the phase as a transparent bulk material.[120] The narrower range of property flexibility demonstrated by $SrAl_2O_4:Eu^{2+},Dy^{3+}$ has meant that since its discovery in 1996 only moderate improvements in its properties have been observed.[5]

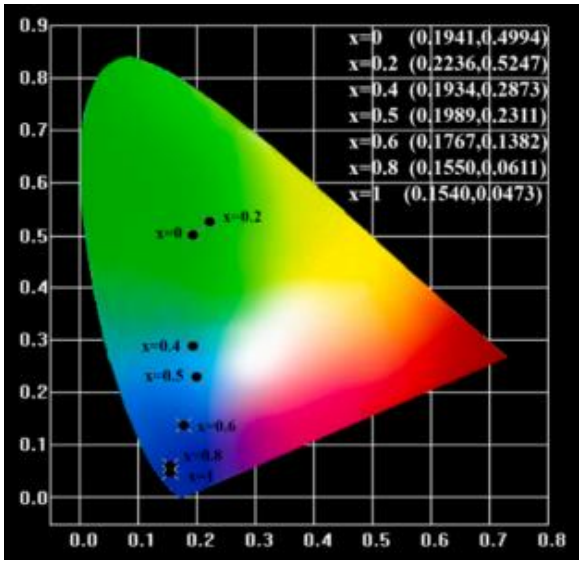

Fig. 1.16. CIE (commission international de l'éclairage) coordinates of the PL emission from the $Sr_{1-x}Ca_xAl_2O_4:Eu^{2+},Dy^{3+}$ (x = 0, 0.2, 0.4, 0.6, 0.8, 1.0) solid solution, when excited with 361 nm light. From [115].

1.5.2. $Sr_{1-x/2}Al_{2-2x}Si_xO_4$

Producing transparent pieces of $SrAl_2O_4:Eu^{2+},Dy^{3+}$ was addressed in the work by V. Castaing *et al.* who investigated the $SrAl_2O_4$-SiO_2 tie line as a route to incorporating Si into the structure.[95] This work successfully synthesised a hexagonal polymorph of $SrAl_2O_4$, according to the solid solution formula $Sr_{1-x/2}Al_{2-2x}Si_xO_4$ ($0.1 \leq x \leq 0.5$). These samples could be made as large transparent ceramic pieces with intense, long lasting PersL properties. Moreover, the PersL emission could be tuned from green to blue by adjusting the Si content. This blue shift was attributed to coordination changes in the Eu^{2+} environment as x increased, leading to a higher contribution of Dy^{3+} in the emission.[95] Interestingly, emission intensity was also found to be tuneable through adjustment of the Si^{4+}/Al^{3+} ratio, which opened another consideration for property tuning in this work. Finally, the phase was synthesised by ADL proving how out-of-equilibrium synthesis can be harnessed in the discovery of new phases. $Sr_{1-x/2}Al_{2-2x}Si_xO_4$ is discussed again at the beginning of Chapter 2 to provide the contextual foundation of the chapter.[21]

1.5.3. $Sr_{1+x/2}Al_{2+x}Si_{2-x}O_8$

Feldspars ($MAl_2Si_2O_8$ – M=Sr, Ca, Ba, Na, K) are one of the most abundant minerals in the earth's crust, and as such have been extensively investigated for potential applications.[121,122] Focussing specifically on optical phenomena, the phase has been found to exhibit highly tuneable PL properties, with blue, red, white and even yellow colours all observed. This colour tuning is achieved by substitution of Sr^{2+} for Ca^{2+} or Ba^{2+} and/or doping of the phase with $Eu^{2+/3+}$, $Ce^{3+}/Tb^{3+}/Sm^{3+}$, (Fig. 1.17.).[20]

In 2014, a former PhD student of the CERAM team, K. Saghir, further extended the limits of $SrAl_2Si_2O_8$, by investigating non-stoichiometry of its hexacelsian polymorph.[48] This polymorph was found as part of a solid solution according to the formula $Sr_{1+x/2}Al_{2+x}Si_{2-x}O_8$ ($0 \leq x \leq 0.4$). Using the full and congruent crystallisation of bulk glass technique (discussed in Section 1.4.2.) large transparent ceramic pieces of this material were synthesised. Again, it was found that by modulating the Al^{3+}/Si^{4+} ratio it was possible to alter the defect occurrence and therefore control the degree of transparency. Similar to the implications of V. Castaing's work on the $Sr_{1-x/2}Al_{2-2x}Si_xO_4$ solid solution, the idea of property tuning through the Al^{3+}/Si^{4+} ratio was highly relevant now that it had been demonstrated to be effective in the tuning of PL, PersL properties as well as transparency. The remaining limitation of the non-stoichiometric hexacelsian polymorph is that it is yet to exhibit PersL properties. If achieved to the same degree of colour tunability and transparency as its stoichiometric counterpart, it could become a potential competitor of the current standard, $SrAl_2O_4:Eu^{2+},Dy^{3+}$.

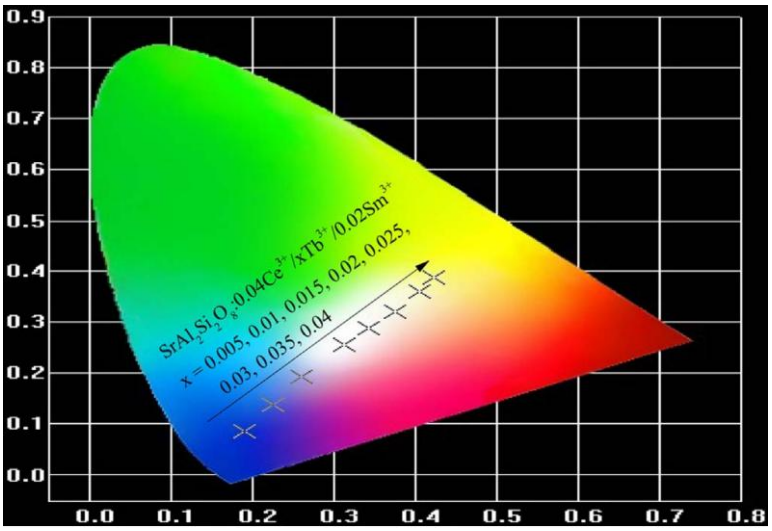

Fig. 1.17. CIE diagram showing the tunability of $SrAl_2Si_2O_8$ when doped with $Ce^{3+}/Tb^{3+}/Sm^{3+}$. From [20].

1.6. Exploration of Mechanoluminescence

Mechanoluminescence (ML) is another optical property investigated in this work. It was first reported by Francis Bacon in 1605, when he noticed the emission of light when sugar was scraped with a knife.[123,124] Despite the time which has passed since its discovery it is still relatively poorly understood and only a handful of materials are known to exhibit this property.[125,126] The phenomena can be described as a material's ability to emit light when mechanical stimulus is applied to it (stimulus can take the form of friction, impact and/or compression etc).[125,127,128] Different names are given to ML depending on the deformation applied: for elastic deformation elasto-mechanoluminescence (EML) is used, for plastic deformation plastico-mechanoluminescence (PML) is used and for fracture deformation fracto-mechanoluminescence (FML) is used. EML in particular, has piqued the interest of construction industries due to its application as stress/strain sensors to monitor the lifetime of structures.[125,129,130]

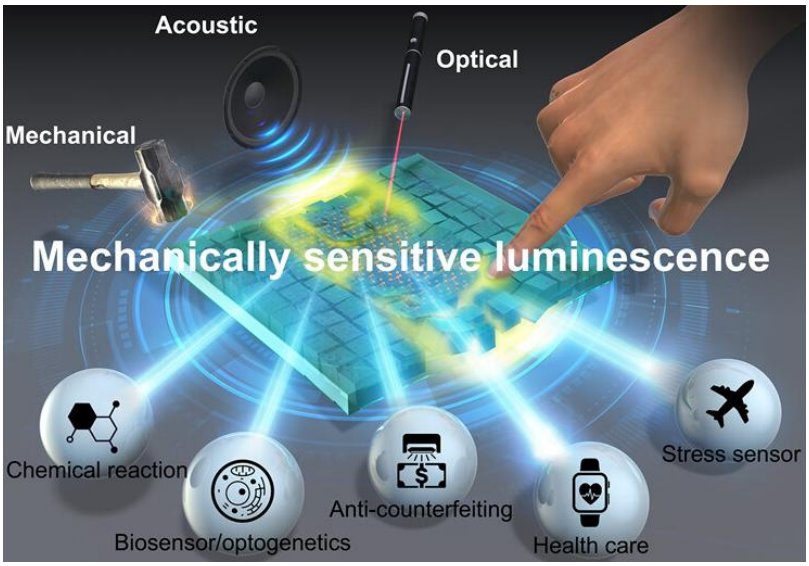

Fig. 1.18. Diagram showing the wide range of potential ML applications. Taken from [131].

For example, ML materials can be applied as an adhesive coating on bridges to monitor their load baring capabilities and ensure the fail point isn't reached.[125] In a similar vein, EML materials are also used in the medical sector, to monitor the load bearing of bones, additional examples are shown in Fig. 1.18. In this work, two new ML samples were found, $Sr_{12}Al_{20}Si_{12}O_{66}$ and $Sr_2Si_3O_8$, which produced green and blue light, respectively, therefore expanding the number of known ML materials.

1.6.1. Understanding the Mechanism of Mechanoluminescence

The exact mechanism that causes the transfer of mechanical energy to the emission of light in these materials is still unclear, due to the numerous factors which seem to play a role. Such as, mechanical effects in the material, polarity of the space group and trap depths of the luminescent centres.[131–133] Particularly, work by P. Smet *et al.* has attempted to summarise the current understanding and models used to describe the ML phenomena.[134] However, building a general mechanism to describe this phenomenon has been difficult, which has made the targeting and optimisation of ML phases difficult. It appears related to PersL properties in that the sample must first be charged (UV, visible light etc.) to trap charge carriers in excited states. The mechanism of release then differs, with the mechanical stimulus facilitating the un-trapping of electrons.[134] Investigations into literature revealed that a number of phases in the $SrO\text{-}AlO_{1.5}\text{-}SiO_2$ diagram, which exhibited PL and PersL properties and had a polar space group, were also ML materials.[131,135,136] This is what initially sparked interest in investigating the martials discovered in Chapters 2 and 3, for potential ML properties.

1.6.2. Examples of Mechanoluminescent Phases

Once again $SrAl_2O_4:Eu^{2+},Dy^{3+}$, was found to produce remarkable green emitting ML properties, which were proportional to the mechanical stress applied.[19,137,138] Due to its ease of synthesis (the solid-state method) it has become the benchmark of ML phases, not only in the $SrO\text{-}AlO_{1.5}\text{-}SiO_2$ diagram. Although an easy method, the solid-state approach prevents transparent ML phases from being explored. Therefore, investigating the synthesis of ML phases using the GC method, could provide a cheap alternative route to these phases with enhanced properties. M. Zhang *et al.*, took the capabilities of $SrAl_2O_4:Eu^{2+},Dy^{3+}$, even further, by showing that controlled substitution of Sr^{2+} for Ca^{2+} allowed the ML colour to be tuned from green to blue, and emission intensity to be tailored.[115] This highlighted substitution as one method of tuning ML properties, however, as shown in Fig. 1.19., many other routes exist. Additionally, it was found that by doping $SrAl_2O_4:Eu^{2+}$ with Er^{3+} or Nd^{3+}, emission could be tuned to the near infra-red (NIR) region.[139] This made investigations into the effect of substitutions and lanthanide doping on the ML properties an interesting research question to explore.

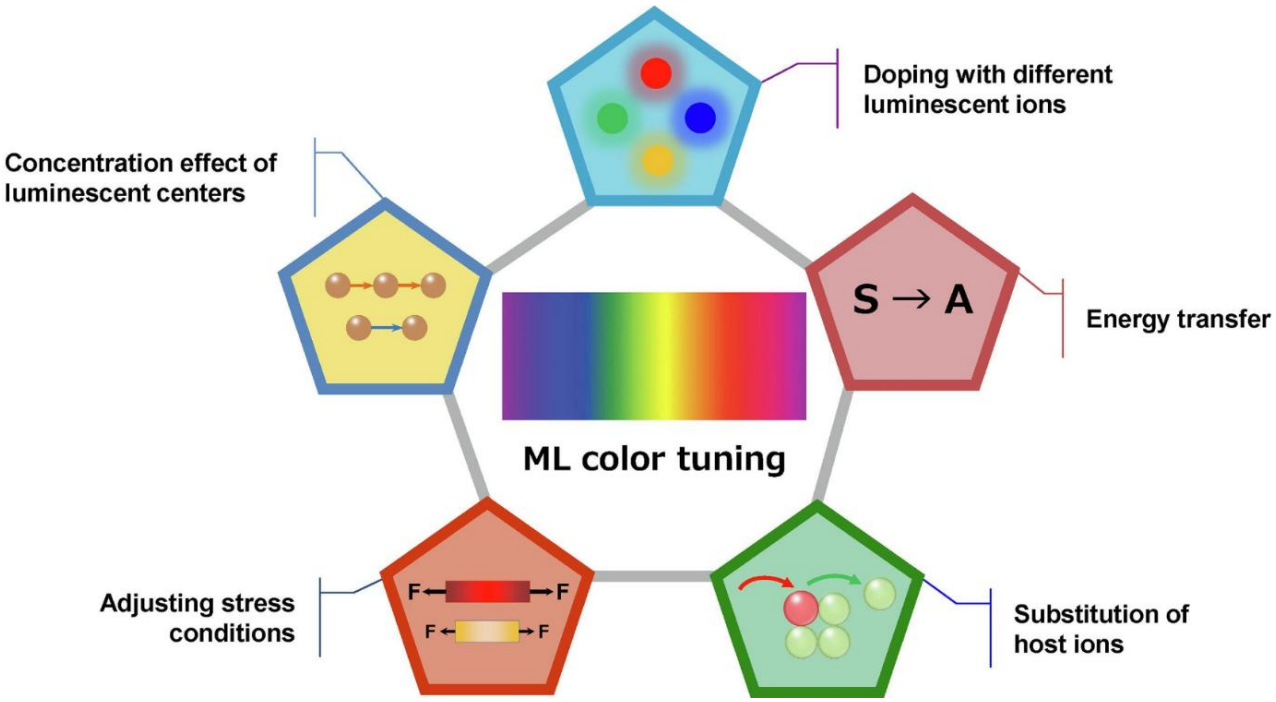

Fig. 1.19. Schematic of the current methods employed to tune ML colour emission. Taken from [125].

$CaAl_2Si_2O_8$ was another phase found to have (blue emitting) EML properties which again were tuneable through Sr^{2+} substitution, although to a lesser extent than $SrAl_2O_4$ Eu^{2+},Dy^{3+}.[130,140] This phase again support the idea of tuning emission colour through substitution of the cation. Which prompted the investigation of analogous compounds to any new phases found in this work as a way of tuning properties, particularly emission colour.

The Ba analogue ($Ba_4Si_6O_{16}$) of the phase discussed in Chapter 3 ($Sr_2Si_3O_8$) is one example of analogous phase searches inspiring property investigation. The analogous relationship between the $Sr_2Si_3O_8$ and $Ba_4Si_6O_{16}$ was realised through comparison of their structure types in the Bilbao crystallographic server.[141,142] $Ba_4Si_6O_{16}$ ($P2_1/c$ – polar, Fig.1.20.(a)) was synthesised using the solid-state method, in addition to the oxynitride method detailed in Chapter 4 (4.1.3.), showing the thermodynamic stability of the phase. This also provided a route to stabilisation of $Sr_2Si_3O_8$, through substitution with Ba^{2+}. Work by A. Duval *et al.*, found that doping $Ba_4Si_6O_{16}$ with Eu^{2+} and another lanthanide, Ho^{3+} in particular, long lasting green PL & EML properties were observed.[143–145] EML emission was induced by exciting the sample with 365 nm light and then applying a stress of 1.8 $MPas^{-1}$ (Fig. 1.20.(b)). Unfortunately, the colour of emission couldn't be tuned by varying the doped lanthanide, stress applied, or wavelength of excitation. This work provided a basis for the functionalisation of $Sr_2Si_3O_8$, discussed in Chapter 3, as it was believed that similar properties would be achieved due to the analogous structure types.

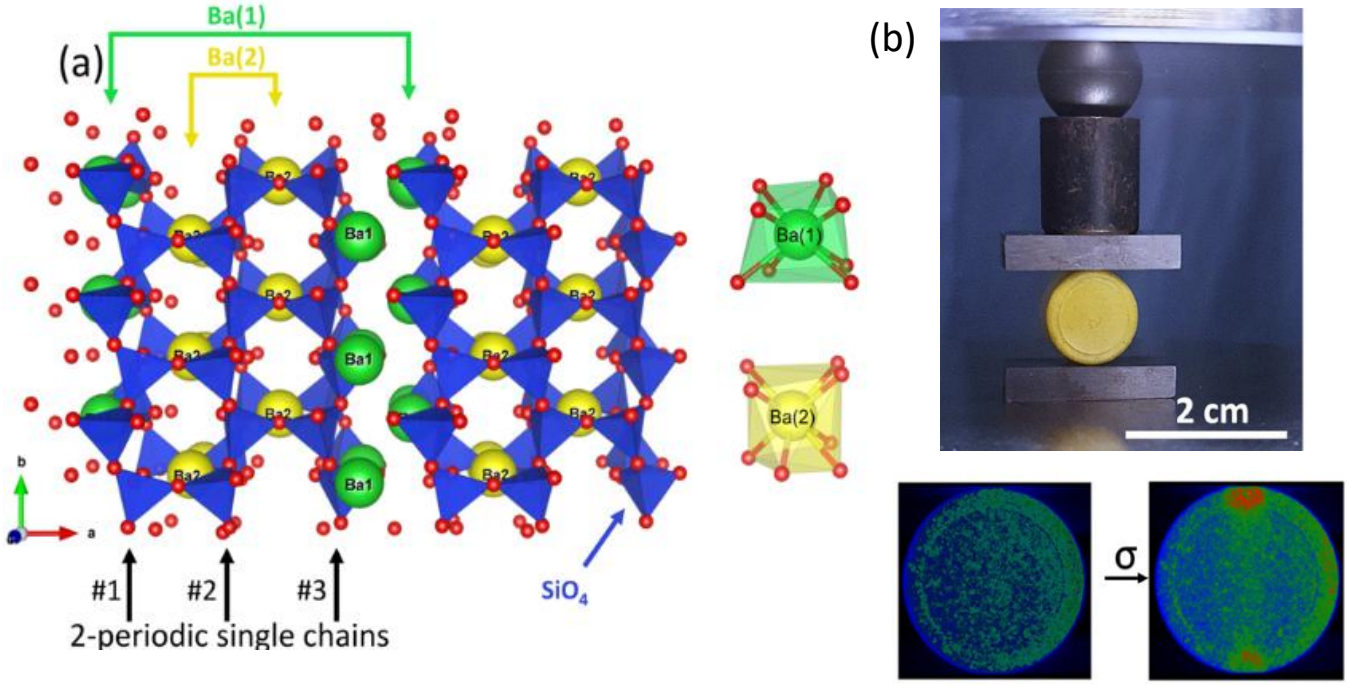

Fig. 1.20. (a) Crystal structure of $Ba_4Si_6O_{16}$, (green/ yellow) Ba1 and Ba2 atoms, (blue) Si based polyhedral, (red) O atoms. **(b)** Photograph of the ML experimental setup, with the sample before and during compression shown below, the increased luminescence shows the ML effect. Figures taken from [143,144].

1.7. Chapter Conclusion

In this chapter, a combined approach involving innovative synthesis methods (crystallisation from out-of-equilibrium states) and computational predictive software is outlined in the search for new glass-ceramic materials, with a particular focus on metastable glass-ceramics within the $SrO\text{-}AlO_{1.5}\text{-}SiO_2$ ternary diagram. This work represents one of the first instances in which combined approach of this type has been applied specifically to novel phase discovery. It aims to partially address the challenges faced by materials science in meeting the ever-increasing demand for improved properties, which can no longer be satisfied through the incremental improvement of existing phases.

The GC approach was primarily adopted in the synthesis of new metastable strontium aluminosilicates, based on preliminary computational work (conducted prior to this thesis) that identified the most amenable regions of the $SrO\text{-}AlO_{1.5}\text{-}SiO_2$ phase diagram. GC was focussed on as an innovative approach due to the ease with which it produces glass, by definition an out-of-equilibrium state, and how it can easily be scaled up for industrial applications. It was also a logical state of matter to target as much of the $SrO\text{-}AlO_{1.5}\text{-}SiO_2$ diagram is vitrifiable. The theory behind why the glassy state makes the ideal starting point for new, metastable, materials was discussed. With its 'activated' state lowering $\triangle E$ of the product formation step and thereby promoting the favourability of products which are missed by conventional techniques, such as the solid-state

method. This is demonstrated in Chapters 2 and 3, as the novel materials discovered in these sections were not accessible by the solid-state method.

Finally, methods for functionalising the materials discovered in this work and their potential applications were discussed. Optical properties were focused on, as investigations into literature found notable phases in the SrO-$AlO_{1.5}$-SiO_2 diagram, ($SrAl_2O_4$:Eu^{2+},Dy^{3+}, $SrAl_2Si_2O_8$:La & $Ba_4Si_6O_{16}$:La, where La=lanthanide(s)) which produced intense and long-lasting PL, PersL and ML effects. The introduction of transparency into discovered phases which exhibited these properties was also discussed. This was made possible through the use of GC, which inherently facilitates transparency by synthesising from glass, as well as benefitting from the volume effect of luminosity. The GC method for producing transparent samples, as discussed in Chapters 2 & 3, was further enhanced through partial glass crystallisation from the bulk.

In conclusion, this chapter has outlined an exciting novel method for the discovery of new crystalline phases. The following chapters will explore and exemplify the advantages of this approach in the synthesis of two new metastable compositions, $Sr_{12}Al_{20}Si_{12}O_{66}$ (Chapter 2) & $Sr_2Si_3O_8$ (Chapter 3), and characterisation of their different luminescence properties.

1.8. References

[1] D. M. Herlach, *Materials Science and Engineering: A*, 1997, **226–228**, 348–356.
[2] O. J. Akinribide, G. N. Mekgwe, S. O. Akinwamide, F. Gamaoun, C. Abeykoon, O. T. Johnson and P. A. Olubambi, *Journal of Materials Research and Technology*, 2022, **21**, 712–738.
[3] C. Greskovich and S. Duclos, *Annual Review of Materials Research*, 1997, 27, 69–88.
[4] N. Almakayeel, G. Velu Kaliyannan and R. Gunasekaran, *Ceramics International*, 2024, **50**, 42392–42403.
[5] D. Van der Heggen, J. J. Joos, A. Feng, V. Fritz, T. Delgado, N. Gartmann, B. Walfort, D. Rytz, H. Hagemann, D. Poelman, B. Viana and P. F. Smet, *Advanced Functional Materials*, 2022, **32**, 2208809.
[6] S. T. S. Bukkapatnam, *IISE Transactions*, 2023, **55**, 75–93.
[7] A. Rajagopal, K. Yao and A. K.-Y. Jen, *Advanced Materials*, 2018, **30**, 1800455.
[8] M. J. Hossain, M. Sun and K. O. Davis, *Solar Energy Materials and Solar Cells*, 2024, **267**, 112715.
[9] C. Collins, L. Daniels, Q. Gibson, M. Gaultois, M. Moran, R. Feetham, M. Pitcher, M. Dyer, C. Delacotte, M. Zanella, C. Murray, G. Glodan, O. Perez, D. Pelloquin, T. Manning, J. Alaria, G. Darling, J. Claridge and M. Rosseinsky, *ANGEWANDTE CHEMIE-INTERNATIONAL EDITION*, 2021, **60**, 16457–16465.
[10] L. Orlova, A. Chainikova, L. Alekseeva and M. Voropaeva, *Russian Journal of Inorganic Chemistry*, 2015, **60**, 1692–1707.
[11] T. Charpentier, K. Okhotnikov, A. N. Novikov, L. Hennet, H. E. Fischer, D. R. Neuville and P. Florian, *J. Phys. Chem. B*, 2018, **122**, 9567–9583.
[12] A. Ellison and I. A. Cornejo, *International Journal of Applied Glass Science*, 2010, **1**, 87–103.
[13] D. P. Shoemaker, Y.-J. Hu, D. Y. Chung, G. J. Halder, P. J. Chupas, L. Soderholm, J. F. Mitchell and M. G. Kanatzidis, *Proceedings of the National Academy of Sciences of the United States of America*, 2014, **111**, 10922–10927.
[14] X. Cui, Y. Liu and Y. Chen, *National Science Review*, 2024, **11**, nwae033.
[15] M. Allix and L. Cormier, *Techniques de l'Ingénieur*, DOI:10.51257/a-v1-n4802.
[16] A. Parija, G. R. Waetzig, J. L. Andrews and S. Banerjee, *J. Phys. Chem. C*, 2018, **122**, 25709–25728.
[17] M. J. McDermott, B. C. McBride, C. E. Regier, G. T. Tran, Y. Chen, A. A. Corrao, M. C. Gallant, G. E. Kamm, C. J. Bartel, K. W. Chapman, P. G. Khalifah, G. Ceder, J. R. Neilson and K. A. Persson, *ACS Cent. Sci.*, 2023, **9**, 1957–1975.
[18] C. Collins, M. S. Dyer, M. J. Pitcher, G. F. S. Whitehead, M. Zanella, P. Mandal, J. B. Claridge, G. R. Darling and M. J. Rosseinsky, *Nature*, 2017, **546**, 280–284.
[19] R. E. Rojas-Hernandez, F. Rubio-Marcos, M. Á. Rodriguez and J. F. Fernandez, *Renewable and Sustainable Energy Reviews*, 2018, **81**, 2759–2770.
[20] Y. Wu, L. Zhu and H. Mao, *Ceramics International*, 2018, **44**, 10015–10019.
[21] A. J. Fernandez-Carrion, K. Al Saghir, E. Veron, A. I. Becerro, F. Porcher, W. Wisniewski, G. Matzen, F. Fayon and M. Allix, *Inorg. Chem.*, 2017, **56**, 14446–14458.
[22] F. Leyvraz, H. Larralde and D. P. Sanders, *The European Physical Journal B - Condensed Matter and Complex Systems*, 2006, **50**, 57–61.

[23] H. B. Callen and R. B. Griffiths, *American Journal of Physics*, 1987, **55**, 860–861.
[24] X. Zhi and A. R. West, *Chem. Mater.*, 2023, **35**, 6790–6798.
[25] T. Takahashi, O. Yamamoto, S. Yamada and S. Hayashi, *Journal of The Electrochemical Society*, 1979, **126**, 1654.
[26] K. H. J. Buschow, *Encyclopedia of materials : science and technology*, Elsevier, Amsterdam, 2001.
[27] A. R. West, *Solid state chemistry and its applications*, John Wiley & Sons, Ltd., Chichester, West Sussex, Second edition, student edition., 2014.
[28] J. Livage, *Current Opinion in Solid State and Materials Science*, 1997, **2**, 132–138.
[29] L. L. Hench and J. K. West, *Chem. Rev.*, 1990, **90**, 33–72.
[30] B. M. Abel, J. M. Morgan, J. C. Mauro and M. M. Smedskjaer, *International Journal of Applied Glass Science*, 2013, **4**, 225–230.
[31] *Nature Physics*, 2022, **18**, 603–603.
[32] E. D. Zanotto and J. C. Mauro, *Journal of Non-Crystalline Solids*, 2017, **471**, 490–495.
[33] J. M. Parker, in *Encyclopedia of Condensed Matter Physics*, eds. F. Bassani, G. L. Liedl and P. Wyder, Elsevier, Oxford, 2005, pp. 273–280.
[34] Z. Zhang and W. Kob, *Phys. Rev. B*, 2024, **110**, 104203.
[35] Y. Murakami, T. Usuki, S. Kohara, Y. Amo and Y. Kameda, *Journal of Non-Crystalline Solids*, 2007, **353**, 2035–2038.
[36] G. Kumar, D. Rector, R. D. Conner and J. Schroers, *Acta Materialia*, 2009, **57**, 3572–3583.
[37] G. H. Beall, *Frontiers in Materials*, 2016, **3**, 37.
[38] J. Deubener, M. Allix, M. J. Davis, A. Duran, T. Höche, T. Honma, T. Komatsu, S. Krüger, I. Mitra, R. Müller, S. Nakane, M. J. Pascual, J. W. P. Schmelzer, E. D. Zanotto and S. Zhou, *Journal of Non-Crystalline Solids*, 2018, **501**, 3–10.
[39] S. Karthika, T. K. Radhakrishnan and P. Kalaichelvi, *Crystal Growth & Design*, 2016, **16**, 6663–6681.
[40] M. C. Weinberg, W. H. Poisl and L. Granasy, *Comptes Rendus Chimie*, 2002, **5**, 765–771.
[41] W. Höland, V. Rheinberger and M. Schweiger, *Philosophical Transactions of The Royal Society A: Mathematical, Physical and Engineering Sciences*, 2003, **361**, 575–589.
[42] Q. Fu, G. Beall and C. Smith, *MRS Bulletin*, 2017, **42**, 220–225.
[43] G. H. Beall, *Annual Review of Materials Research*, 1992, 22, 91–119.
[44] V. M. Fokin, E. D. Zanotto, N. S. Yuritsyn and J. W. P. Schmelzer, *Journal of Non-Crystalline Solids*, 2006, **352**, 2681–2714.
[45] A. Babu, A. Ebrahimi, K.-H. Wu, I. M. Richardson and M. J. M. Hermans, *Journal of Materials Research and Technology*, 2023, **26**, 1508–1526.
[46] G. G. Santos, F. C. Serbena, V. M. Fokin and E. D. Zanotto, *Acta Materialia*, 2017, **130**, 347–360.
[47] E. Kleebusch, C. Patzig, M. Krause, Y. Hu, T. Höche and C. Rüssel, *Ceramics International*, 2020, **46**, 3498–3501.
[48] K. Al Saghir, S. Chenu, E. Veron, F. Fayon, M. Suchomel, C. Genevois, F. Porcher, G. Matzen, D. Massiot and M. Allix, *Chem. Mater.*, 2015, **27**, 508–514.
[49] A. Shearer, M. Montazerian, B. Deng, J. J. Sly and J. C. Mauro, *International Journal of Ceramic Engineering & Science*, 2024, **6**, e10200.
[50] E. Kleebusch, C. Patzig, T. Höche and C. Rüssel, *Journal of Materials Science*, 2016, **51**, 10127–10138.
[51] W. Xu, X. Tian, J. Wang, L. Li and J. Han, *Ceramics International*, 2024, **50**, 23150–23156.
[52] A. V. DeCeanne, L. R. Rodrigues, C. J. Wilkinson, J. C. Mauro and E. D. Zanotto, *Journal of Non-Crystalline Solids*, 2022, **591**, 121714.
[53] X. Fang, M. Yao, L. Guo, Y. Xu, W. Zhou, M. Zhuo, C. Shi, L. Liu, L. Wang, X. Li and W. Chen, *ACS Sustainable Chem. Eng.*, 2017, **5**, 10735–10743.
[54] C. J. Benmore and J. K. R. Weber, *Advances in Physics: X*, 2017, **2**, 717–736.
[55] X. Fang, V. Castaing, A. Becerro, W. Cao, E. Veron, D. Zanghi, M. Dyer, C. Genevois, M. Allix and M. Pitcher, 2024, preprint, DOI: 10.26434/chemrxiv-2024-1s1wc.
[56] W. Cao, A. I. Becerro, V. Castaing, X. Fang, P. Florian, F. Fayon, D. Zanghi, E. Veron, A. Zandonà, C. Genevois, M. J. Pitcher and M. Allix, *Adv Funct Materials*, 2023, **33**, 2213418.
[57] C. Collins, G. R. Darling and M. J. Rosseinsky, *Faraday Discuss.*, 2018, **211**, 117–131.
[58] V. Kahlenberg and H. Krüger, *Solid State Sciences*, 2004, **6**, 553–560.
[59] M. R. Cicconi and D. Neuville, 2019, pp. 771–812.
[60] A. R. Cooper, *Journal of Non-Crystalline Solids*, 1982, **49**, 1–17.
[61] E. M. Duncan, A. Ridouard, F. Fayon, E. Veron, C. Genevois, M. Allix, C. M. Collins and M. J. Pitcher, *Chem. Commun.*, 2023, **59**, 10544–10547.
[62] S. Machida, K. Maeda, K. Katsumata and A. Yasumori, *ACS Omega*, 2022, **7**, 33266–33272.
[63] M. Allix, S. Alahrache, F. Fayon, M. Suchomel, F. Porcher, T. Cardinal and G. Matzen, *Advanced Materials*, 2012, **24**, 5570–5575.
[64] G. Patton, F. Moretti, A. Belsky, K. Al Saghir, S. Chenu, G. Matzen, M. Allix and C. Dujardin, *Phys. Chem. Chem. Phys.*, 2014, **16**, 24824–24829.
[65] M. Boyer, E. Véron, A. I. Becerro, F. Porcher, M. R. Suchomel, G. Matzen and M. Allix, *CrystEngComm*, 2015, **17**, 6127–6135.
[66] M. Boyer, A. J. F. Carrion, S. Ory, A. I. Becerro, S. Villette, S. V. Eliseeva, S. Petoud, P. Aballea, G. Matzen and M. Allix, *J. Mater. Chem. C*, 2016, **4**, 3238–3247.
[67] Haytem Bazzaoui. Synthesis and Complete Characterisation of new Oxide Materials by full and Congruent Crystallisation from Glass or the Molten liquid. Materials Science [cond-mat.mtrl-sci]. Université d'Orléans, 2022.
[68] M. Moszyński, T. Ludziejewski, D. Wolski, W. Klamra and L. O. Norlin, *Nuclear Instruments and Methods in Physics Research Section A: Accelerators, Spectrometers, Detectors and Associated Equipment*, 1994, **345**, 461–467.
[69] G. H. Beall and D. A. Duke, *Glass: Science and Technology*, 1983, **1**, 404.
[70] A. Khorassani and A. R. West, *Journal of Solid State Chemistry*, 1984, **53**, 369–375.
[71] K. Essaki, K. Nakagawa, M. Kato and H. Uemoto, *Journal of Chemical Engineering of Japan*, 2004, **37**, 772–777.

[72] S. Stookey, *Industrial & Engineering Chemistry*, 1953, **45**, 115–118.
[73] E. M. Levin and H. F. McMurdie, .
[74] M. Matveev and V. Velya, *Glass and Ceramics*, 1959, **16**, 543–549.
[75] A. R. West and F. P. Glasser, *Materials Research Bulletin*, 1970, **5**, 837–842.
[76] K. Takahashi, L. E. Cross and R. E. Newnham, *Materials Research Bulletin*, 1975, **10**, 599–602.
[77] L. W. Martin and A. M. Rappe, *Nature Reviews Materials*, 2016, **2**, 16087.
[78] L. Fu, H. Engqvist and W. Xia, *Materials*, DOI:10.3390/ma13051049.
[79] I. Alekseeva, O. Dymshits, M. Tsenter, A. Zhilin, V. Golubkov, I. Denisov, N. Skoptsov, A. Malyarevich and K. Yumashev, *Journal of Non-Crystalline Solids*, 2010, **356**, 3042–3058.
[80] A. R. BOCCACCINI, in *Biomaterials, Artificial Organs and Tissue Engineering*, eds. L. L. Hench and J. R. Jones, Woodhead Publishing, 2005, pp. 26–36.
[81] S. F. Wang, J. Zhang, D. W. Luo, F. Gu, D. Y. Tang, Z. L. Dong, G. E. B. Tan, W. X. Que, T. S. Zhang, S. Li and L. B. Kong, *Progress in Solid State Chemistry*, 2013, **41**, 20–54.
[82] P. A. Tick, N. F. Borrelli and I. M. Reaney, *Optical Materials*, 2000, **15**, 81–91.
[83] S. P. Singh and A. D. Sontakke, *Crystals*, 2021, **11**, 156.
[84] X. Zhao, Q. Fang, C. Xia, Y. Xie, D. Wu, X. Chao and Z. Yang, *Journal of the American Ceramic Society*, 2023, **106**, 527–537.
[85] A. Ikesue and Y. L. Aung, *Nature Photonics*, 2008, **2**, 721–727.
[86] H. Shahbazi, M. Tataei, M. H. Enayati, A. Shafeiey and M. Azizi. Malekabadi, *Journal of Alloys and Compounds*, 2019, **785**, 260–285.
[87] T. Dunch and S. D. Jackson, *Opt. Mater. Express*, 2022, **12**, 2595–2608.
[88] D. L. Andrews, in *Encyclopedia of Spectroscopy and Spectrometry (Third Edition)*, eds. J. C. Lindon, G. E. Tranter and D. W. Koppenaal, Academic Press, Oxford, 2017, pp. 924–930.
[89] J. Hostaša, F. Picelli, S. Hříbalová and V. Nečina, *Open Ceramics*, 2021, **7**, 100137.
[90] I. Milisavljevic, M. J. Pitcher, J. Li, S. Chenu, M. Allix and Y. Wu, *International Materials Reviews*, 2023, **68**, 648–676.
[91] Amandine Ridouard. *Caractérisation de nouvelles céramiques transparentes et verres nanostructurés par spectroscopie RMN haute résolution du solide*. These Université Orléans, *2023.*
[92] Kholoud Al Saghir. Transparent ceramics by full crystallization from glass : application to strontium aluminosilicates. Other. Université d'Orléans, 2014.
[93] S. Alahraché, K. Al Saghir, S. Chenu, E. Véron, D. De Sousa Meneses, A. I. Becerro, M. Ocaña, F. Moretti, G. Patton, C. Dujardin, F. Cussó, J.-P. Guin, M. Nivard, J.-C. Sangleboeuf, G. Matzen and M. Allix, *Chem. Mater.*, 2013, **25**, 4017–4024.
[94] Z. Xiao, S. Yu, Y. Li, S. Ruan, L. B. Kong, Q. Huang, Z. Huang, K. Zhou, H. Su, Z. Yao, W. or W. X. Que, Y. Liu, T. Zhang, J. Wang, P. Liu, D. Shen, M. Allix, J. Zhang and D. Tang, *Materials Science and Engineering: R: Reports*, 2019, **139**, 100518.
[95] V. Castaing, C. Monteiro, A. D. Sontakke, K. Asami, J. Xu, A. J. Fernández-Carrión, M. G. Brik, S. Tanabe, M. Allix and B. Viana, *Dalton Trans.*, 2020, **49**, 16849–16859.
[96] A. Bertrand, J. Carreaud, S. Chenu, M. Allix, E. Véron, J.-R. Duclère, Y. Launay, T. Hayakawa, C. Genevois, F. Brisset, F. Célarié, P. Thomas and G. Delaizir, *Advanced Optical Materials*, 2016, **4**, n/a-n/a.
[97] W. Wisniewski, K. Takano, Y. Takahashi, T. Fujiwara and C. Rüssel, *Scientific Reports*, 2015, **5**, 9069.
[98] B. Valeur and M. N. Berberan-Santos, *J. Chem. Educ.*, 2011, **88**, 731–738.
[99] J. Xu, J. Ueda, K. Kuroishi and S. Tanabe, *Scripta Materialia*, 2015, **102**, 47–50.
[100] K. Van Den Eeckhout, P. F. Smet and D. Poelman, *Materials*, 2010, **3**, 2536–2566.
[101] P. M. Woodward, P. Karen, J. S. O. Evans and T. Vogt, *Solid State Materials Chemistry*, Cambridge University Press, Cambridge, 2021.
[102] Y. Li, C. Guo, J. Yuan, X. Yang, H. Ji, M. Wu, L. Wu and Y. Qin, *Chemical Engineering Journal*, 2024, **487**, 150424.
[103] A. Jain, A. Kumar, S. J. Dhoble and D. R. Peshwe, *Renewable and Sustainable Energy Reviews*, 2016, **65**, 135–153.
[104] M. Lastusaari, T. Laamanen, M. Malkamäki, K. O. Eskola, A. Kotlov, S. Carlson, E. Welter, H. F. Brito, M. Bettinelli, H. Jungner and J. Hölsä, *European Journal of Mineralogy*, 2012, **24**, 885–890.
[105] P. F. Smet, I. Moreels, Z. Hens and D. Poelman, *Materials*, 2010, **3**, 2834–2883.
[106] J. Xu and S. Tanabe, *Journal of Luminescence*, 2019, **205**, 581–620.
[107] C. Li, X. Cai, Y. Qiang, X. Shi, Y. Jiang, Y. Chen, F. Lai, B. Wang, Y. Leng and W. You, *Journal of Luminescence*, 2024, **270**, 120537.
[108] T. Maldiney, A. Lecointre, B. Viana, A. Bessière, M. Bessodes, D. Gourier, C. Richard and D. Scherman, *J. Am. Chem. Soc.*, 2011, **133**, 11810–11815.
[109] K. Ariga, *Advanced Physics Research*, DOI:10.1002/apxr.202200113.
[110] Y. Zhuang, J. Ueda and S. Tanabe, *Optical Materials Express*, 2012, **2**, 1378–1383.
[111] T. Matsuzawa, Y. Aoki, N. Takeuchi and Y. Murayama, *Journal of The Electrochemical Society*, 1996, **143**, 2670.
[112] T. Delgado, J. Bierwagen, N. Gartmann, B. Walfort, I. Kinski, M. Pollnau, and H. Hagemann, 2020, vol. 11357, p. 113571C.
[113] H. Wang, X. Liang, K. Liu, Q. Zhou, P. Chen, J. Wang and J. Li, *Optical Materials*, 2016, **53**, 94–100.
[114] N. Yu, F. Liu, X. Li and Z. Pan, *Applied Physics Letters*, 2009, **95**, 231110.
[115] M. Zhang, Y. Li, Y. Wang, L. Yin, L. Pan and P. D. Townsend, *Optical Materials*, 2024, **148**, 114936.
[116] Y. Cai, X. Wang and Y. M. Huang, *Results in Physics*, 2024, **60**, 107656.
[117] H. Yamamoto and T. Matsuzawa, *Journal of Luminescence*, 1997, **72–74**, 287–289.
[118] W. S. Park, S. J. Kim and J. S. Kim, *Materials Science Forum*, 2004, **449–452**, 745–748.
[119] J. Qiao and Z. Xia, *Journal of Applied Physics*, 2021, **129**, 200903.
[120] Y. Lu, L. Chen, Q. Zhang, B. A. Goodman, W. Deng, D. Xiong and S. Xu, *Journal of Luminescence*, 2023, **253**, 119472.
[121] V. Fuertes, J. J. Reinosa, J. F. Fernández and E. Enríquez, *Journal of the European Ceramic Society*, 2022, **42**, 307–326.

[122] G. Yuan, Y. Cao, H.-M. Schulz, F. Hao, J. Gluyas, K. Liu, T. Yang, Y. Wang, K. Xi and F. Li, *Earth-Science Reviews*, 2019, **191**, 114–140.
[123] H. Virk, *History of Luminescence from Ancient to Modern Times*, 2014.
[124] F. Bacon, *The advancement of learning*, Macmillan & Company, Limited, 1910.
[125] J.-C. Zhang, X. Wang, G. Marriott and C.-N. Xu, *Progress in Materials Science*, 2019, **103**, 678–742.
[126] P. Jha and B. P. Chandra, *Luminescence*, 2014, **29**, 977–993.
[127] Z. Huang, X. Li, T. Liang, B. Ren, X. Zhang, Y. Zheng, Q. Zhang, Z. Fang, M. Wu, M. Zulfiqar, L. Jing, S. Qu, B. Chen, J. Gan and D.Peng, *Responsive Materials*, 2024, **2**, e20240019.
[128] B. P. Chandra, in *Luminescence of Solids*, ed. D. R. Vij, Springer US, Boston, MA, 1998, pp. 361–389.
[129] Z. Li, Y. Yan, T. Wang, S. Wang, L. Guo, W. Feng, L. Zhao, Z. Wang, F. Zhao, J. Chen, Z. Zhang, X. Xu and X. Yu, *Journal of Rare Earths*, 2023, **41**, 1869–1875.
[130] L. Zhang, H. Yamada, Y. Imai and C.-N. Xu, *Journal of The Electrochemical Society*, 2007, **155**, J63.
[131] Y. Hirai, *ACS Appl. Opt. Mater.*, 2024, **2**, 1025–1045.
[132] Z. Xie, Z. Mao, H. Wang, Y. Xiao, X. Zhang, T. Yu, Z. An and W. Huang, *Light: Science & Applications*, 2024, **13**, 85.
[133] J.-C. Zhang, Y.-Z. Long, X. Yan, X. Wang and F. Wang, *Chem. Mater.*, 2016, **28**, 4052–4057.
[134] A. Feng and P. F. Smet, *Materials*, DOI:10.3390/ma11040484.
[135] F. Zhang, Y. Xie, Y. He, J. Pei, Y. Xing, S. Wang and J. Zhang, *Buildings*, 2024, **14**, 2152.
[136] S. Xue, M. Li, Y. Han and Y. Chen, *Dyes and Pigments*, 2021, **193**, 109484.
[137] M. Dubernet, Y. Gueguen, P. Houizot, F. Célarié, J.-C. Sangleboeuf, H. Orain and T. Rouxel, *Applied Physics Letters*, 2015, **107**, 151906.
[138] P. Jha and B. P. Chandra, *Journal of Luminescence*, 2013, **143**, 280–287.
[139] Y. Terasawa, C. N. Xu, H. Yamada and M. Kubo, *IOP Conference Series: Materials Science and Engineering*, 2011, **18**, 212013.
[140] L. Zhang, C.-N. Xu, H. Yamada and N. bu, *Journal of The Electrochemical Society*, 2010, **157**, J50.
[141] M. I. Aroyo, J. M. Perez-Mato, C. Capillas, E. Kroumova, S. Ivantchev, G. Madariaga, A. Kirov and H. Wondratschek, 2006, **221**, 15–27.
[142] M. I. Aroyo, A. Kirov, C. Capillas, J. M. Perez-Mato and H. Wondratschek, *Acta Crystallographica Section A*, 2006, **62**, 115–128.
[143] A. Duval, P. Houizot, X. Rocquefelte and T. Rouxel, *Applied Physics Letters*, 2023, **123**, 011905.
[144] A. Duval, Y. Suffren, M. Benabdesselam, P. Houizot and T. Rouxel, *The Journal of Chemical Physics*, 2023, **159**, 134501.
[145] Alexis Duval. Elaboration, structure and mechanical characterization of oxynitride glasses and mechanoluminescent glass-ceramics from the BaO-SiO_2-Si_3N_4 chemical system. 2023.

Chapter 2: Study of Two New Strontium Aluminosilicates

Contents Page

2.1. A Fertile Zone of Exploration in the SrO-$AlO_{1.5}$-SiO_2 Phase Space

2.1.1. Introduction

The monoclinic phase, $SrAl_2O_4$, is an extremely well-studied ceramic material within the SrO–$AlO_{1.5}$–SiO_2 ternary diagram. When doped with 1mol% Eu^{2+}/ 2mol% Dy^{3+}, and excited with near UV radiation, it produces intense, long-lasting green emission, which has found applications in numerous industries.[1–4] As discussed in the introduction, a drawback of this composition is that it is challenging to manufacture as a large transparent ceramic piece, which limits its applications.[5] One method to address this problem is to try and add a network-forming element into the composition and thus improve its glass-forming capabilities. With this in mind, the $SrAl_2O_4$–SiO_2 tie line becomes an interesting zone to investigate, any inclusion of Si^{4+} into the structure of $SrAl_2O_4$ opens the possibility for transparent bulk samples.

In work by A. Fernandez-Carrion *et al.*, and V. Castaing *et al.* (discussed in Section 1.5.2.), this tie line was investigated using the formula $Sr_{1-x/2}Al_{2-2x}Si_xO_4$ (green dashed line of Fig. 2.1.(a)). Between the values $0.2 \leq x \leq 0.5$ a hexagonal polymorph of $SrAl_2O_4$ with a 3D framework was found, this polymorph could be made into large bulk transparent pieces by a glass crystallisation (GC) approach.[6,7] Moreover, just like the original $SrAl_2O_4$ phase, when the new polymorph was doped with Eu^{2+} and Dy^{3+} long lasting persistent luminescent (PersL) properties were observed, as shown in Fig. 2.1. Interestingly, the colour of the PersL was found to be green-blue tuneable, when the Si^{4+} content was increased.

Further investigation of the $SrAl_2O_4$-SiO_2 tie line by K. Al Saghir *et al.*, discovered a second solid solution (pink line of Fig. 2.1.(b)), according to the formula $Sr_{1+x/2}Al_{2+x}Si_{2-x}O_8$ ($0.0 \leq x \leq 0.4$).[8] This solution, again found by GC, represented hexacelsian-type polymorphs of the known $SrAl_2Si_2O_8$ phase and adopted layered 2D aluminosilicate frameworks. The solution was found to be readily synthesisable as bulk transparent ceramics and could easily be scaled up thanks to its high Si^{4+} content. However, this phase lacked the PersL properties of the first solid solution and the nominal $SrAl_2Si_2O_8$ phase.

Finally, investigation of the phase space between these two solid solutions, again by K. Al Saghir, revealed a third intermediate composition (blue spot of Fig. 2.1.), described as the structural 'missing link' of the two solid solutions.[9,10] According to the formula $Sr_{1+x/2}Al_{2+x}Si_{2-x}O_8$, this solid solution was observed between $0.66 \leq x \leq 0.75$, with x=0.66 compositions, approximated to $SrAl_2SiO_6$, showing the highest degree of crystallinity and purity. It was noted that all of the discussed phases on the $SrAl_2O_4$-SiO_2 tie line were metastable and decomposed into their respective equilibrium products above a certain temperature. Therefore, owing to the number of phases already discovered in this fertile zone of the SrO-$AlO_{1.5}$-SiO_2 diagram, further investigation was warranted in the search for novel metastable glass-ceramics.

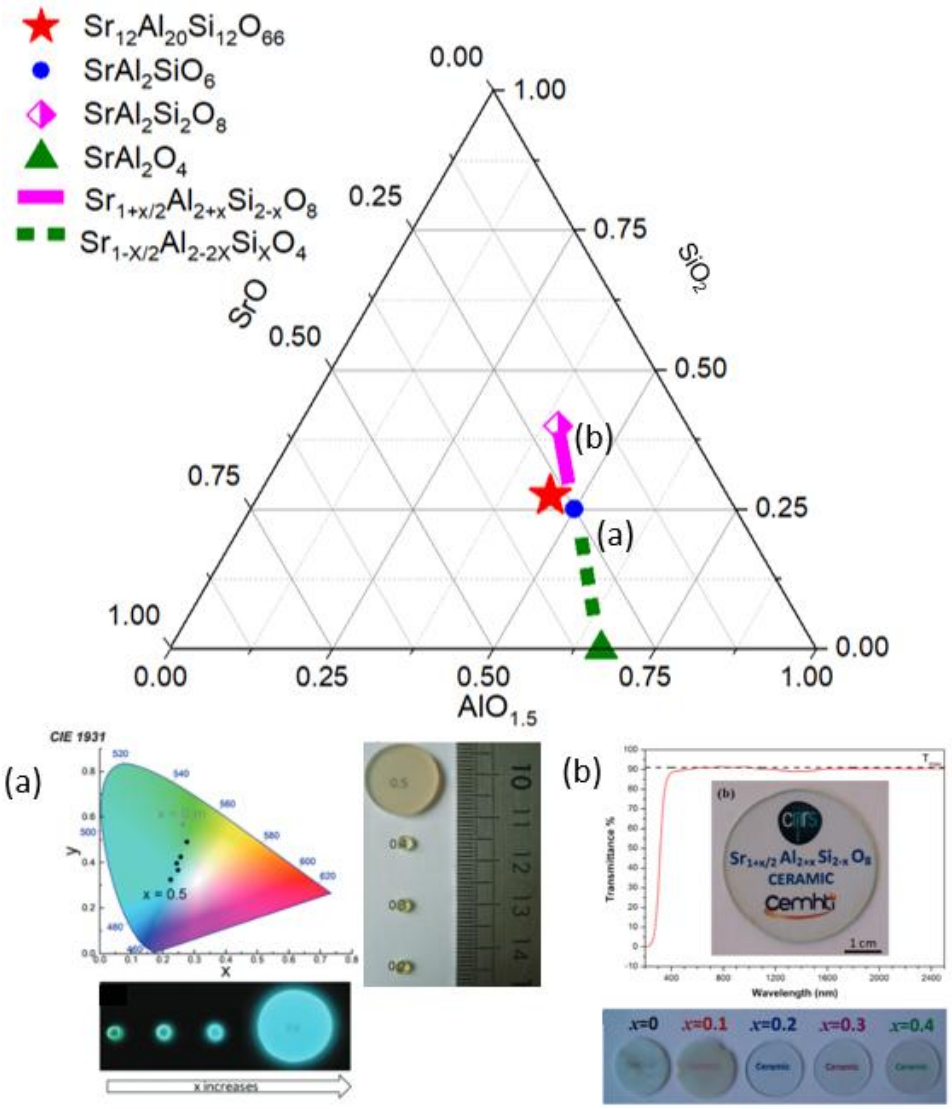

Fig. 2.1. $SrO–AlO_{1.5}–SiO_2$ ternary phase diagram showing the compositional ranges of both solid solutions and the positions of the two new metastable compositions discussed in this chapter. Insets **(a)** from [8]. Inset **(b)** from [6].

Previous work had determined the composition and structure of $SrAl_2SiO_6$, and found it to exhibit a topologically unique and complex crystalline framework which shared structural features with the two solid solutions. However, phase-pure synthesis had never been achieved which prevented functionalisation and a properties study from being conducted. Achieving this formed the initial aim of this chapter's work, transparency and PersL properties were expected due to the structural commonalities of $SrAl_2SiO_6$ and the solid solutions.

Through this work, an entirely separate metastable phase was discovered, which bore no structural relation to the aforementioned samples, (Fig. 2.1.). The synthesis optimisation, structural determination, and functionalisation of the new phase, $Sr_{12}Al_{20}Si_{12}O_{66}$, formed the primary goal of this chapter. It represented a small departure from the $SrAl_2O_4–SiO_2$ tie line, and opened the possibility of a second solid solution running parallel to those already identified. Despite this divergence, the desired properties of transparency, PersL were still observed, alongside the additional property of mechanoluminescence (ML).

When $Sr_{12}Al_{20}Si_{12}O_{66}$ was compared to the probe structure prediction map, it was found to lie in a low energy well of the diagram, just beyond the threshold for synthesis trials imposed during the initial study (zone B of Fig. 1.8.).[11] Although the energy map was not the inspiration for exploring this area, the discovery of $Sr_{12}Al_{20}Si_{12}O_{66}$ highlighted the value of this approach. Moreover, this abundant zone was accessible only through the use of the innovative GC technique, thereby exemplifying the aim of this project: the discovery of metastable phases with new functionalised properties, facilitated by out-of-equilibrium synthesis techniques.

2.1.2. Previously Solved Structure of $SrAl_2SiO_6$

The $SrAl_2SiO_6$ synthesis method optimised by K. Al Saghir, yielded sufficiently high-quality crystalline phase for structural determination to be performed from powder diffraction data, using an *ab-initio* charge-flipping (CF) method, despite not being phase-pure. Samples were prepared using the GC technique; Binary oxide powders $SrCO_3$ (Strem 99.9%), Al_2O_3 (Alfa Aesar 99.98%) and SiO_2 (Alfa Aesar 99.8%) were dried overnight and then weighed according to the $SrAl_2SiO_6$ stoichiometric ratio. Glass was then made using the classic melt-quenching method in a muffle furnace set to 1600°C for 1.5 hours. The formation of glass was confirmed by the absence of Bragg peaks in the PXRD pattern. Once formed, the glass was finely crushed and pressed into 5mm ϕ pellets that were then sintered in a Pt crucible placed in a muffle furnace at 1100°C for 4 hours. This protocol was chosen as it had proved successful in the isolation of the metastable 3D $SrAl_2O_4$-type ($0.2 \leq x \leq 0.5$) and 2D $SrAl_2Si_2O_8$-type ($0.8 \leq x \leq 1$) members. The resultant sample was then analysed by synchrotron and neutron powder diffraction (SPD & NPD) sources for high-quality data collection, which was necessary for structural determination to be performed. The 11BM beam line at the Advanced Photon source, Argonne National Laboratory (U.S.A.) was chosen for high-intensity, high-resolution SPD data collection. While the 3T2 diffractometer at the Laboratoire Léon Brillouin (Saclay, France) was used for high-resolution NPD data collection.

Phase identification carried out using the ICDD Powder Diffraction File (PDF database), identified the impurity phase as the hexagonal $SrAl_2O_4$ polymorph. An auto-indexing analysis of the collected SPD data by the DICVOL and TREOR indexing routines, utilised in the FullProf suite, provided a cell which could be described by either the *Pmc*2_1, *P*2*cm, or Pmcm* space groups.[12–14] CF, conducted with SUPERFLIP implemented in JANA2006 software, and Rietveld refinement, in JANA2006 software, then identified the best solution out of these possibilities.[15–17] The orthorhombic *Pmc*2_1 space group provided the best refinement of the data, with it assigning all of the cation positions and most of the oxide positions. Final oxide positions were assigned through Fourier difference mapping of the NPD data.

The structure was found to be based on corner linked $(Al,Si)O_4$ tetrahedra with Sr^{2+} ions occupying the channels formed by the framework voids (Fig. 2.2.).

The *a*- projection of Fig. 2.2., shows that the corner linked $(Al/Si)O_4$ tetrahedra form 6 membered rings, of two different configurations. The cyan coloured hexagons demonstrate a *dddudu* (3 per unit cell, d = tetrahedra orientated downwards/ antiparallel to the *a* cell vector, u = orientated upwards/parallel to *a*) configuration, while the orange rings present a *ududud* (1 per unit cell) arrangement. This 1:3 ratio of the rings gives $SrAl_2SiO_6$ an anisotropic structure type which is uncharacteristic of 3D frameworks. The *b/c*-projection revealed alternating *ABAB* stacking along the *a*- axis and structural similarities to 2D frameworks. The A layer of Fig. 2.2., was found to contain both 4- and 6- membered $(Al/Si)O_4$ rings, whilst the B layer only contained 6-membered ones, making them under connected in comparison. Altogether, seven unique Sr^{2+} coordination sites were identified within the unit cell, five of these were found to be almost fully occupied with refined occupancy factors of >0.975. While the remaining two sites, positioned in the under connected B layers, were found to have considerably lower occupancies of 0.09-0.29, (a full refined atomic parameters table is shown later in table 2.1.). Bond valence sum calculations supported these findings and indicated that Sr^{2+} ions were too small to occupy sites in the B layer. $SrAl_2SiO_6$ is described as pseudo-3D structure owing to its similarities with 2D frameworks and overall anisotropic nature. When the topologies of the two solid solutions were compared to $SrAl_2SiO_6$, a structural evolution was identified and the reason for the pseudo-3D behaviour became clear.[9]

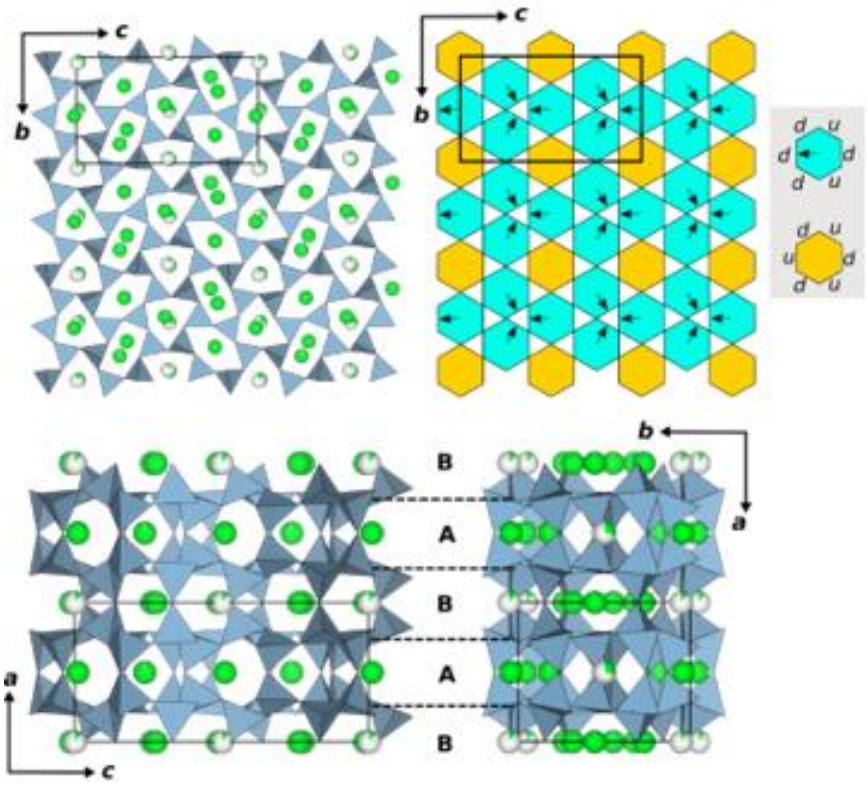

Fig. 2.2. Crystal structure of $SrAl_2SiO_6$, as viewed down the a- axis and b-axis. The cyan and orange hexagons show the *dddudu* / *ududud* 1:3 ring arrangement. The b- projection shows the pseudo-2D ABAB stacked layers. Green atoms = Sr^{2+}, blue tetrahedra = $(Al,Si)O_4$, unit cell outlined in black.

2.1.3. Topological Description of $SrAl_2SiO_6$

A crystal can be described through its unit cell, symmetry and atomic coordinates in what is known as a crystallographic representation. While this method for structural characterisation is extremely useful, it can make it hard for structural analogues to be identified. In these cases, a topological description can be used, this approach simplifies the geometry of crystalline structures and describes them purely as networks (Fig. 2.3.).[18] Atoms, molecules, and polyanions are reduced to vertices and linkers which simplifies the structure into an easily comparable form, even between phases with different compositions and space groups. For example, the 2D hexacelsian polymorph of $SrAl_2Si_2O_8$, is described topologically as $\{4^3.6^3\}$, meaning that each vertex is at the meeting point of three 4-membered rings and three 6-membered rings. It therefore belongs to the point symbol, *(6,3)Ia*, of which there are 291 other examples in TOPOS databases.[19]

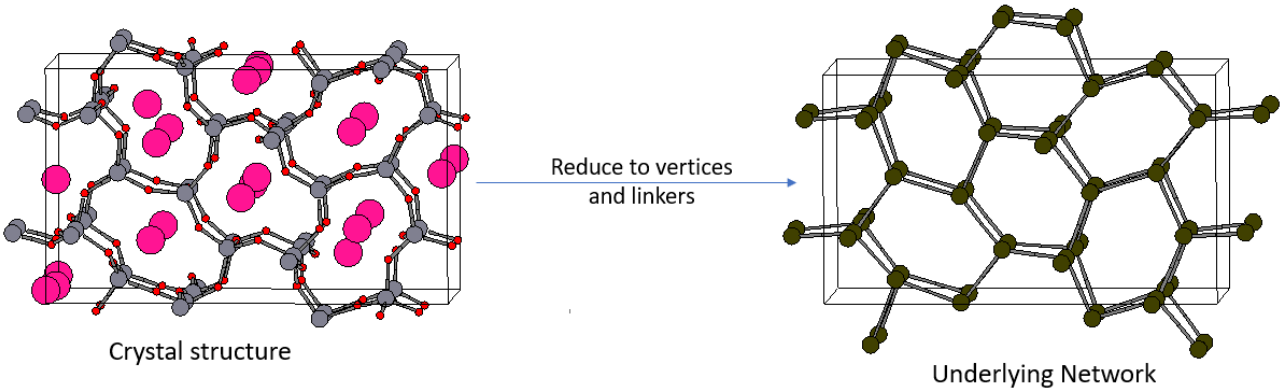

Fig. 2.3. Topological analysis of $SrAl_2SiO_6$, structure was found to belong to the previously theorised network point symbol of $\{4.6^5\}_3\{4^3.6^3\}\ \{6^6\}_4$.

When topological analysis was applied to $SrAl_2SiO_6$, it could be described by the point symbol $\{4.6^5\}_3\{4^3.6^3\}\{6^6\}_4$, as shown in Fig. 2.3. (the complexity of the point symbol has increased as the structure is 3D meaning it contains three types of node instead of one as in the 2D example). When compared to the TOPOS database there were no other experimentally-realised structure types with this topology, meaning $SrAl_2SiO_6$ is topologically unique.[20,21] As mentioned, this analysis also identified structural similarities between the hexagonal $SrAl_2O_4$ and hexacelsian $SrAl_2Si_2O_8$ phases, as illustrated by Fig. 2.4. It was found that $SrAl_2SiO_6$ contained features related to both the tridymite- ($\{6^6\}$) of $SrAl_2O_4$ and ($\{4^3.6^3\}$) of $SrAl_2Si_2O_8$, by inverting the orientation of some the tetrahedra in $SrAl_2SiO_6$ (those marked in yellow in Fig. 2.4.) each structure can be formed. The structural evolution along this series can be viewed stepwise and is associated with a reduction in dimensionality, which supports the pseudo-3D structure assignment.

Whilst $SrAl_2SiO_6$ is the structural intermediate of both solid solutions, its structure is more closely related to the stuffed-tridymite ($SrAl_2O_4$) than it is to the hexacelsian polymorph. This encouraged the belief that PersL properties would be observed, although producing large transparent ceramics may be more challenging. However, the orthorhombic space group suggested that transparency could still be achieved through preferred orientation (PO) of the crystallites.

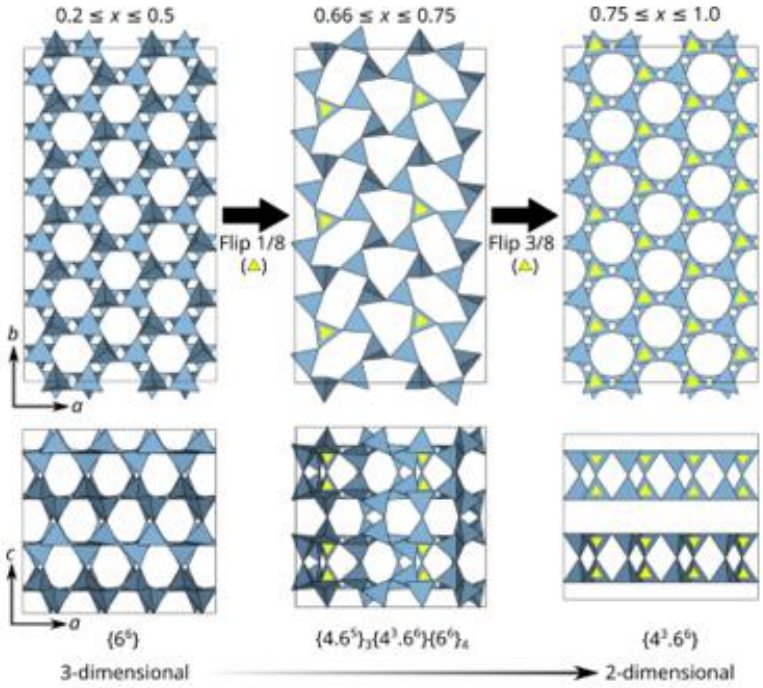

Fig. 2.4. Structural framework topologies of the three phases, displayed on a common unit cell and with Sr^{2+} omitted for clarity. The corresponding topological net point symbols are shown below each structure.

2.2. Phase-Pure Synthesis of Doped $SrAl_2SiO_6$

2.2.1. Synthesis Optimisation Through *In-Situ* VTXRD & DSC

The phase-pure synthesis of $SrAl_2SiO_6$ had not yet been achieved, which prevented functionalisation and a properties study being conducted. Therefore, with the structure solved, the aim of this work became achieving phase-pure synthesis and functionalisation. The aforementioned, structural similarities with $SrAl_2O_4$, a known photoluminescent (PL) material, suggested doping $SrAl_2SiO_6$ with photo-active elements such as Eu^{2+} and Dy^{3+} was a good place to start in functionalisation of the phase.

Initially, Eu^{2+} was doped into $SrAl_2SiO_6$ to see how the structure responded before more complex co-doping was attempted. Glass was prepared using the method discussed in Section 2.1.2, except Eu_2O_3 (99.999% Strem) was substituted for $SrCO_3$, giving the desired formula $Sr_{0.99}Eu_{0.01}Al_2SiO_6$, abbreviated to $SrAl_2SiO_6:Eu^{2+}$. The use of high-purity optical reagents was essential as impurities had been shown to negatively affect optical performance. Again, the synthesis of glass was confirmed by the lack of Bragg diffraction peaks in the PXRD pattern, an angular range of 15° - 45°, step size of 0.021° and measurement time per step of 0.1 s was used for the scan. The presence of Eu^{3+} in the glass was confirmed by its characteristic orange glow, observed when the sample was excited by a broad-spectrum UV lamp.

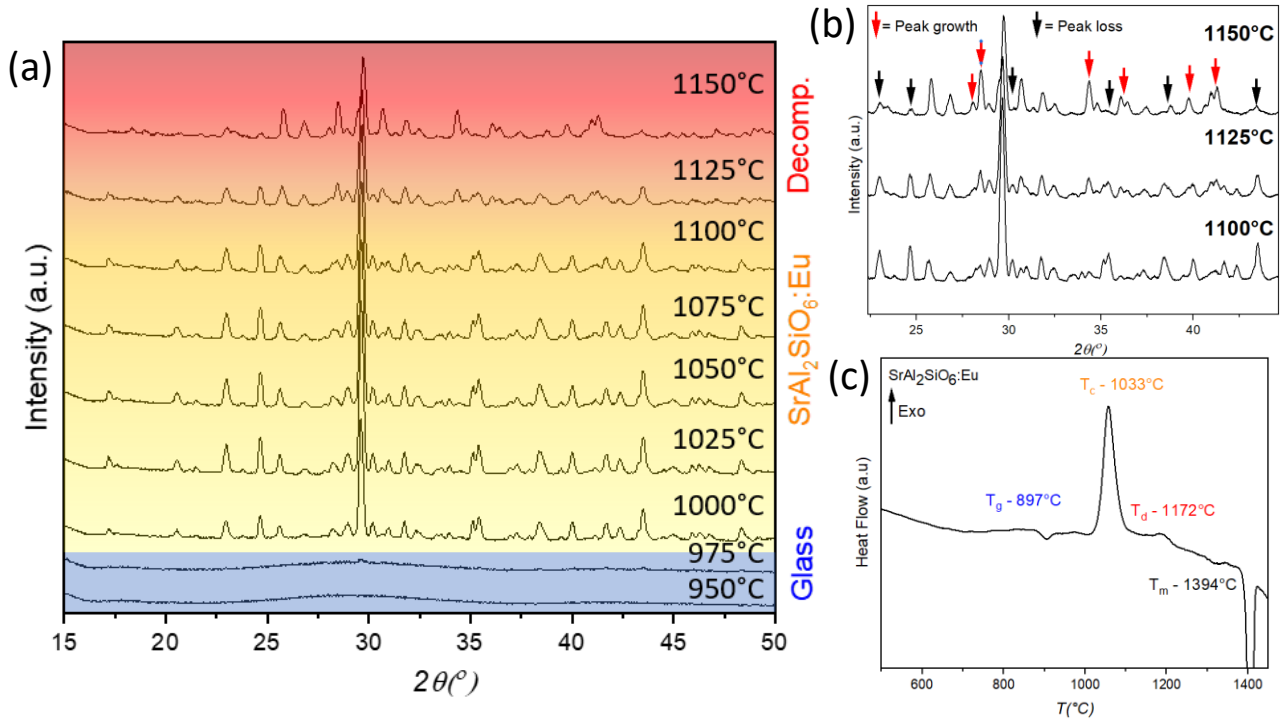

Fig. 2.5. (a) *In-situ* VTXRD of $SrAl_2SiO_6:Eu^{2+}$, showing crystallisation at 975°C and decomposition at 1125°C. **(b)** Magnification of the decomposition zone, red arrows show peak growth while black ones show peak loss. **(c)** DSC of $SrAl_2SiO_6:Eu^{2+}$ showing the T_g, T_c, T_d, and T_m.

The previous work by K. Al Saghir, showed that 4h sintering's at 1100°C, produced a small amount of $SrAl_2O_4$ polymorph impurity. This was hypothesised to be due to thermal decomposition of the metastable $SrAl_2SiO_6$ phase. Therefore, lower annealing temperatures should result in phase purity, to verify this DSC and *in-situ* VTXRD measurements were conducted, (Fig. 2.5.). Indeed, the results showed that $SrAl_2SiO_6:Eu^{2+}$ crystallisation took place at temperatures lower than 1100°C. The T_c (1033°C) and T_d (1172°C) events, observed in the DSC trace, indicated a stability range of 139°C. In contrast, the *in-situ* VTXRD spectra revealed a slightly reduced phase-pure stability range of 1000-1100°C.

An expected second exothermic event, typical of metastable phases, was not observed by both DSC and *in-situ* VTXRD. Rather, a slow decomposition of $SrAl_2SiO_6$ (shown by the yellow to red colour gradient in Fig. 2.5.(a)) was observed after ~1125°C. The new peaks which formed, could not be indexed to any known phase and it was only being realised later that they belonged to the second novel metastable phase discussed in this chapter, $Sr_{12}Al_{20}Si_{12}O_{66}$. With this in mind, GC synthesis trials started on crushed glass samples of $SrAl_2SiO_6:Eu^{2+}$, from a temperature of 1000°C.

2.2.2. GC Synthesis of $SrAl_2SiO_6:Eu^{2+}$ Powders

Phase-pure synthesis trials started on powdered $SrAl_2SiO_6:Eu^{2+}$ pellets to determine if the phase had PL properties and thus justify further experimentation to produce functional bulk samples. The glass was first finely crushed in an agate mortar and then pressed into 5 mm ϕ pellets. These were then sintered in a tube

furnace under the necessary N_2:H_2 (94:6) atmosphere for Eu^{3+} to Eu^{2+} reduction. Annealing times of 1-3 hours and temperatures of 1000–1050°C were used, with the results shown in Fig. 2.6.

Each annealed sample was then crushed, dispersed on a Pt-wafer with the help of ethanol and analysed by PXRD. An angular range of 5-50°, time per step of 0.3s and increment of 0.021° was used. As expected, the results showed that highly crystalline $SrAl_2SiO_6$:Eu^{2+} sample could be obtained at temperatures below 1100°C. Minor secondary phase peaks, indicated by the black arrows in Fig. 2.6., were noticed in the 1025°C and 1000°C patterns, again they matched the $Sr_{12}Al_{20}Si_{12}O_{66}$ phase when it was discovered later. For the 1050°C sample, no secondary phase or residual glass was observed meaning the first goal of this chapter had been achieved, for the synthesis of $SrAl_2SiO_6$:Eu^{2+} as a ceramic powder, by the following GC protocol:

$$RT \xrightarrow{2h} 1050^oC \xrightarrow{1h} 1050^oC \longrightarrow RT$$

These results demonstrated one of the advantages of GC with shorter annealing times and lower temperatures being required for phase-pure synthesis, compared to the original protocol of 4h at 1100°C. A good agreement was observed between the DSC and *in-situ* VTXRD results, as the optimum protocol lay within their predicted temperature ranges. When the PXRD data from optimised GC synthesis of $SrAl_2SiO_6$:Eu^{2+}, was Pawley refined using the *Pmc*2_1 space group, all the peaks were matched, clearly showing that phase purity had been achieved. However, to be certain and to refine the phase-pure atomic positions, higher quality PXRD data was gathered and analysed by the Rietveld method.

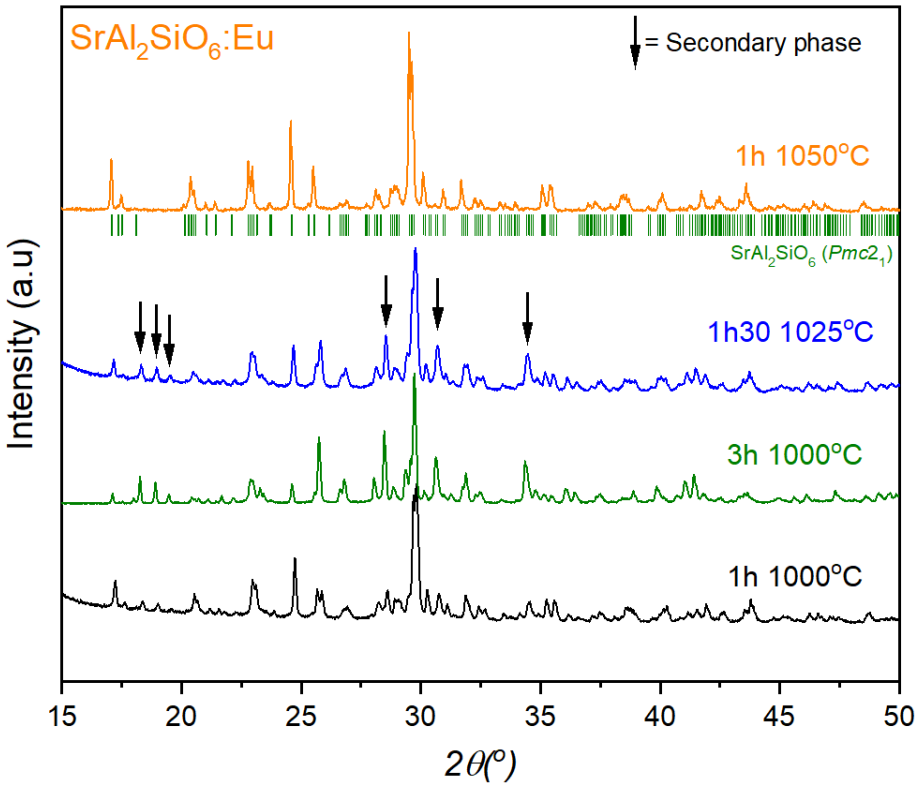

Fig. 2.6. Comparison of the sintering's attempted to obtain phase-pure $SrAl_2SiO_6$:Eu^{2+} powdered ceramics. The black arrows indicate the main secondary phase peaks present in the black, green and blue patterns.

2.2.3. Rietveld Refinement of $SrAl_2SiO_6:Eu^{2+}$

High-quality lab-PXRD data was collected on the optimised $SrAl_2SiO_6:Eu^{2+}$ sample, an angular range of 5-130°, time per step of 2.3s and increment of 0.019° was used, giving a 4h scan time. Sample preparation for PXRD measurement involved packing finely crushed crystalline sample into a deep silicon holder, which was rotated during measurement to provide better powder averaging.

The orthorhombic *Pmc*2_1 unit cell, already determined from NPD and SPD refinements was used as the basis for Rietveld refinement. In jedit software, a refinement file was created with a background function consisting of 10 parameters to model the baseline, six profile functions (TCHZ functions) and 35 atomic sites. The Sr^{2+} sites were not given full occupancy (table 2.1.) sites 1–5 were given an occupancy of ~0.9, while the 6th and 7th sites had considerably lower occupancies of 0.091 and 0.288, respectively, these values were not refined. The eight Al^{3+}/Si^{4+} sites were given a partial ordering, Al occupied 2/3 of the sites meaning Si occupied the remaining 1/3. The orthorhombic symmetry allowed the (*a-, b-* and *c-*) lattice parameters to be refined, with final dimensions of *a- = 8.2985(1) Å, b- = 10.2217(1) Å* and *c- = 17.5010(2) Å* being determined, giving an overall cell volume of 1484.52(3) *Å^3*.

With these parameters refined, a final R_{wp} of 9.739%, χ of 3.904, and atomic parameters shown in table 2.1. were achieved. This gave a reasonable refinement of the data, as shown in Fig. 2.7. Peak intensity discrepancies were observed at low angle, which may be caused by the partial ordering of the Al/Si atoms. However, refinement of these occupancies was impossible, based on PXRD data alone, as Al^{3+} and Si^{4+} cations are isoelectronic. In such cases, where differentiating between chemically similar elements is important, NMR can be used.

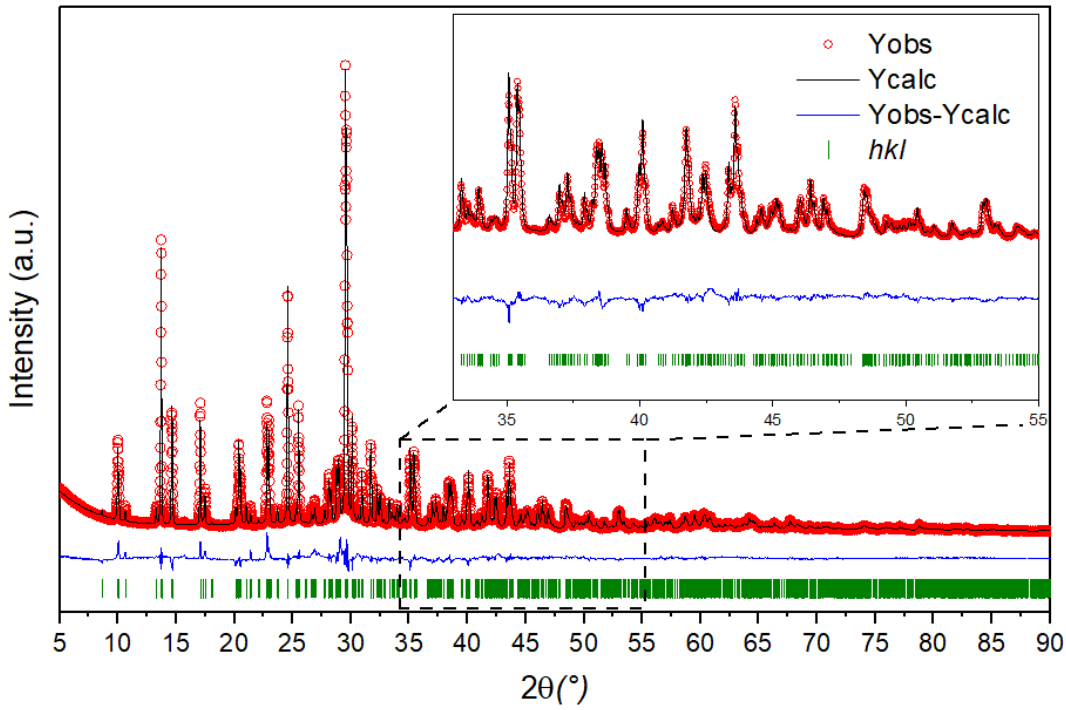

Fig. 2.7. Rietveld refinement of the phase-pure $SrAl_2SiO_6:Eu^{2+}$ ceramic, R_{wp} of 9.739% and χ of 3.904, synthesised from GC with a powder sintering step of 1h at 1050°C. The inset shows a zoom of the refinement at high angle.

Table 2.1. Final refined structural parameters obtained from lab-PXRD data, collected at room temperature on a powdered sample of $SrAl_2SiO_6:Eu^{2+}$ (*Pmc*2_1 space group, *a- = 8.2985(1) Å, b- = 10.2217(1) Å* and *c- = 17.5010(2) Å* and cell volume = 1484.52(3) *Å*^{3}).

Atom	Position	x	y	z	Occ	B_{iso}
Sr1	2b	0.5	0.8171	0.2385	0.975	1
Sr2	2a	0	0.5536	-0.0135	0.982	1
Sr3	2a	0	0.2677	0.2619	0.995	1
Sr4	2b	0.5	0.0417	0.0110	0.998	1
Sr5	2a	0	0.6790	0.2770	0.995	1
Sr6	2a	0	0.0507	0.0013	0.091	1
Sr7	2b	0.5	0.4953	0.0098	0.288	1
Al/Si1	4c	0.2979	0.5351	0.1698	0.667/0.333	1
Al/Si2	4c	0.3125	1.0841	0.1735	0.667/0.333	1
Al/Si3	4c	0.1856	0.2967	0.0698	0.667/0.333	1
Al/Si4	4c	-0.3054	0.2764	-0.0922	0.667/0.333	1
Al/Si5	4c	0.1896	0.9915	0.3423	0.667/0.333	1
Al/Si6	4c	-0.3004	0.5505	-0.1626	0.667/0.333	1
Al/Si7	4c	0.3032	0.7842	-0.0551	0.667/0.333	1
Al/Si8	4c	0.1840	0.8101	0.1119	0.667/0.333	1
O1	4c	-0.2213	0.4302	-0.1047	1	1
O2	2a	0	0.3028	0.0314	1	1
O3	4c	0.1873	0.7401	0.0219	1	1
O4	4c	0.2216	0.4564	0.0902	1	1
O5	2b	0.5	0.5272	0.1672	1	1
O6	4c	-0.1944	0.1768	-0.1536	1	1
O7	2b	0.5	0.2552	-0.1261	1	1
O8	4c	0.1813	0.2029	0.1507	1	1
O9	4c	0.3074	0.2329	0.0026	1	1
O10	2b	0.5	0.1394	0.1534	1	1
O11	4c	-0.2060	0.5304	-0.2488	1	1
O12	2b	0.5	0.5475	-0.1617	1	1
O13	4c	0.2950	1.0285	0.2638	1	1
O14	4c	0.3121	0.9439	0.1165	1	1
O15	4c	0.2802	1.0524	0.4211	1	1
O16	4c	-0.2155	0.6887	-0.1268	1	1
O17	2a	0	0.8474	0.1405	1	1
O18	2b	0.5	0.7638	-0.0373	1	1
O19	4c	0.25160	0.6949	0.1749	1	1
O20	2a	0	0.0496	0.3322	1	1

2.2.4. Synthesis of $SrAl_2SiO_6:Eu^{2+},Dy^{3+}$ as a Bulk Glass-Ceramic

With the synthesis of phase-pure powdered $SrAl_2SiO_6:Eu^{2+}$ now optimised, its functional bulk synthesis was investigated. When powdered sample was tested under a UV lamp (312, 365, 254 nm), $SrAl_2SiO_6:Eu^{2+}$ exhibited moderate PL properties, which spurred on functionalisation. Given the structural links of $SrAl_2SiO_6:Eu^{2+}$ to the previously mentioned solid solutions, ($Sr_{1-X/2}Al_{2-2X}Si_XO_4$ and $Sr_{1+x/2}Al_{2+x}Si_{2-x}O_8$), it was expected that a combination of their properties could be achieved. In essence, large transparent $SrAl_2SiO_6:Eu^{2+}$ ceramic pieces with long lasting PersL properties. Although, the phases orthorhombic symmetry suggested that achieving transparency would be complicated, by conventional methods.

With this in mind, the full glass crystallisation approach, discussed in Section 1.4.2. of Chapter 1 was adopted.[22,23] If successfully achieved, PersL properties were expected from the $SrAl_2SiO_6:Eu^{2+}$ crystalline phase, while the similar densities of the glass and crystals would allow transparency to be retained, and enhanced if orientated surface crystallisation was achieved. Vigorous control of the crystallisation process

was required to achieve orientated crystallisation, which would permit light to pass from one domain to another with minimal birefringent effects. Moreover, as discussed in Section 1.4.1. of Chapter 1, other factors such as impurities, porosity, defects, and cracks would also have to be controlled to permit transparency.

Synthesis of these bulk ceramic pieces was attempted directly with co-doping levels of 1mol% Eu^{2+} and Dy^{3+}, giving a desired composition of $Sr_{0.98}Eu_{0.01}Dy_{0.01}Al_2SiO_6$, abbreviated to B-$SrAl_2SiO_6$:$Eu^{2+}$,$Dy^{3+}$. Co-doping was directly attempted as literature had demonstrated that PersL properties dramatically increased with co-doping compared to single doping.[24] Co-doping levels of 1mol% were chosen as literature had also shown this to be adequate for PersL properties to be observed.[1,25,26]

Bulk glass samples were prepared using the same approach outlined in Section 2.1.2., except after quenching the Pt crucible in water, an annealing step of 15 mins at 1600°C was added, after which samples were cooled ambiently. This step allowed bubbles within the melt to rise to the surface and reduced the risk of cracks forming during crystallisation, therefore increasing the likelihood of transparency. Initial, unpolished, samples were crystallised, for 1h, 4h, and 8h at 1050°C, 1020°C and 1000°C, respectively, under an N_2:H_2 atmosphere (94:6), with a temperature plateau of 3h at 500°C, to facilitate the complete reduction of Eu^{3+}. Whilst these samples exhibited transparency, insufficient crystallisation had occurred for PL or PersL properties to be observed.

A final sample was attempted, with an annealing at 1025°C for 8h. The reduction plateau was again used, with the resultant sample shown in the inset of Fig. 2.8. Before heat treatment, the sample was polished into a circular disk (15 mm Ø x 2 mm). Polishing was expected to increase transparency and the chances of orientated surface crystals by removing nucleating sites on the surface. After sintering, a cross-section of the sample was analysed by scanning electron microscopy (SEM) to determine the depth of crystallisation. A depth of 11.5 μm was observed (Fig. 2.8.), which approximately represented 5% of the total sample thickness.

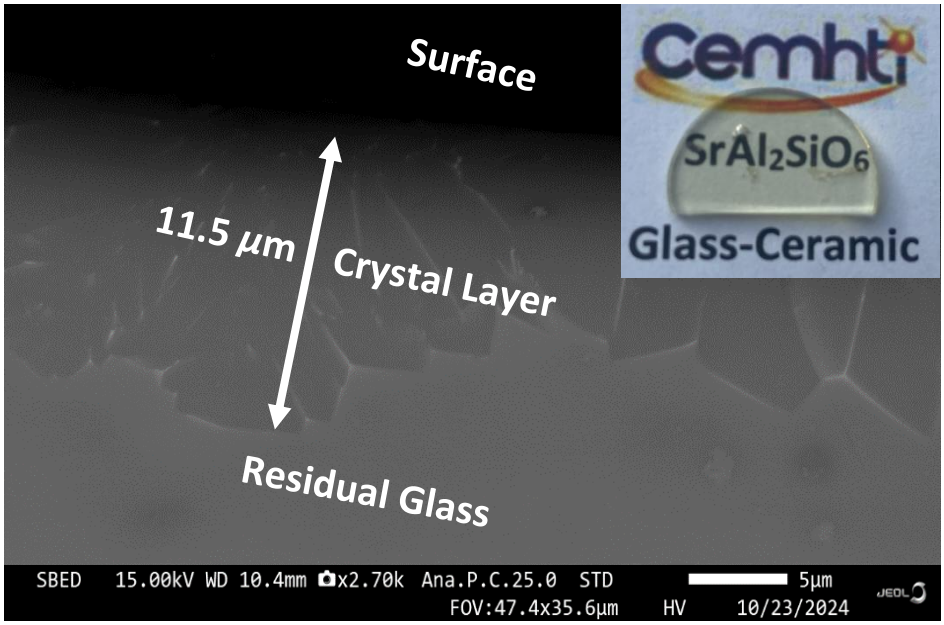

Fig. 2.8. Cross-section SEM image of the bulk crystallised sample (1025°C 8h) showing the depth of crystallisation, 11.5 μm in a 2 mm thick sample. Inset shows the level of transparency achieved in the sample.

PXRD analysis (Appendix 1, A.2.1.) suggested that phase purity had been achieved in B-$SrAl_2SiO_6$:Eu^{2+},Dy^{3+}, although the thin crystalline layer resulted in weak Bragg reflections. An electron backscatter diffraction (EBSD) study should be conducted on this sample to study its crystallite orientations and hence aid in controlling orientations of samples synthesised in the future.

Ultimately, a transparent glass-ceramic had successfully been synthesised, which showed green PL and PersL properties when excited by a UV light, quantitative analysis of these properties is discussed in Section 2.7.1. This sample expanded the full glass crystallisation approach by demonstrating that transparency could also be achieved through partial crystallisation of the surface layer. Partial surface crystallisation was therefore investigated as a means of introducing transparency in the bulk crystallised samples of $Sr_{12}Al_{20}Si_{12}O_{66}$, the second metastable phase discussed in this chapter.

2.3. Discovery & Synthesis Optimisation of $Sr_{12}Al_{20}Si_{12}O_{66}$

2.3.1. Discovery of $Sr_{12}Al_{20}Si_{12}O_{66}$ as an Alternative Crystallisation Product of $SrAl_2SiO_6$ Glass

As discussed in Section 2.1.1., $SrAl_2SiO_6$ was previously discovered as part of a solid solution according to the formula $Sr_{1+x/2}Al_{2+x}Si_{2-x}O_8$ ($0.66 \leq x \leq 0.75$). In this work, experiments were conducted to verify the limits of this solid solution and to determine the optimum x value for $SrAl_2SiO_6$ crystallisation. During experimentation trials however, unindexable peaks were observed in the PXRD patterns of the x=0.7 and 0.75 compositions, corresponding to the formulae, $Sr_{1.35}Al_{2.7}Si_{1.3}O_8$ & $Sr_{1.375}Al_{2.75}Si_{1.25}O_8$, respectively. The x=0.7 composition, obtained by GC with a sintering of 1050°C for 1h, was found to yield the highest intensity of new phase peaks and so optimisation continued at this x value.

The major phase in this sample was unindexable in the ICDD database, whilst the minor phase was indexed to $SrAl_2SiO_6$:Eu^{2+} (Fig. 2.9.). The lack of data on the major phase suggested that it was new and therefore, structural solution using a CF approach was attempted using TOPASV7 software.[27] High quality lab-PXRD data was collected on the x=0.7 sample annealed for 1h at 1050°C but unfortunately, the CF approach failed to determine the structure due to the presence of convoluted $SrAl_2SiO_6$:Eu^{2+} peaks and the low resolution of the lab-PXRD, especially at small *d*-spacings. Both of these factors can severely effect the success of structural solution when the CF method is used.[28,29] Secondary phase impurities were reduced through optimisation of the GC approach, it was found that by slowly cooling the Pt crucible ambiently (air quenched (AQ)) small crystallites formed in the glass (Fig. 2.9.(b)). When this partially-crystallised glass was sintered the quality and intensity of new phase peaks increased.

If the $Sr_{1.35}Al_{2.7}Si_{1.3}O_8$ glass was heated above 1550°C, the small crystallites didn't form and below 1400°C there wasn't sufficient energy to melt the precursors.

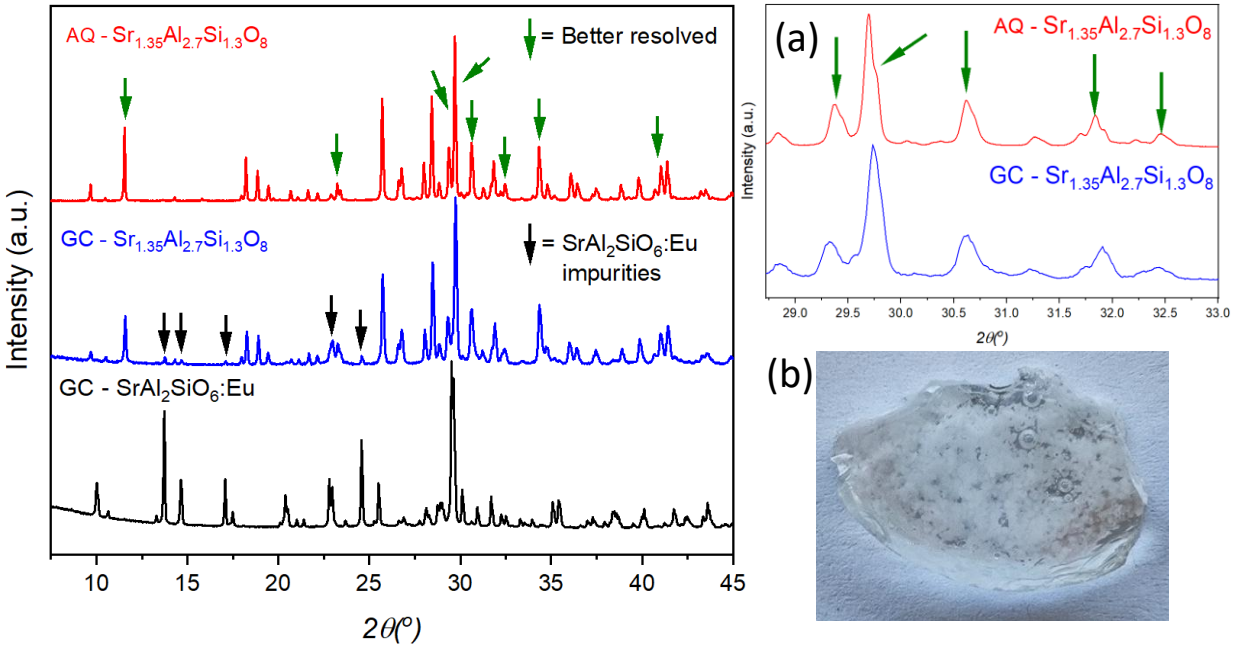

Fig. 2.9. Comparison of the original GC synthesised $Sr_{1.35}Al_{2.7}Si_{1.3}O_8$ composition, compared against $SrAl_2SiO_6:Eu^{2+}$ sample to show the impurity peaks (black arrows) and AQ, 1h 1075°C sintered $Sr_{1.35}Al_{2.7}Si_{1.3}O_8$ which showed better peak resolution (green arrows) and lead to successful structural determination. Inset **(a)** shows a zoom of the PXRD patterns and the better peak resolution observed in the AQ sample. Inset **(b)** shows the optimised AQ sample with small crystallites inside.

Therefore, the optimum temperature to air quench from was found to be 1500°C. This resulted in a polyphasic material composed of $Sr_3Al_{10}SiO_{20}$ (*I*2/*m*), $SrAl_2Si_2O_8$ (*P*-3$_c$1 & *I*2/*m*) and $Sr(Al_{12}O_{19})$ (*P*6$_3$/*mmc*). Crystallisation of this material was then attempted at 1050°C, 1075°C and 1100°C for 1h, with the highest crystallinity and phase purity being achieved at 1075°C, (Fig. 2.9.). Other optimisation methods were also attempted, such as tuning the composition around the x=0.7 point and trying to induce full crystallisation directly from the melt by ADL, however, the AQ method still proved the most successful.

With high-quality, almost phase-pure sample now achieved, the second problem was tackled. High-resolution and high-quality SPD and NPD data was collected on the AQ optimised sample, using the CRISTAL beamline at Soleil and the D2B beamline at the Institut Laue Langevin, respectively. SPD data was collected from an undiluted spinning sample held in 1 mm Ø capillaries (muR= 0.78), between a 0.5-45° 2*Θ* range, with a 0.001° step size and incident wavelength of 0.5904 *Å*. For NPD data collection, a 5-gram powdered sample was analysed over a 5-160° 2*Θ* range, using a 0.05° step size and monochromatic incident beam of 2.3996 *Å*. Analysis of this data was supported by selected area electron diffraction (SAED) of powdered crystals.

2.3.2. Structure Solution of $Sr_{12}Al_{20}Si_{12}O_{66}$ & Finding the Nominal Formula

First analysis of the SPD and NPD data by the DICVOL and TREOR routines, utilised in the FullProf suite, identified a hexagonal cell with lattice parameters *a/b- = 9.72 Å* and *c- = 18.21 Å*.[12] This cell could be described by three possible space groups, *P*6$_3$, *P*6$_3$*m* and *P*6$_3$22, and was supported by SAED analysis which showed one

condition, 00l l=2n, when the crystal was orientated down the [010]* axis (Fig. 2.10.(a)). Orientation down the [001]* and [1$\bar{1}$0]* axes (Fig. 2.10.(b),(c)) identified lattice parameters which corresponded to those generated in FullProf. Pawley refinement of the diffraction data was conducted to refine the cell parameters of the three identified space groups ($P6_3$ refinement shown in Fig. 2.11.(a), $P63m$ and $P6_322$ refinements shown in Appendix 1, A.2.2/3.). This refinement also provided initial reflection intensities of the peaks which were used to generate a Fourier electron density map of the cell. The CF approach using SUPERFLIP, utilised in JANA2006 software, was then attempted on the combined SPD/NPD data to build structural models based on this electron density map and the symmetry constraints imposed by the $P6_3$, $P63m$ and $P6_322$ space groups.[16] Specific details of the CF approach used are covered here, while the general methodology is described in Section 4.4.3. of Chapter 4. Using an iterative process first the heaviest ions, Sr^{2+} in this case, were assigned as they contributed the most electron density. With these contributions removed, the positions of the lighter ions in the cell, Al^{3+}, Si^{4+} and O^{2-} became more obvious. The typical Sr-Al/Si bond lengths (~3.5 *Å*) observed in strontium aluminosilicates was compared against the distance between the assigned Sr^{2+} sites and the remaining electron densities, to help identify the Al^{3+} and Si^{4+}. The specific Al^{3+} or Si^{4+} site occupancy factors at the tetrahedra positions were not refined as there is no appreciable X-ray scattering contrast between these species. Meaning, from diffraction data alone the possible orderings of Al^{3+}/Si^{4+} could not be probed directly.

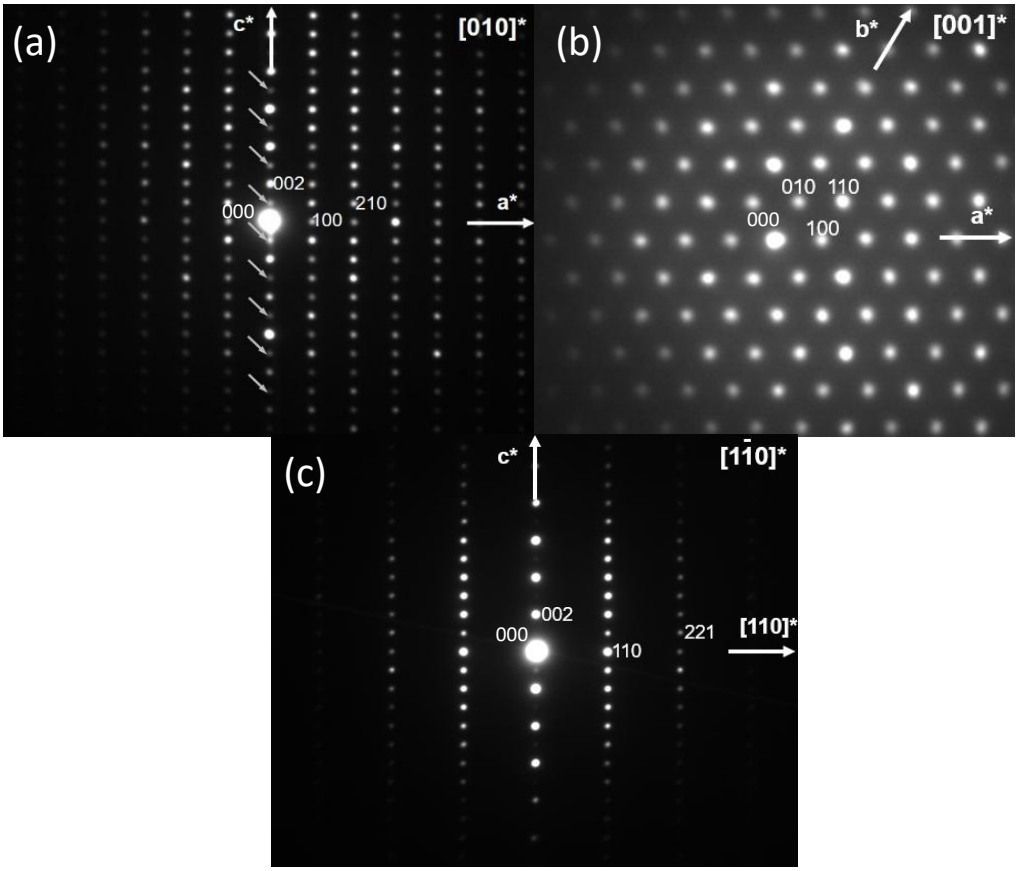

Fig. 2.10. Electron diffraction patterns (SAED) of $Sr_{12}Al_{20}Si_{12}O_{66}$, orientated along the, **(a)** [010]*, **(b)** [001]*, and **(c)** [1$\bar{1}$0]*, respectively, which indexed the crystals to a hexagonal cell with lattice parameters *a/b-* = 9.72 *Å* and *c-* = 18.21 *Å*.

Again, assignment of Al^{3+}/Si^{4+} positions was iterative with each placement removing electron density and making it easier to build the rest of the model.

Once complete structural models had been generated for the *P*6$_3$, *P*6$_3$*m* and *P*6$_3$22 space groups, they were then refined using the Rietveld method. Refinement of the *P*6$_3$ model against the combined SPD/NPD data provided the best fit to the data, with the refinement achieved for the SPD data shown in Fig. 2.11.(b). Structural determination had found the Sr^{2+}, O^{2-} and tetrahedra sites to be fully occupied, therefore to maintain charge neutrality of the crystalline framework a 2:1 ratio or 0.667/0.333 occupancy was applied to the Al^{3+}/Si^{4+} sites, the same as for $SrAl_2SiO_6$. From this analysis a nominal formula of $SrAl_{1.667}SiO_{5.5}$ was found, which was scaled up to $Sr_{12}Al_{20}Si_{12}O_{66}$ and marked a significant departure from the original $Sr_{1.35}Al_{2.7}Si_{1.3}O_8$ point, (Appendix 1, A.2.4.) and the $SrAl_2O_4$-SiO_2 tie line. Additionally, when this refined formula was compared to the computationally predicted SrO-$AlO_{1.5}$-SiO_2 diagram, $Sr_{12}Al_{20}Si_{12}O_{66}$ was found to exist in a low energy region, which was just above the energy threshold for investigation (Appendix 1, A.2.5.) highlighting the diagrams effectiveness for novel phase discovery.

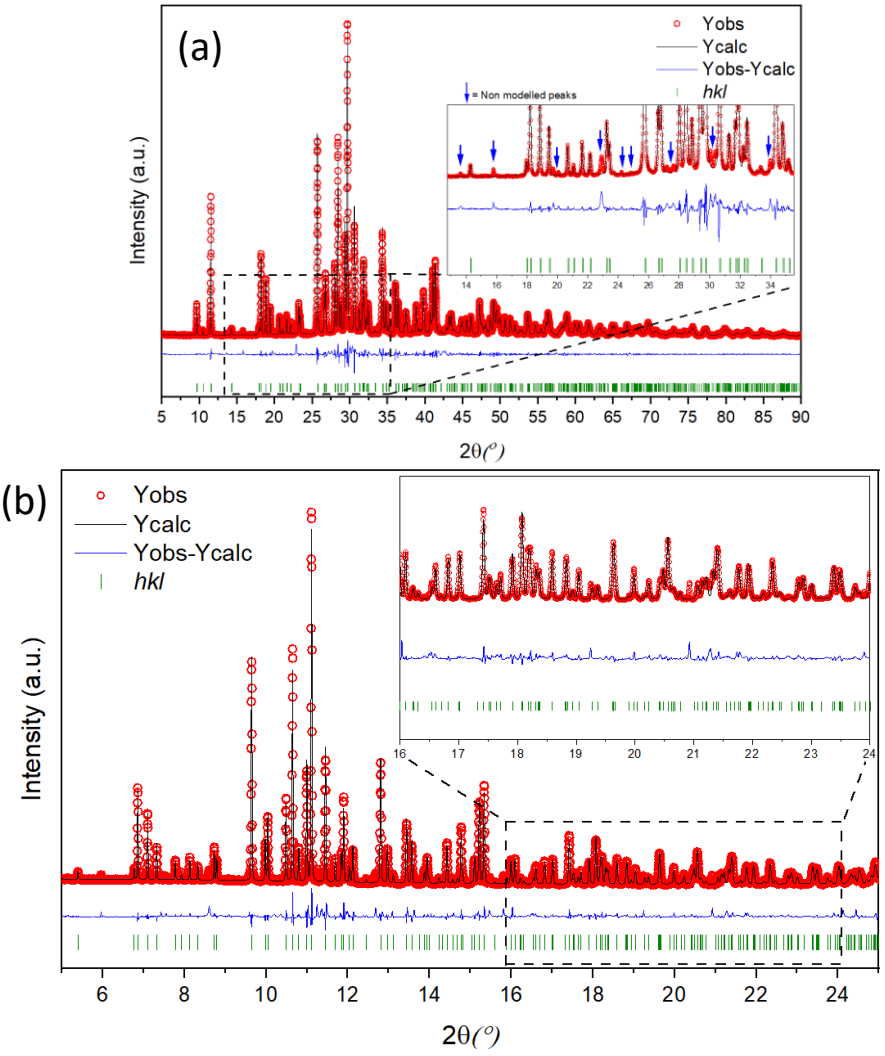

Fig. 2.11. (a) Pawley refinement of the $Sr_{12}Al_{20}Si_{12}O_{66}$ lab-PXRD data using the *P*6$_3$ cell. The blue arrows indicate secondary phase peaks not modelled by this space group **(b)** Refinement of the SPD data (λ=0.5904 *Å*) (R_{wp}=8.1%) collected on the optimised AQ $Sr_{1.35}Al_{2.7}Si_{1.3}O_8$ sample.

Energy dispersive X-ray spectroscopy (EDS) analysis by transmission electron microscopy (TEM) and SEM (SEM result in table 2.2) supported this formula and synthesis from this point helped reduce the crystallisation $SrAl_2SiO_6$, as shown in Fig. 2.13. after synthesis optimisation had been conducted. crystallisation however, optimisation of the synthesis protocol was still required. The Rietveld refinement of the NPD data is shown in Appendix 1, A.2.6.

Table 2.2. Quantitative analysis (atomic % with standard deviation) obtained by EDS analysis on $Sr_{12}Al_{20}Si_{12}O_{66}$ glass and crystallised (1h 1075°C) $Sr_{12}Al_{20}Si_{12}O_{66}$ sample.

Sample	Sr (At%)	Si (At%)	Al (At%)
Glass	27(2)	27(1)	46(1)
Crystal	27(1)	27(2)	46(2)

2.3.3. Obtaining Phase-Pure $Sr_{12}Al_{20}Si_{12}O_{66}$ by Synthesis Protocol Optimisation

With the structure solved and nominal formula found, the synthesis of $Sr_{12}Al_{20}Si_{12}O_{66}$ could be optimised. It was expected that, phase-pure fully crystallised samples, would now be obtained by GC, owing to synthesis from the true composition. If achieved then detailed structural characterisation and functionalisation could take place. Obtaining phase-pure samples for ^{29}Si MAS (magic angle spinning) and ^{27}Al MQ-MAS (multiple quantum magic angle spinning) NMR measurements was of particular importance to assign the specific Al^{3+} and Si^{4+} sites. The un-matched peaks from $P6_3$ Pawley refinement of the original sample aided in optimisation by highlighting which peaks corresponded to $Sr_{12}Al_{20}Si_{12}O_{66}$. Once again, both bulk and powdered phase-pure synthesis was targeted, with the goal of functionalisation afterwards. Two routes were discovered that led to the phase-pure synthesis of powdered $Sr_{12}Al_{20}Si_{12}O_{66}$; the first, discussed here, was through optimisation of the synthesis protocol and the second is discussed in the following section.

Glass of $Sr_{12}Al_{20}Si_{12}O_{66}$ was prepared by melt-quenching the sample, contained in a Pt crucible, from 1600°C, after it had been equilibrated at this temperature for 1.5 hours. Initial optimisation of the crystallisation protocol was then conducted by *in-situ* VTXRD and DSC on the glassy phase, (Fig. 2.12). The *in-situ* VTXRD result shows mixed-phase crystallisation occurring from a 'glassy' state, at 1000°C, which agrees with the T_c event observed by DSC at 1035°C. The state is called 'glassy' as some small $Sr_{12}Al_{20}Si_{12}O_{66}$ crystallites can already be observed forming in the glass. Crystallisation at 1000°C is described as being mixed-phased due to indexation of the pattern revealing additional peaks belonging to $SrAl_2SiO_6$, Rietveld refinement of the 1120°C pattern showed a $SrAl_2SiO_6$ content of 21wt.%. After 1140°C, these secondary phase peaks almost entirely disappear from the *in-situ* VTXRD spectra (7wt.% from Rietveld refinement) and the patterns can now be indexed by $Sr_{12}Al_{20}Si_{12}O_{66}$. When compared to the DSC trace, this transition to a single crystalline phase corresponded to the bump at 1209°C and was therefore labelled, T_p. The appearance of $SrAl_2SiO_6$ peaks in $Sr_{12}Al_{20}Si_{12}O_{66}$ pattern, is what inspired the investigation of $Sr_{12}Al_{20}Si_{12}O_{66}$ as the secondary phase observed in the optimisation of $SrAl_2SiO_6:Eu^{2+}$.

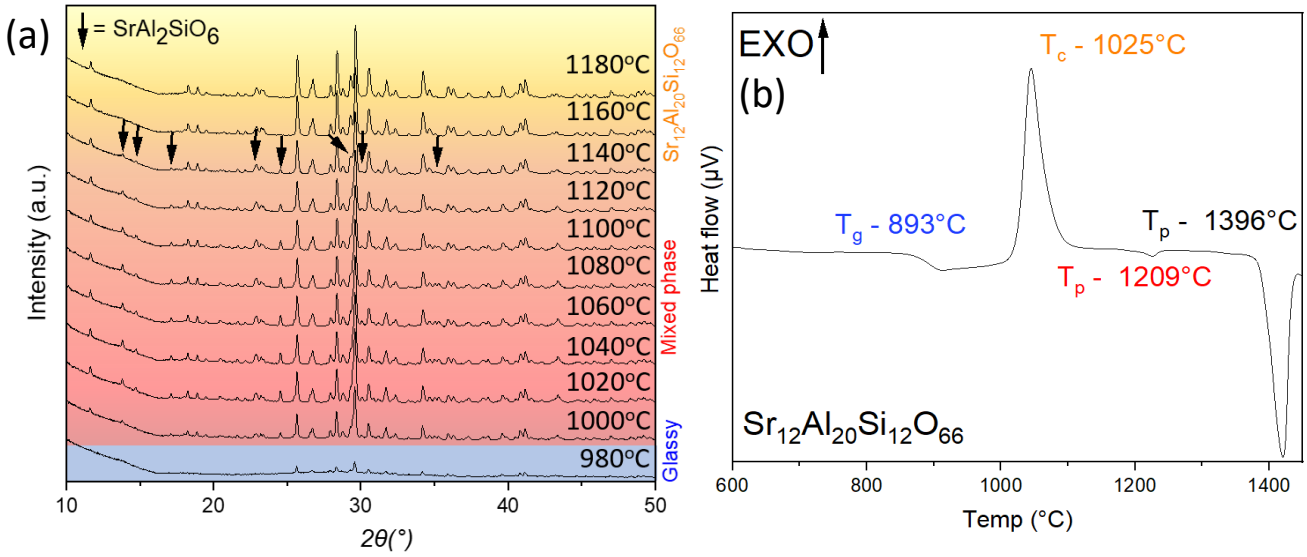

Fig. 2.12. (a) *In-Situ* VTXRD of $Sr_{12}Al_{20}Si_{12}O_{66}$ with the $SrAl_2SiO_6$ peaks marked by black arrows. **(b)** DSC of $Sr_{12}Al_{20}Si_{12}O_{66}$ showing the T_g, T_c, T_p, and T_m.

This relationship between the two phases, suggested that it may be possible to stabilise both of them in the one sample. Researching this question may be a way of tuning the properties of the functionalised phases, tailoring them between $Sr_{12}Al_{20}Si_{12}O_{66}$ and $SrAl_2SiO_6$ depending on the ratio of crystalline phases present. *In-situ* VTXRD analysis of $Sr_{12}Al_{20}Si_{12}O_{66}$ showed it to be stable up to at least 1200°C (maximum operating T of the Anton Parr HTK1200 furnace), and no obvious signal due to decomposition was observed in the DSC trace up to the onset of melting at ~1396°C. *Ex-situ* GC's were, therefore attempted from a temperature of 1200°C and time of 1h (Appendix 1, A.2.7.) to determine whether the compound is indeed metastable. These experiments showed that $Sr_{12}Al_{20}Si_{12}O_{66}$ decomposed into stoichiometric $SrAl_2Si_2O_8$, (*C2/m*), at temperatures above 1400°C, giving a synthesis range of 1140-1400°C, and proving its metastability. The lack of a T_d in the DSC trace was reasoned to be due to samples melting point, T_m – 1396°C, being too close to the crystallisation temperature of $SrAl_2Si_2O_8$. The high decomposition temperature of $Sr_{12}Al_{20}Si_{12}O_{66}$ provoked the question of whether it could be synthesised by the solid-state method. Three annealing's were conducted at 1100°C, 1200°C and 1300°C, for 12 hours, however primarily $SrAl_2Si_2O_8$ (*C2/m*) and $Sr_2Al_2SiO_7$ ($P\text{-}42_1m$) was observed crystallising, showing that $Sr_{12}Al_{20}Si_{12}O_{66}$ could not be synthesised by a solid-state approach.

Phase-pure GC synthesis trials started with an annealing temperature of 1075°C for 1h, as despite this temperature being below the experimentally identified range, it had been proven to yield highly crystalline specimens of the original non-nominal formula (Section 2.3.1. Fig.2.9.). Rietveld analysis determined that this annealing produced a sample with 11wt.% $SrAl_2SiO_6$ and 2wt.% $SrAl_2Si_2O_8$ as secondary phases, corresponding to the peaks at 22.9° and 27.5° in Fig. 2.13. Sintering at a higher temperature reduced the fraction of $SrAl_2SiO_6$ secondary phase, however, it also increased $SrAl_2Si_2O_8$ crystallisation due to being closer to the decomposition temperature of $Sr_{12}Al_{20}Si_{12}O_{66}$ (1h 1150°C pattern of Fig. 2.13.). This suggested

that annealing time should now be optimised as further increasing the temperature would only lead to more $SrAl_2Si_2O_8$ crystallisation. An annealing of 48h at 1150°C, was subsequently attempted (Fig. 2.13.) with the resultant PXRD showing no secondary phase. Therefore, the first phase-pure synthesis procedure for powdered ceramic $Sr_{12}Al_{20}Si_{12}O_{66}$ (1150°C for 48h) had been uncovered.

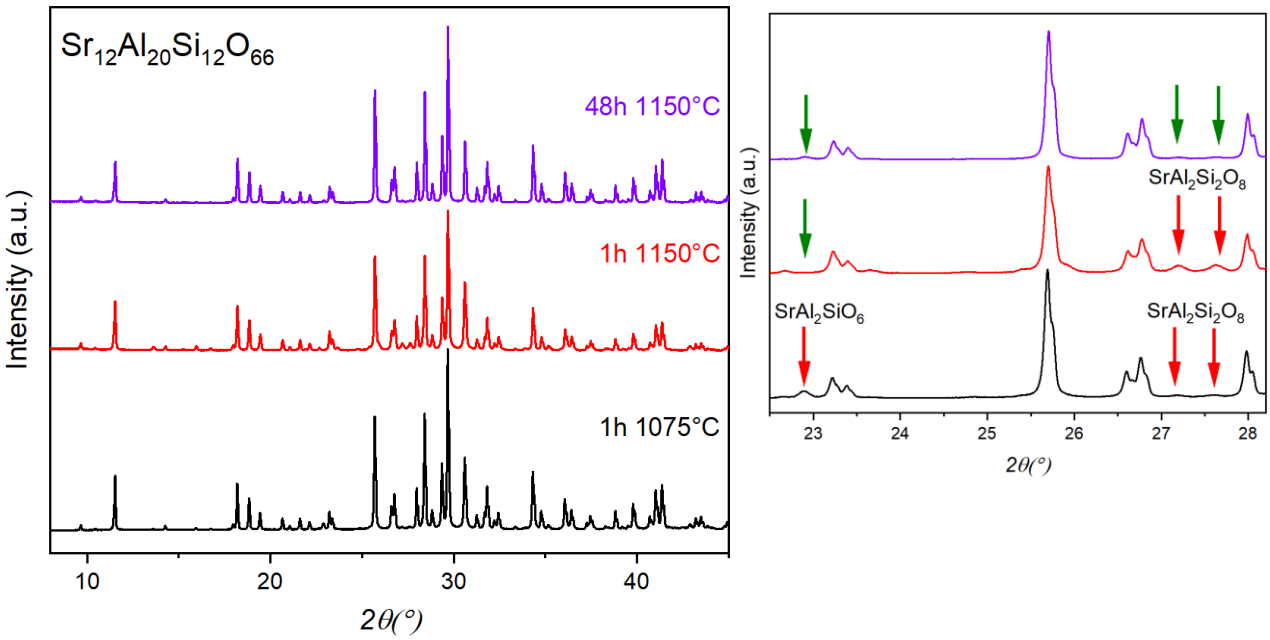

Fig. 2.13. Comparison of the PXRD patterns produced from the 1h 1075°C, 1h 1150°C and 48h 1150°C sintered samples. Inset shows a zoom of the main secondary phases ($SrAl_2SiO_6$ & $SrAl_2Si_2O_8$), red arrows show the presence of secondary phase while green arrows show its removal.

2.3.4. Obtaining Phase-Pure $Sr_{12}Al_{20}Si_{12}O_{66}$ by Modifying the Stoichiometry

Another explanation was theorised to explain the presence of secondary phases. Small variations in the Al^{3+}/Si^{4+} ratio could be compensated by Sr^{2+} vacancies or additions, other related aluminosilicates have demonstrated this behaviour (the $SrAl_2O_4$-$SrAl_2Si_2O_8$ series). The structure solution and refinement may not be sensitive to these subtle changes, leading to small alterations in the Al^{3+}/Si^{4+} ratio. An excess of Al^{3+} or Si^{4+} in the formula could explain the presence of secondary phases. To investigate this, minor modifications to the $Sr_{12}Al_{20}Si_{12}O_{66}$ formula were made and synthesis trials were conducted.

Annealing trials (1h 1150°C) began by testing several compositions further away from the $SrAl_2SiO_6$ point in the ternary diagram, i.e. Si was added and Al removed, as shown in Fig. 2.14.(b). PXRD analysis of these phases revealed an increase in secondary phases (mainly $SrAl_2Si_2O_8$), rather than the expected decrease. EDS measurements were, therefore, conducted on crystals of $Sr_{12}Al_{20}Si_{12}O_{66}$ in a multiphasic sample to determine what elemental excess was causing secondary phases ($SrAl_2SiO_6$ & $SrAl_2Si_2O_8$) to form. Comparing the atomic percentage (at.%) of $SrAl_2SiO_6$ to $Sr_{12}Al_{20}Si_{12}O_{66}$ showed an excess of ~4mol% Si, as shown in table 2.3.

Table 2.3. Quantitative analysis (Atomic % with standard deviation) obtained by EDS analysis of 1h 1150°C annealed, multiphasic $Sr_{12}Al_{20}Si_{12}O_{66}$ sample, comparing the atomic %'s of $Sr_{12}Al_{20}Si_{12}O_{66}$ and $SrAl_2SiO_6$ to show the Si excess.

Sample	Sr (At%)	Si (At%)	Al (At%)
$Sr_{12}Al_{20}Si_{12}O_{66}$	27(2)	27(1)	46(1)
$SrAl_2SiO_6$	24(2)	29(7)	47(1)

This combined with the Si excess observed when the $Sr_{12}Al_{20}Si_{12}O_{66}$ and $SrAl_2Si_2O_8$ formulas are compared suggested removing Si from the formula.

4mol% Si was removed from the $Sr_{12}Al_{20}Si_{12}O_{66}$ formula, giving a new composition of $Sr_{12}Al_{20}Si_{11.52}O_{65.04}$, abbreviated to P4-SrAlSiO (where P represents Si poor), as shown in Fig. 2.14.(b). When this glass was prepared and sintered for 1h at 1150°C, the PXRD pattern in Fig. 2.14.(a). was achieved. This phase showed no secondary phases, as indicated by the black arrows, extremely well resolved peaks and roughly the same lattice parameters as the first optimised protocol when they were refined by the Pawley method (1st *a*- = 9.72011(6)*Å, b*- = 18.2284(1) *Å*, 2nd *a*- = 9.7177(1) *Å b*- = 18.2078(3)*Å*). Meaning, a second optimised synthesis protocol for powdered ceramic sample had been found by modifying the composition. This suggested that, there may be cation vacancies within the framework which could be exploited for tuning of the phases properties. More analysis was first required to determine this and so Rietveld analysis (Section 2.4.1.) and NMR measurements (Section 2.4) were conducted.

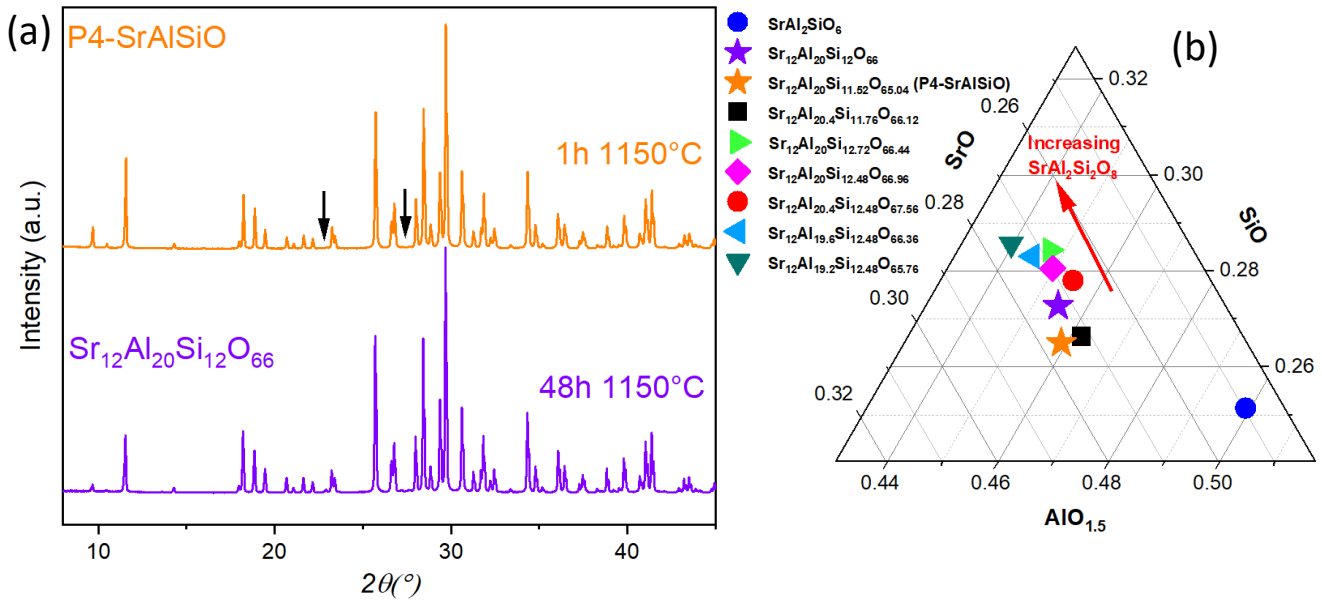

Fig. 2.14. (a) Comparison of the PXRD patterns from the two optimised protocols for phase-pure $Sr_{12}Al_{20}Si_{12}O_{66}$ synthesis. **(b)** Zoom of the SrO-$AlO_{1.5}$-SiO_2 diagram showing the various compositions attempted in the optimisation of the formula.

2.3.5. Surface Glass Crystallisation of Bulk P4-SrAlSiO:Eu^{2+},Dy^{3+}

As discussed in Section 1.4.2. of Chapter 1, transparency had been achieved in polycrystalline bulk samples of hexacelsian-type $Sr_{1+x/2}Al_{2+x}Si_{2-x}O_8$ ($0 \leq x \leq 0.4$), using a full congruent crystallisation from bulk glass approach, despite the phases non-cubic space group.[8,23] The work by Al. Saghir had shown that large crystallites and structural disorder from Sr^{2+} occupancies and Al^{3+}/Si^{4+} ordering had enabled near maximum levels of transmission to be reached in a hexagonal system. Additionally, Wisniewski *et al.* had shown crystallisation in both hexacelsian-type $Sr_{1+x/2}Al_{2+x}Si_{2-x}O_8$ and $SrAl_2O_4$-type $Sr_{1-X/2}Al_{2-2X}Si_XO_4$ to occur from the surface.[9] The shared hexagonal symmetry between the hexacelsian-type polymorph and $Sr_{12}Al_{20}Si_{12}O_{66}$ as well as its tendency for surface-crystallisation suggested that full crystallisation from bulk glass approach would also be successful here. Factors like phase purity, porosity, grain boundary sizes, crystal orientations and defects would have to be controlled, as they had all been shown to impact transparency.[30–32]

Synthesis was attempted using the full glass crystallisation technique on the P4-SrAlSiO formula. This formula was chosen due to its shorter phase-pure sintering times. Once again, for functionalisation purposes, bulk optimisation was attempted on compositions co-doped with 1mol% Eu^{2+} and Dy^{3+}. Eu_2O_3 (99.999% Strem) and Dy_2O_3 (99.999% Strem) were doped for $SrCO_3$ giving the desired composition of $Sr_{11.74}Eu_{0.12}Dy_{0.12}Al_{20}Si_{11.52}O_{65}$, abbreviated to B-$Sr_{12}Al_{20}Si_{12}O_{66}$:$Eu^{2+}$,$Dy^{3+}$. Once reaction mixtures had been prepared, glass was made using the same technique in Section 2.2.4. This resulted in transparent, bubble-less pieces of B-$Sr_{12}Al_{20}Si_{12}O_{66}$:$Eu^{2+}$,$Dy^{3+}$ glasses, as expected. These rough bulk samples were then cut to approximate oval dimensions of (15 mm length x 12 mm width x 3 mm thickness) and polished. The polished uniform surface increased the chances of retaining transparency after crystallisation by reducing the number of heterogenous nucleation points. Three samples were prepared for sintering in this manner, crystallisations occurred in a tube furnace under an N_2:H_2 (94:6) atmosphere to permit the reduction of Eu^{3+}.

Three procedures were used (a) 6h at 1050°C, (b) 12h at 1075°C and (c) 12h at 1100°C, resulting in two glass-ceramic samples and one fully crystallised ceramic sample, with three different states of transparency according to the level of crystallisation (Fig. 2.15.). Phase purity of the bulk ceramic sample was confirmed by PXRD (Appendix 1, A.2.8.) however, insufficient crystallisation had occurred to verify the glass-ceramic samples, although their deep blue PersL emission suggested $Sr_{12}Al_{20}Si_{12}O_{66}$ had formed.

SEM was conducted on polished cross sections of the bulk sintered samples, results in Fig. 2.15. Sample (a) was found to have the highest degree of transparency, with a crystalline depth layer around 70 μm. The depth of the crystalline layer increases to approximately 350 μm in sample (b) and with it, transparency decreases. Only by looking at the cross section image of Fig. 2.15.(b) can a transparent glassy layer be viewed.

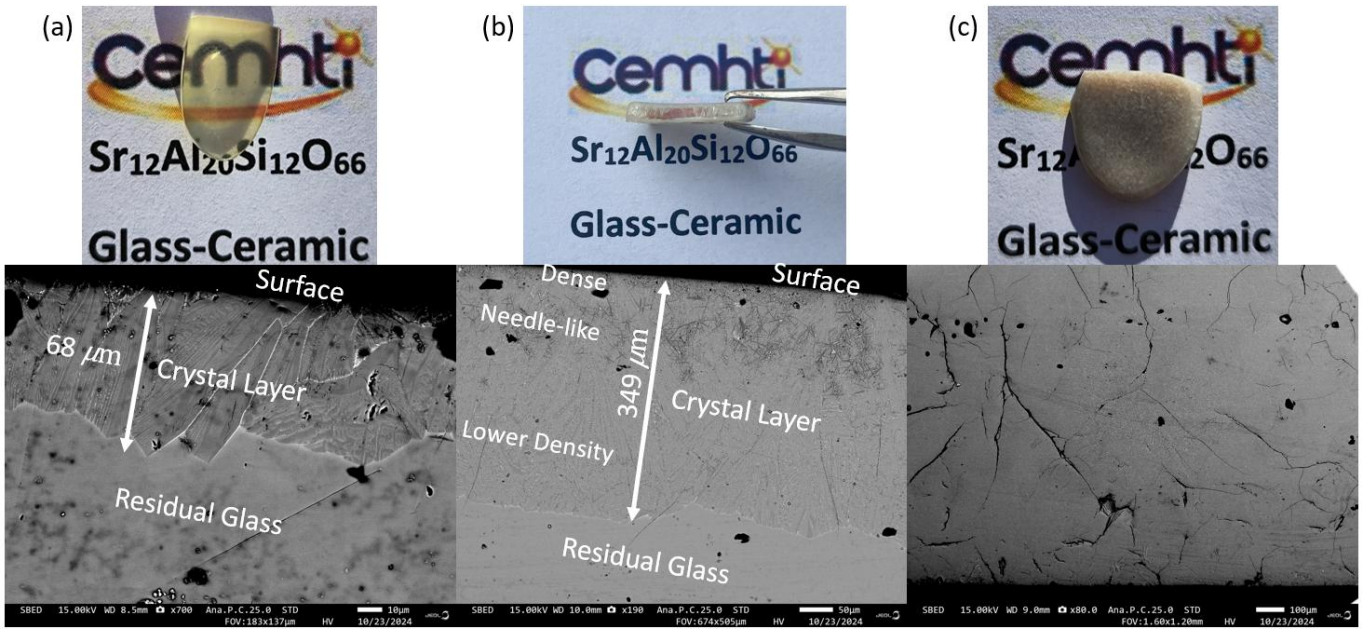

Fig. 2.15. Transparency and depth of crystalline layer (from SEM) achieved by sintering's of B-$Sr_{12}Al_{20}Si_{12}O_{66}$:$Eu^{2+}$,$Dy^{3+}$ at **(a)** 6h at 1050°C. **(b)** 12h at 1075°C. **(c)** 12h at 1100°C.

Small zones of potentially orientated crystalline domains can be viewed, meaning synthesis can be optimised to increase transparency. For example, three types of microstructure are observed in sample (b), small densely packed crystallites at the surface, densely packed needle-like crystallites further down, and then a lower density of crystallites for the rest of the layer. By understanding why three types of crystallisation are observed and controlling the process to favour only one type during annealing, transparency could be increased. In the final sample (c), the SEM image shows un-orientated full crystallisation, resulting in an opaque ceramic sample. Large cracks and pores are also visible, which must be reduced for transparency to be achieved in this sample.

Again similar to the bulk synthesis of $SrAl_2SiO_6$:Eu^{2+},Dy^{3+} (Section 2.2.4.) EBSD measurements should be conducted on all of the samples, (a), (b) and (c) in Fig. 2.15, so that the crystallite orientation of these phases can be determined and used to optimise the transparency of these samples. Pores are also visible in the crystalline layer of these samples, and additionally, cracks are visible in sample (c), which reduces transparency and leaves room for synthesis optimisation, which as mentioned can be supported by EBSD measurements.

These initial results expanded the idea of full glass crystallisation as a route to transparency, by showing that partial surface crystallisation can also maintain transparency, while still giving properties, discussed in Section 2.7., from the crystalline layer. The crystalline layers of samples (a) and (b) represented 5% and 22.3% respectively, of the total sample thickness. By preparing thinner samples, it may be possible to increase these percentages, potentially resulting in transparent ceramic samples. The preparation methods and synthesis procedures would need to be fully optimised for this result to be achievable.

2.4. Structural Analysis of $Sr_{12}Al_{20}Si_{12}O_{66}$

2.4.1. Rietveld Refinement of P4-SrAlSiO

With synthesis now optimised for powdered and bulk samples of $Sr_{12}Al_{20}Si_{12}O_{66}$, Rietveld modelling of single-phase material was attempted. This provided another method to confirm the SPD/NPD generated $P6_3$ model and refine the atomic positions of samples synthesised from the new formula. The necessary high-resolution lab-PXRD data was collected on a sample of P4-SrAlSiO, across an angular range of 5-130°, with a scan time per step of 2.3s and an angle increment of 0.019°. A deep silicon sample holder was used, which rotated during measurement and provided better powder averaging by sampling from a larger area. By allowing the powder to naturally compact in the holder, (i.e. an ethanol mull wasn't used) the chances of PO were reduced. Hexagonal space groups have been shown to permit the growth of anisotropic crystallites, such as needles or plates. These crystal morphologies are known to lead to PO, especially when concentrated on the surface of the PXRD sample holder, leading to the over representation of specific crystal planes or axis. In $Sr_{12}Al_{20}Si_{12}O_{66}$, the *c*- axis in particular, could be susceptible to PO overrepresentation due to larger size compared to the *a/ b*- axes (18.21 *Å* vs. 9.72 *Å*).

The hexagonal $P6_3$ unit cell (a/b = 9.72 *Å*, c = 18.21 *Å*) identified previously was used as a basis for the Rietveld refinement, using TOPASV7 and jedit software. A refinement file with a background function consisting of 10 parameters, 6 TCHZ profile functions and 23 atomic sites was created. The atomic displacement parameters (ADPs) of all atomic sites were refined by grouping the atoms together, with reasonable values being obtained, (table 2.4.). Only the atomic positions of Sr^{2+} were refined due to the lack of diffraction contrast between Al^{3+} and Si^{4+} ions. Again, to balance the formula an Al^{3+}/Si^{4+} ordering of 3:1 was imposed upon the occupancies of the Al^{3+}/Si^{4+} ions. A correction for PO also wasn't needed, with peak intensities being well matched. The refinement file gave a R_{wp} of 7.123% and χ of 2.875, with the refinement achieved shown in Fig. 2.16. When the 48h 1150°C data was refined by the Rietveld method a similarly good refinement was achieved (Appendix 1 A.2.9.). This gave updated lattice parameters of *a/b*- = 9.72011(6) *Å* and *c*- = 18.228(1) *Å* and a cell volume of 1491.46 (2) $Å^3$.

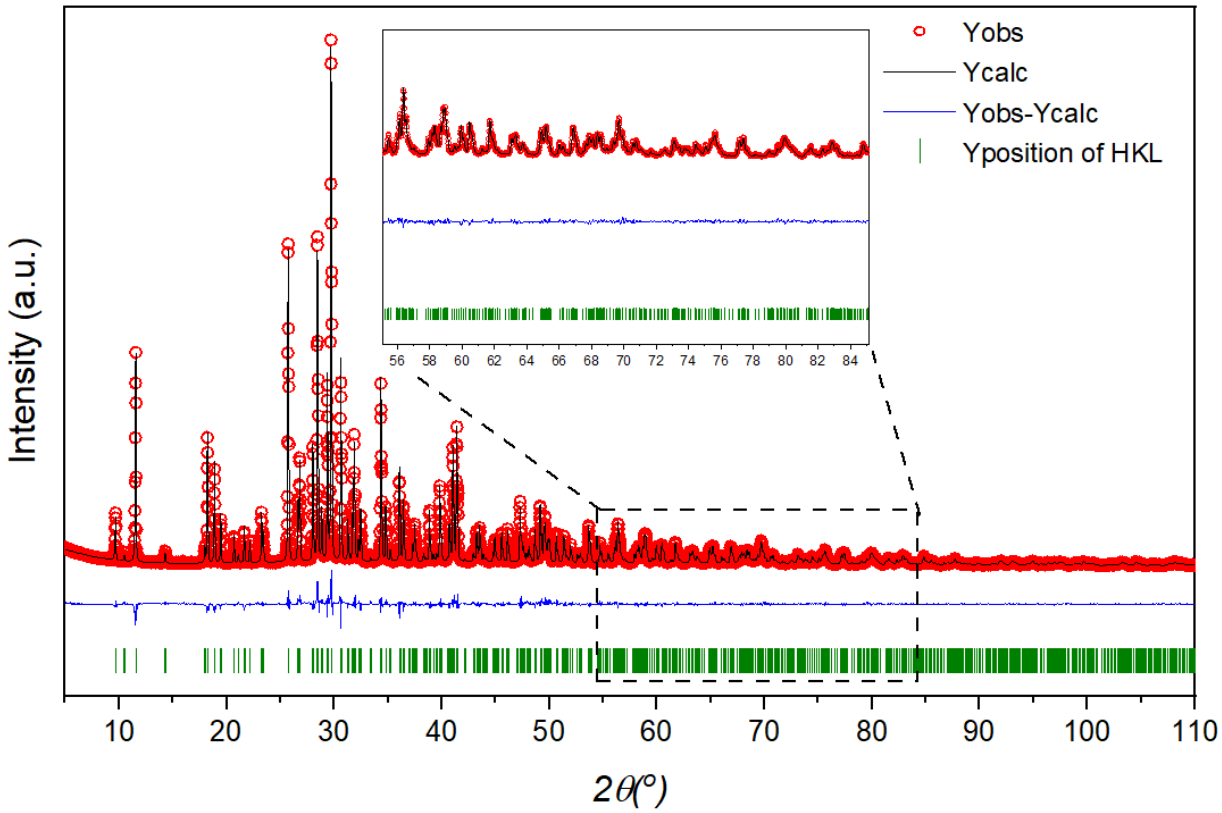

Fig. 2.16. Rietveld refinement of the phase-pure P4-SrAlSiO ceramic powder from lab-PXRD data, synthesised by GC with a powder sintering step of 1h at 1150ºC. A R_{wp} of 7.123% and χ of 2.875 was achieved. The zoom inset shows the refinement at high angle.

Table 2.4. Final refined structural parameters obtained from lab-PXRD data, collected at room temperature on a powdered sample of $Sr_{12}Al_{20}Si_{12}O_{66}$ ($P6_3$ space group, *a*- = 9.72011(6) *Å*, *b*- = 9.72011(6) *Å* and *c*- = 18.228(1) *Å* and cell volume = 1491.46 (2) *Å*^{3}).

Atom	Position	x	y	z	Occ	B_{iso}
Sr1	6c	0.2614(2)	0.3774(2)	0.6940(1)	1	2.36(3)[a]
Sr2	6c	-0.0996(2)	0.5907(2)	0.884(1)	1	2.36(3)[a]
Al/Si1	2b	1/3	2/3	0.8535	0.667/0.333	1.58(5)[b]
Al/Si2	6c	0.2418	0.9171	0.5202	0.667/0.333	1.58(5)[b]
Al/Si3	2b	1/3	2/3	0.5613	0.667/0.333	1.58(5)[b]
Al/Si4	2a	0.0000	1.0000	0.5861	0.667/0.333	1.58(5)[b]
Al/Si5	6c	-0.1443	0.3411	0.6442	0.667/0.333	1.58(5)[b]
Al/Si6	2a	0	1	0.7700	0.667/0.333	1.58(5)[b]
Al/Si7	6c	0.9253	0.6915	0.8540	0.667/0.333	1.58(5)[b]
Al/Si8	6c	-0.0094	0.4090	0.8058	0.667/0.333	1.58(5)[b]
O1	6c	0.4493	0.3833	0.8110	1	2.20(7)[c]
O2	6c	0.7408	0.6373	0.8684	1	2.20(7)[c]
O3	6c	-0.1643	0.5046	0.6458	1	2.20(7)[c]
O4	6c	-0.0107	0.3617	0.7165	1	2.20(7)[c]
O5	6c	0.2163	0.7301	0.5304	1	2.20(7)[c]
O6	6c	-0.0601	0.3445	0.5627	1	2.20(7)[c]
O7	6c	0.2765	1.0072	0.4294	1	2.20(7)[c]
O8	2b	-1/3	1/3	0.4460	1	2.20(7)[c]
O9	2a	0.0000	1.0000	0.6759	1	2.20(7)[c]
O10	6c	0.1509	0.1743	0.7977	1	2.20(7)[c]
O11	6c	0.1940	0.5039	0.8271	1	2.20(7)[c]
O12	6c	0.1325	0.1908	0.5536	1	2.20(7)[c]
O13	2b	1/3	2/3	0.6504	1	2.20(7)[c]

2.4.2. Structure of $Sr_{12}Al_{20}Si_{12}O_{66}$

After Rietveld refinement, the visualisation of the hexagonal *P*6$_3$ structure of $Sr_{12}Al_{20}Si_{12}O_{66}$, with refined Sr^{2+} positions, was possible using VESTA software, (Fig. 2.17). [33] It was found that the structure's framework is comprised of corner sharing $(Al,Si)O_4$ tetrahedra, anti-parallelly stacked in an *ABAB* arrangement along the *c*-axis. Similar to the $SrAl_2SiO_6$ structure, the B layer demonstrated less inter layer linkers than the A layer, which resulted in an anisotropic-3D anisotropic structure overall. Two fully occupied Sr^{2+} sites sat in the voids created by the $(Al/Si)O_4$ tetrahedra, with the 'empty' layer containing 7-fold coordinated Sr^{2+} ions and the 'full' layer containing 6-fold coordinated Sr^{2+} ions. This structure was then confirmed by HAADF-STEM imaging, as discussed in the following section.

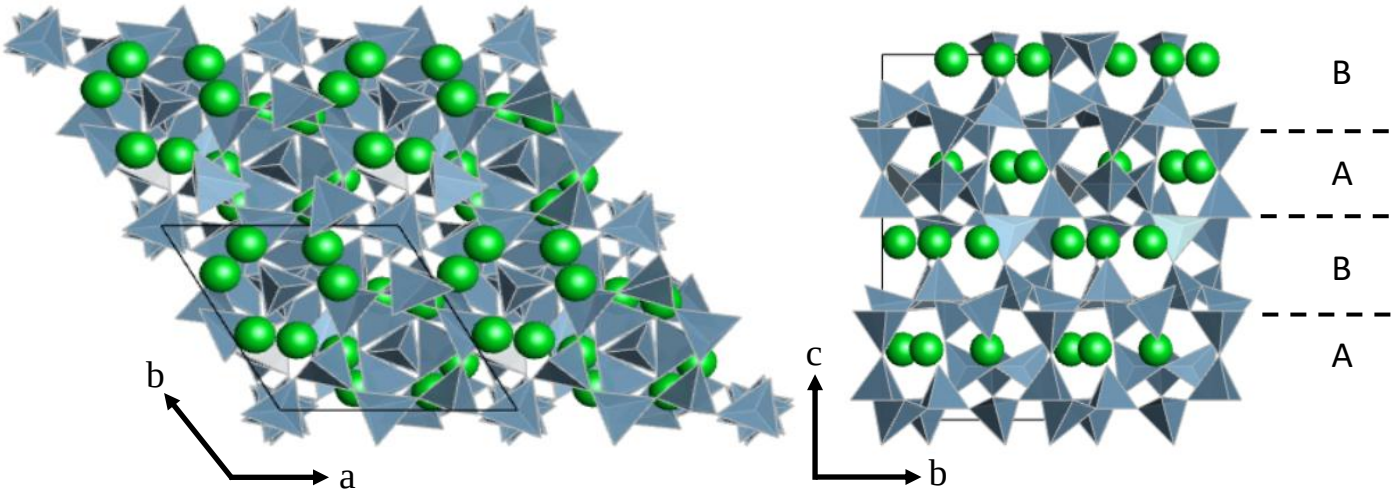

Fig. 2.17. Structural model of $Sr_{12}Al_{20}Si_{12}O_{66}$, as viewed down the *c*- and *a*- axes respectively. Structure generated from Rietveld refinement and visualised with VESTA software, the unit cell is shown in black.

2.4.3. Atomic-Resolution HAADF-STEM Imaging of $Sr_{12}Al_{20}Si_{12}O_{66}$

Atomic-resolution HAADF-STEM was used as a complementary method to confirm the structural model. The use of a high energy electron beam allows heavy, electron dense atoms like Sr and Al/Si to be visualised. Inspection of the structure in VESTA software, identified the *a/b*- and *b/c*- planes as target orientations for structure confirmation. When viewed down the *c*- axis, the structure showed repeating hexagonal rings made up of Sr atoms, with Al^{3+}/Si^{4+} sites found at their centre and at the joining point of three of these rings. These features, as well as the stacked *ABAB* structure viewed down the *a*- axis, would be visually prominent by HAADF-STEM, and so were targeted.

Initially, a powdered sample was prepared and deposited onto a holey carbon matrix, using the technique discussed in Chapter 4 (4.6.2.). However, resolution problems were encountered due to uneven sample thickness and difficulties finding the *h,k,l* planes of interest. To solve this, a sintered bulk piece of $Sr_{12}Al_{20}Si_{12}O_{66}$ was polished, using a tripod and inlaid diamond discs, to a thickness of 50 μm. PIPS GATAN

argon milling was then used to further reduce the thickness to 20nm, as discussed in Chapter 4 (4.6.2.). With this, atomic-resolution images of both targeted orientations were observed, as seen in Fig. 2.18. The even sample thickness resulted in no loss of image resolution when scanning across the sample and the extreme thinness allowed atomic-resolution to clearly be achieved (<3.5 *Å*). As predicted, the *a/b*- plane showed regularly repeating hexagonal Sr^{2+} rings (shown in green), with Al^{3+}/Si^{4+} sites viewed at their centre (shown in red). Specific Al^{3+}/Si^{4+} sites could even be viewed due to the difference in their intensity. The atoms at the centre of the hexagonal rings (shown in red) appeared brighter than those outside, owing to the higher number of Al^{3+}/Si^{4+} sites stacked in their atomic column, with their cumulative contributions resulting in a brighter spot.

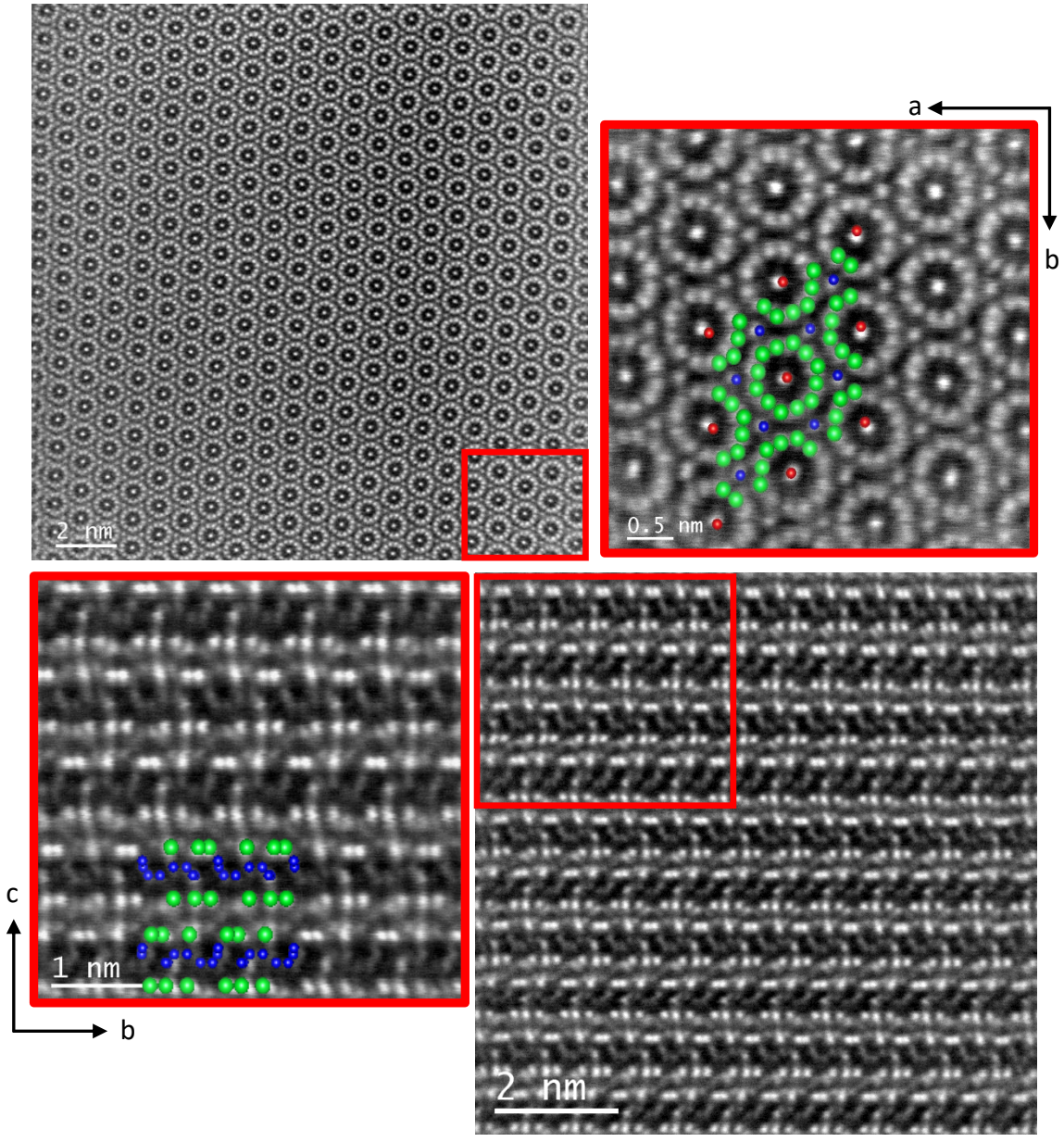

Fig. 2.18. Atomic-resolution HAADF-STEM (<3.5 *Å*) images of $Sr_{12}Al_{20}Si_{12}O_{66}$, showing the *a/b* and *b/c* planes respectively. Inset images shows magnified regions with the $Sr_{12}Al_{20}Si_{12}O_{66}$ unit cell superimposed. Red atoms show the brighter Al^{3+}/Si^{4+} spots at the centre of the hexagonal rings, while blue atoms show the less intense spots and the worm-like chains.

At the centre of the rings, 4 Al^{3+}/Si^{4+} positions are stacked in the unit cell whereas only 2 are stacked for those outside the rings (shown in blue). In HAADF-STEM image contrast comes from both Z-number differences and multiplicity of the site in the column. Equally, when the *b/c*- plane was viewed, the antiparallel stacking of the Sr atoms was clearly visible. Worm-like chains (shown in blue) formed by Al/Si atoms and arranged anti-parallel to each other were found between the Sr^{2+} layers. These were characterised as left-facing and right-facing due to brighter spots observed at their respective 'heads', again due to cumulative stacking effects. This, previously unnoticed feature, was matched along with the other described structural features when a simplified unit cell was superimposed upon these images, (Fig. 2.18.). This analysis therefore confirmed the structural model of $Sr_{12}Al_{20}Si_{12}O_{66}$.

2.4.4. Topological Analysis of $Sr_{12}Al_{20}Si_{12}O_{66}$

With the structure of $Sr_{12}Al_{20}Si_{12}O_{66}$ solved and confirmed by the Rietveld method and atomic-resolution STEM-HAADF imaging, its topology was analysed to determine the novelty of its structure type. Through this the structure was found to be far more complex than those of $SrAl_2SiO_6$, the hexacelsian-type $Sr_{1+x/2}Al_{2+x}Si_{2-x}O_8$ and $SrAl_2O_4$-type $Sr_{1-X/2}Al_{2-2X}Si_XO_4$; containing 3, 5, 6, 7, 8 and 9 membered rings, formed by the $(Al/Si)O_4$ tetrahedra. Topological analysis of $Sr_{12}Al_{20}Si_{12}O_{66}$ described it by the point group $\{3.5^2.6.7^2\}_3\{5.6^5\}_3\{5^2.6^3.8\}_3\{6^3.7^2.9\}_3\{6^3\}_2\{6^6\}_2$. Interestingly, despite being compositionally close to the $SrAl_2O_4$ – $SrAl_2Si_2O_8$ tie line, no structural similarities were found to the three phases discovered along this line, which suggested that potentially new properties could be found.

Despite the complex topological point group, this framework already existed in the form of $Ba_{13}Al_{22}Si_{10}O_{66}$, discovered by Gebert and functionalised by Denis *et al.*[34,35] In the work by Denis *et al.* they had found $Ba_{13}Al_{22}Si_{10}O_{66}$ to be readily synthesisable by the solid-state method, which suggested an increased stability of this phase, compared to $Sr_{12}Al_{20}Si_{12}O_{66}$. Structurally, $Ba_{13}Al_{22}Si_{10}O_{66}$ is analogous to $Sr_{12}Al_{20}Si_{12}O_{66}$, with the main difference being an extra 1/3rd occupied Ba site, as shown in Fig. 2.19. The structure was also found as part of a solid solution according to the formula $(Ba,Sr)_{13-x}Al_{22-2x}Si_{10+2x}O_{66}$ for Sr substitutions up to x=7.8. The existence of a direct strontium analogue, $Sr_{13}Al_{22}Si_{10}O_{66}$, was proposed by the researchers but they were unable to synthesise it by solid-state reactions. A preferential ordering of the Al^{3+}/Si^{4+} sites was found by bond valence sum (BVS) calculations with respect to Al^{3+}, with the lower valance tetrahedral sites found to be occupied by Al^{3+} ions. Finally, this work also succeeded in the functionalisation of $Ba_{13}Al_{22}Si_{10}O_{66}$ through doping with Eu^{2+}, which produced white fluorescence and phosphorescence for Eu^{2+} doping levels lower than 4%.

The existence of $Ba_{13}Al_{22}Si_{10}O_{66}$, a phase with the same aluminosilicate framework-type raised several questions about the possible compositional range of $Sr_{12}Al_{20}Si_{12}O_{66}$ and its functionalisation:

1. Does $Sr_{12}Al_{20}Si_{12}O_{66}$ exist as part of a solid solution, according to the formula $Sr_{12+x}Al_{20+2x}Si_{12-2x}O_{66}$?

If $Sr_{13}Al_{20}Si_{12}O_{66}$ was successfully synthesised by a GC approach, a solid solution may exist between $0 \leq x \leq 1$. Theoretically, the solution could extend to x=3 by fully filling the vacant A site (which is 1/3 occupied in the Ba analogue) with Sr^{2+}, corresponding to a formula of $Sr_{15}Al_{26}Si_6O_{66}$.

2. Is it possible to create Sr/ Ba/ Ca mixed phase solid solutions according to the formulae $Sr_{12-x}(Ba/Ca)_xAl_{20+2x}Si_{12-2x}O_{66}$ and $Sr_{12}(Ba/Ca)_xAl_{20+2x}Si_{12-2x}O_{66}$?

$Sr_{7.80}Ba_{5.07}Eu_{0.13}Al_{22}Si_{10}O_{66}$ had successfully been synthesised. With $Sr_{12}Al_{20}Si_{12}O_{66}$ now found, it was possible that similar substitution rates could be achieved with Ba^{2+} and Ca^{2+}.

3. Do fully substituted Ba and Ca analogues exist? i.e. $Ba_{12}Al_{20}Si_{12}O_{66}$ and $Ca_{12}Al_{20}Si_{12}O_{66}$.
4. Does a mixed Ca/Ba phase exist, $Ba_xCa_xAl_{20+2x}Si_{12-2x}O_{66}$ for some value(s) of x?
5. Do any of these phases have PersL properties and can the colour/ intensity be tuned through their theorised solid solutions?

White PL and PersL properties were observed in $Ba_{13}Al_{22}Si_{10}O_{66}:Eu^{2+}$, therefore it is reasonable to assume they will be present in $Sr_{12}Al_{20}Si_{12}O_{66}$.

These questions of solid solutions and functionalisation will be addressed in Section 2.5. onwards.

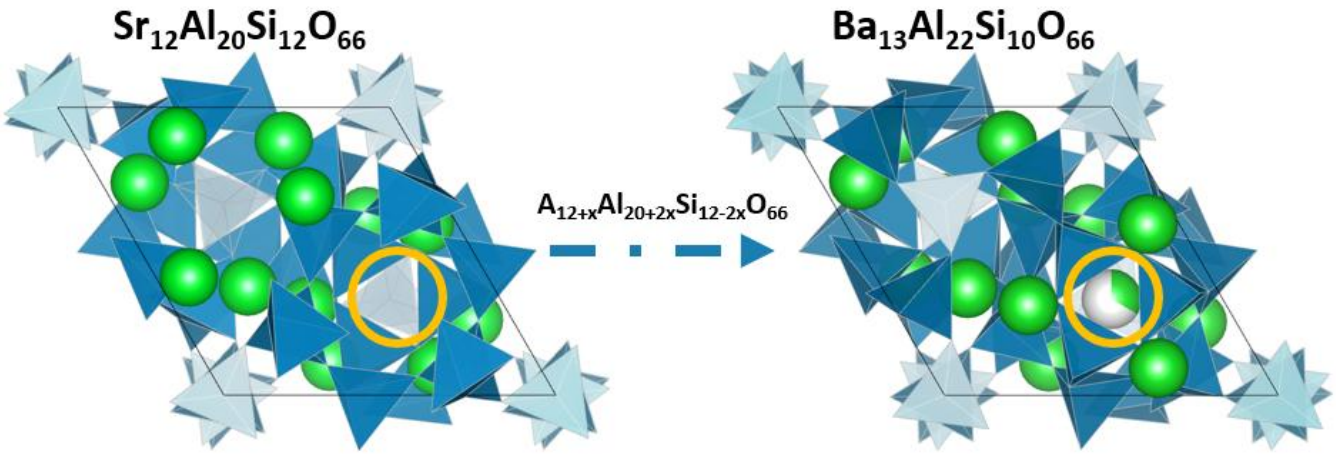

Fig. 2.19. Structures of $Sr_{12}Al_{20}Si_{12}O_{66}$ and $Ba_{13}Al_{22}Si_{10}O_{66}$, as viewed down the c- axis. The 3rd cation site, filled as x increases is shown by a yellow ring.

2.5. Investigation of Al^{3+}/Si^{4+} Ordering Within $Sr_{12}Al_{20}Si_{12}O_{66}$

2.5.1. Assigning Al^{3+}/Si^{4+} Sites Based on Diffraction Data

With the structure of $Sr_{12}Al_{20}Si_{12}O_{66}$ confirmed by Rietveld refinement and HAADF-STEM imaging, the specific occupancies of the Al^{3+} and Si^{4+} sites were examined. As discussed, full occupancy of the Sr^{2+} sites and a 3:1 occupancy of the Al^{3+}/Si^{4+} sites had been assumed across all of their atomic positions, as this maintained charge neutrality of the formula. The validity of this assumption was examined, by comparing the bond valence sums (BVS) of the Al^{3+} environments, to the expected values of Si^{4+} or Al^{3+} sites, results in table 2.5. Specifically, the bond lengths generated from the SPD/NPD data were chosen for this analysis as despite being generated from data collected on a non-nominal formula, $Sr_{1.35}Al_{2.7}Si_{1.3}O_8$, its NPD component showed the greatest sensitivity to O^{2-} positions.

To consider mixed occupancies across all of the Al^{3+}/Si^{4+} sites in a (1x1x1) cell, then several million configurations would have to be calculated. This number was far too large for each possible model to be computed and so constraints were applied:

1. Each site had to be fully occupied by either Al^{3+} or Si^{4+}.
2. The formula had to be maintained.
3. Chemical rules, such as minimising Lowenstein rules, must be followed.

Table 2.5. Average tetrahedra environments in $Sr_{12}Al_{20}Si_{12}O_{66}$ corresponding to the 8 Al^{3+}/Si^{4+} sites shown in table 2.4, M = Al^{3+} or Si^{4+}. The bond lengths values were used to calculate the bond valence sums (BVS) of Al^{3+} environments to suggest if the site is occupied by Al^{3+} or Si^{4+}. An R_0 of 1.651 and B of 0.37 was used for the calculations.

Site	Multiplicity	Connectivity	Average M-O distance (*Å*)	Tetrahedron volume (*Å*^{3})	BVS calc. of Al^{3+}
T1	1	Q3	1.589(2)	2.058	4.7
T2	3	Q4	1.733(13)	2.561	3.2
T3	1	Q3	1.636(3)	2.249	4.2
T4	1	Q4	1.721(10)	2.614	3.3
T5	3	Q4	1.735(12)	2.663	3.2
T6	1	Q4	1.682(8)	2.437	3.7
T7	3	Q4	1.614(10)	2.141	4.4
T8	3	Q4	1.720(12)	2.577	3.3

Comparing the BVS results of the Al^{3+} environments allowed all but the M6 site to be assigned, with the M6 site appearing to lie between the two expected values of 3 or 4. This site was assigned based on the second constraint i.e. what did the formula demand this site be, with respect to the already assigned positions. From this, it was realised that 2 Si atoms were missing, which enabled M6 to be assigned as an Si position. This generated the first model, m0, occupancies summarised in table 2.6.

When the bonding in this model was examined, specifically Si-O-Si bonding, it was found to contain 6 of these connections. Lowenstein's rule postulates that Al-O-Si linkages are enthalpically more favourable than Si-O-Si and Al-O-Al ones, meaning where possible, a structure will avoid their formation. [36,37] This also means that the lowest energy/ equilibrium form of any aluminosilicate will contain the fewest Lowenstein defects. Based on the formula, $Sr_{12}Al_{20}Si_{12}O_{66}$, the formation of Al-O-Al bonds was unavoidable, however the number of Si-O-Si connections could be minimised. Following this principle enabled a second model, m1, to be developed, which removed all Si-O-Si bonding while still obeying the formula, table 2.6. summarises this model. However, in this model diffraction-based bond lengths were now ignored.

Table 2.6. Summary of the m0 and m1 models, based on full occupancy of the sites and a (1x1x1) cell.

Model (1x1x1 cell)	T1	T2	T3	T4	T5	T6	T7	T8	N(Si-O-Si)
m0	2Si1	6Al2	2Si3	2Al4	6Al5	2Si6	6Si7	6Al8	6
m1	2Si1	6Al2	2Si3	2Si4	6Al5	2Al6	6Si7	6Al8	0

2.5.2. Comparison of Theoretical & Experimental ^{29}Si MAS and ^{27}Al MQMAS Results

To test the accuracy of these two models, they were first built using the supercell code, relaxed by DFT calculations, and then their theoretical solid-state ^{29}Si MAS and ^{27}Al MQMAS NMR spectra were computed by a GIPAW-DFT approach implemented in the CASTEP code.[38–41] This data was then compared to the experimental ^{29}Si MAS and ^{27}Al MQMAS spectrums collected on the optimised, 48h 1150°C sintered $Sr_{12}Al_{20}Si_{12}O_{66}$ sample. This sample was chosen as its long sintering time permitted the Al^{3+} and Si^{4+} ions to reach their equilibrium positions. As shown in Fig. 2.20., poor agreement was observed between the theoretical and experimental ^{29}Si and ^{27}Al spectra for m0, with it generating some non-existent T sites, and so this model was immediately discarded. A better agreement was found for m1 in the ^{29}Si MAS spectrum, however, when compared to the ^{27}Al MQMAS spectrum the model failed to account for certain intensities (shown by the grey arrows) and so this model was also discarded. These results suggested that more complex models, i.e. mixed occupancy of the Al^{3+}/Si^{4+} sites, was needed to accurately model the experimental data.

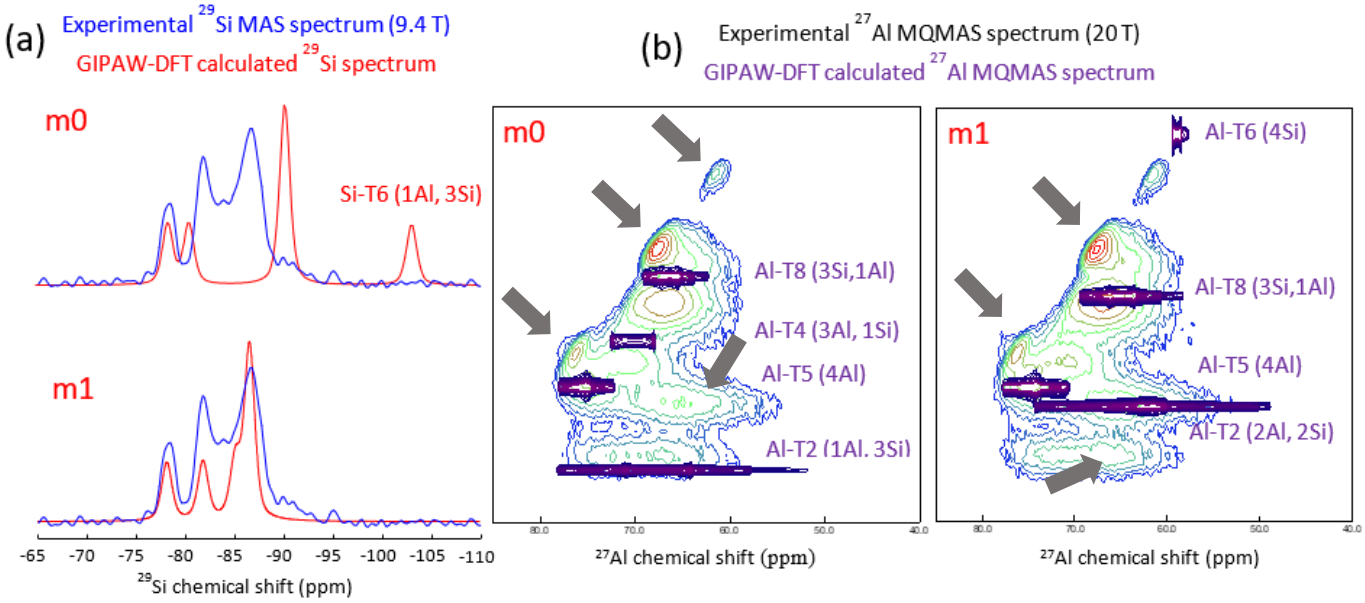

Fig. 2.20. Comparison of the m0 and m1 theoretical (shown in red) and experimental (shown in blue) **(a)** ^{29}Si MAS NMR spectra and **(b)** ^{27}Al MQMAS spectra. Experimental spectra obtained on a sample of $Sr_{12}Al_{20}Si_{12}O_{66}$ sintered for 48h at 11500°C. The GIPAW-DFT approach implemented in the CASTEP code was used for the calculations.

2.5.3. Mixed Occupancy of the Al^{3+}/Si^{4+} Sites

As mentioned previously, considering mixed occupancies on all of the Al^{3+}/Si^{4+} positions generated too many models to be realistically computed. Therefore, a first batch of mixed site models, was calculated on a (1x1x1) cell, assuming that only the highest multiplicity Al^{3+} sites (T2, T5, T8) had mixed occupancies. Computations based on this assumption and using the supercell code and DFT geometry optimisations revealed 15 possible configurations which merged down to 3 symmetrically distinct structures with inequivalent energies and multiplicities of 6, 6, and 3.[40] Following this, a second batch of models was calculated, again on a (1x1x1) cell, this time also allowing the T4 and T6 sites to have mixed occupancies. This produced 12 possible configurations which merged to 2 inequivalent structures each with multiplicities of 6. The occupancies of all the models and corresponding theoretical ^{29}Si NMR patterns not discussed here are shown in Appendix 1, T.2.1. and A.2.10. The theoretical ^{29}Si MAS and ^{27}Al MQMAS NMR spectra of all the inequivalent structures and their multiplicities generated by both sets of assumptions was then calculated using a GIPAW-DFT approach and subsequently compared to the experimentally observed results. Additionally, the △E values (stability of the DFT-relaxed structure), in relation to the lowest energy model (m1), and number of Si-O-Si linkages was also calculated in these models to provide an additional way of comparing each model's plausibility.

Through this comparison, the inequivalent structures of models m3 and m11 were found to provide a good agreement (Fig. 2.21.), the occupancies of these models are shown in table 2.7. While each multiplicity of

these models matched most of the NMR intensities, some subtle discrepancies were noticed. Since there was no reason to assume only one Al^{3+}/Si^{4+} ordering was observed across the entire infinite unit cell. Two statistically averaged models were created of the m3 and m11 models, with respect to the multiplicities observed for each configuration, i.e. a higher weighting was placed on the configurations which showed higher multiplicities. For example, the three representations of the m3 model showed respective multiplicities of 6, 6 and 3, meaning the first two were represented more in the statistically averaged model. The ^{29}Si MAS and ^{27}Al MQMAS spectra of these two models were then calculated and compared to the experimental results, as shown in Fig. 2.21.

Table 2.7. Summary of the m3 and m11 models, based on miced occupancy of the T4 and T5 sites and a (1x1x1) cell.

Model (1x1x1 cell)	T1	T2	T3	T4	T5	T6	T7	T8
m3	2Si1	6Al2	2Si3	2Al4	4Al5, 2Si5	2Al6	6Si7	6Al8
m11	2Si1	6Al2	2Si3	1Al4, 1Si4	5Al5, 1Si5	2Al6	6Si7	6Al8

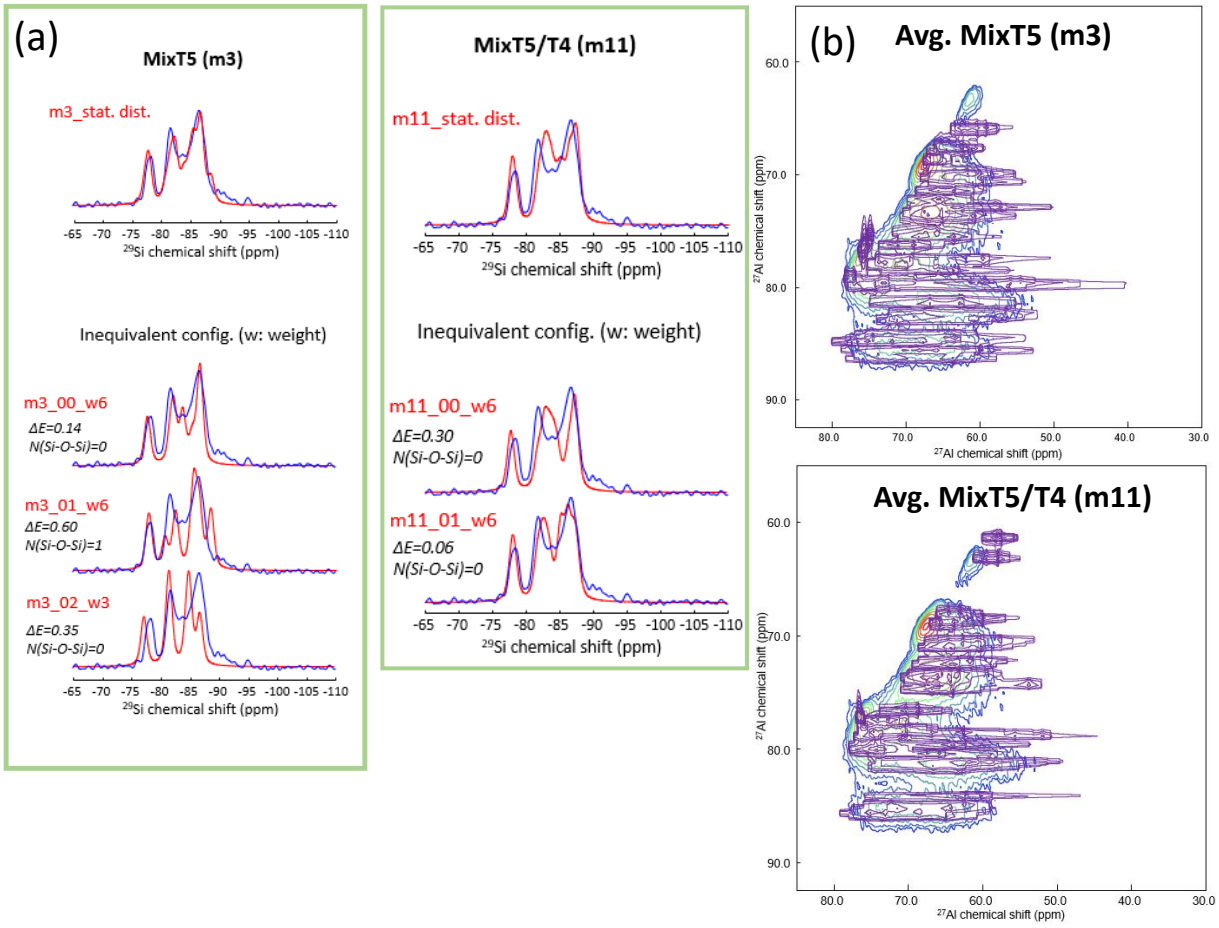

Fig. 2.21. (a) Comparison of the theoretical (shown in red) and experimental (shown in blue) ^{29}Si MAS NMR spectra from each iteration of the m3 and m11 models, the △E in relation to model m1 and the number of Si-O-Si linkages is shown. **(b)** Comparison of the theoretical and experimental ^{27}Al MQMAS spectra from the average (statistically weighted) m3 and m11 models. Experimental spectra were obtained on a sample of $Sr_{12}Al_{20}Si_{12}O_{66}$ sintered for 48h at 11500°C. Supercell and the GIPAW-DFT approach implemented in the CASTEP code was used for the calculations.

Clearly, the average (statistically weighted) models demonstrated a high level of agreement with both sets of experimental data. In particular, these results strongly suggested that an Al^{3+}/Si^{4+} ordering was occurring on at least the T5 site, as both models allowed mixed occupancies on this position. Additionally, when these models, structures shown in Fig. 2.22., were refined using the Rietveld method, no difference in the fits was observed when compared to the original refinement (Appendix 1, A.2.11.).

So far models have been built based on constraints, such as the (1x1x1) unit cell. Future work could take the m3 and m11 models and generate them in a (2x2x2) unit cell to see if the agreement still holds. Additionally, in regards to how the average, statistical models were weighted, rather than basing it on the multiplicity of a configuration, their energies (△E values) could be used instead. With lower energy multiplicities being weighted more in the statistically averaged models than the higher energy ones.

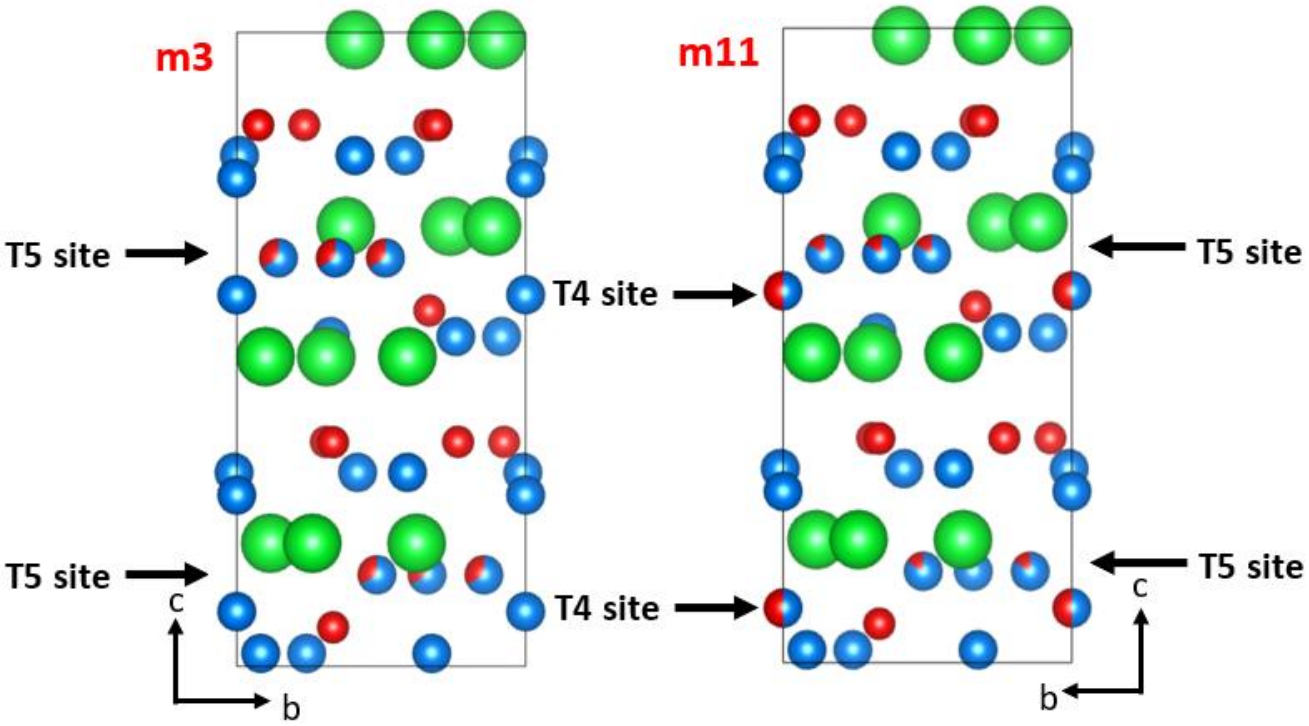

Fig. 2.22. Vesta generated images of the m3 and m11 models, developed by assuming mixed occupancy of the T4 and T5 sites, while still maintaining charge neutrality of the formula in a (1x1x1) cell. Sr^{2+} is shown in green, while Si^{4+} and Al^{3+} are shown in red and blue respectively. Bonds and oxygens have been removed for clarity.

2.6. Exploring the Compositional Limits of $Sr_{12}Al_{20}Si_{12}O_{66}$

2.6.1. The $Sr_{12+x}Al_{20+2x}Si_{12-2x}O_{66}$ Solid Solution

The existence of $Ba_{13}Al_{22}Si_{10}O_{66}$ and the proposed existence of its Sr analogue $Sr_{13}Al_{22}Si_{10}O_{66}$, made exploring the compositional range of $Sr_{12}Al_{20}Si_{12}O_{66}$ worthwhile. Investigations were conducted according to the formula $Sr_{12+x}Al_{20+2x}Si_{12-2x}O_{66}$, for values x=0.3, 0.5, 0.6, 0.9 and 1. This gave the desired formulae of $Sr_{12.3}Al_{20.6}Si_{11.4}O_{66}$, $Sr_{12.5}Al_{21}Si_{11}O_{66}$, $Sr_{12.6}Al_{21.2}Si_{10.8}O_{66}$, $Sr_{12.9}Al_{21.8}Si_{10.2}O_{66}$ and $Sr_{13}Al_{22}Si_{10}O_{66}$ respectively. Attempts at extending the range to x=3, for a fully occupied 3rd cation site, were also attempted, x=1.5, 2 and 3. All samples were prepared by GC, following the glass synthesis protocol discussed in Section 2.3.4. The optimised temperature and time of 1150°C for 1h was then used to test if these formulae still produced the expected $Sr_{12}Al_{20}Si_{12}O_{66}$ PXRD pattern. Optimisation of the sintering protocol was then undertaken where necessary. Cell volumes were determined using the Pawley method on PXRD scans of samples in deep holders, an angular range of 5-130°, scan time per step of 2.3s, and an angle increment of 0.019° was used. Refined volumes were then plotted against their respective x values. If a linear trend was observed between all/some of the x values then they could be said to obey Vegard's law. Which is an empirical method for determining the existence of solid solutions; a linear trend in cell volume as a function of x means there is a solid solution.[42] Clearly, in Fig. 2.23.(a), a linear trend is observed between x=0 and 1, meaning that a solid solution exists, which answers the first question of Section 2.4.4. "Does $Sr_{12}Al_{20}Si_{12}O_{66}$ exist as part of a solid solution, according to the formula $Sr_{12+x}Al_{20+2x}Si_{12-2x}O_{66}$?"

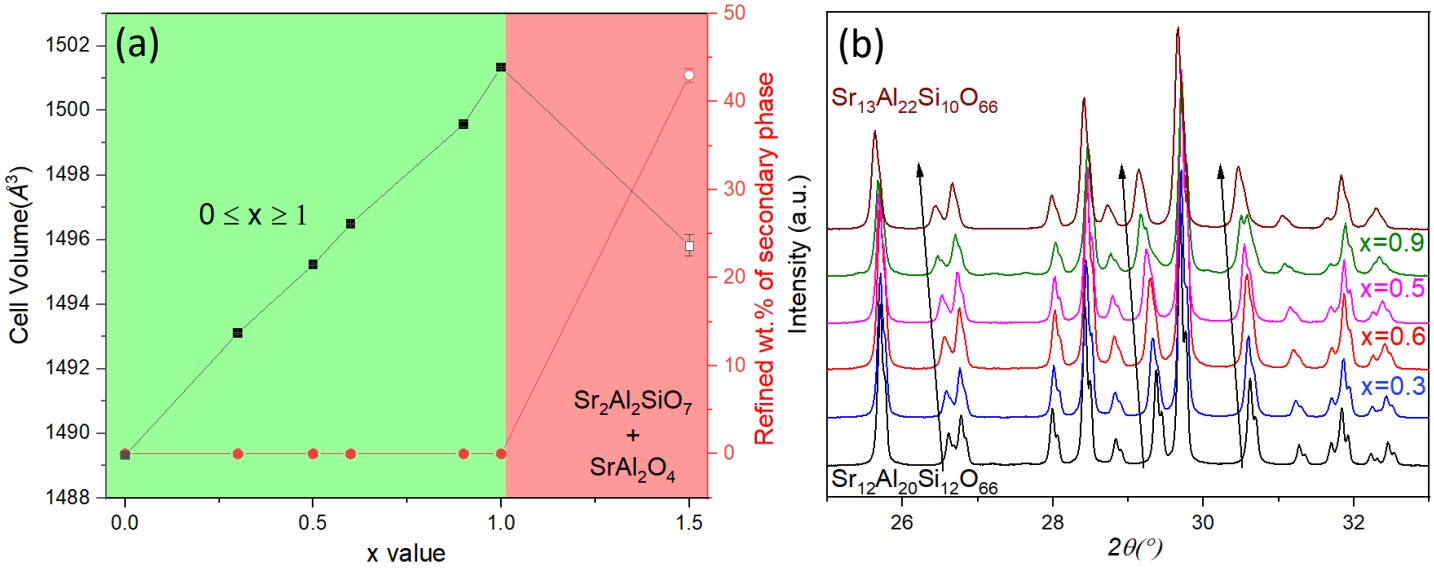

Fig. 2.23. (a) Cell volume plotted as a function of x, according to the formula $Sr_{12+x}Al_{20+2x}Si_{12-2x}O_{66}$. The linear trend between x=0 - 1 shows the existence of a solid solution. **(b)** Stacked plot of the PXRD patterns observed for x values 0, 0.3, 0.5, 0.6, 0.9, and 1.

This also proved the existence of the proposed $Sr_{13}Al_{22}Si_{10}O_{66}$, when synthesised using a GC approach, which demonstrated its effectiveness in targeting metastable phases as it had succeeded where the solid-state method failed. The sintering temperature of this phase was lowered to 1100°C for phase-pure synthesis to be observed. When the PXRD spectra of these samples were compared, the characteristic shift to lower 2Θ angle was observed with the expanding unit cell. However, this shift was not common amongst all the peaks, which indicated an anisotropic expansion of the cell, as shown in Fig. 2.23.(b). Examining the lattice parameters found that expansion was more prevalent in the *c*- axis rather than the *a*- or *b*- axes.

After x=1.0, secondary phases of, $Sr_2Al_2SiO_7$ (tetragonal, $P\text{-}42_1m$) and $SrAl_2O_4$ (monoclinic, $P2_1$), began forming, starting as minor phases before becoming the majority phases, after x = 1.5. The formation of these secondary phases was logical as they are relatively Sr and Al rich phases and the solid solution formula is saturating the structure with these elements. The discovery of this solid solution ($Sr_{12+x}Al_{20+2x}Si_{12-2x}O_{66}$, x=0 – 1) provided an excellent starting point for the optimisation and tailoring of the properties in $Sr_{12}Al_{10}Si_{12}O_{66}$. Moreover, it suggested the existence of a potential solid solution for $Ba_{13-x}Al_{22-2x}Si_{10+2x}O_{66}$ by a GC approach which would be an interesting line of research to investigate in the future.

2.6.2. Mixed Cation Solid Solutions According to the Formula $Sr_{12-x}(Ba/Ca)_xAl_{20+2x}Si_{12-2x}O_{66}$

Potential solid solutions were also explored in terms of substituting Sr for Ba or Ca. As discussed, the work by Denis *et al.* had demonstrated that that the structure could support mixed cation occupancies.[35] This was therefore investigated for Ba^{2+} and Ca^{2+} substitutions, according to the formula $Sr_{12-x}(Ba/Ca)_xAl_{20+2x}Si_{12-2x}O_{66}$, with $0<x\leq12$. Synthesis of fully substituted Ba^{2+} or Ca^{2+} samples was also attempted at the limits of these solutions, i.e. $Ba_{12}Al_{20}Si_{12}O_{66}$ and $Ca_{12}Al_{20}Si_{12}O_{66}$. Finally, $Ba_{12-x}Ca_xAl_{20}Si_{12}O_{33}$ samples and a triple substituted Sr/Ba/Ca sample, $Sr_4Ba_4Ca_4Al_{20}Si_{12}O_{66}$, were also attempted.

All experiments were conducted using the same optimised GC synthesis approach, of melting the precursors at 1600°C for 1.5 hours, with $BaCO_3$ and $CaCO_3$ (99.999% Strem) being used as the substituting precursors. The resultant glasses were then crushed and formed into 5mm Ø pellets for sintering in Pt crucibles, an annealing time of 1h was used for each sample. Table 2.8. summarises the x values attempted for each formula as well as their optimised temperature for phase-pure synthesis. The Pawley method was used to determine the cell volume of each sample, which was then plotted as a function of x.

Table 2.8. Summary of the optimised phase-pure synthesis conditions. An X means unsuccessful synthesis, the grey box means synthesis not attempted and * means almost phase-pure.

X value	$Sr_{12-x}Ba_xAl_{20}Si_{12}O_{66}$	$Sr_{12-x}Ca_xAl_{20}Si_{12}O_{66}$	$Ba_{12-x}Ca_xAl_{20}Si_{12}O_{66}$
1.2	1150°C	1050°C	*1050°C
2.4	1150°C	950°C	X
3.6	1150°C	1150°C	X
6	1150°C		
12	1150°C	X	X

$Sr_{12-x}Ba_xAl_{20+2x}Si_{12-2x}O_{66}$

The substitution of Ba into $Sr_{12}Al_{20}Si_{12}O_{66}$ occurred readily for all x values ($0 \leq x \leq 12$). As shown in table 2.8., no further optimisation of the synthesis conditions was required. The linear increase of cell volume as a function of x means that Ba^{2+} substitution can be described as following Vegard's law, Fig. 2.24.(a). The expected peak shift to lower 2Θ values was also observed in correlation with the increasing cell size, caused by substitution of the larger Ba^{2+} atom, Fig. 2.24(b). The fully substituted end member, $Ba_{12}Al_{20}Si_{12}O_{66}$, was successfully synthesised which represented the true Ba analogue of $Sr_{12}Al_{20}Si_{12}O_{66}$.

$Sr_{12-x}Ca_xAl_{20}Si_{12}O_{66}$

Substitution of Ca^{2+} for Sr^{2+} showed a reduced solid solution range, $0 \leq x \leq 2.4$. Optimisation of the synthesis conditions was also necessary, with a reduction in phase-pure sintering temperature observed as x increases. Again, by PXRD the expected peak shift to higher 2*Θ* angles was observed, corresponding to a shrinking of the unit cell as the smaller Ca^{2+} ion was substituted for Sr^{2+}, Fig. 2.24.(c). The x=3.6 sample did not follow the linear trend, despite appearing to give a highly crystalline PXRD pattern. Close inspection of the pattern revealed a minor secondary phase of $SrAl_2Si_2O_8$ (*I*2/*m*), which accounted for the departure from the trend. The fully substituted phase, $Ca_{12}Al_{20}Si_{12}O_{66}$, was never obtained, even when sintering temperatures were varied. Instead the phases $CaAl_2Si_2O_8$ (*P*-1) and $Ca_2Al_2SiO_7$ (*P*-42_1m) formed (Appendix 1 A.2.12.). This result, suggests that a Ca analogue of $Sr_{12}Al_{20}Si_{12}O_{66}$ cannot be made by GC methods.

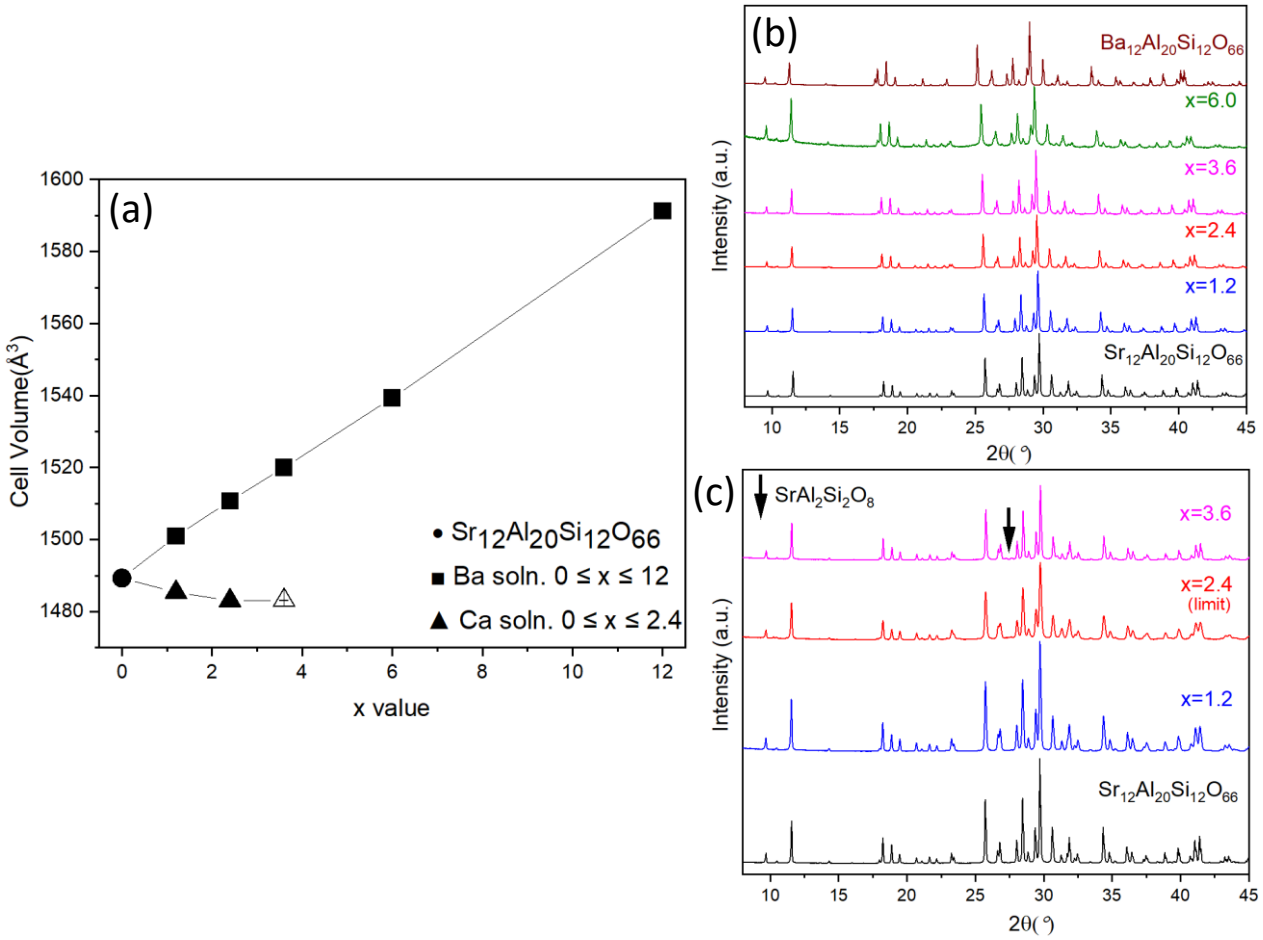

Fig. 2.24. (a) Cell volume vs. x value plot for the solid solutions $Sr_{12-x}Ba_xAl_{20+2x}Si_{12-2x}O_{66}$ & $Sr_{12-x}Ca_xAl_{20}Si_{12}O_{66}$. **(b)** Stacked PXRD plots of the $Sr_{12-x}Ba_xAl_{20+2x}Si_{12-2x}O_{66}$ solid solution, $0 \leq x \leq 12$. **(c)** Stacked PXRD plots of the $Sr_{12-x}Ca_xAl_{20}Si_{12}O_{66}$ solid solution, $0 \leq x \leq 2.4$.

$Ba_{12-x}Ca_xAl_{20}Si_{12}O_{66}$ & $Sr_4Ba_4Ca_4Al_{20}Si_{12}O_{66}$

Ca substitutions were also attempted from a base formula of $Ba_{12}Al_{20}Si_{12}O_{66}$. Only an x value of 1.2 was synthesised almost phase-pure, (Appendix 1, A.2.13.). Two minor secondary phases (<5wt.%) of $BaAl_2Si_2O_8$ ($P6_3/mcm$) and $Sr(Al_2Si_2O_8)$ (P-3c1) were detected, which increased in intensity with x. This phase showed a peak shift similar to that of $Ba_{12}Al_{20}Si_{12}O_{66}$, as expected. Increasing the 1h sintering time of this phase may aid in reducing the crystalline phase fraction of secondary phase.

The synthesis of a triply substituted, $Sr_4Ba_4Ca_4Al_{20}Si_{12}O_{66}$, phase was also attempted, the average ionic radius of this phase would be comparable to that of the pure Sr phase. However, even when sintering temperatures were adjusted the reactions failed. Only the equilibrium products, $SrAl_2Si_2O_8$ ($P2_1/c$), $BaAl_2Si_2O_8$ ($P6_3/mcm$) and $Ca_2Al_2SiO_7$ (tetragonal P-42$_1m$) were synthesised, (Appendix 1, A.2.14.). Based on the previous results, it was reasoned that a triply substituted composition may be possible if the Ca substitution was reduced, as Ca showed the lowest favourability for incorporation into the framework.

2.7. Functionalisation of $SrAl_2SiO_6:Eu^{2+},Dy^{3+}$ & $Sr_{12}Al_{20}Si_{12}O_{66}:Eu^{2+},Dy^{3+}$

As discussed in Chapter 1, strontium aluminosilicate phases have been known to exhibit persistent luminescence (PersL) and mechanoluminescence (ML).[2,25,43–45] Additionally, the structural links of $SrAl_2SiO_8$ to $Sr_{1-X/2}Al_{2-2X}Si_XO_4$ and the discovery of long lasting PersL in $Ba_{13}Al_{22}Si_{10}O_{66}$, suggested that optical properties would be attainable in the two new phases discussed here.[6,7,35,46] With these goals in mind, precursor powders of $SrAl_2SiO_6$ and $Sr_{12}Al_{20}Si_{12}O_{66}$ were doped with 1%Eu_2O_3 (99.999% Strem) and Dy_2O_3 (99.999% Strem), for desired formulae of $Sr_{0.98}Eu_{0.01}Dy_{0.01}Al_2SiO_6$ and $Sr_{11.76}Eu_{0.12}Dy_{0.12}Al_{20}Si_{12}O_{66}$. These formulae were abbreviated to $SrAl_2SiO_6:Eu^{2+},Dy^{3+}$ and $Sr_{12}Al_{20}Si_{12}O_{66}:Eu^{2+},Dy^{3+}$. The synthesis and optimisation of bulk functional phases has already been discussed in Sections, 2.2.4 (B-$SrAl_2SiO_6:Eu^{2+},Dy^{3+}$) and 2.3.5. (B-$Sr_{12}Al_{20}Si_{12}O_{66}:Eu^{2+},Dy^{3+}$). Different co-doping elements (Cr^{3+} and Tm^{3+}), concentrations (0.5 and 2%), and ratios (1:2) were also attempted, however the 1mol%Eu^{2+}/Dy^{3+} was always found, by eye, to give the best PersL emission and so full analysis continued at this doping level. These doping levels aligned with those observed for the reference $SrAl_2O_4:Eu^{2+},Dy^{3+}$ sample.[2] All samples were crystallised in a tube furnace under N_2:H_2 (94:6) atmosphere, with an annealing plateau of 3h at 500°C to facilitate the reduction of Eu^{3+} into Eu^{2+}. After crystallisation of $Sr_{12}Al_{20}Si_{12}O_{66}$ PersL properties were observed being induced by solar charging of the powder and bulk samples, this suggested that quantitative analysis of the properties would show high levels of performance. These PL and PersL measurements were conducted using the instruments and methods discussed in Chapter 4 (4.7.1.). in collaboration with Dr. Victor Castaing and Dr. Ana I. Becerro (CSIC, Seville, Spain).

2.7.1. Optical Properties of $SrAl_2SiO_6:Eu^{2+},Dy^{3+}$ & B-$SrAl_2SiO_6:Eu^{2+},Dy^{3+}$

Initially, PersL properties were observed, by eye, in $SrAl_2SiO_6:Eu^{2+}$ when it was placed inside a black box equipped with a broad-spectrum UV lamp (312, 365, and 254 nm). The green PersL afterglow was found to massively increase, in duration and intensity, when co-doped with Dy^{3+}. However, the synthesis of the co-doped sample had to again be optimised as an increase in $Sr_{12}Al_{20}Si_{12}O_{66}$ secondary phase crystallisation (30wt.% from Rietveld refinement) was observed. By reducing the synthesis temperature to 1025°C for 1h, $SrAl_2SiO_6:Eu^{2+},Dy^{3+}$ was made single-phase. However, a larger amorphous content was observed in the PXRD pattern, due to the lower sintering temperature, meaning a glass-ceramic rather than ceramic powder now formed, as shown in Appendix 1, A.2.15.

Both powdered ($SrAl_2SiO_6:Eu^{2+},Dy^{3+}$ - 1h 1025°C) and bulk glass-ceramic samples (B-$SrAl_2SiO_6:Eu^{2+},Dy^{3+}$ - 8h 1025°C), were analysed for PersL properties. First, the optimum excitation wavelength (PLE) was determined for $SrAl_2SiO_6:Eu^{2+},Dy^{3+}$, with a wavelength of 270 nm being determined (Fig. 2.25.(a)). As the same crystalline phase was observed in both samples, this wavelength was used for both their PL and PersL studies. Broad PL

emission in the 485 nm wavelength range was observed for both samples (Fig. 2.25.(a)) confirming the green emission colour observed by eye. Emission intensity was noted as being more intense in $SrAl_2SiO_6:Eu^{2+},Dy^{3+}$, which was consistent with the lower crystalline phase fraction of B-$SrAl_2SiO_6$. PersL measurements were then conducted again using the maximum PLE of 270 nm. After excitation for 300s, detectable levels of light were still observed in both samples after 1h (Fig. 2.25.(b)) and again, the intensity and duration of emission in B-$SrAl_2SiO_6$ was slightly lower.

It was noted that both samples showed similar PL spectra to that produced by the Eu^{2+}/Dy^{3+} doped $Sr_{1-x/2}Al_{2-2x}Si_xO_4$ solid solution, in that all featured broad band emission centred at 485 nm. This was linked to the substantial amount of local disorder in the Sr^{2+} sublattice, which offered a range of coordination environments for the Eu^{2+} and Dy^{3+} ions. The same emission tuneability observed for $Sr_{1-x/2}Al_{2-2x}Si_xO_4$ was not observed here as only the x=0.66 composition had been analysed.

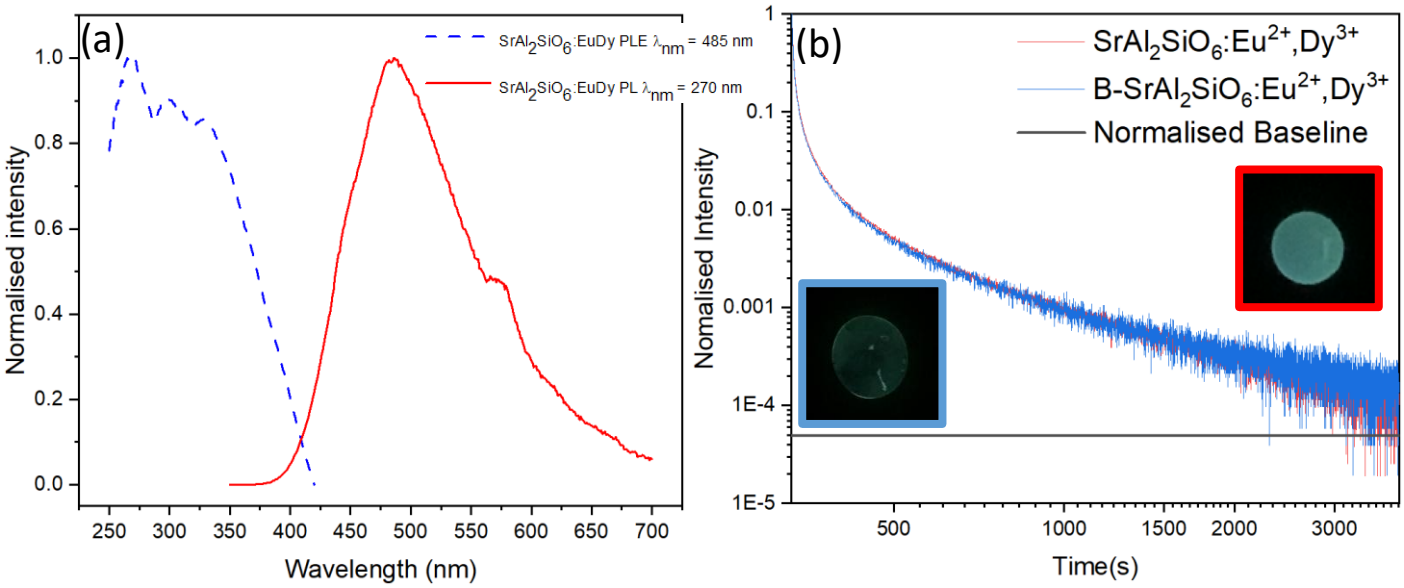

Fig. 2.25. (a) Normalised PLE (λ_{em}=485nm) and PL (λ_{ex}=270nm) of $SrAl_2SiO_6:Eu^{2+},Dy^{3+}$, showing green emission at 485 nm. **(b)** PersL curve (λ_{ex}=270nm) of $SrAl_2SiO_6:Eu^{2+},Dy^{3+}$ and B-$SrAl_2SiO_6:Eu^{2+},Dy^{3+}$, with images of the respective samples shown in the red and blue boxes.

2.7.2. Optical Properties of $Sr_{12}Al_{20}Si_{12}O_{66}:Eu^{2+},Dy^{3+}$ & B-$Sr_{12}Al_{20}Si_{12}O_{66}$

Both powdered $Sr_{12}Al_{20}Si_{12}O_{66}:Eu^{2+},Dy^{3+}$ (1h 1150°C) and bulk B-$Sr_{12}Al_{20}Si_{12}O_{66}:Eu^{2+},Dy^{3+}$ (12h 1075°C) were analysed for PL and PersL properties. For this, the maximum PLE wavelength of both samples was measured, in B-$Sr_{12}Al_{20}Si_{12}O_{66}:Eu^{2+},Dy^{3+}$ it was found to be 270 nm, whereas in $Sr_{12}Al_{20}Si_{12}O_{66}:Eu^{2+},Dy^{3+}$ it was 325 nm, (Fig. 2.26.(a)). To reflect this, three PLE wavelengths, 270, 300 and 325 nm, were used for irradiation in PL analysis. Overall, 270 nm was found to give the highest PL intensity in both samples. At this wavelength narrow emission spectra, with respect to the 4f6–5d1 to 4f7–5d0 transition of Eu^{2+}, with maximums at 420 nm were observed, giving the samples intense blue emission. This matched the emission observed in

co-doped $Ba_{13}Al_{22}Si_{10}O_{66}$.[46] The narrower emission spectra of $Sr_{12}Al_{20}Si_{12}O_{66}:Eu^{2+},Dy^{3+}$ compared to $SrAl_2SiO_6:Eu^{2+},Dy^{3+}$, was attributed to the more consistent coordination environments provided by its fully occupied Sr^{2+} sites. The PersL properties of $SrAl_2Si_{12}O_{66}:Eu^{2+},Dy^{3+}$ and B-$Sr_{12}Al_{20}Si_{12}O_{66}:Eu^{2+},Dy^{3+}$ were then measured, using a PLE wavelength of 300 nm. A high intensity of emitted light, compared to $SrAl_2SiO_6:Eu^{2+},Dy^{3+}$, was still detectable after 1h, so a longer overnight measurement was conducted. This result showed that B-$Sr_{12}Al_{20}Si_{12}O_{66}:Eu^{2+},Dy^{3+}$ still has detectable persistent luminescence emission 12h after excitation, as shown in Fig. 2.26.(b).

For both $SrAl_2SiO_6:Eu^{2+},Dy^{3+}$ and $Sr_{12}Al_{20}Si_{12}O_{66}:Eu^{2+},Dy^{3+}$, PersL measurements were repeated at different wavelengths, with the emission wavelength being monitored each time. This allowed a CIE (Commission Internationale de l'Eclairage) diagram to be generated and the true colours of persistent emission (blue and green) plotted, as shown in Fig. 2.26.(c). The emission colour difference between $Sr_{12}Al_{20}Si_{12}O_{66}$ and $SrAl_2SiO_6$ reflected their unrelated structure types. Qualitatively, the PersL emission of B-$Sr_{12}Al_{20}Si_{12}O_{66}:Eu^{2+},Dy^{3+}$ was observed to increase, with increasing crystalline phase fraction, as shown in Fig. 2.26.(d). With intense PersL properties now found for Eu^{2+}/Dy^{3+} co-doped $Sr_{12}Al_{20}Si_{12}O_{66}$, methods of tuning the emission colour and intensity and thereby increasing functionality, were investigated.

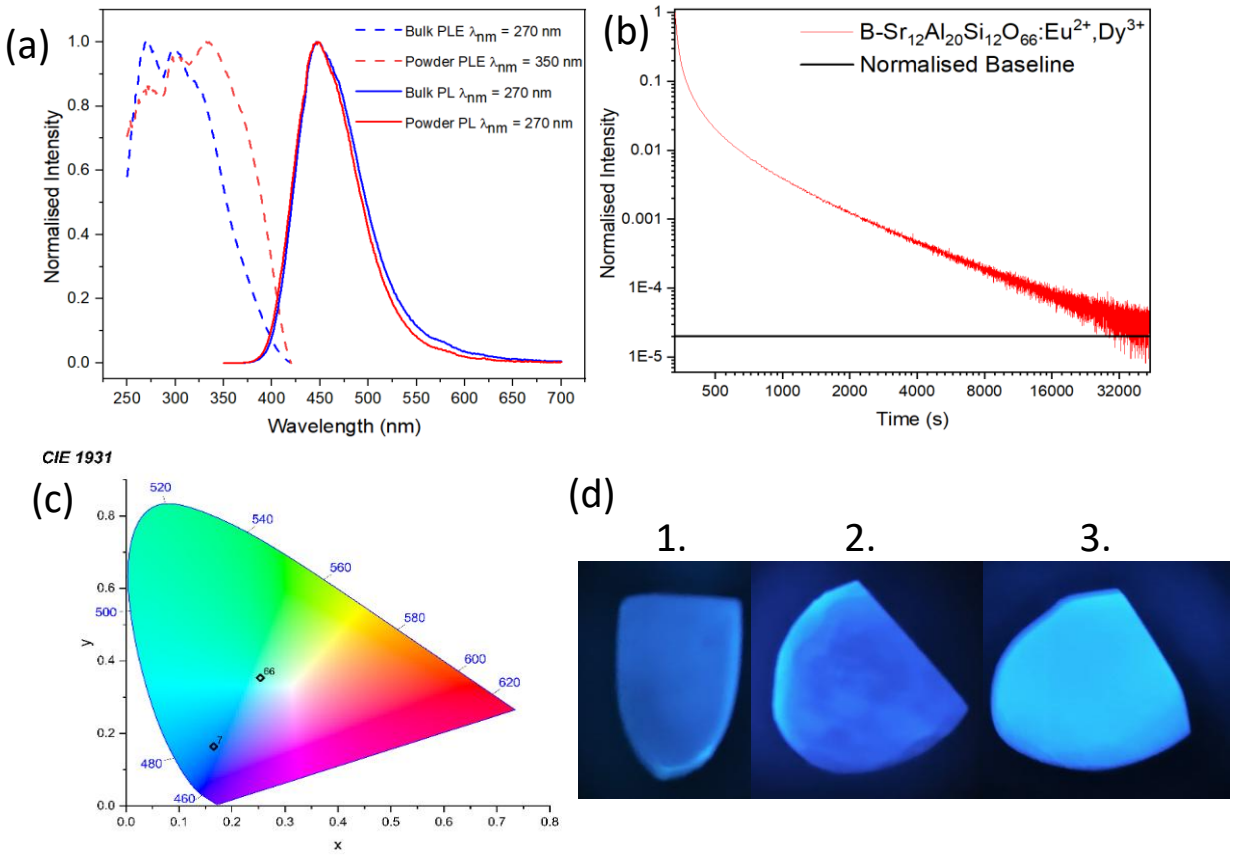

Fig. 2.26. (a) Normalised PLE and PL (λ_{exc}= 270 nm) of bulk and powdered $Sr_{12}Al_{20}Si_{12}O_{66}:Eu^{2+},Dy^{3+}$.**(b)** Normalised PersL curve (λ_{em}=420nm) of B-$Sr_{12}Al_{20}Si_{12}O_{66}$ (12h 1075°C) co-doped with 1% Eu^{2+},Dy^{3+}. **(c)** CIE coordinates of $SrAl_2SiO_6:Eu^{2+},Dy^{3+}$ and $sr_{12}Al_{20}Si_{12}O_{66}:Eu^{2+},Dy^{3+}$. **(d)** Images of the PersL achieved for the three bulk samples of $Sr_{12}Al_{20}Si_{12}O_{66}:Eu^{2+},Dy^{3+}$, synthesised in Section 2.3.6. (1. 6h 1050°C, 2. 12h 1075°C - used for optical analysis, 3. 12h 1100°C).

2.7.3. Effect of Host Composition on PersL Emission

The tuning of emission colour and intensity had already been partially investigated through the doping of different lanthanides. Therefore, the other main route of tuning colour, changing the host composition, was focussed on. Specifically, this was achieved through lanthanide doping of the formulae $Sr_{12+x}Al_{20+2x}Si_{12-2x}O_{66}$ and $Sr_{12-x}Ba_xAl_{20+2x}Si_{12-2x}O_{66}$ or partial substitution of the A or B sites. These ideas were found in the state of the art to change emission colour by altering the band gaps of their respective crystalline frameworks, resulting in a different energy of photon emission.

All samples, compositions in table 2.9., were sintered in a tube furnace under an N_2:H_2 (94:6) atmosphere, with a protocol of 3h at 500°C before ramping to 1150°C for 1h. PXRD analysis was then conducted to determine if $Sr_{12}Al_{20}Si_{12}O_{66}$ structure had successfully crystallised. Finally, the PL and PersL properties were qualitatively observed using a broad-spectrum UV lamp (254, 312, and 365 nm), to see if the intensity or colour of light had changed, and if quantitative analysis was necessary.

Table 2.9. Eu^{2+},Dy^{3+} doping levels, substituting elements and full composition of the samples tested, in the aim of tuning PersL colour and/or intensity.

Sample	Doping (mol%)	Substitution	Composition
1	1%Eu/Dy	-	$Sr_{12.642}Eu_{0.129}Dy_{0.129}Al_{20}Si_{12}O_{66}$
2	1%Eu/Dy	50%Ba	$Sr_6Ba_6Eu_{0.12}Dy_{0.12}Al_{20}Si_{12}O_{66}$
3	1%Eu/Dy	30%Ba	$Sr_{8.364}Ba_{3.69}Eu_{0.123}Dy_{0.123}Al_{20.6}Si_{11.4}O_{66}$
4	1%Eu/Dy	30%B	$Sr_{11.76}Eu_{0.12}Dy_{0.12}Al_{14}B_6Si_{12}O_{66}$
5	1%Eu/Dy	30%Ga	$Sr_{11.76}Eu_{0.12}Dy_{0.12}Al_{14}Ga_6Si_{12}O_{66}$
6	1%Eu/Dy	30%Ge	$Sr_{11.76}Eu_{0.12}Dy_{0.12}Al_{20}Si_{8.4}Ge_{3.6}O_{66}$
7	1%Eu/Dy	10% La 10% K	$Sr_{9.36}La_{1.2}K_{1.2}Eu_{0.12}Dy_{0.12}Al_{20}Si_{12}O_{66}$
8	1%Eu/Dy	10% La 10% Na	$Sr_{9.36}La_{1.2}Na_{1.2}Eu_{0.12}Dy_{0.12}Al_{20}Si_{12}O_{66}$

Non-stoichiometry

PXRD analysis proved the successful phase-pure synthesis and doping of compositions 1, 2 and 3, as shown in Fig. 2.27.(a). The expected peak shifts to higher angles was observed for all. Qualitative observations also showed that each sample retained intense long lasting PersL properties, unfortunately however, no colour changes or increase in intensity was observed. Although disappointing, this was logical as the analogous composition $Ba_{13}Al_{22}Si_{10}O_{66}$ had presented blue emission PersL properties when co-doped with Eu^{2+} and Dy^{3+}. This explains why compositions 4, 5, 6, 7 and 8 were tested as they represented a bigger departure from the known and tested crystallographic framework.

A & B site substitution

When analysed by PXRD, samples 4 and 6 (which substituted for the Al and Si B sites, respectively) were found to be unsuccessful. Instead of the desired phases, $SrAl_2Si_2O_8$ (I_2/m) formed in sample 4, suggesting B

had dissolved into the glass, and a multiphasic sample of $Sr_2(GeO_4)$ ($P2_1nb$), Al_2O_3 (R-3c), GeO_2 ($pnnm$), and $SrAl_2O_4$ ($P2_1$) formed instead.

Samples, 5, 7 and 8 (sample 5 substituted for the B site, while 7 and 8 substituted for the A site), however, did form the desired $Sr_{12}Al_{20}Si_{12}O_{66}$ phase, with only a small amount of $SrAl_2Si_2O_8$ secondary phase being observed. It is believed that this phase can be removed by optimisation of the sintering conditions, as has been shown for the undoped phase.

Sample 5 formed a highly crystalline phase, with less impurity, as shown in Fig. 2.27.(b), which suggested that Ga^{3+} could be readily substituted into the structure. The expected peak shift of each sample was also observed which confirmed successful substitution of the respective elements.

These samples were the tested, by eye under a UV lamp, and while samples 7 and 8 showed PersL properties no change in the colour or intensity of the light was observed. Sample 5 was interesting as despite forming a highly crystalline phase which matched the $Sr_{12}Al_{20}Si_{12}O_{66}$ pattern no PersL properties were observed. This suggested that the trap depths of the crystalline framework had changed. Therefore, this sample would make a good candidate for further exploration by changing the doped lanthanides, especially the co-doped one.

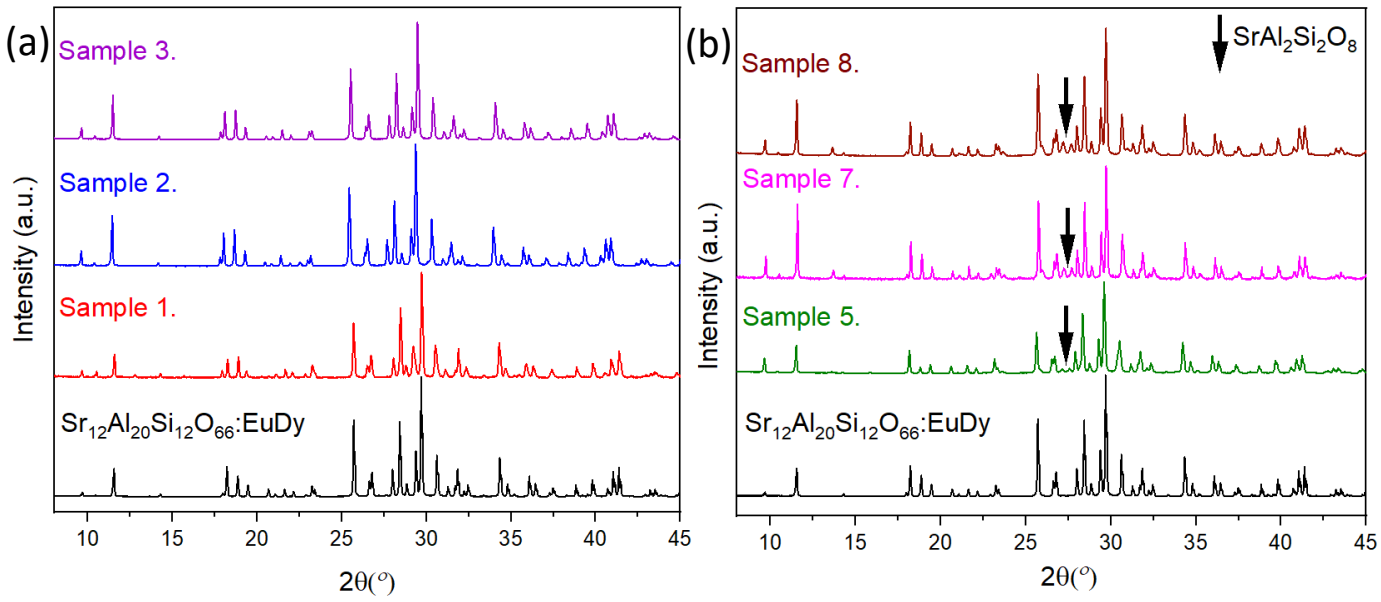

Fig. 2.27. Lab-PXRD patterns produced from **(a)** samples 1, 2, and 3 and **(b)** samples 5, 7, and 8, compared to $Sr_{12}Al_{20}Si_{12}O_{66}:Eu^{2+},Dy^{3+}$.

2.7.4. Mechanoluminescence Measurements

The polar space group and strong PersL properties observed in B-$Sr_{12}Al_{20}Si_{12}O_{66}:Eu^{2+},Dy^{3+}$ made testing for ML properties a worthwhile endeavour.[47] These experiments were conducted in collaboration with the University of Rennes. Due to size requirements for ML measurements, a sample of P4-SrAlSiO was prepared by volume crystallisation from a bulk piece of glass. The compositionally optimised formula, P4-SrAlSiO, was chosen due to its shorter phase-pure synthesis times and increased transparency. Additionally, 1mol% Eu_2O_3

(99.999% Strem) and 1.5% Dy_2O_3 (99.999% Strem) was doped for Sr in P4-SrAlSiO, giving a formula of $Sr_{11.7}Eu_{0.12}Dy_{0.18}Al_{20}Si_{11.53}O_{65.04}$ – abbreviated to P4-SrAlSiO:Eu^{2+},Dy^{3+}. These dopant values were based on those used for $SrAl_2O_4$:Eu^{2+},Dy^{3+} ML measurements, the current best-in-class.[2,48,49] P4-SrAlSiO:Eu^{2+},Dy^{3+} glass was prepared in the optimised fashion, but after initial quenching in water the glass was annealed for 15 mins at 1600°C before quenching in air, to relax internal stress. Purity of the amorphous phase was confirmed by PXRD measurement. The resultant bulk glass was then crystallised in a tube furnace under a reducing, N_2:H_2 (94:6) atmosphere for 10h at 1075°C. This resulted in a surface crystallised opaque glass-ceramic, the phase purity of which was confirmed by PXRD analysis, (Appendix 1, A.2.16.). The glass-ceramic piece was then cut and polished to a parallelepiped size of 4(width) × 4(depth) × 4.5(height) mm^3 for ML measurements to be conducted. The ML experimental setup described in Chapter 4 (Section 4.7.2) was used, with the results shown in Fig. 2.28. Charging of the sample with 365 nm UV light for 30s showed intense blue light emission from the crystallised areas of P4-SrAlSiO:Eu^{2+},Dy^{3+}, green and orange zones of inset 1. in Fig. 2.28. (blue areas represent glass). The long PersL curve is then viewed once charging stops at 0s. After 1500s a uniaxial compression force of 60 MPa was applied to the sample for 10s. An intense ML response is clearly visible during compression, yellow/white zone of inset 2. proving that the phase has ML properties. A higher intensity of ML response is viewed in the bottom left corner of inset 2., which may be due to a slight departure from a perfect parallelepiped shape.

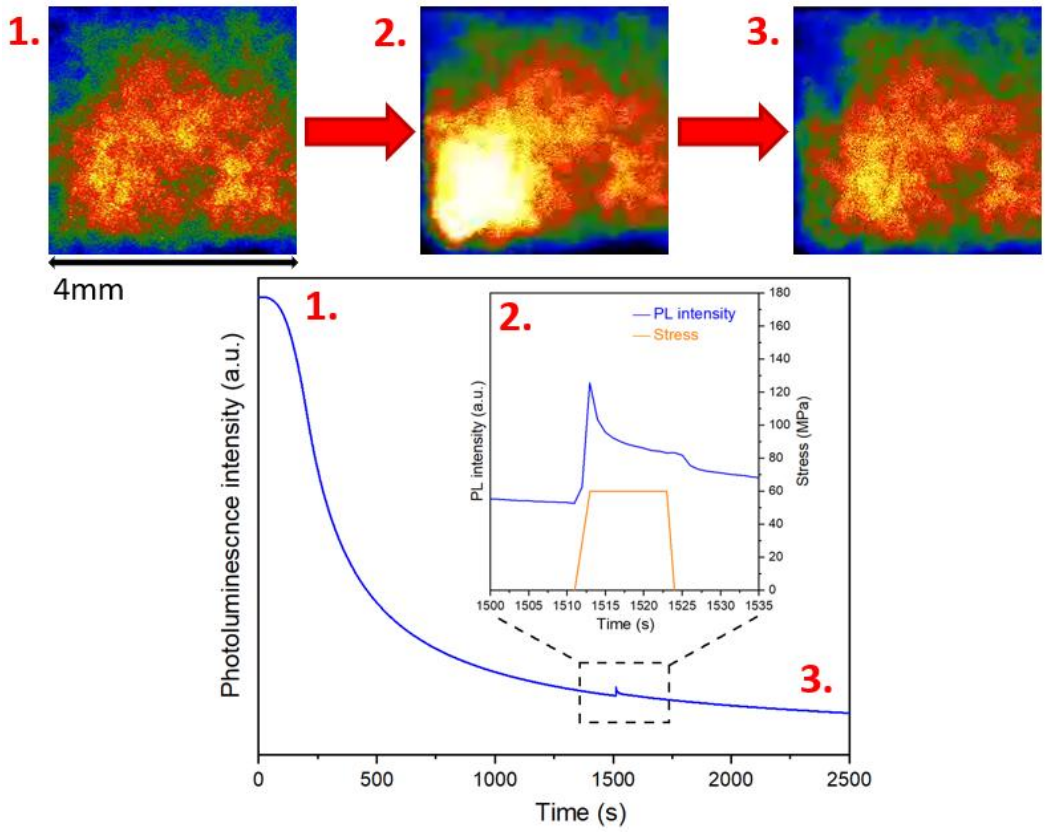

Fig. 2.28. EML response of P4-SrAlSiO:Eu^{2+},Dy^{3+}, after 30 s of 365 nm UV charging and uniaxial compression of 60 MPa, 1500 s later. Insets 1. 2. and 3. show the PL intensity before, during and after compression, respectively.

The ML response is more sensitive at the start of compression with a sharp peak in PL intensity visible before it plateaus. After release of the compression, PL intensity returns to almost baseline levels, indicating EML behaviour.[50] The baseline is slightly higher after decompression due to an increased number of de-trapped electrons, which increases PL intensity but lowers overall lifetime.

Direct comparison of the optical responses of crystalline phases can be challenging due to differing quantum efficiencies and wavelengths of excitation.[51] However, the ML response of P4-SrAlSiO:Eu^{2+},Dy^{3+} was noted as being particularly intense and on a par with commercially available materials when qualitatively compared by eye. Given the room for optimisation of synthesis, full crystallisation rather than surface crystallisation, and doping elements/ concentrations, P4-SrAlSiO:Eu^{2+},Dy^{3+} represents an exciting addition to the relatively small compendium of ML materials.

2.8. Chapter Conclusion & Perspectives

In this chapter, two new metastable crystalline phases, $SrAl_2SiO_6$ and $Sr_{12}Al_{20}Si_{12}O_{66}$, have been presented. The initial objective was to synthesise $SrAl_2SiO_6$ as a phase-pure powdered and bulk sample, to permit a study of its properties, PL and PersL. However, the discovery of $Sr_{12}Si_{20}Si_{12}O_{66}$ introduced the primary aims of this chapter, the structural determination, synthesis optimisation and functionalisation of the phase. PL, PersL and ML functionalisation was targeted for powdered and transparent bulk samples, through doping with Eu^{2+} and Dy^{3+}, as this had proven successful for other aluminosilicates ($Ba_{13}Al_{20}Si_{10}O_{66}$ - PL and PersL, $SrAl_2O_4$ – PL, PersL and ML).

The objectives for $SrAl_2SiO_6$ were successfully achieved, through a GC approach and sintering step of 1h at 1050°C. This protocol was optimised through DSC and *in-situ* VTXRD measurements. The use of a GC approach and partial crystallisation of the bulk, facilitated the synthesis of powdered phase-pure ceramic powder and large transparent glass-ceramic piece, which expand the phases applicational potential.

Doping of the powdered and bulk samples with 1mol% Eu^{2+} and Dy^{3+}, allowed PL and PersL emission to be observed. Although, it was noted that their addition made achieving highly crystalline phase-pure samples harder, especially in the powdered ceramic sample, which was synthesised as a powdered single-phase glass-ceramic after doping. These properties were then quantified, for both the powdered and bulk samples, at the CSIC in Seville. Intense, green PL emission, in the 485 nm range, and a moderate PersL curve of 1h was observed instrumentally.

Optimisation of $SrAl_2SiO_6$, led to the discovery of $Sr_{12}Al_{20}Si_{12}O_{66}$ and the main objectives of this chapter. The structure was solved and nominal composition found through a combined approach of phase indexation from high quality SPD/NPD data, SAED analysis and the charge-flipping method. Again, phase-pure optimisation was achieved for both powdered and bulk samples. Through partial crystallisation of the bulk glass varying degrees of transparency were achieved, while still maintaining phase purity. The solved structure was

confirmed by Rietveld analysis and atomic-resolution HAADF-STEM imaging, performed of a thin foil bulk sample. A study of the specific Al^{3+}/Si^{4+} sites, and their potential ordering was investigated by ^{29}Si MAS and ^{27}MQMAS NMR. These studies revealed two probable models with complex mixed occupancy of at least the T_5 site and potentially the T_4 site.

$Sr_{12}Al_{20}Si_{12}O_{66}$ was found to form three solid solutions with varying limits, $Sr_{12-x}Al_{20+2x}Si_{12-2x}O_{66}$ and $Sr_{12-x}(Ba/Ca)_xAl_{20+2x}Si_{12-2x}O_{66}$. An extended range was found for Sr^{2+} and Ba^{2+} additions, revealing the only before theorised compositions, $Sr_{13}Al_{22}Si_{10}O_{66}$ and $Ba_{12}Al_{20}Si_{12}O_{66}$.

At the CSIC in Seville, again the PL and PersL properties of $Sr_{12}Al_{20}Si_{12}O_{66}$ were studied. Intense and long-lasting blue PL and PersL properties were observed in the 420 nm range, with light still detectable after 12h. Methods of tuning the colour and intensity of the emission, through changing of the host composition, unfortunately, failed. However, successful A and B site substitution did prove the compositional flexibility of the $Sr_{12}Al_{20}Si_{12}O_{66}$ structure. At the IPR in Rennes, the EML properties of a partially crystallised bulk sample were quantified for a doping level of 1%Eu^{2+} and 1.5%Dy^{3+}. An intense EML response was observed and found to be of a similar magnitude to the current market leader $SrAl_2O_4:Eu^{2+},Dy^{3+}$. This resulted in a patent application being filed on the material and a potential Premat project being undertaken to optimise the PersL and EML properties.

When combined with transparency, the impressive PL, PersL (which can be induced by solar charging) and EML properties observed in $Sr_{12}Al_{20}Si_{12}O_{66}$, offer the phase a range of possible optical applications. Especially when it is considered that these properties have room for optimisation. It may be possible to increase the transparency of bulk vitroceramic samples if the crystallites can be orientated at the surface, and even achieved in fully-crystallised samples if they are made thin enough and without secondary phases. Tuning of PersL colour and intensity may be achieved through changing of the doping element/ concentration or host composition. For example, the lack of emission in sample 5 ($Sr_{11.76}Eu_{0.12}Dy_{0.12}Al_{14}Ga_6Si_{12}O_{66}$) suggests that different lanthanide dopings will be needed to generate interesting luminescence properties in this compound. Finally, scope for improvement of the ML properties exists through full crystallisation of the bulk sample and chemical tuning. Even the probable mixed site occupancies observed by NMR offers a route to the tuning of properties by varying the Al^{3+}/Si^{4+} ordering.

2.9. References

[1] T. Matsuzawa, Y. Aoki, N. Takeuchi and Y. Murayama, *Journal of The Electrochemical Society*, 1996, **143**, 2670.

[2] R. E. Rojas-Hernandez, F. Rubio-Marcos, M. Á. Rodriguez and J. F. Fernandez, *Renewable and Sustainable Energy Reviews*, 2018, **81**, 2759–2770.

[3] R. Rojas Hernandez, F. Rubio-Marcos, A. Serrano, I. Hussainova and J. Fernández, *Journal of the European Ceramic Society*, DOI:10.1016/j.jeurceramsoc.2019.11.019.

[4] V. Chernov, P. Salas-Castillo, L. A. Díaz-Torres, N. J. Zúñiga-Rivera, R. Ruiz-Torres, R. Meléndrez and M. Barboza-Flores, *Optical Materials*, 2019, **92**, 46–52.

[5] J. Ueda, K. Kuroishi and S. Tanabe, *Applied Physics Express*, 2014, **7**, 062201.

[6] V. Castaing, C. Monteiro, A. D. Sontakke, K. Asami, J. Xu, A. J. Fernández-Carrión, M. G. Brik, S. Tanabe, M. Allix and B. Viana, *Dalton Trans.*, 2020, **49**, 16849–16859.
[7] A. J. Fernandez-Carrion, K. Al Saghir, E. Veron, A. I. Becerro, F. Porcher, W. Wisniewski, G. Matzen, F. Fayon and M. Allix, *Inorg. Chem.*, 2017, **56**, 14446–14458.
[8] K. Al Saghir, S. Chenu, E. Veron, F. Fayon, M. Suchomel, C. Genevois, F. Porcher, G. Matzen, D. Massiot and M. Allix, *Chem. Mater.*, 2015, **27**, 508–514.
[9] W. Wisniewski, A. J. Fernández-Carrión, P. Schöppe, C. Rüssel and M. Allix, *CrystEngComm*, 2018, **20**, 3455–3466.
[10] K. Al Saghir, S. Chenu, E. Veron, F. Fayon, M. Suchomel, C. Genevois, F. Porcher, G. Matzen, D. Massiot and M. Allix, *Chem. Mater.*, 2015, **27**, 508–514.
[11] E. M. Duncan, A. Ridouard, F. Fayon, E. Veron, C. Genevois, M. Allix, C. M. Collins and M. J. Pitcher, *Chem. Commun.*, 2023, **59**, 10544–10547.
[12] J. Gonzalez-Platas, A. Filhol and J. Rodriguez-Carvajal, *Last version of the FullProf suite for Windows, Linux and Mac OS X*, 2008.
[13] A. Boultif and D. Louër, *Journal of Applied Crystallography - J APPL CRYST*, 2004, **37**, 724–731.
[14] 1964, **120**, 375–387.
[15] L. Palatinus and G. Chapuis, *Journal of Applied Crystallography*, DOI:10.1107/S0021889807029238.
[16] V. Petrícek, M. Dusek and L. Palatinus, *Zeitschrift für Kristallographie - Crystalline Materials*, DOI:10.1515/zkri-2014-1737.
[17] H. M. Rietveld, *J Appl Crystallogr*, 1969, **2**, 65–71.
[18] V. A. Blatov, A. P. Shevchenko and D. M. Proserpio, *Crystal Growth & Design*, 2014, **14**, 3576–3586.
[19] V. A. Blatov, *Structural Chemistry*, 2012, **23**, 955–963.
[20] A. Simperler, M. D. Foster, R. G. Bell and J. Klinowski, *J. Phys. Chem. B*, 2004, **108**, 869–879.
[21] Y. G. Bushuev and G. Sastre, *J. Phys. Chem. C*, 2010, **114**, 19157–19168.
[22] Amandine Ridouard. *Caractérisation de nouvelles céramiques transparentes et verres nanostructurés par spectroscopie RMN haute résolution du solide*. These Université Orléans, *2023.*
[23] Kholoud Al Saghir. Transparent ceramics by full crystallization from glass : application to strontium aluminosilicates. Other. Université d'Orléans, 2014.
[24] K. Van Den Eeckhout, P. F. Smet and D. Poelman, *Materials*, 2010, **3**, 2536–2566.
[25] J. Kuang, Y. Liu and J. Zhang, *Journal of Solid State Chemistry*, 2006, **179**, 266–269.
[26] L. Fernández-Rodríguez, M. Allix, G. Gorni, A. Canizarès, S. Ory, G. C. Mather, A. Durán, D. Levy and M. J. Pascual, *Journal of the European Ceramic Society*, 2022, **42**, 7596–7608.
[27] T. Runčevski, *Journal of Applied Crystallography*, DOI:10.1107/S1600576719011178.
[28] G. Oszlányi and A. Süto, *Acta Crystallographica Section A*, 2004, **60**, 134–141.
[29] D. Šišak, C. Baerlocher, L. B. McCusker and C. J. Gilmore, *J Appl Crystallogr*, 2012, **45**, 1125–1135.
[30] T. Ashikaga, B.-N. Kim, H. Kiyono and T. S. Suzuki, *Journal of the European Ceramic Society*, 2018, **38**, 2735–2741.
[31] F. G. Melchiades, B. T. Rego, S. M. Higa, H. J. Alves and A. O. Boschi, *Journal of the European Ceramic Society*, 2010, **30**, 2443–2449.
[32] W. Ming, Z. Jiang, G. Luo, Y. Xu, W. He, Z. Xie, D. Shen and L. Li, *Nanomaterials*, DOI:10.3390/nano12091491.
[33] K. Momma and F. Izumi, *Journal of Applied Crystallography - J APPL CRYST*, 2008, **41**, 653–658.
[34] 1972, **135**, 437–452.
[35] G. Denis, P. Deniard, E. Gautron, F. Clabau, A. Garcia and S. Jobic, *Inorg. Chem.*, 2008, **47**, 4226–4235.
[36] W. Loewenstein, *American Mineralogist*, 1954, **39**, 92–96.
[37] M. Turchi, S. Perera, S. Ramsheh, A. J. Popel, D. V. Okhrimenko, S. L. S. Stipp, M. Solvang, M. P. Andersson and T. R. Walsh, *Journal of Non-Crystalline Solids*, 2021, **567**, 120924.
[38] P. Hohenberg and W. Kohn, *Phys. Rev.*, 1964, **136**, B864–B871.
[39] S. Clark, M. Segall, C. Pickard, P. Hasnip, M. Probert, K. Refson and M. Payne, *Zeitschrift für Kristallographie*, DOI:10.1524/zkri.220.5.567.65075.
[40] K. Okhotnikov, T. Charpentier and S. Cadars, *Journal of Cheminformatics*, 2016, **8**, 17.
[41] A. R. Ferreira, *J. Phys. Chem. C*, 2019, **123**, 9371–9381.
[42] A. R. Denton and N. W. Ashcroft, *Phys. Rev. A*, 1991, **43**, 3161–3164.
[43] Y. Wu, L. Zhu and H. Mao, *Ceramics International*, 2018, **44**, 10015–10019.
[44] P. Jha and B. P. Chandra, *Journal of Luminescence*, 2013, **143**, 280–287.
[45] F. Zhang, Y. Xie, Y. He, J. Pei, Y. Xing, S. Wang and J. Zhang, *Buildings*, 2024, **14**, 2152.
[46] J. Zhao, L. Lei, R. Ye, J. Zhang, X. Zhang and S. Xu, *J Adv Ceram*, 2022, **11**, 974–983.
[47] A. Feng and P. F. Smet, *Materials*, DOI:10.3390/ma11040484.
[48] A. Duval, Y. Suffren, M. Benabdesselam, P. Houizot and T. Rouxel, *The Journal of Chemical Physics*, 2023, **159**, 134501.
[49] M. Dubernet, Y. Gueguen, P. Houizot, F. Célarié, J.-C. Sangleboeuf, H. Orain and T. Rouxel, *Applied Physics Letters*, 2015, **107**, 151906.
[50] M. Dubernet, E. Bruyer, Y. Gueguen, P. Houizot, J. C. Hameline, X. Rocquefelte and T. Rouxel, *Scientific Reports*, 2020, **10**, 19495.
[51] G. Gauglitz, in *Photochromism*, eds. H. Dürr and H. Bouas-Laurent, Elsevier Science, Amsterdam, 2003, pp. 15–63.

Chapter 3: Synthesis, Characterisation & Functionalisation of the New Ternary Silicate $Sr_2Si_3O_8$

Contents Page

3.1. Initial Discovery of $Sr_2Si_3O_8$ by Investigating a Low Energy Region of the SrO-$AlO_{1.5}$-SiO_2 Computationally Predicted Diagram

3.1.1. Introduction & Aims

A new ternary silicate, $Sr_2Si_3O_8$, was identified at CEMHTI shortly before the start of this thesis in December 2021. The work described in this chapter concerns a detailed study of the synthesis and stability of this new compound, and attempts to develop it into a functional material. This introductory section (3.1.1) describes the essential background to this project, and outlines the specific objectives of the work.

As discussed in the introduction, the interest in combining glass-crystallisation techniques with the probe structure predication approach (Fig. 3.1.(a)) had motivated an investigation of the SrO-$AlO_{1.5}$-SiO_2 pseudo-ternary phase diagram.[1,2] This investigation (carried out by M. Pitcher & C. Collins) led to the discovery of $Sr_2Si_3O_8$ as the crystalline component of a compositionally heterogeneous glass-ceramic. The relevant work already completed on this diagram and the problems which still needed answering, including the isolation of $Sr_2Si_3O_8$ as a compositionally homogeneous highly crystalline material, and its functionalisation, are outlined in the following pages. The context provided by this discussion influenced the main bulk of work which was completed in this chapter.

The FUSE generated diagram allowed for efficient investigation of the phase diagram by simplifying it into three low energy zones, noted as A, B and C in Fig. 3.1.(b). Synthesis in zone B yielded a mixture of $Sr_2Al_2SiO_7$ and the feldspar-type $SrAl_2Si_2O_8$, both known thermodynamically stable compositions.[3,4] Furthermore, zone C mainly yielded a phase resembling $Sr_{0.9}Al_{1.8}Si_{0.2}O_4$, again a known phase.[5]

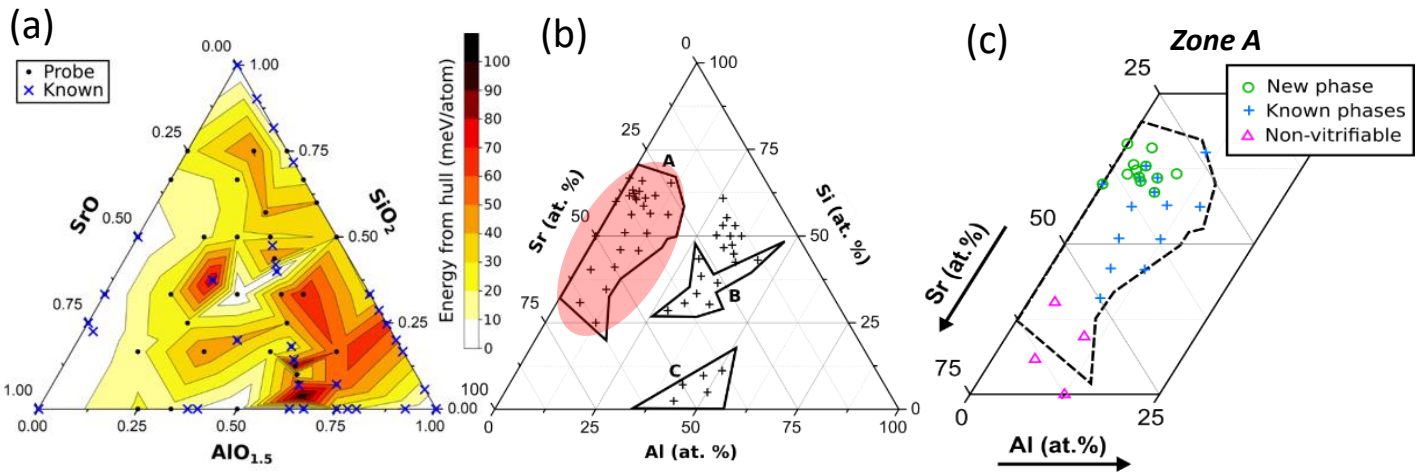

Fig. 3.1.(a) Convex hull calculated phase diagram for the SrO–$AlO_{1.5}$–SiO_2 system. Light blue dots indicate the 42 probe structure compositions. Dark blue crosses indicate products from the equilibrium diagram and/or ICSD. In cases where points coincided the lower energy structure was used for the calculation. **(b)** SrO–$AlO_{1.5}$–SiO_2 diagram with regions of interest, (A, B, C), highlighted for exploration. **(c)** Zoom of zone A, with the green circles showing where the new phase was synthesised. Adapted from [6].

However, inspection of zone A revealed several points which, when analysed by PXRD, produced patterns with unindexed peaks. These points are shown by the green circles in Fig.3.1.(c). Of the phases marked in green, one – corresponding to the nominal formula $Sr_{0.344}Al_{0.033}Si_{0.623}O_4$ and abbreviated to $Sr_2Si_3O_8$:Al – was selected for further optimisation, with the aims of increasing the crystalline volume fraction of the new phase.

The optimum synthesis conditions were found to be glass crystallisation (GC) with a sintering step of 900°C for 1 hour. After collection of neutron (NPD) and synchrotron (SPD) X-ray diffraction data, peak indexation and Pawley refinement was conducted and a primitive monoclinic unit cell model with a $P2_1/c$ space group was developed. The $Sr_2Si_3O_8$ structural model was then built using an *ab-initio* simulated annealing (SA) approach of the Sr^{2+} ions and $[SiO_4]^{2-}$ rigid tetrahedra. When this model was refined using the Rietveld method an excellent refinement of both the NPD and SPD data was achieved, confirming the compositional formula of $Sr_2Si_3O_8$. Visualisation of the phase, found it to have a one-dimensional structure, whose framework comprised of $[Si_6O_{16}]^{8-}$ ribbons, each formed by three zweier chains.[8] These zweier chains linked to form 6-membered rings of tetrahedra connected in an ududud (u, up, and d, down, refers to the direction the respective tetrahedra points) orientation (Fig. 3.2.(a)).

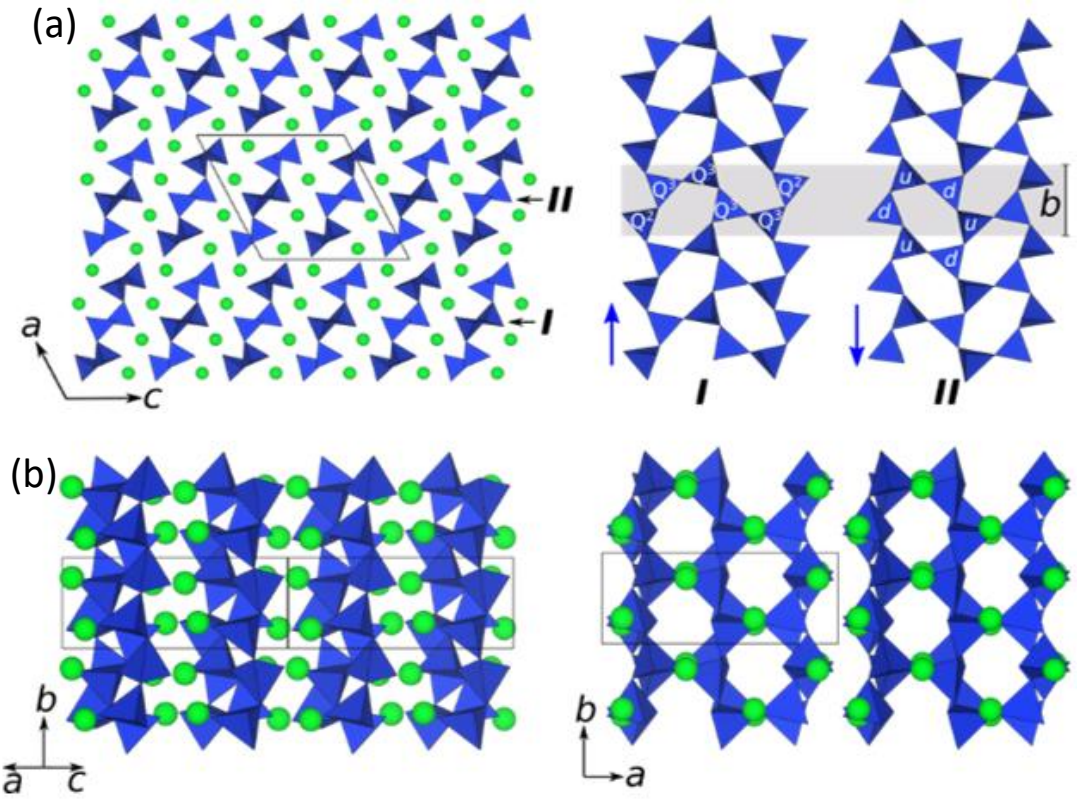

Fig. 3.2. Crystal structure projections of $Sr_2Si_3O_8$, obtained by GC of $Sr_2Si_3O_8$:Al. **(a)** shows the b projection of the SPD-refined structure, showing the antiparallel arrangement of the $[Si_6O_{16}]^{8-}$ ribbons, where I and II represent ''up'' and ''down'' orientations. Green atoms = Sr^{2+}, tetrahedra = $[SiO_4]$.

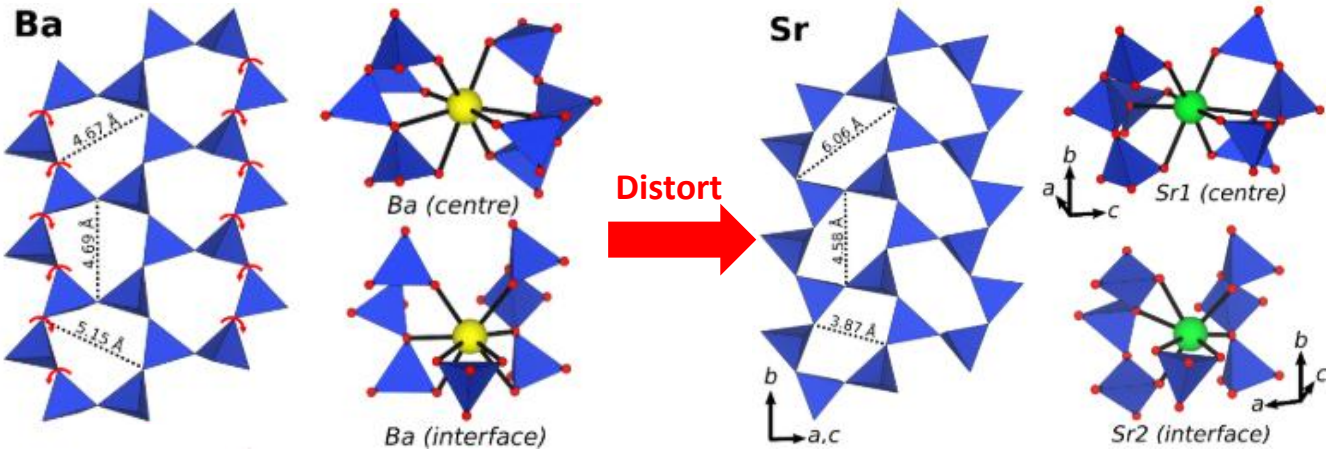

Fig. 3.3. Structure of $Ba_4Si_6O_{16}$ (left, Hesse and Liebau [7]) compared to $Sr_2Si_3O_8$ (right). The $[Si_6O_{16}]^{8-}$ ribbons are related by a cooperative twisting of the external $[SiO_4]$ chains (red arrows), producing distorted hexagonal rings for $Sr_2Si_3O_8$. Sr_1 (green) and Ba's (yellow) 8-fold environment at the centre of the ribbons is formed by two neighbouring ribbons from the same stack. The coordination environment between two stacks, formed by bonds to the external $[SiO_4]$ chains of three neighbouring ribbons, is more distorted in $Sr_2Si_3O_8$ with Sr_2 in 7-fold coordination, compared to the more symmetrical 8-fold Ba site in $Ba_4Si_6O_{16}$.

The tetrahedral rings generated two Si atoms in Q^2 sites (connected to 2 bridging atoms) and four Si atoms in Q^3 sites (connected to three bridging atoms). Despite the ribbons being polar, their anti-parallel stacking meant that overall, $Sr_2Si_3O_8$ has a non-polar structure. Stacked between the ribbons, 7 and 8-fold Sr^{2+} ions are found, (Fig. 3.3.(c)(d)), giving rise to two unique Sr sites, (Sr_2 7-fold coordinated and Sr_1 8-fold coordinated). The structure bears a close relationship to the known phase, $Ba_4Si_6O_{16}$, with this phase's framework also being largely comprised of $[Si_6O_{16}]^{8-}$ ribbons. The main difference between the two structures is the stacking arrangement of the ribbons, in $Ba_4Si_6O_{16}$ a stripe-like arrangement is observed, whereas in $Sr_2Si_3O_8$ it is checkerboard-like, as shown in Annex II, Fig. 1.

With the structure modelled and apparent composition of the crystalline phase found, an obvious point was then discussed; How could the compositional disagreement between the parent glass and crystalline phase (i.e. the missing Al^{3+}) be accounted for?

Inspection of the model provided no obvious mechanism in which the missing Al^{3+} ions could be incorporated into the structure and so ^{29}Si MAS and ^{27}Al MQMAS NMR experiments were conducted (^{29}Si MAS shown in Fig. 3.4.). As well as confirming the crystal structure, NMR analysis confirmed the presence of a substantial amount of glassy phase which accounted for 58% of the Si^{4+} in the sample. The ^{27}Al MQMAS NMR analysis revealed that all of the Al^{3+} was found within this uncrystallised glassy phase and hence, unincorporated into the crystal structure of $Sr_2Si_3O_8$. Meaning, a compositionally heterogenous glass-ceramic, was being synthesised, rather than a homogeneous one, as desired.[9] This conclusion was further supported by transmission electron microscopy (TEM) imaging of the sample (inset of Fig. 3.4.) which clearly showed by contrast, $Sr_2Si_3O_8$ crystals embedded within an SiO_2-rich glassy matrix.

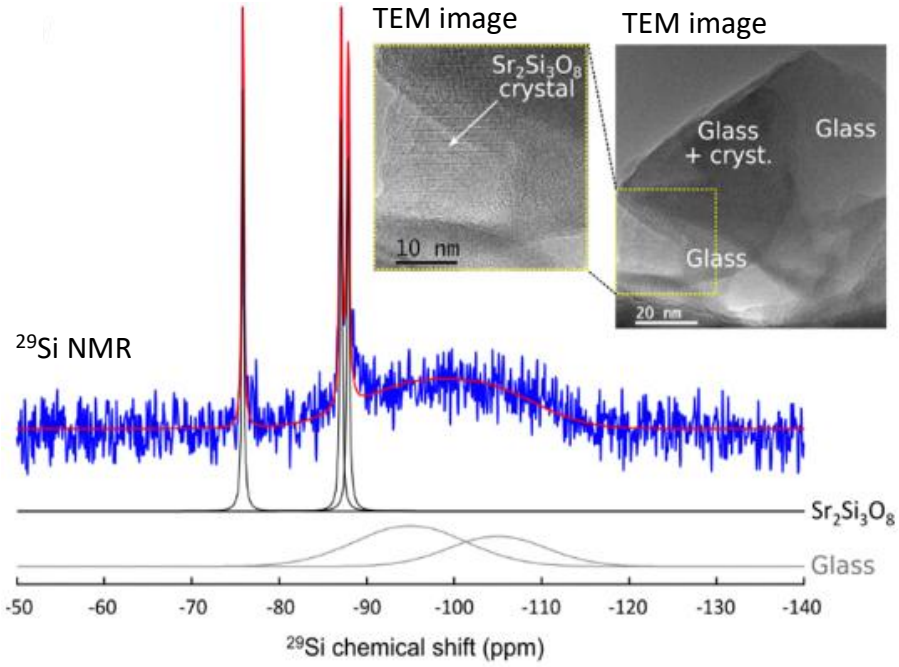

Fig. 3.4. ^{29}Si NMR spectra of crystallised $Sr_2Si_3O_8$:Al, showing three sharp resonances of inequivalent Si atoms with a Q^2/Q^3 ratio that was expected from the $Sr_2Si_3O_8$ model. A broad resonance bump shows Si^{4+} in an amorphous Q^3 and Q^4 configuration, which accounts for 58% of the Si nuclei. Insets show TEM images of $Sr_2Si_3O_8$ crystals embedded in a glassy matrix, consistent with the NMR data.

3.1.2. $Sr_2Si_3O_8$: Key Research Questions

Although the work above succeeded in crystallising $Sr_2Si_3O_8$ as the major crystalline component of a compositionally heterogeneous glass-ceramic, solving its structure and providing a refined formula, it failed to demonstrate that $Sr_2Si_3O_8$ could be synthesised as a fully crystallised, phase-pure material from the binary $SrO–SiO_2$ line, as the formula suggested. Moreover, the remaining sizeable glassy phase complicates efforts to functionalise the material and study its properties. As described in Chapter 1, in addition to their discovery the functionalisation of new inorganic oxides was a key aspect of this projects work. This led to the formulation of three research questions, which will be explored in the following sections of this chapter:

1. Can $Sr_2Si_3O_8$ glass-ceramics be synthesised by a GC of $40SrO–60SiO_2$ glass, (i.e. without the presence of Al)?
2. Can ceramic $Sr_2Si_3O_8$ be synthesised by increasing the crystalline phase fraction to 100%, or at least maximised, if full ceramic synthesis is not possible?
3. Can optimised $Sr_2Si_3O_8$ be functionalised to have persistent luminescent or mechanoluminescent properties, e.g. through doping with lanthanides such as Eu^{2+}, Dy^{3+}, and Cr^{3+} etc?

Photoluminescent (PL), persistent luminescent (PersL) and mechanoluminescent (ML) properties were targeted due to the properties demonstrated by $SrAl_2O_4:Eu^{2+},Dy^{3+}$ and $Ba_4Si_6O_{16}:Eu^{2+},Ho^{3+}$. These phases,

described in Sections 1.5.1. and 1.6.2. of Chapter 1 respectively, were found to have strong PL, PersL and ML properties with useful real-world applications.[10–12] The analogous structures of $Sr_2Si_3O_8$ and $Ba_4Si_6O_{16}$ suggested that similar properties would be attained in the newly discovered phase. Although, for the final question to be answered it is important that the sample first be synthesised phase-pure and with no (or minimal) residual glass. Such conditions would allow the properties to be accurately studied without interference from other phases. With these goals in mind, the following sections address the steps undertaken and challenges faced in the phase-pure, fully crystallised synthesis of $Sr_2Si_3O_8$.

3.2. Glass Crystallisation of $Sr_2Si_3O_8$

3.2.1. Preparation of $Sr_2Si_3O_8$ Glass

Some optimisation of the general GC approach discussed in Chapter 4 (4.1.1.) was required for the synthesis of $Sr_2Si_3O_8$ glass, such as melting temperature and equilibration time. Investigation of the SrO-SiO_2 binary diagram determined that a melting temperature of 1650°C would be more than sufficient to vitrify the $Sr_2Si_3O_8$ precursors without leading to their volatilisation.[13] To this end, the relevant high-purity reagents, $SrCO_3$ (99.999% Strem) and SiO_2 (99.999% Strem), were weighed in the stoichiometric ratio for $Sr_2Si_3O_8$, mixed, and placed in a Pt crucible. Once the sample had melted and equilibrated for 1.5 hours, the crucible was quenched in water, resulting in a transparent glass. The samples transparency qualitatively indicated that a compositionally homogenous glass had formed, with heterogenous or split phase glasses typically looking opaque.[14] Glass formation was then quantitatively confirmed by powder X-ray diffraction (PXRD), which showed no Bragg peaks (Fig. 3.5.).

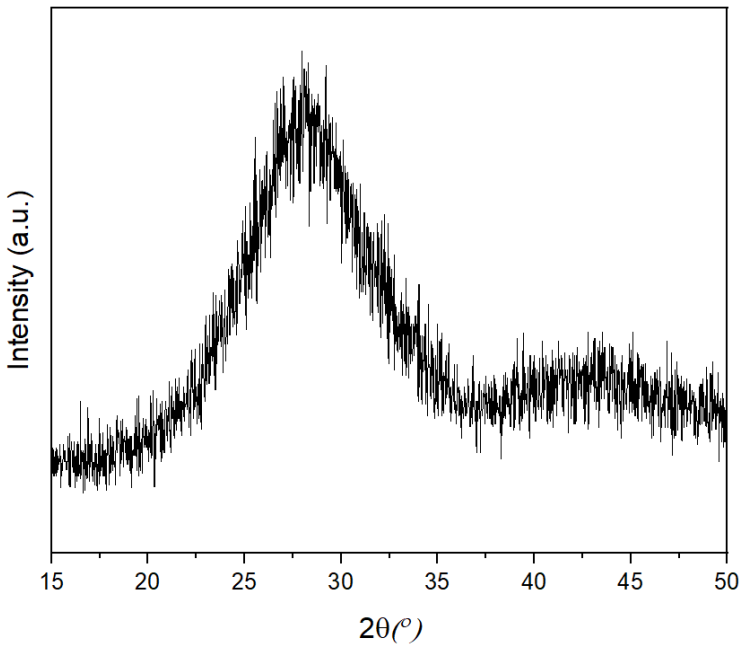

Fig. 3.5. PXRD pattern produced from the quenched $Sr_2Si_3O_8$ precursors after a heat for treatment of 1650°C for 1.5 hours.

Glass was prepared for PXRD measurement by first finely crushing it in an agate mortar, and then dispersing it onto an Si wafer using an ethanol mull. For the scan, an angular range of 15° to 45° was used, with a step size of 0.021° and measurement time per step of 0.1 s.

3.2.2. Optimisation of $Sr_2Si_3O_8$ Crystallisation by DSC

Before sintering of the glass could be attempted, determination of the crystallisation temperature of $Sr_2Si_3O_8$ was needed, as it may have changed through the removal of Al^{3+}. To do this, first DSC analysis was performed on the $Sr_2Si_3O_8$ glass (Fig. 3.6.). A 200mg sample of $Sr_2Si_3O_8$ glass was heated from 24-1600°C, with a heating rate of 10°C/ min. The results extracted the temperature of $Sr_2Si_3O_8$ crystallisation (T_c), the temperature of decomposition (T_d), the glass transition temperature (T_g) and finally the melting temperature (T_m), where the sample formed a molten liquid, (Fig. 3.6.)

An initial T_c event was observed at 859°C before a second one (T_d) at 1110°C, the presence of two crystallisation events suggested a metastable phase was forming. After crystallisation the T_m event was observed at 1290°C, where the sample became molten again. While these temperatures provided initial guidelines for $Sr_2Si_3O_8$ crystallisation, *in-situ* VTXRD analysis was required to determine which phases were forming at these events.

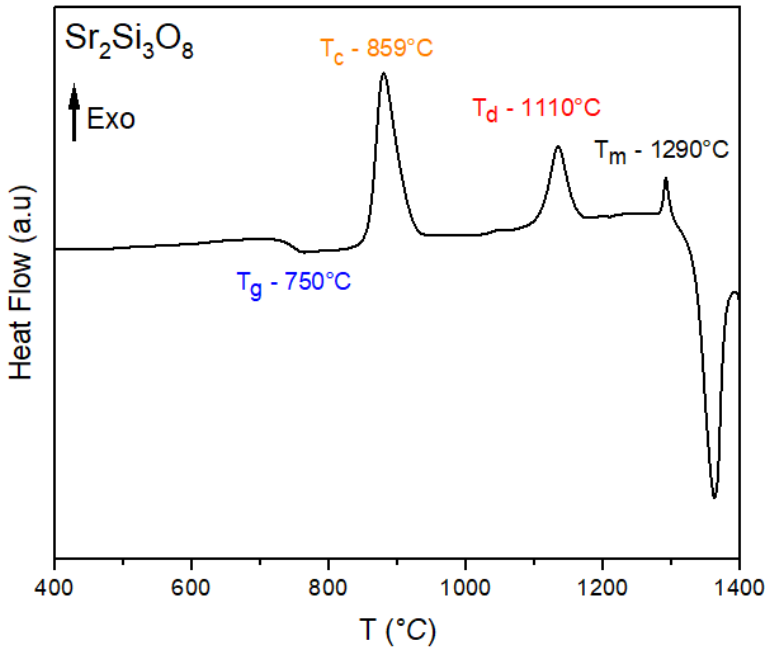

Fig. 3.6. DSC of $Sr_2Si_3O_8$ glass, with 4 events annotated. T_g is the glass transition temp, T_c is the crystallisation of $Sr_2Si_3O_8$, T_d is the crystallisation of $SrSiO_3$ and T_m is the melting temperature.

3.2.3. Optimisation of $Sr_2Si_3O_8$ Crystallisation Through *In-Situ* VTXRD

In-situ VTXRD was conducted on a powdered sample of $Sr_2Si_3O_8$ glass (Fig. 3.7.), a temperature range of 600-1200°C with scans every 25°C, angular range of 5-45°, step size of 0.2461° and time per step of 0.4s was used. A maximum temperature of 1200°C proved sufficient to see both the crystallisation of $Sr_2Si_3O_8$, as well as its subsequent decomposition. In agreement with the DSC analysis, Fig. 3.7. shows that $Sr_2Si_3O_8$ crystallises between 850-1050°C, with the sample remaining amorphous before this temperature. The small discrepancy in temperatures observed between DSC and *in-situ* VTXRD was reasoned to be due to the different temperature calibrations and heating rates of the instruments rather than a difference in crystallisation kinetics.

In-situ VTXRD analysis indicated that *ex-situ* sintering conducted within an 850-1050°C temperature range would be successful in the synthesis of $Sr_2Si_3O_8$. It was also observed that both crystallinity and intensity of the peaks developed with temperature, with the isolated pattern at 925°C showing the sharpest, best resolved pattern with no trace of secondary phase. Synthesis conditions would therefore have to be carefully optimised with respect to both temperature and time, as the steady growth of $Sr_2Si_3O_8$ observed between 850-1050°C, could be explained by either the increased temperature or longer annealing time.

The 925°C pattern was isolated for further study. It was found to be un-indexable to any known phase in the ICDD database, which again proved the novelty of $Sr_2Si_3O_8$. This pattern was then compared to the lab PXRD pattern collected on $Sr_2Si_3O_8$:Al, and although the 925°C scan showed broader peaks, a good agreement was observed. This provided the first indication that it would be possible to synthesise $Sr_2Si_3O_8$ from the binary SrO-SiO_2 line. After 1050°C, decomposition of $Sr_2Si_3O_8$ was observed occurring with its main peaks at 25°, 28° and 33°, either completely disappearing or changing in concordance with the growth of the new phase (main peak at 30°). The high temperature phase was indexed, using EVA software and the ICDD database, to $SrSiO_3$ (*C2/c*), which (along with quartz) is the known thermodynamically stable product of this region the SrO-$AlO_{1.5}$-SiO_2 diagram.[15] The excess SiO_2 was not observed as crystallised quartz and so it was believed to reside in the glassy phase.

While these results proved the metastability of $Sr_2Si_3O_8$, owing to its decomposition above a certain temperature, it highlighted the difficulty of stabilising metastable phases. The 150°C synthesis window was relatively small when compared to other systems, for example those synthesised by solid-state reaction.

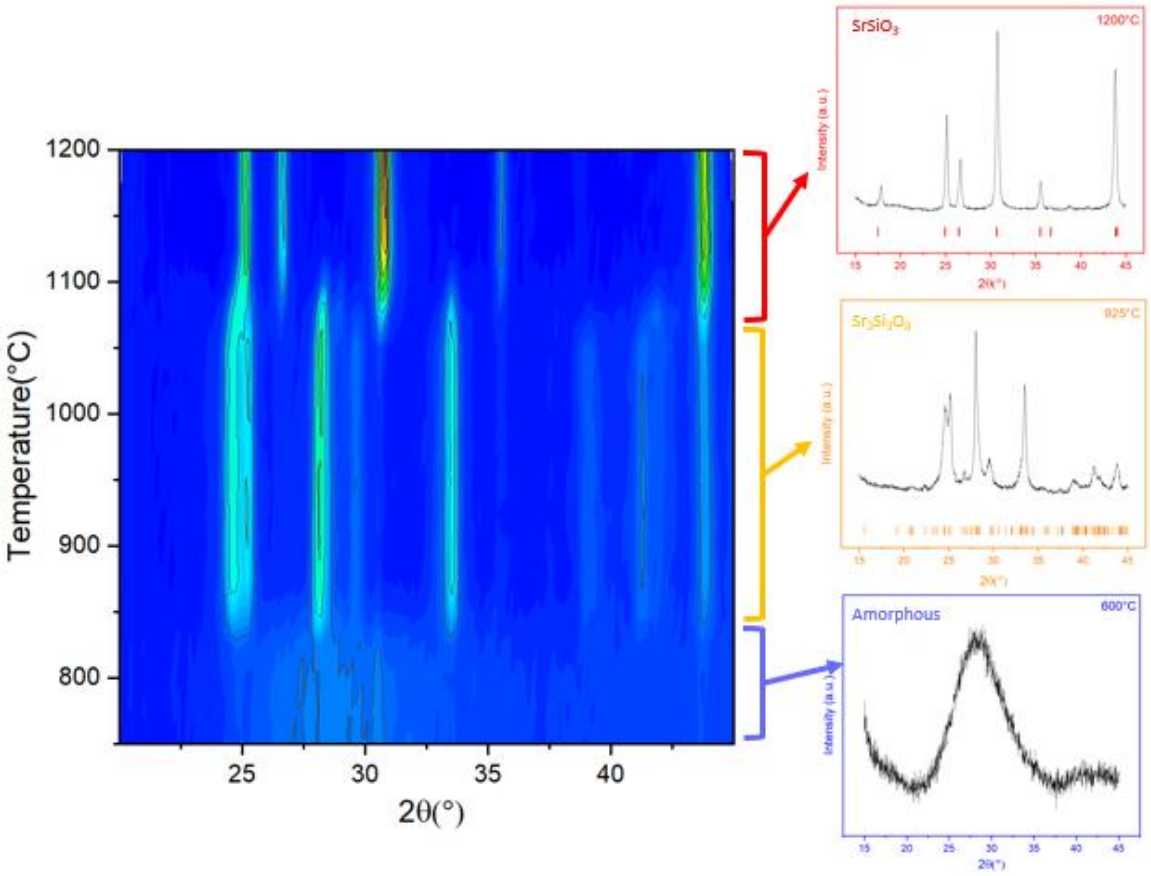

Fig. 3.7. *In-situ* VTXD from $Sr_2Si_3O_8$ glass plotted as a 2D contour plot. Two crystallisation events can be seen with the excerpts showing the PXRD patterns produced from each of these zones.

3.2.4. Crystallisation Trials Conducted on $Sr_2Si_3O_8$ Glass

Overall, *in-situ* VTXRD and DSC analysis set a temperature range of 750-1050°C for sintering trials, with the lower limit corresponding to the T_g of the parent glass (by DSC) and the upper limit to the thermal decomposition temperature of $Sr_2Si_3O_8$. Synthesis trials began in 50°C intervals between this temperature range, using the GC technique and annealing times of 4h (Fig. 3.8.).

The previously made $Sr_2Si_3O_8$ glass was formed into several 5 mm ϕ, 0.25 g pellets, and then placed into separate Pt crucibles before being sintered at the aforementioned temperatures in an open-air muffle furnace. The resultant samples were then analysed by PXRD, using a simple phase ID scan, with an angular range of 5°–50° (2Θ), step size of 0.021° and a measurement time of 0.3 s/step, the results are shown in Fig. 3.8.

An extra trial was added at 925°C after it was observed that the phase decomposed after 4 hours at 950°C, much lower than initially expected. This gave a new stability range, when GC was used, of 850–925°C. Below this temperature range the sample was still clearly amorphous, even at 800°C only some small crystallites had formed.

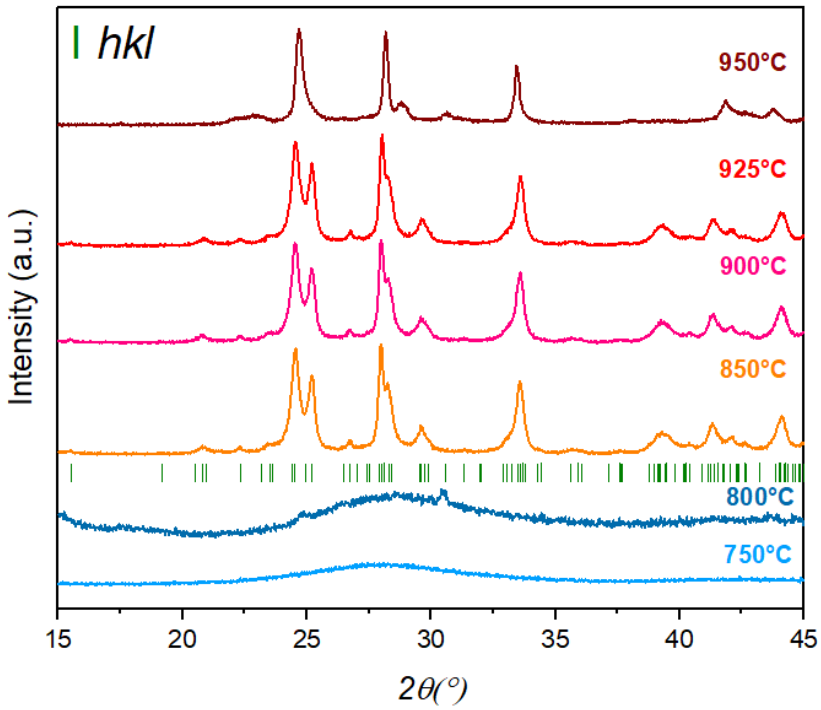

Fig. 3.8. Room temperature PXRDs comparing the *ex-situ* GC syntheses attempted on $Sr_2Si_3O_8$ between the temperature range 750–950°C, identified from DSC and *in-situ* VTXRD analysis, with a 4h annealing time. The *h,k,l* markers for $Sr_2Si_3O_8$ ($P2_1/c$) are shown in green.

When the PXRD patterns of $Sr_2Si_3O_8$, synthesised between 850-925°C, were compared to the original PXRD pattern produced by $Sr_2Si_3O_8$:Al a reasonable agreement was observed. This proved that $Sr_2Si_3O_8$ could indeed be synthesised as the sole crystalline phase from a precursor glass of the same composition, answering the first research question from Section 3.1.2, ("Can $Sr_2Si_3O_8$ be made as a binary phase?").

At 950°C a new PXRD pattern was observed which could be fully indexed to the thermodynamic product, $SrSiO_3$ (*C2/c*), meaning some SiO_2 remained uncrystallised. This allowed the 950°C temperature to be discarded, along with 750°C and 800°C as the phases remained amorphous at these temperatures. However, the remaining samples (850-925°C) showed similar peak resolutions and intensities, i.e. no clear difference in crystallinity.

To determine whether the amorphous phase fraction was the same in these samples, they were spiked with Al_2O_3 and analysed by the PXRD method outlined in Section 4.4.5. of Chapter 4 (this method was used for the crystalline wt.% determination of all samples in this section). These calculated values allowed the effectiveness of different annealing conditions and synthesis methods, to be compared, which aided in answering the second research question from Section 3.1.2, ("Can the crystalline phase fraction of $Sr_2Si_3O_8$ be increased to 100%?").

Through this analysis, the 925°C sample was discounted from further analysis as it was found to have an amorphous wt.% of 29.0(2)wt.%, compared to the 23.0(2)wt.% and 20.0(2)wt.% achieved for 850°C and 900°C respectively. This suggested a higher content of $SrSiO_3$ in the sample, due to the higher annealing

temperature. Further experiments continued at 850°C and 900°C, with the annealing time being varied (1h, 4h, 12h, and 24h). Table 3.1. shows the amorphous wt.% of the experiments at 850°C and their respective annealing times. This analysis determined that the lowest amorphous wt.% was achieved by a 12h sintering at 850°C. A minimum value of 3% amorphous phase was achieved with this protocol, however, the result was not repeated after 4 attempts and so the average value of 11.0(2)wt.%, is reported in table 3.1. The increase in amorphous content observed after 24h of annealing was believed to be due to enhanced thermal decomposition ($SrSiO_3$ crystalline & SiO_2 amorphous) with the longer annealing time. The optimum synthesis of powdered glass-ceramic $Sr_2Si_3O_8$ can be stated as GC with a sintering step of:

$$RT \xrightarrow{2\ h30} 850°C \xrightarrow{12\ h} 850°C \longrightarrow RT$$

With this sintering protocol, a pure phase sample of $Sr_2Si_3O_8$, with minimal residual amorphous phase, could be synthesised. The average crystalline phase fraction of 89.0(3)wt.%, is a substantial improvement upon the 42wt.% achieved for the original ternary ($Sr_2Si_3O_8$:Al) composition.

Table 3.1. Amorphous wt.%'s of $Sr_2Si_3O_8$ sintered at 850°C for 1h, 4h, 12h and 24h, respectively.

Annealing time (h)	Amorphous content (wt.%)
1	28.0 (2)
4	23.0 (2)
12	11.0 (2)
24	19.0 (1)

3.2.5. Confirming the GC Approach by Comparison with the Solid-State Method

GC was the main synthesis method used in this chapter. To test the necessity of this method, conventional solid-state synthesis of $Sr_2Si_3O_8$ was also attempted. The high-purity precursors, $SrCO_3$ (99.999% Strem) and SiO_2 (99.999% Strem) were weighed and mixed in an agate mortar. The resultant powder was then pressed into 0.5g, 5mm ϕ pellets and placed in Pt crucibles for sintering. Afterwards, literature was consulted to determine the sintering temperature, Duval *et al.'s* work on the analogous $Ba_4Si_6O_{16}$ demonstrated that crystallisation occurred at 1200°C, however, DSC analysis of $Sr_2Si_3O_8$ (Fig. 3.6.) had revealed that the sample melted at 1290°C and so a reduced temperature range of 900-1100°C was used for solid-state crystallisation trials.[10,16] An annealing time of 12h was used for each sample, and as shown in Fig. 3.9., the 900°C experiment was repeated 3 times to ensure equilibrium had been reached.

PXRD analysis was conducted on the post-annealed samples (Fig. 3.9.). As shown, the solid-state method resulted in the formation of primarily $SrSiO_3$ (*C*2/*c*) in all the 900°C and the 1000°C trials, while at 1100°C $Sr_2(SiO_4)$ (*Pnma*) is observed forming, as expected from the equilibrium phase diagram of SrO-SiO_2.[13] These products represented the thermodynamically stable products of this zone in the ternary diagram and demonstrated how conventional approaches, such as the solid-state method, missed potentially interesting

phases. Therefore, although the solid-state method failed to synthesise $Sr_2Si_3O_8$, its attempt was still useful in valorising the use of out-of-equilibrium synthesis methods for synthesising metastable phases.

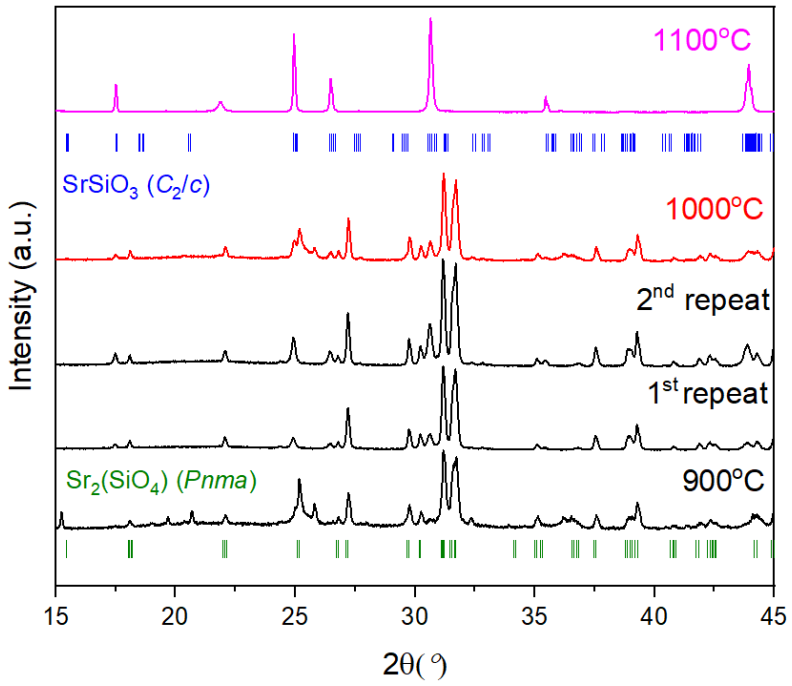

Fig 3.9. PXRD patterns produced from use of the solid-state method (12h at 900, 1000, 1100, 1200°C, respectively. $SrSiO_3$ (*C2/c*) is indicated by blue *h,k,l* markers, while the green ones indicate $Sr_2(SiO_4)$ (*Pnma*).

3.2.6. Verifying the $Sr_2Si_3O_8$ Formula by Scanning Electron Microscopy

Scanning Electron Microscopy (SEM) imaging, combined with Energy dispersive X-ray spectroscopy (EDS) measurements, was attempted on crystallised (12h 850°C) and glassy $Sr_2Si_3O_8$ to determine if a compositional difference was observed between the crystalline phase and glass. Therefore, indicating that the $Sr_2Si_3O_8$ formula wasn't nominal. Sample was prepared by embedding a sintered pellet (12h 850°C) and bulk glass piece in epoxy resin and then polishing the surface of the disk until all scratches had been removed. SEM imaging of the crystalline phase (Fig.3.10.) showed $Sr_2Si_3O_8$ crystals embedded in a significant amorphous matrix, supporting the NMR and amorphous content analysis. From the formula of the glass, a crystalline phase of $40SrO\text{-}60SiO_2$ was expected and as shown by the EDS results in table 3.2., this is approximately what is observed for both the crystalline and glassy phase, meaning congruent crystallisation had been achieved. Although, the concordant compositions of the glass and crystals further complicated why full crystallisation of $Sr_2Si_3O_8$ wasn't observed, as it meant synthesis was occurring from the nominal formula. Additionally, no atom rich or deficient zones were observed across the crystalline sample, (Appendix 2, A.3.17.), which indicated that a compositionally homogeneous sample had been synthesised.

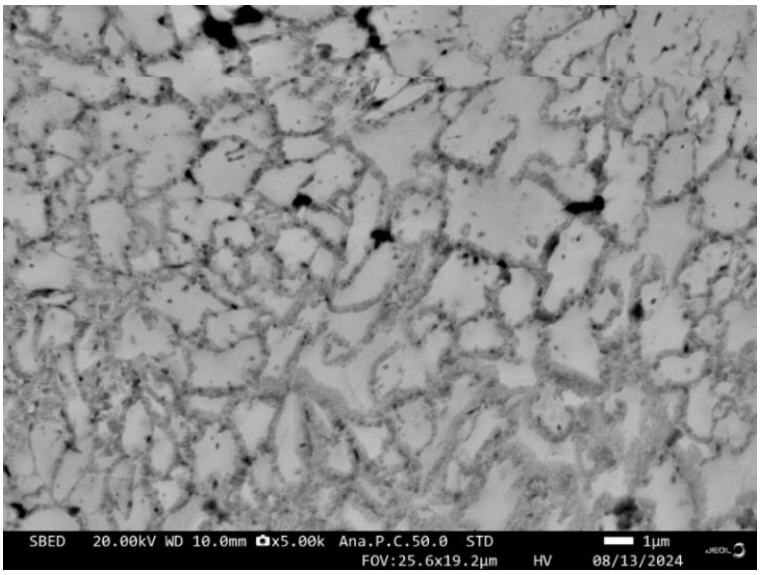

Fig. 3.10. The SEM image used for EDS measurements of crystalline $Sr_2Si_3O_8$, showing crystallised zones surrounded by a glassy matrix.

Table 3.2. Atomic % of Sr and Si within the crystallised (12h 850°C) $Sr_2Si_3O_8$ and its parent glass, obtained from EDS analysis.

Sample	Nbr analyses		Sr (At%)	Si (At%)
Crystal	5	Average	36.4(2)	63.5(2)
Glass	17	Average	36.2(2)	63.77(8)

3.3. Structural Analysis of $Sr_2Si_3O_8$

3.3.1. Rietveld Refinement of $Sr_2Si_3O_8$

With a high-quality sample of $Sr_2Si_3O_8$ now synthesised by congruent crystallisation of its parent 40SrO-60SiO_2 glass, its structure could be investigated using the Rietveld method.[17,18] This analysis required equally high-quality PXRD data to be collected, an angular range of 5-110°, step size of 0.02051°, and time per step of 2s, was used. These parameters, alongside the use of a deep sample holder, improved the signal to noise ratio and powder averaging, resulting in easier indexation of weak reflections at high angles, when compared to the shorter phase ID scan.

The monoclinic, $P2_1/c$, (a=13.342273(2)Å, b= 4.565349(5)Å, c=13.488184(15)Å, β = 116.49939(29)°) model solved from NPD and lab PXRD data of $Sr_2Si_3O_8$:Al, was used as the basis for refinement, conducted in TOPASV7 and jedit software. A Rietveld refinement file with a background function featuring 10 parameters, zero shift, axial divergence, a TCHZ function with 6 parameters, and 16 atomic sites was created.[19] This file led to a R_{wp} of 11.789% and χ=3.608 being achieved, with the refinement shown in Fig. 3.11.(a) and table of refinement shown in Appendix 2, T.3.2. Although this initial refinement file provided a reasonable fit to the data, intensity issues were noticed on the main peaks at 25°, 29° and 34°.

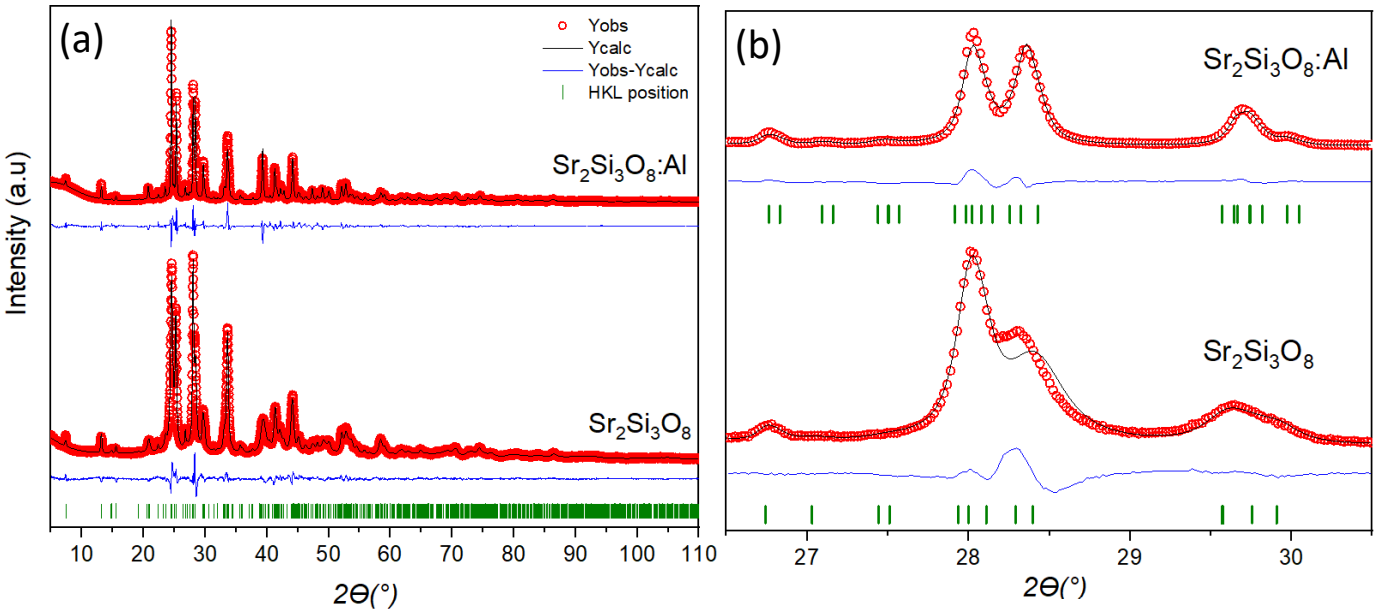

Fig. 3.11. (a) Rietveld refinements of $Sr_2Si_3O_8$ and $Sr_2Si_3O_8$:Al achieved from room temperature lab-PXRD data collected on the 850°C 12h annealed $Sr_2Si_3O_8$ (R_{wp} of 6.964% and χ of 2.138) & the 900°C 1h annealed $Sr_2Si_3O_8$:Al (R_{wp} of 7.377% and χ of 3.90). **(b)** Zoom of the 'shoulder' which was refined in the $Sr_2Si_3O_8$:Al sample but not in the $Sr_2Si_3O_8$ sample.

Fig. 3.11.(b) shows that these issues didn't occur for the $Sr_2Si_3O_8$:Al refinement suggesting that the removal of Al^{3+} had altered the crystal structure of $Sr_2Si_3O_8$ in some way (table of refined parameters for $Sr_2Si_3O_8$:Al shown in Appendix 2, T.3.3.). Investigations into literature found that the Stephens monoclinic macro had improved refinements of monoclinic cells which showed anisotropic peak broadening in its crystallites.[20]

Introducing this macro into the refinement file accounted for these broadenings by adding individual strain contributions on specific *h,k,l* planes. After its inclusion, a marked improvement of the refinement was observed, and peak intensity issues were mostly resolved. The fit achieved with and with Stephens macro is shown in Appendix 2, A.3.18,19. With a better refinement now achieved, sensitive parameters such as the atomic positions and isotropic thermal contributions of the Sr and Si atoms could be refined. The refinement of these parameters gave a final R_{wp} of 6.964% and χ of 2.138, (which improved upon the R_{wp}=11.789% and χ=3.608, when the macro wasn't used). Additionally, comparison of the refined structures and atomic parameters of $Sr_2Si_3O_8$ and $Sr_2Si_3O_8$:Al showed good agreement which again proved that $Sr_2Si_3O_8$ could be made without Al^{3+}, (Refined structure of $Sr_2Si_3O_8$ shown in Appendix 2, A.3.20.).

When the Rietveld refinements of the binary $Sr_2Si_3O_8$ and ternary $Sr_2Si_3O_8$:Al, were compared two interesting points were observed, (Fig. 3.11.(a)). First of all, the resolution of the peaks was much higher for the ternary phase than the binary one, especially the main peaks. Secondly, as seen in Fig. 3.10.(b) a 'shoulder' on the peak at 28° (3, 0, -4) which was previously modelled by the $P2_1/c$ space group was now no longer refined. This was due to a subtle shifting of the peak (3, 0, -4) in $Sr_2Si_3O_8$, which can be indicative of an extended defect such as a stacking fault. The first point suggested that Al^{3+} within the glass matrix was playing a larger role than previously thought in the crystallisation of $Sr_2Si_3O_8$. The second point suggested that its absence

was causing an increase in disorder or deformation within the unit cell, which was not accounted for in the model. Microstructure analysis was needed to investigate the cause of this defect.

3.3.2. Microstructure Analysis of $Sr_2Si_3O_8$ by High-Resolution TEM

If the shoulder at 28° was being caused by some form of disorder – strain broadening, shear plane, stacking fault etc. – then a more accurate idea of its origin was needed to model it using the Rietveld method. Without a clear understanding of the disorder, modelling would be an almost impossible task. To this end, powerful microstructural analysis techniques (high-resolution TEM and selected area electron diffraction (SAED)) were attempted to visualise the microstructure and determine the cause of the disorder. If indeed some kind of extended defect existed within the structure then these techniques would provide a high enough degree of magnification and resolution to visualise it, as demonstrated by the HAADF-STEM study conducted in Chapter 2 (Section 2.4.3.).

Optimised $Sr_2Si_3O_8$ sample (crystallised from glass - 12h at 850°C) was prepared for high-resolution TEM by suspending powdered $Sr_2Si_3O_8$ sample in ethanol, and then dropping it onto an amorphous, porous carbon matrix that was coated onto a copper grid, (Chapter 4 – 4.6.2.).

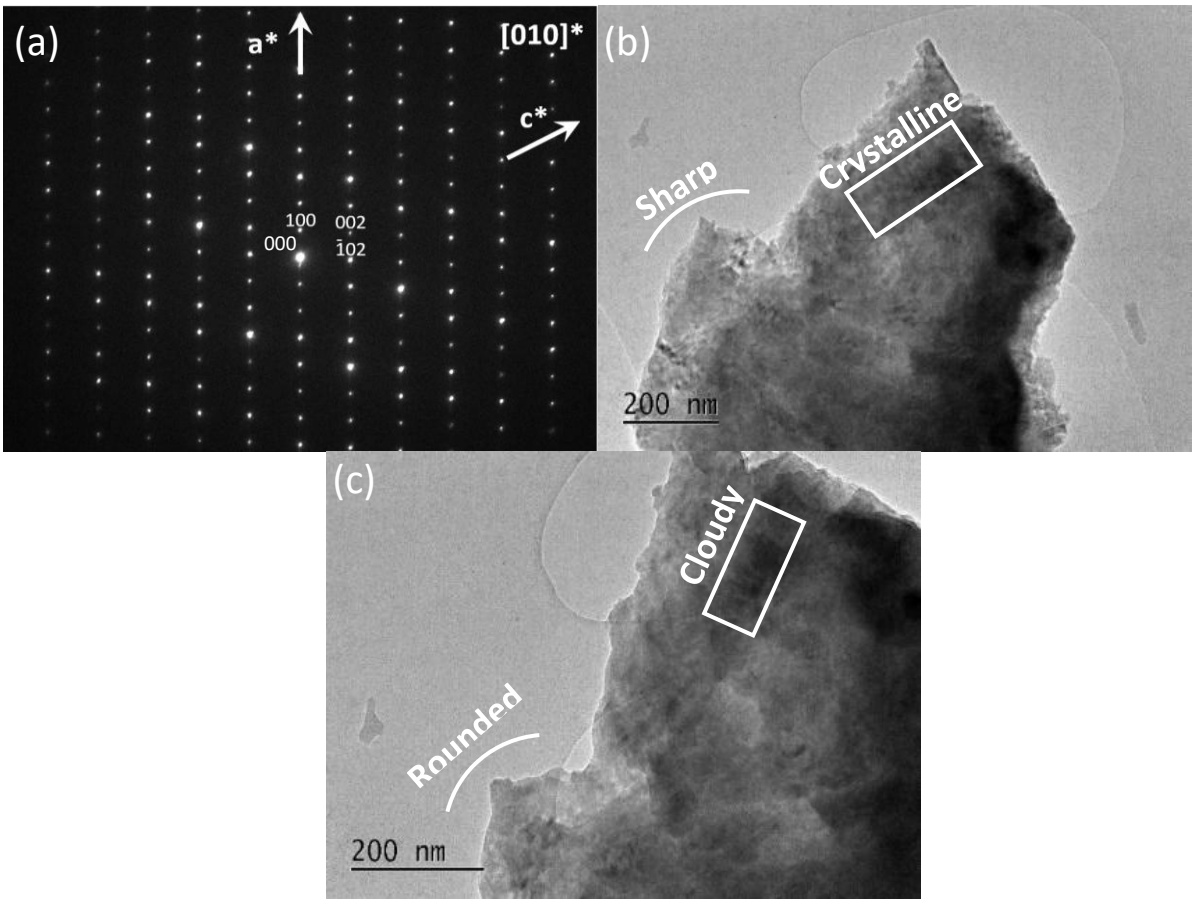

Fig. 3.12. (a) SAED spectra, orientated along the [010]* zone axis and indexed to $SrSiO_3$ (*C2/c*). **(b)** Highest magnification (80 keV) achieved by TEM before $Sr_2Si_3O_8$ decomposed. **(c)** TEM image showing the beginning of $Sr_2Si_3O_8$ decomposition under the beam.

The electron diffraction pattern (SAED) of powdered $Sr_2Si_3O_8$ crystals orientated to its [010]* zone axis, indexed the phase to a *C*2/*c* cell (Fig. 3.12.(a)) indicating the decomposed $SrSiO_3$ had formed under the beam. Unfortunately, it was found that the metastable nature of $Sr_2Si_3O_8$ prevented the use of a high-voltage electron beam (200keV), necessary for atomic scale magnification and visualisation of the microstructure, from being used. The highest voltage achieved (80 keV) before decomposition is shown in Fig. 3.12.(b), sharp well-defined crystallised zones can be viewed, which lose their definition when beam intensity is increased, (Fig. 3.12.(c)).

Due to the lack of microstructural data on the defect, several attempts were made to model the disorder based on structural comparisons between $Ba_4Si_6O_{16}$ and $Sr_2Si_3O_8$. For example, a shear defect was randomly simulated throughout the structure, which made the framework more closely resemble the $Ba_4Si_6O_{16}$ phase. A more detailed explanation of the attempted models is discussed in Annex I. but unfortunately none were successful.

3.4. Alternative Synthesis Strategies for Improved Stability & Crystallinity

$Sr_2Si_3O_8$ decomposed too easily under an electron beam for high-resolution TEM images to be collected, and the GC approach only produced moderate-quality samples (residual glass; uncharacterised modification of the crystal structure). Together, these motivated the investigation of alternative synthesis routes, and the introduction of possible stabilising substitutions. Different ideas were discussed to increase the stability window of $Sr_2Si_3O_8$ (i.e. the difference between the glass crystallisation, T_c, and thermal decomposition temperatures, T_d). For example, changing the synthesis method: Direct crystallisation of the phase by aerodynamic levitation (ADL), high-energy milling (HEM) and the solid-state reaction method. As discussed in Chapter 1 (Sections 1.2.8 & 9.), both, ADL and HEM have been shown to provide more homogenous 'activated' glass precursors, with lower activation energies ($\triangle$E) and therefore, could increase the synthesis range of $Sr_2Si_3O_8$.[21,22] Additionally, this effect could also aid in the complete crystallisation of $Sr_2Si_3O_8$, helping to answer the second research question of Section 3.1.2. ("Can the crystallinity of $Sr_2Si_3O_8$ be increased and will it still remain phase-pure?"). The following section will discuss the results from using HEM and the solid-state method however, the results of the ADL work can be found in Annex II.

3.4.1. Increasing the Surface Area of $Sr_2Si_3O_8$ Glass Particles by HEM

One of the most common mechanisms of crystallisation is surface crystallisation, which seems to be the case for $Sr_2Si_3O_8$, as annealing of bulk glass beads from ADL leads to a lower crystalline phase fraction and reduced crystallinity (Annex II). This means that by reducing particle size and thereby increasing surface area, through HEM, improved crystallisation kinetics should be observed and therefore a higher crystalline phase

fraction.[23–26] For particle size determination a Partica LA-960V2 particle size distribution analyser from HORIBA was used.

After $Sr_2Si_3O_8$ glass had been prepared and ball milled using the method described in Appendix 2, 4.1.4., the resultant particle sizes from each step were analysed (table 3.3.). The 10th percentile particle sizes (D10) are quoted rather than the average sizes as it can be seen that the average size actually increases when milling bead sizes are decreased, (table 3.3.). This effect was caused by agglomeration of the particles, a phenomenon known to be more pronounced with longer milling times due to the increase in surface energy.[27,28] Therefore, the 10th percentile values were used for analysis as they represented the un-agglomerated particle size or smallest particle size achieved after each HEM experiment.

Table 3.3. Conditions of the ball milling experiments and the resultant particle size produced.

Bead Size (mm)	RPM	Milling time (mins)	AVG. particle size (μm)	D10 particle size (μm)
10	800	15	54(2)	6.8(3)
5	1500	60	39(2)	4.3(2)
1	1500	60	175(8)	1.9(1)

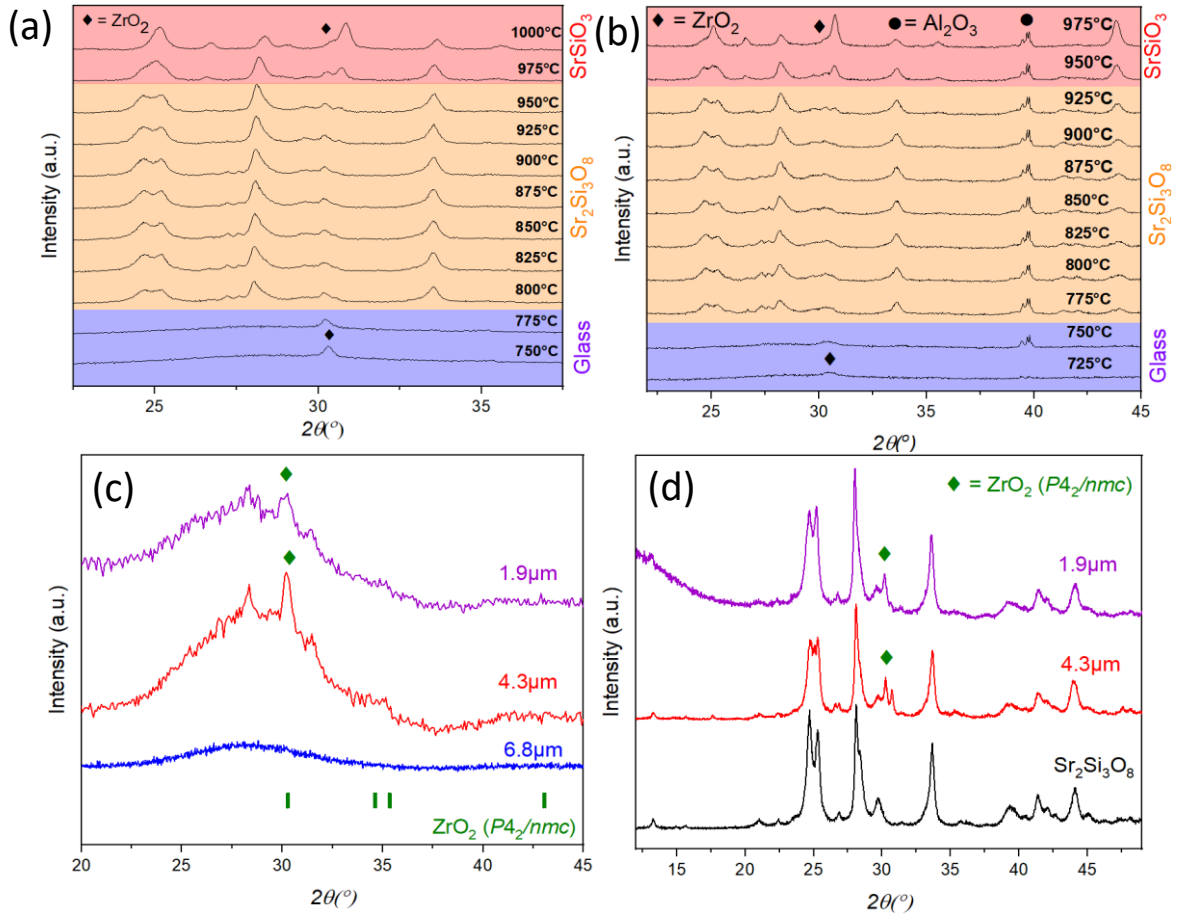

Fig. 3.13. (a) *In-situ* VTXRD of the 4.3 μm powder. **(b)** *In-situ* VTXRD of the 1.9 μm powder. **(c)** *ex-situ* VTXRD of the glasses after ball milling, with the ZrO_2 impurity marked by a green diamond. **(d)** The 4.3 1.9 μm powders after sintering for 12h at 800°C, again the impurity is marked by a green diamond.

Before crystallising, the resultant powders, 4.3 and 1.9 μm, were first analysed by *in-situ* VTXRD (Fig. 3.13.(a)(b)) to determine if the optimum annealing temperature had change and if a greater stability window was observed. It can be seen that indeed; the synthesis range had reduced. For the 4.3 μm powder the range decreased by 50°C and for the 1.9 μm powder the range decreased by a further 25°C giving new temperature ranges of 800-950°C and 775-925°C respectively. However, the reduction in $Sr_2Si_3O_8$ synthesis temperature also coincided with a reduction in the decomposition temperature (Fig. 3.13.(a)(b)) and therefore this technique did not achieve its intended goal of increasing phase stability.

The $Sr_2Si_3O_8$ glass was analysed by PXRD after HEM (Fig. 3.13.(c)). This analysis identified another problem which arose from HEM, contamination from the ZrO_2 beads. The contamination peaks at 31° are marked by green diamonds in Fig. 3.13.(c)(d) and can be indexed to a tetragonal ZrO_2 ($P4_2/nmc$) phase. The peak appears more diffuse and broader as particle size decreases, 4.3 to 1.9 μm samples, due to the smaller particle size of the contaminant, by PXRD nm scale particles appear as broad diffuse peaks. This peak persisted as a small impurity when the glasses were crystallised, as seen in Fig. 3.13.(d). The 4.3 μm powder showed the lowest levels of ZrO_2 contamination and so was selected for sintering trials, and subsequent crystalline wt.% determination of the optimum sample (12h 800°C). However, a maximum crystalline phase fraction of 75% was achieved, 12% less than that observed for the un-milled glass.

It was concluded that HEM, as an alternative synthesis route, was not viable for increasing the stability and crystallinity of $Sr_2Si_3O_8$. Moreover, when the resulting ball-milled glass and annealed samples were refined using the Rietveld method, the 28° (3, 0, -4) shoulder could still not be modelled.

3.5. Improving $Sr_2Si_3O_8$ Crystallisation Through Substitutions & Nucleating Agents

Given the difficulty in synthesising highly crystalline $Sr_2Si_3O_8$ with a wide stability range, substitutions and nucleating agents were investigated as ways of addressing these issues. Ideally a sample whose PXRD pattern (crystallinity) resembled $Sr_2Si_3O_8$:Al would be achieved but with a much higher crystalline phase fraction (~100%). A sample such as this would allow the properties of functionalised $Sr_2Si_3O_8$ to be studied.

The Ba analogue to $Sr_2Si_3O_8$ had been shown by Duval *et al*. to be highly stable and crystalline, as evidenced by its ability to be synthesised by the solid-state method.[7,10,16] This implies that substitutions of Ba^{2+} for Sr^{2+} in $Sr_2Si_3O_8$ might simultaneously promote phase stability as well as improve crystallinity. Permitting the accurate modelling of the structure and/or microstructural defect analysis by SEM and TEM. By similar logic, Ca^{2+} was also considered as a substitution for Sr^{2+}.

As discussed in Section 1.2.6. of Chapter 1, nucleating agents such as ZrO_2, $ZrTiO_4$ and Ag had been shown to improve crystallinity by lowering $\triangle E$. Literature showed that the addition of these inert centres in the glassy matrix provided a surface for the nucleation of crystals, leading to highly crystalline glass-ceramics.[29–33]

Several nucleating agents were attempted in this work, ZrO_2, Ag, Au, $ZrTiO_4$ and P_2O_5, however only the first two are described in detail in this section, as they were found to be representative of the others.

3.5.1. Substituting $Sr_2Si_3O_8$ with Ba^{2+} According to the Formula $Sr_{2-x}Ba_xSi_3O_8$

Substitutions of Ba^{2+} for Sr^{2+} were attempted according to the formula $Sr_{2-x}Ba_xSi_3O_8$ for x values $0<x\leq0.5$. Specifically, x=0.1, 0.2 and 0.5 were attempted, giving the nominal formulae $Sr_{1.9}Ba_{0.1}Si_3O_8$, $Sr_{1.8}Ba_{0.2}Si_3O_8$, and $Sr_{1.5}Ba_{0.5}Si_3O_8$, respectively. The same optimised GC procedure outlined in Section 3.2. was used, with high-purity $BaCO_3$ (99.997% Strem) substituting for $SrCO_3$.

Fig. 3.14.(a) shows that synthesis of x=0.2 and 0.5 compositions were successful, with the same PXRD patterns being observed as for the un-substituted $Sr_2Si_3O_8$. The expected peak shift to lower 2Θ angles was observed in these samples, owing to the substitution of the larger Ba atom increasing the unit cell dimensions. This along with the absence of secondary phases proved the successful substitution of Ba^{2+} into the $Sr_2Si_3O_8$ framework. Interestingly, the lowest level of Ba^{2+} substitution, x=0.1, was unsuccessful, even when the experiment was repeated, with primarily $SrSiO_3$ (*C*2/*c*) being observed by PXRD. A small amount of another phase, identified in literature as a metasilicate polymorph of $SrSiO_3$, was also observed, as marked by the orange diamonds in Fig. 3.14.(a).[34] Comparison of the PXRD patterns for $Sr_{1.8}Ba_{0.2}Si_3O_8$ and $Sr_{1.5}Ba_{0.5}Si_3O_8$, revealed intensity differences on the peaks at 24° (2, 1, 0), 25° (2, 0, 2), and 33° (3, 0, -4) when compared to $Sr_2Si_3O_8$. The doublet at 24/25° inverted its intensities until the second peak became the dominant one, Fig. 3.14(a). A reduction of intensity was also observed for the peak at 33°. Finally, an unknown intermediate phase (shown in yellow in Fig. 3.14(b).) was also observed between 1025-1100°C. Attempts to isolate and index this phase are described in Annex III.

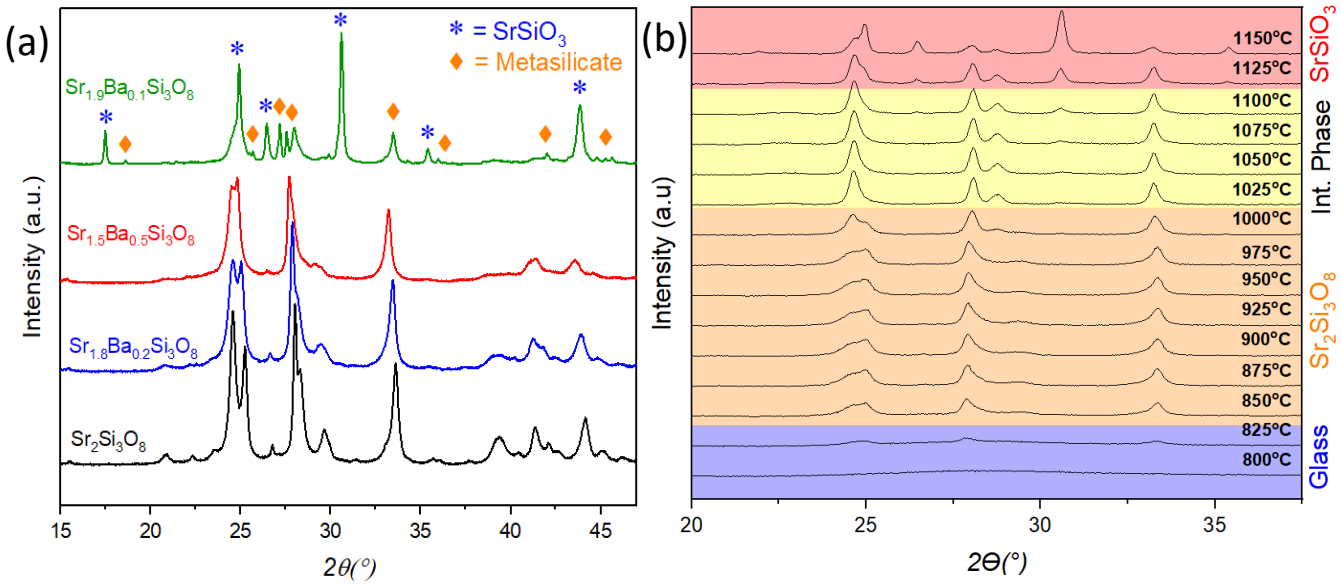

Fig. 3.14. (a) Comparison of the PXRD patterns of $Sr_2Si_3O_8$, $Sr_{1.9}Ba_{0.1}Si_3O_8$, $Sr_{1.8}Ba_{0.2}Si_3O_8$ and $Sr_{1.5}Ba_{0.5}Si_3O_8$ respectively, with a blue star and orange diamond marking the phases synthesised in the x=0.1 sample. **(b)** *In-situ* VTXRD of $Sr_{1.8}Ba_{0.2}Si_3O_8$.

3.5.2. Rietveld Refinement of $Sr_{1.8}Ba_{0.2}Si_3O_8$

Fig. 3.14.(b) showed that Ba^{2+} substitution had failed to improve the stability of $Sr_2Si_3O_8$, and in fact had reduced it from 850-1050°C to 850-1000°C. However, perhaps it had succeeded in the secondary goal of either removing or modelling the 'shoulder' at 28° (3, 0, -4). The synthesis of $Sr_{1.8}Ba_{0.2}Si_3O_8$, was optimised to determine this. DSC was conducted (Fig. 3.16.) which revealed an unchanged T_c of 859°C, which suggested that the same optimised synthesis procedure developed for undoped $Sr_2Si_3O_8$ (12h at 850°C) may also be optimal here. Synthesis of $Sr_{1.8}Ba_{0.2}Si_3O_8$ was conducted according to this protocol, with the resultant sample then being scanned by PXRD, using the parameters defined in Section 3.3.1. Rietveld refinement of this sample, permitted the crystalline phase fraction to be determined, using the method outlined in Section 4.4.5. of Chapter 4, pattern shown in Appendix 2, A.3.21.

The same $P2_1/c$ model and refinement file as $Sr_2Si_3O_8$ was used, except two Ba^{2+} sites were added in equivalent positions to the Sr^{2+} ones. Their occupancy was fixed to 0.1, as examination of the structure found no reason for preferential substitution between the sites. The lab PXRD data was also of insufficient quality for this parameter to be accurately refined. However, the increase in cell volume, shown in table 3.4. proved the successful substitution of Ba^{2+} into the structure. The larger ionic radius of Ba^{2+} compared to Sr^{2+} meant that its substitution into the unit cell increased cell dimensions and volume (Fig. 3.15.). From Bragg's law, it is known that this results in a lower 2Θ angle of peak diffraction, (Eq. 4.2.).[35]

When compared to $Sr_2Si_3O_8$, the $Sr_{1.8}Ba_{0.2}Si_3O_8$ model gave a similar R_{wp} of 7.507% and χ of 2.490 respectively (table of refined parameters shown in Appendix 2, T.3.4.). Again, the Stephens monoclinic macro for anisotropic peak broadening, improved the quality of the Rietveld refinement. Combined with the continued presence of the shoulder at 28°, which remained unrefined, it can be said that the substitution of Ba^{2+} failed to remove the microstructural defect.

Table 3.4. Comparison of lattice parameters, β angle and cell volume between $Sr_2Si_3O_8$, $Sr_{1.8}Ba_{0.2}Si_3O_8$ and $Sr_{1.9}Ca_{0.1}Si_3O_8$.

Composition	a (Å)	b (Å)	c (Å)	β (°)	Volume (Å)³
$Sr_2Si_3O_8$	13.338(1)	4.5633(5)	13.486(1)	116.486(3)	734.7(1)
$Sr_{1.8}Ba_{0.2}Si_3O_8$	13.394(2)	4.5533(9)	13.567(2)	116.317(5)	741.7(2)
$Sr_{1.9}Ca_{0.1}Si_3O_8$	13.322(2)	4.552(7)	13.479(2)	116.391(4)	732.2(1)

The crystalline phase fraction of $Sr_{1.8}Ba_{0.2}Si_3O_8$ was then analysed and found to be 62wt.%, meaning that a significant amorphous fraction of 38wt.% still remained; much larger than the 11wt.% achieved for $Sr_2Si_3O_8$. This sizeable amorphous phase and inability to model the shoulder at 28° meant that substituting Ba^{2+} for Sr^{2+} had failed in achieving the goals of improving stability and reducing anisotropic peak broadening. However, it can be said that a reduction in the shoulders size and shape had occurred, (Fig. 3.15.). Substituting with Ca^{2+}, according to the formula $Sr_{2-x}Ca_xSi_3O_8$ ($0 < x < 0.2$) was attempted next.

3.5.3. Substituting $Sr_2Si_3O_8$ with Ca^{2+} According to the Formula $Sr_{2-x}Ca_xSi_3O_8$

The Ba analogue of $Sr_2Si_3O_8$ made investigating the existence of a Ca analogue worthwhile. However, the smaller ionic radius of Ca^{2+} made it unclear what levels of substitution the structure could tolerate. Due to this, only x values of 0.1 and 0.2 were attempted, corresponding the respective formulae of $Sr_{1.9}Ca_{0.1}Si_3O_8$, and $Sr_{1.8}Ca_{0.2}Si_3O_8$. High-purity $CaCO_3$ (99.99% Alfa) was used as the substituting agent for $SrCO_3$. The same optimised GC approach, detailed in Section 3.2., was then used to form glass and subsequently anneal it, for initial comparison of the samples.

The phase ID PXRD patterns of $Sr_{1.9}Ca_{0.1}Si_3O_8$, and $Sr_{1.8}Ca_{0.2}Si_3O_8$, both showed the expected $Sr_2Si_3O_8$ phase. A shift to higher 2Θ angles was noted which, combined with the reduction in lattice parameters (table 3.4.), confirmed the successful substitution of the smaller Ca^{2+} ion. Qualitative comparison of the PXRD patterns (Appendix 2, A.3.22.) showed slightly better crystallisation, with respect to peak sharpness and overall crystalline phase fraction, of $Sr_{1.8}Ca_{0.2}Si_3O_8$, over $Sr_{1.9}Ca_{0.1}Si_3O_8$, so optimisation continued on this composition. *In-situ* VTXRD (Appendix 2, A.3.23.), revealed that $Sr_{1.8}Ca_{0.2}Si_3O_8$ had a slightly smaller stability range, of 850-1000°C, when compared to $Sr_2Si_3O_8$, but that its T_c was the same, 859°C, (Fig. 3.16.). Again, the unknown intermediate phase, was observed by *in-situ* VTXRD after 1000°C (Annex III). The similarity of these results to those from $Sr_{1.8}Ba_{0.2}Si_3O_8$, suggested that the same heat treatment of 12h at 850°C, would also be optimal for $Sr_{1.8}Ca_{0.2}Si_3O_8$. Finally, experiments were conducted to synthesise the end-member of the formula, $Ca_2Si_3O_8$, from a GC approach, but unfortunately, they were unsuccessful and only $CaSiO_3$ (*A*2/*a*) and SiO_2 ($P3_221$) was synthesised.

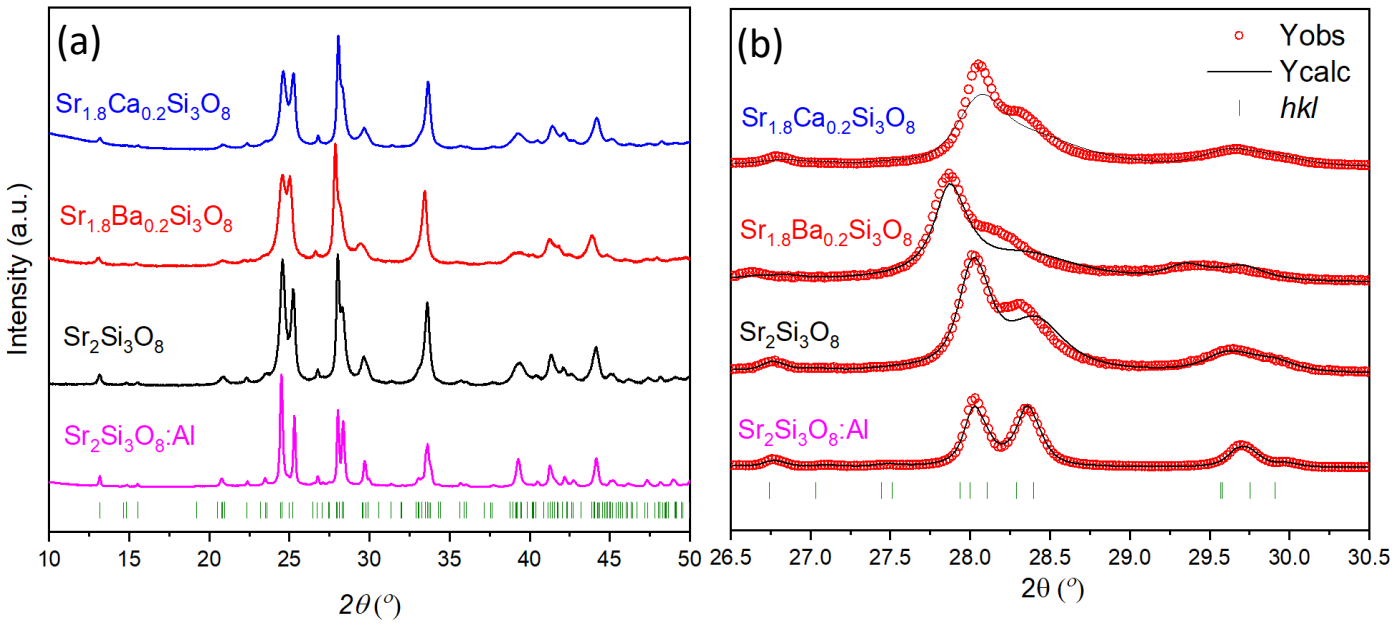

Fig. 3.15. (a) Comparison of the optimised synthesis of $Sr_2Si_3O_8$:Al (1h 900°C), $Sr_2Si_3O_8$, $Sr_{1.8}Ba_{0.2}Si_3O_8$ and $Sr_{1.8}Ca_{0.2}Si_3O_8$ (12h at 850°C). The $SrAl_2SiO_6$:Al pattern is shown to demonstrate the ideal PXRD that was desired. **(b)** Comparison of the respective Rietveld refinements achieved of the shoulder at 28° (3, 0, -4).

3.5.4. Rietveld Refinement of $Sr_{1.8}Ca_{0.2}Si_3O_8$

Synthesis trials of $Sr_{1.8}Ca_{0.2}Si_3O_8$ did indeed conclude that the optimum synthesis protocol was 12h at 850°C. High-quality lab-PXRD data of this sample was collected and refined by the Rietveld method, to determine if the 'shoulder' at 28° (3, 0, -4) could now be modelled and to quantify the crystalline phase fraction. The same initial refinement file as $Sr_{1.8}Ba_{0.2}Si_3O_8$ was used, except the Ba sites were changed to Ca ones. This refinement gave a slightly higher R_{wp} of 7.829%, and much higher χ of 5.348 (refined parameters shown in Appendix 2, T.3.5.) when compared to $Sr_2Si_3O_8$. A reduction in the *a*- and *c*- lattice parameters (table 3.4), and slight shifting of the peaks to higher angles was observed (Fig. 3.15.(a)), which confirmed the successful substitution of Ca^{2+}. Similarly, to $Sr_{1.8}Ba_{0.2}Si_3O_8$, despite the shoulder at 28° reducing in intensity, it still remained unrefined (Fig. 3.15(b)) meaning that Ca^{2+} substitutions were unsuccessful in their goal of allowing this peak to be modelled. Finally, the crystalline phase fraction of $Sr_{1.8}Ca_{0.2}Si_3O_8$ (12h 850°C) was calculated and found to be 60wt.% which was lower that of the $Sr_{1.8}Ba_{0.2}Si_3O_8$ and $Sr_2Si_3O_8$ samples, 62wt.% and 89wt.%, respectively, (refinement shown in Appendix 2, A.3.24.). It was concluded that, the substitution of Sr^{2+} for Ba^{2+} or Ca^{2+} was unsuccessful in the stabilisation of $Sr_2Si_3O_8$. Overall, substitutions lowered the crystalline phase fraction and prevented a microstructural study of the ribbons to model the defect.

3.5.5. Stabilisation of $Sr_2Si_3O_8$ Glass

DSC scans of $Sr_2Si_3O_8$, $Sr_{1.8}Ba_{0.2}Si_3O_8$ and $Sr_{1.8}Ca_{0.2}Si_3O_8$, measured under the same conditions, are shown in Fig. 3.16. When the samples were recovered after the experiments it was noted that the substituted samples were glassy whereas $Sr_2Si_3O_8$ was mainly crystalline. This suggested a greater glass-forming ability of the substituted samples. As shown in Fig. 3.16., this is supported by an increase in T_c-T_g between $Sr_2Si_3O_8$, $Sr_{1.8}Ca_{0.2}Si_3O_8$ and $Sr_{1.8}Ba_{0.2}Si_3O_8$, 109°C, 113°C, and 118°C respectively. This trend shows that, despite the T_d increasing for $Sr_{1.8}Ba_{0.2}Si_3O_8$, the substitutions were likely stabilising the glassy phase more than the $Sr_2Si_3O_8$ one. It was also noted that the T_c was broader in $Sr_{1.8}Ba_{0.2}Si_3O_8$ and $Sr_{1.8}Ca_{0.2}Si_3O_8$ than $Sr_2Si_3O_8$ meaning a slower crystallisation was occurring, which again suggested substitutions weren't aiding the crystallisation of $Sr_2Si_3O_8$. Experimentation on increasing $Sr_2Si_3O_8$ stability and crystallinity through substitutions therefore stopped, and nucleating agents were investigated instead.

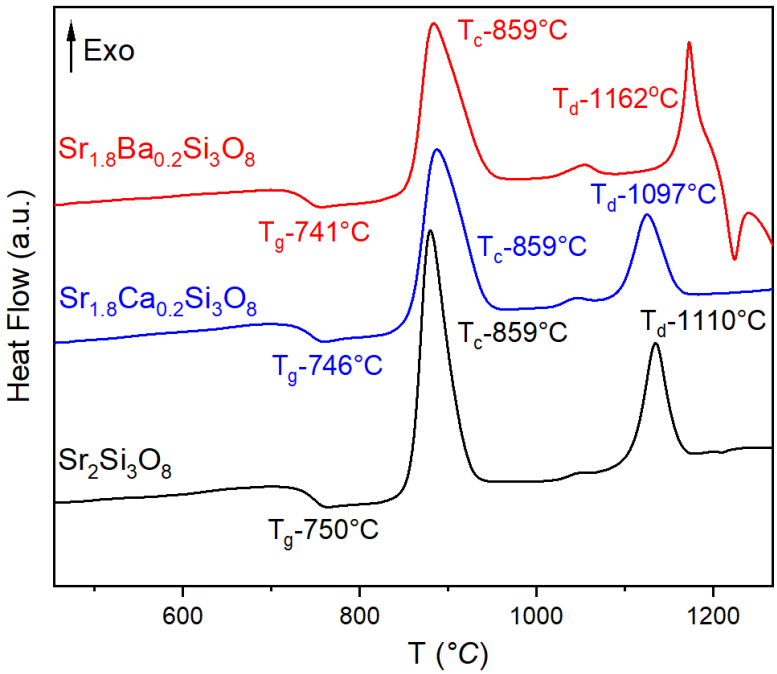

Fig. 3.16. DSC comparison of $Sr_2Si_3O_8$, $Sr_{1.8}Ca_{0.2}Si_3O_8$ and $Sr_{1.8}Ba_{0.2}Si_3O_8$ showing the decreasing T_g and stabilisation of the glassy phase.

3.5.6. ZrO_2 as a Nucleating Agent for $Sr_2Si_3O_8$ Crystallisation

Nucleating agents, such as ZrO_2, have been shown to increase the crystallinity of glass-ceramics, when they are added to the glassy matrix.[32,36] They provide an inert nucleating centre for crystal growth without being incorporated into the structure.[37,38] Nucleating agents have even been shown to improve transparency in samples by controlling domain and grain boundary sizes.[30] This could make them ideal for crystallising the residual glassy $Sr_2Si_3O_8$ phase while still retaining a phase-pure sample which could be functionalised and studied.

Experiments started with ZrO_2. Starting concentrations were based upon literature demonstrating that only 3-10wt.% of ZrO_2 is required to nucleate the crystallisation of Li_2O–Al_2O_3–SiO_2 glass.[31] Consequently, values of 3 and 7wt.% ZrO_2, based on the mass of glass being prepared, were initially chosen. For example, 1g of $Sr_2Si_3O_8$ precursor – nucleated by 3wt.% of ZrO_2 (99.999% Strem) – was prepared by adding 0.03g of ZrO_2 to the already weighed $SrSiO_3$ and SiO_2 precursor mixture. Glass was then made using the optimised melt-quenching method outlined in Section 3.2.1. Crystallised samples were then analysed by PXRD to determine the optimal nucleating %. While both samples had improved peak resolution (Fig. 3.17.(a)), the $Sr_2Si_3O_8$:7wt.%ZrO_2 sample showed the largest improvement compared to $Sr_2Si_3O_8$ and so experimentation continued at this value.

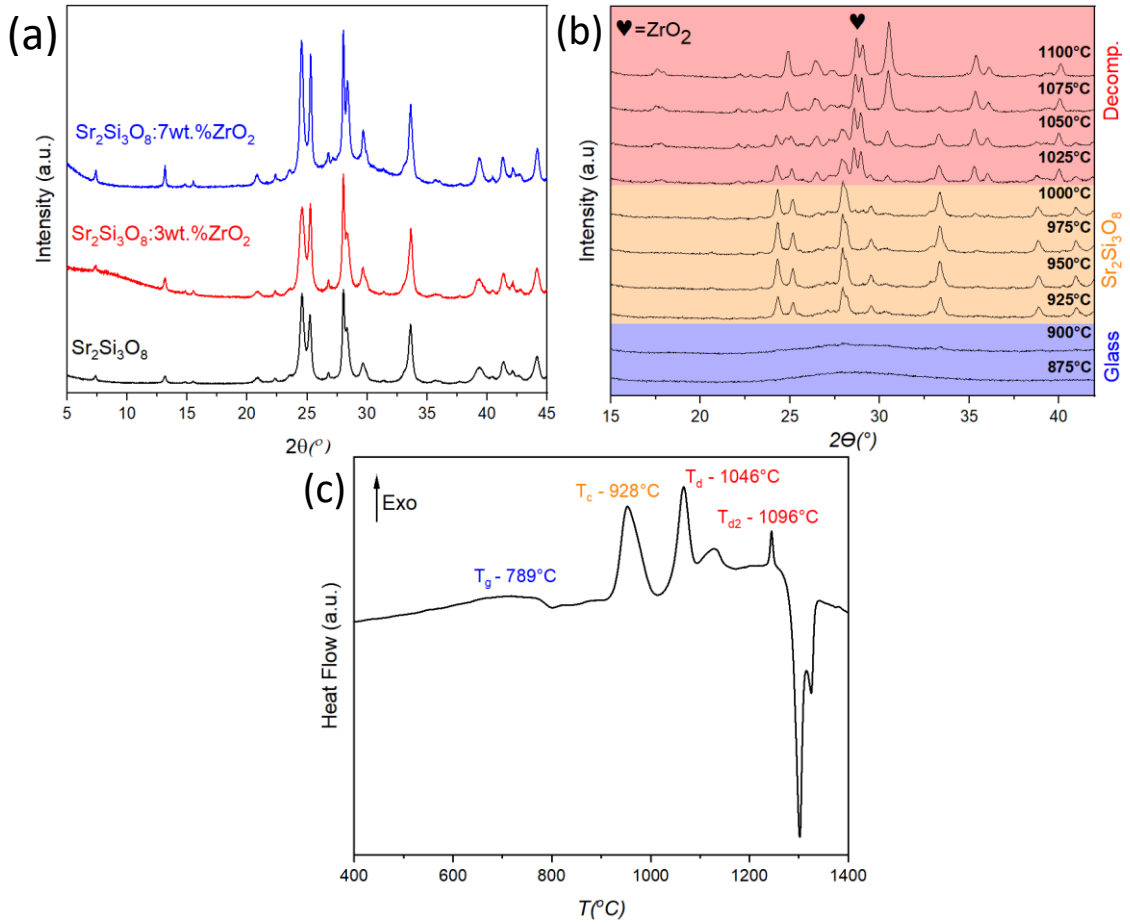

Fig. 3.17. (a) Comparison of the room temperature lab-PXRD patterns collected on powdered $Sr_2Si_3O_8$:7wt.%ZrO_2 and $Sr_2Si_3O_8$:3wt.%ZrO_2. Both were sintered at 850°C for 12h. **(b)** *In-situ* VTXRD of $Sr_2Si_3O_8$:7wt% ZrO_2. **(c)** DSC trace of $Sr_2Si_3O_8$:7wt% ZrO_2.

In-situ-VTXRD and DSC was conducted to see the effect nucleation had on the stability of $Sr_2Si_3O_8$, (Fig. 3.17(b)(c)). A large reduction in stability range was seen from both DSC and *in-situ* VTXRD, with ranges of 928–1046°C (DSC) and 925–1000°C (PXRD), now observed. This represented a reduction of 100°C on average, which was attributed to the crystallisation of monoclinic ZrO_2 ($P2_1/c$), now present in the glass. As shown in Fig. 3.17(a), the peaks at 29° which formed at 1025°C and above (Fig. 3.17.(b)), corresponded to ZrO_2 crystallisation. The DSC data showed this event occurring at 1046°C, meaning it now occurred before the decomposition of $Sr_2Si_3O_8$ (T_{d2}) which was observed at 1096°C in the DSC, thus reducing the phase-pure stability range of $Sr_2Si_3O_8$.

3.5.7. Rietveld Refinement of $Sr_2Si_3O_8$:7wt.% ZrO_2

Ex-situ crystallisations $Sr_2Si_3O_8$:7wt.% ZrO_2 glass were attempted for 12h at 850 and 875°C, to reflect the increased T_c temperature of this composition. In the 875°C crystallised sample, despite it appearing more crystalline, small peaks were observed which could be indexed to ZrO_2 ($P2_1/c$) (Appendix 2, A.3.25.). No

decomposition or ZrO_2 crystallisation was observed for the 850°C annealed sample and so the Rietveld method was applied to this sample, on lab PXRD data collected using the parameters outlined in Section 3.3.1.

The $Sr_2Si_3O_8$ ($P2_1/c$) model was used as the initial refinement file, this gave an excellent visual fit to the data, with R_{wp} of 5.620 % and χ of 1.949 (table of refined parameters shown in Appendix 2, T.3.6.). Making this the best refinement achieved so far, with peak resolutions comparable to the original $Sr_2Si_3O_8$:Al composition, as shown in Fig. 3.18.(a). This allowed the 'shoulder' at 28° (3, 0, -4) to again be modelled, which meant that ZrO_2 nucleation had produced a sample more faithful to the $P2_1/c$ model. The refined parameters of $Sr_2Si_3O_8$ and $Sr_2Si_3O_8$:7wt.% ZrO_2 were compared to explain this improvement (Appendix 2, T.3.2. & T.3.6.).

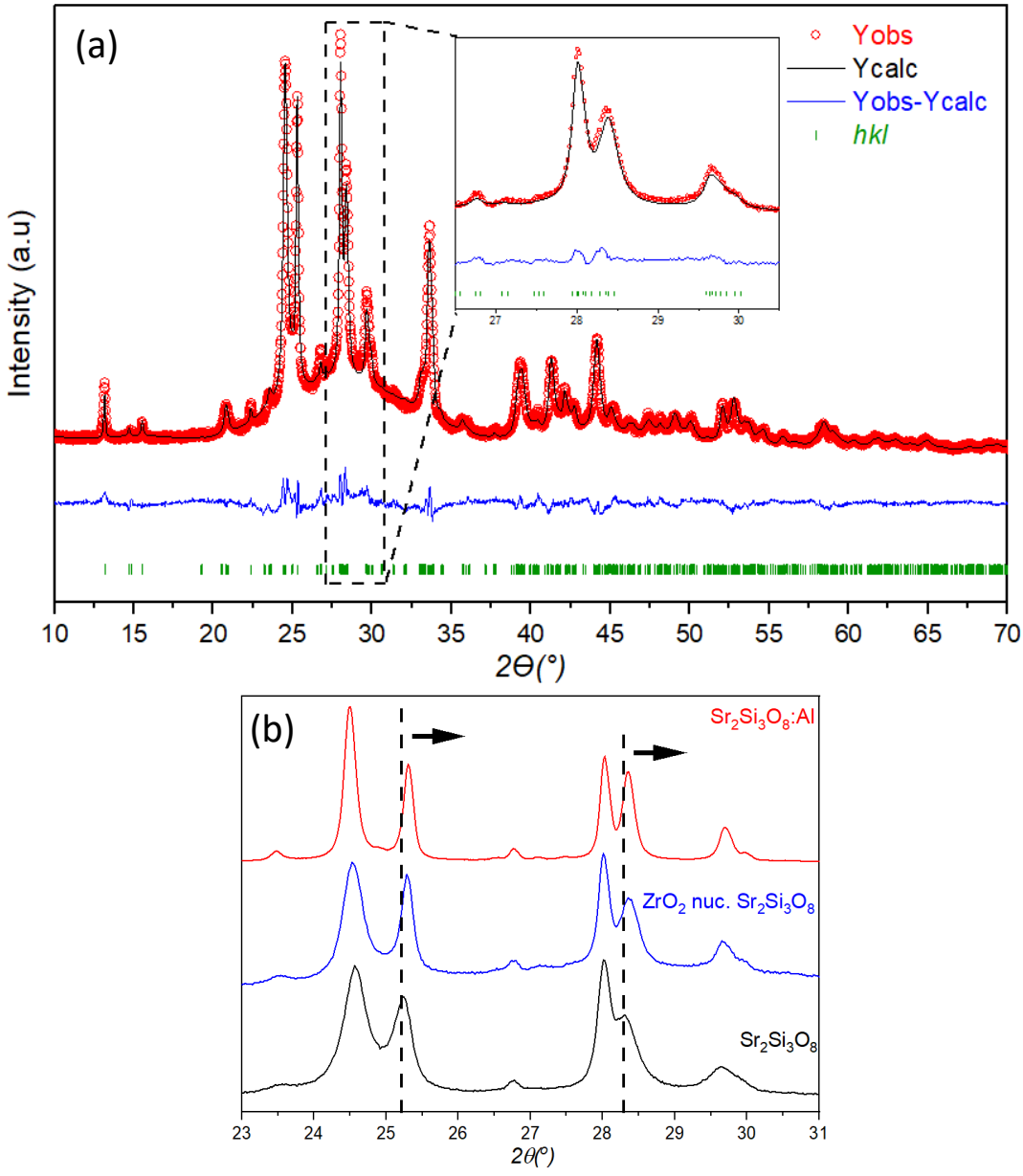

Fig. 3.18. (a) Lab-PXRD Rietveld refinement of 7wt.% ZrO_2 nucleated $Sr_2Si_3O_8$, R_{wp} = 5.620 % and χ = 1.949. **(b)** Comparison of $Sr_2Si_3O_8$, nuc. $Sr_2Si_3O_8$ and $Sr_{0.344}Al_{0.033}Si_{0.623}O_4$ showing the shift of the peaks at 25° (2, 0, 2) and 28° (3, 1, -2).

However, no significant difference in atomic positions was found to explain the observed shift to higher angles of the peaks at 25° (2, 0, 2) and 28° (3, 1, -2) in both the ZrO_2 and Al containing samples, Fig. 3.18.(b). At least, no differences in the lattice parameters or Sr-Si distances were observed, which strongly suggested that Zr^{4+} was not being incorporated into the structure.

Clearly, when $Sr_2Si_3O_8$ was crystallised in the presence of Al_2O_3 or ZrO_2 a more ordered structure was synthesised. However, this improvement in crystal quality by ZrO_2 nucleation was matched by a decrease in crystalline phase fraction, which is similar to the Al_2O_3-containing system. When analysed, the ZrO_2 nucleated sample was found to have a crystalline phase fraction of only 36wt.%, the lowest so far observed (Appendix 2, A.3.26.). SEM imaging of bulk crystallised samples (Appendix 2, A.3.27.), supported this by showing small flower shaped crystallites embedded within glassy matrixes. It was concluded, that while ZrO_2 nucleation improved $Sr_2Si_3O_8$ synthesis in regards to crystallinity and agreement with the $P2_1/c$ model, it also reduced phase stability to such a degree that the crystalline phase fraction of $Sr_2Si_3O_8$ dramatically decreased. Other nucleating agents were therefore investigated.

3.5.8. $AgNO_3$ as a Nucleating Agent for $Sr_2Si_3O_8$ Crystallisation

Ag in the form of $AgNO_3$, was also tried as a nucleating agent. While AgI is the common reagent for this, here $AgNO_3$ (99.97% Alfa) was used.[33,39,40] Again, 7wt.% based on the mass of precursor, was used for nucleation. The optimum synthesis of $AgNO_3$ nucleated $Sr_2Si_3O_8$ ($Sr_2Si_3O_8$:7wt.%$AgNO_3$) was found to be 12h at 850°C, from *in-situ* VTXRD, (Appendix 2, A.3.28.), and DSC analysis (Fig. 3.20.(a)). *In-situ* VTXRD showed that nucleation with $AgNO_3$ gave the same $Sr_2S_3O_8$ synthesis range of 850–1050°C as observed for the un-nucleated sample. This was in close agreement with the values obtained from DSC which showed T_c and T_d peaks of 838 and 1077°C respectively. Both DSC and *in-situ* VTXRD showed formation of the unknown intermediate phase described in Annex III, although to a lesser extent than that of the Ba^{2+} and Ca^{2+} doped samples.

When optimised $Sr_2Si_3O_8$:7wt.%$AgNO_3$ was scanned by PXRD and refined by the Rietveld method, a of R_{wp} 7.475 and χ of 3.829 was achieved and problems modelling the 'shoulder' were once again observed (refined parameters in Appendix 2, T.3.7.). In addition to this, intensity issues on the main doublet peaks (24°/25°), were also now observed, as shown in Fig. 3.19. The crystalline phase fraction was then found to be 71wt.%, (Appendix 2, A.3.29.), the highest out of all the substituted or nucleated samples tested so far, however, it still was less than the crystalline phase fraction achieved for pure $Sr_2Si_3O_8$, 89wt.%, on average. Interestingly, the crystallisation of $AgNO_3$ was never observed by *in-situ* VTXRD or DSC. However, no difference was observed in the lattice parameters of $Sr_2Si_3O_8$:7wt.%$AgNO_3$ and pure $Sr_2Si_3O_8$, which combined with the similar PXRD patterns and increased amorphous wt.% suggested that $AgNO_3$ wasn't acting as a nucleating agent and instead was likely being oxidised and dissolved into the glass as a modifier cation.

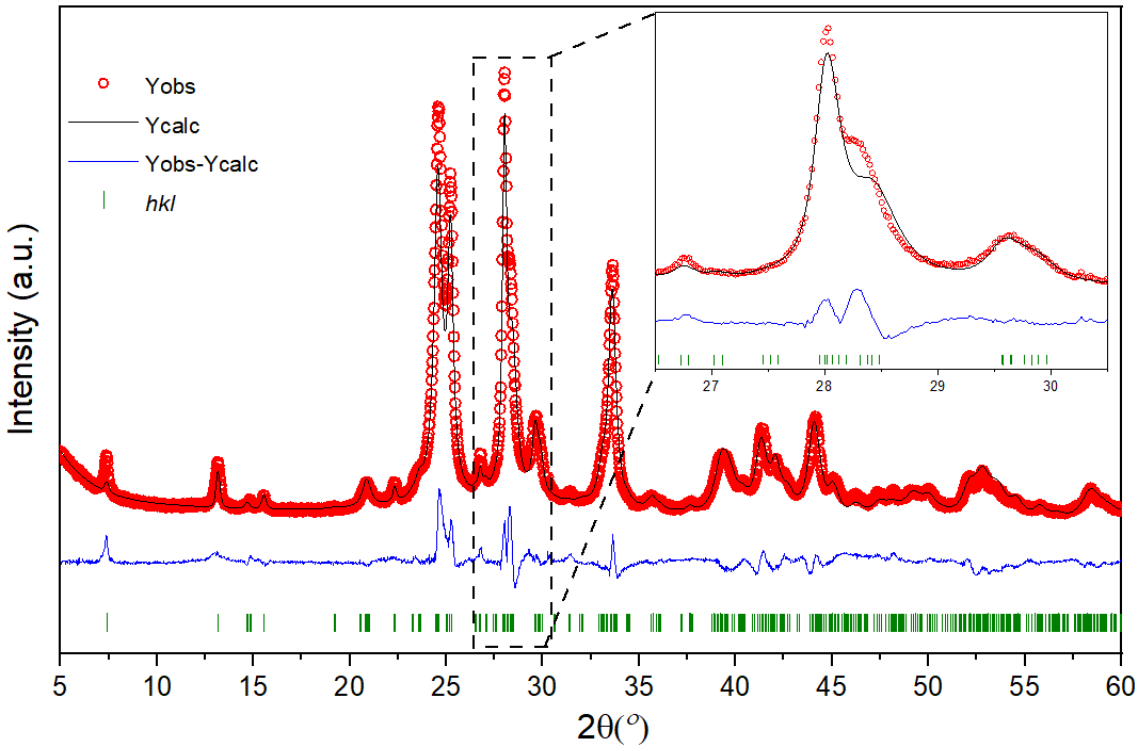

Fig. 3.19. Rietveld refinement achieved for $Sr_2Si_3O_8$:7wt.%$AgNO_3$, from lab-PXRD R_{wp} = 7.475 and χ =3.829. Inset shows a zoom of the refinement achieved on the 'shoulder' peak.

3.5.9. Summary of Substituents & Nucleating agents, Two Families of Behaviour

In addition to those already described, 7wt.%Au in the form of $HAuCl_4*3H_2O$, 7wt.% $TiZrO_4$ and 7wt.% P_2O_5 were also tested as nucleating agents. These results are not discussed here as they almost all had similar effects on $Sr_2Si_3O_8$ synthesis as Ba^{2+}/Ca^{2+} substitutions or $ZrO_2/AgNO_3$ nucleations. Although, in the case of nucleation by P_2O_5, phase indexations revealed that nucleation was causing $Sr_{10}(PO_4)_6$ ($P6_3/m$) to form as the major phase, (Appendix 2, A.3.30.). All additional samples had their synthesis optimised by a combination of *in-situ* VTXRD and DSC analysis, (*in-situ* VTXRD results shown in Appendix 2 A.3.31-34. And T.3.8.).

Two main families of behaviour were observed when the DSCs of all the samples were compared, as shown in Fig. 3.20.(a). Family A, contained the Ba^{2+}, Ca^{2+} substituents as well as the $AgNO_3$ and Au nucleating agents. This family either increased or maintained the same, ~250°C, stability window of $Sr_2Si_3O_8$ and produced similar PXRD patterns, with unresolved peaks. Unfortunately, these samples lowered the crystalline phase fraction of $Sr_2Si_3O_8$, with a 26wt.% decrease being observed, on average. As shown in Fig. 3.20.(b), this was believed to be due to these samples increasing the T_c-T_g gap and therefore stabilising the glassy phase rather than the crystalline one. These samples also failed to produce PXRD patterns with sharp Bragg peaks which could be refined by the $P2_1/c$ model and allow refinement of the 'shoulder' on the peak at 28° (3, 0, -4).

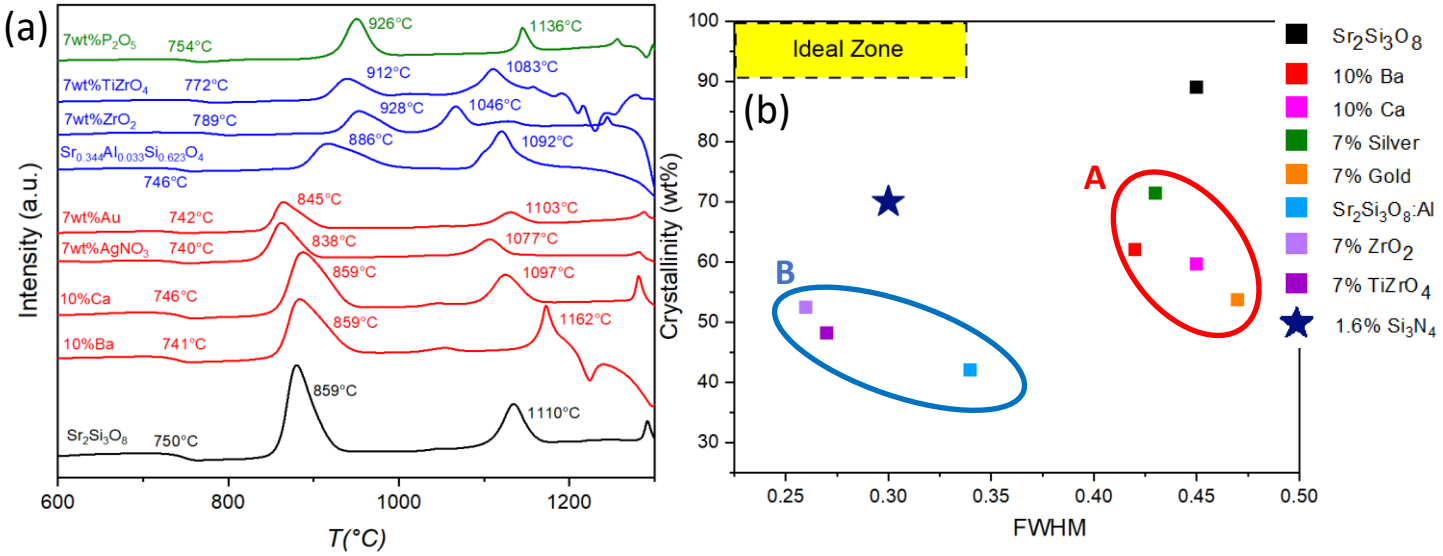

Fig. 3.20. (a) DSC comparison of all substituted and nucleated samples, family A in red, family B in blue. **(b)** Crystallinity vs. FWHM (peak at 33° (5, 0, -2)) of all the samples, family A (in red) & B (in blue), as well as the oxynitride sample discussed in the next section, the ideal zone of synthesis is marked in the yellow box.

This could not be linked to the lower crystalline phase fraction, as family B allowed this modelling but had an even lower crystalline phase fraction. Moreover, within a small temperature range, this family stabilised the unknown intermediate phase described in Annex III.

Family B, contained the original Al^{3+} containing phase and the other two nucleating agents, ZrO_2 and $TiZrO_4$. From DSC, (Fig. 3.20.(a)), it was seen that these samples increased the T_c of $Sr_2Si_3O_8$ by ~50°C, and decreased its T_d by ~86°C. A crystalline phase fraction of ~48wt.% was observed for these samples, due to this narrow stability range. However, this inversely corresponded to the sharpest and best resolved peaks in the PXRD patterns. The high-resolution allowed refinement of the 'shoulder' on the peak at 28° (3, 0, -4), with it almost being resolved as its own peak in these compositions. It was concluded that family B reduced disorder in $Sr_2Si_3O_8$, but also prevented samples with a high crystalline phase fraction being synthesised.

Ultimately, neither family A or B achieved all of their intended goals of increasing crystallinity, allowing a study of the properties in $Sr_2Si_3O_8$ and reducing disorder. As shown in Fig. 3.20.(b), the ideal zone for synthesis of $Sr_2Si_3O_8$ existed within a zone of low full width half maximum (FWHM) and high crystalline phase fraction. If achieved, it would allow $Sr_2Si_3O_8$ to be functionalised and its properties accurately studied.

3.6. Functionalisation of $Sr_2Si_3O_8$

A final method, oxynitride synthesis, was found in literature to achieve this ideal zone of synthesis for $Ba_4Si_6O_{16}$ and to enhance its EML properties when doped with rare-earths. This method was therefore attempted on $Sr_2Si_3O_8$ in collaboration with Patrick Houizot and Tanguy Rouxel at the University of Rennes.

The incorporation of nitrogen – oxynitride synthesis - into $Ba_4Si_6O_{16}$ glass had been shown by Duval *etS al*. to improve crystallinity and stability of the phase.[10,16] By replacing 2-fold coordinated O atoms with 3-fold coordinated N atoms in the glassy matrix, the number of interatomic linkages was increased. This improved the mechanical properties, the elastic moduli and increased the T_g range, of the glass. Which in turn improved the crystallisation kinetics of $Ba_4Si_6O_{16}$. The reagent used for N^{3+} substitution was Si_3N_4, incorporated by grinding the relevant precursors with Si_3N_4 and then melt-quenching them under N_2:H_2 (94:6) atmosphere to form a glass. When combined with rare earth (RE) co-doping, crystallised $Ba_4Si_6O_{16}$:Eu^{2+},Ho^{3+} was then shown to have enhanced ML properties, when prepared by this method.[16] The N^{3+} from Si_3N_4 leaves with the excess of Eu_2O_3 during the crystallisation step, reducing Eu^{3+} to Eu^{2+}.[41,42] Clearly, oxynitride synthesis was of great interest in answering the 2nd and 3rd research questions of this chapter, providing a route to both improved crystallinity and functionalisation of $Sr_2Si_3O_8$.

3.6.1. Partial Nitridation of $Sr_2Si_3O_8$ Glass

Experimentation started by optimising the incorporation of Si_3N_4 into $Sr_2Si_3O_8$. Based on the work of Duval *et al*. 1.6 mol% of Si_3N_4 powder was added to the glass precursors for a molar composition of $58.4SiO_2$-40SrO-$1.6Si_3N_4$. This powder was hand mixed in ethanol for 15 mins before being melted at 1650°C for 6h in a BN crucible. The molten sample was then cast and annealed at 700°C (T_g – 50°C) for 3h, to remove stress in the glass. This procedure was conducted in a specialised glove box, (4.1.3. Chapter 4), which permitted reactions to be conducted under an atmosphere - N_2:H_2 (94:6) in this case and prevented the loss of N atoms from the melt. This explained the use of a BN crucible, as Pt ones had been shown to form alloys under reducing atmospheres. Any subsequent BN which formed on the surface of the glass was polished off before crystallisation. PXRD analysis of the glass showed that a pure amorphous phase had been synthesised and so annealings were conducted.

The synthesis of $Sr_2Si_3O_8$ was optimised as both a bulk and pelletised powder sample, the Rietveld refinement achieved for the bulk sample is shown in Fig. 3.21.(a). Sinterings were conducted in Pt crucibles and open-air furnaces, with fixed times of 12h, to reduce the number of variables. The temperature was varied every 100°C between 650-850°C, as a reduction in the T_c and T_d was expected due to the incorporation of 3-fold coordinated N^{3+}, a strong network former. As expected, PXRD analysis of the bulk sample, crystallised at 850°C, showed a significant $SrSiO_3$ (*C*2/*c*) content, 21wt.% from Rietveld refinement. The pelletised sample

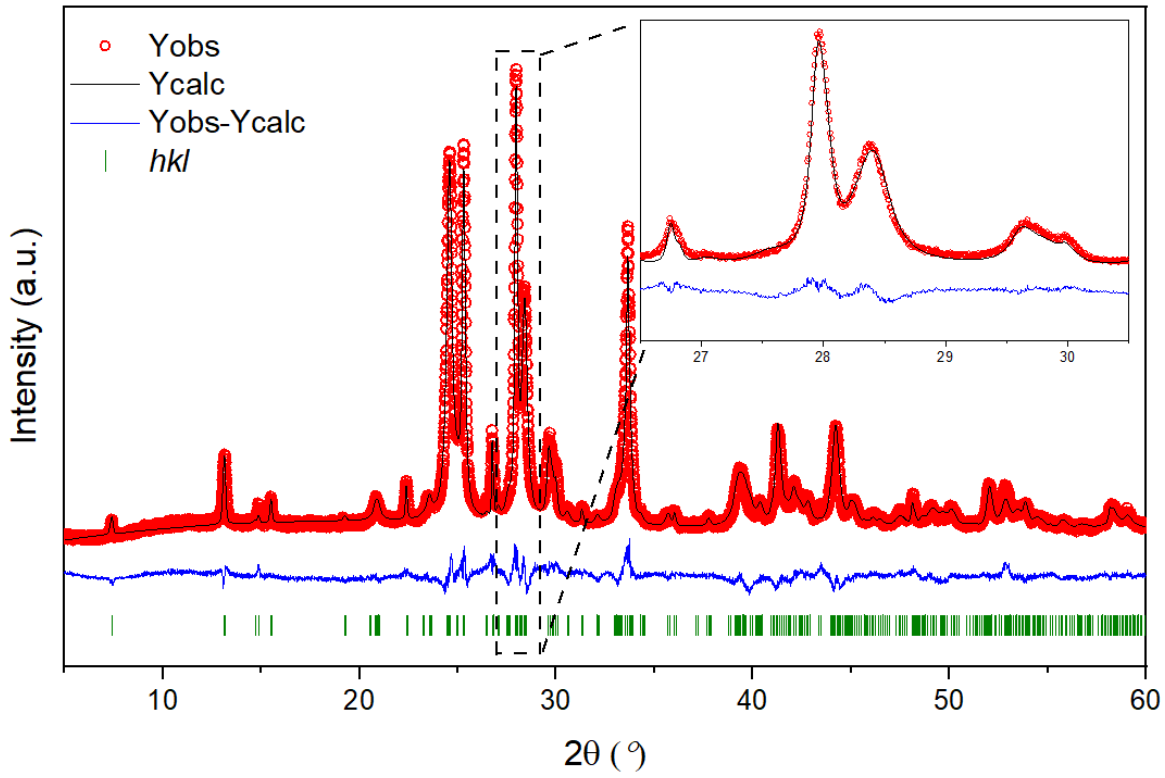

Fig. 3.21. (a) Rietveld refinement achieved for 1.6% Si_3N_4 $Sr_2Si_3O_8$ (12h at 800°C), R_{wp} = 11.332% and χ = 1.89. Inset shows a zoom of the refinement achieved on the 'shoulder' peak. **(b)** Updated Crystallinity vs. FWHM (peak at 33°) graph.

only formed $SrSiO_3$, with no $Sr_2Si_3O_8$ detected. At 650°C no crystallisation was observed, while at 750°C small crystallites were observed forming. Crystallisation at 800°C was therefore attempted, with a single-phase high crystallinity bulk sample of $Sr_2Si_3O_8$ being achieved, as shown in Fig. 3.21.(a). In the pelletised sample crystallised at 800°C for 12h a higher content of $SrSiO_3$, 21wt.%, was observed, which was reasoned to be due faster crystallisation kinetics from the increased surface are.[19] This resulted in a lower decomposition temperature in the powdered samples, due to their much larger surface area compared to the bulk samples. The bulk sample was then crushed and PXRD scanned using the high-resolution parameters discussed in Section 3.3.1. The data was analysed with the Rietveld method and TOPASV7 software, so that its crystallinity and FWHM could be compared to the others, indicated by the star in Fig. 3.20.(b). The same refinement file used in Section 3.3.1. was used, which achieved a R_{wp} of 7.332% and χ of 1.894. The Stephens macro for anisotropic peak broadening wasn't needed for the 'shoulder' to be modelled.

This, along with the good peak resolution of the sample, suggested that oxynitride synthesis had aided in the crystallisation of $Sr_2Si_3O_8$. Combined with Fig. 3.20.(b), it could be said that oxynitride synthesis had produced a sample with a comparable peak resolution to family B but the crystalline phase fraction of family A. This promising result motivated further research, i.e. doping the phase with Eu^{2+} and Dy^{3+} to study its ML properties.

3.6.2. Partial Nitridation of $Sr_2Si_3O_8$ Glass with 1%Eu^{2+}/1.5%Dy^{3+} Doping

To study the potential mechanoluminescent (ML) properties of $Sr_2Si_3O_8$, the phase had to be doped with lanthanides. Here, Eu_2O_3 and Dy_2O_3 were doped for SrO giving a new molar formula of 58.4SiO_2-37.5SrO-1.6Si_3N_4-1Eu_2O_3-1.5Dy_2O_3. The Eu^{2+} and Dy^{3+} doping levels were based on the current leading ML phase, $SrAl_2O_4$:1%Eu^{2+},1.5%Dy^{3+}.[10,12,43] The same optimised oxynitride glass synthesis procedure and crystallisation, 12h 800°C, was then used on both bulk and pellet samples. Si_3N_4 in the glass, is proposed to act as a reducing agent, reducing Eu^{3+} into Eu^{2+}, through the reaction – Si_3N_4 + 6Eu_2O_3 → 12EuO + 3SiO_2 + 2N_2 (gas).[16]

The addition of lanthanides was less favourable as the crystallisation of another side product, $Sr_3Ln_2Si_6O_{18}$ (*C*2/*c*) Ln = Eu^{2+} or Dy^{3+}, was now observed in addition to $SrSiO_3$ contents of 7.33% and 2.07% for bulk and pelletised sintering's respectively.[44] As shown in Fig. 3.22., 1%Eu^{2+}/1.5%Dy^{3+} doping reduced $SrSiO_3$ formation in the powder sample but $Sr_3Ln_2Si_6O_{18}$ was still present. Other sintering temperatures were attempted but 12h at 800°C still gave the best crystallisation, with $Sr_2Si_3O_8$ as the majority phase.

To reduce side product formation, the mass of Si_3N_4 added was doubled to 3.2%, encouraging the complete reduction of Eu_2O_3 and preventing $Sr_3Ln_2Si_6O_{18}$ formation. However, it failed to achieve these aims, with unincorporated Eu^{2+} and quartz now also indexable in the pattern. It was decided to send both bulk and pelletised samples of 1.6% Si_3N_4 $Sr_2Si_3O_8$, crystallised for 12h at 800°C, to Rennes so that that the ML properties of $Sr_2Si_3O_8$ could be studied through comparison of the spectra.

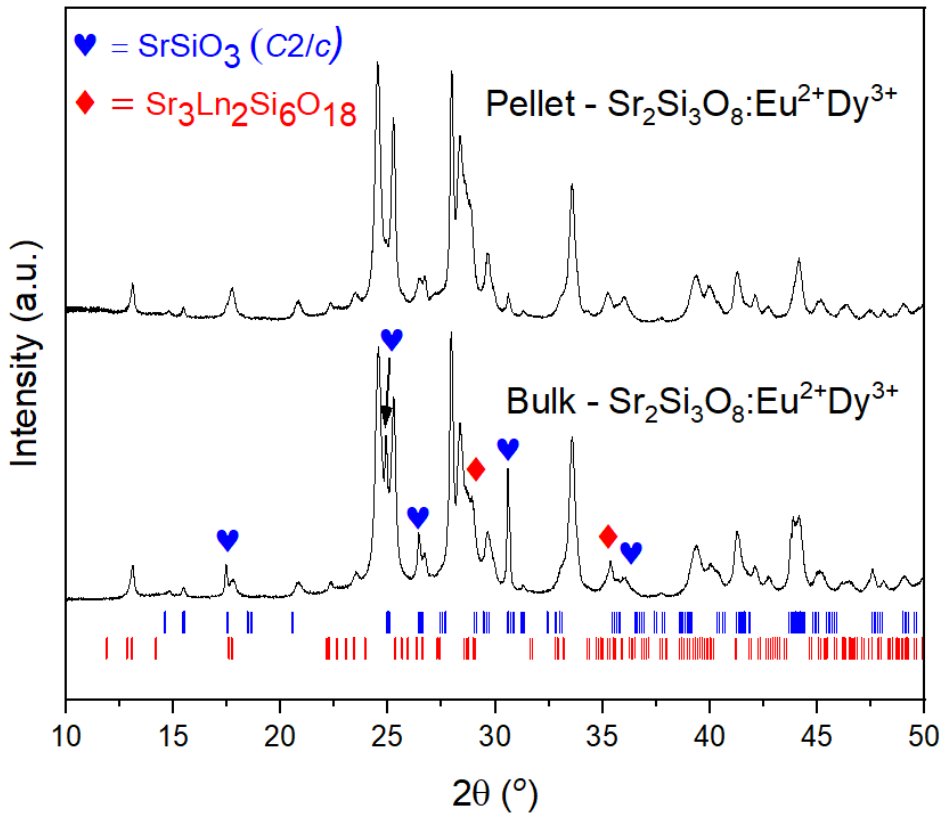

Fig. 3.22. Comparison of the PXRD patterns obtained for bulk and pelletised powder samples of 58.4SiO_2-37.5SrO-1.6Si_3N_4-1Eu_2O_3-1.5Dy_2O_3, crystallised for 12h at 800°C, with the impurities marked.

3.6.3. Mechanoluminescent Properties of $Sr_2Si_3O_8$

A bulk sample and large pellet were cut and polished to make parallelepiped of size 4(width) × 4(depth) × 4.5(height) mm^3, this was necessary for an even compression force to be applied in the ML experiments. It was necessary to measure the elastic-ML (EML) properties of both samples as the impurity phase, $SrSiO_3:Eu^{2+}$, was reported to have EML properties.[45] The second impurity, $Sr_3Ln_2Si_6O_{18}$, is reported to have PL properties but not EML ones.[44] It was reasoned that if the same EML spectra were recorded for both samples then, it could be said that $Sr_2Si_3O_8$ was responsible for the EML emission. Due to the powder crystallised sample containing less $SrSiO_3$ than the bulk one, 2.07% vs. 7.33%, (Fig. 3.22.).

The experimental setup for ML tests is described in Section 4.7.2. of Chapter 4. When this was applied to both samples, the spectra shown in Fig. 3.23. were recorded. Before measurement samples were irradiated with 354 nm UV radiation for 30s, to charge the Eu^{2+} and Dy^{3+} traps, when charged green PL emission was noted. The rapid decay of the PersL emission is visible in the spectra, when the charging was stopped, time 0s. It was noticed that the decay of the pelletised samples emission was much faster than the bulk sample, suggesting a faster emptying of traps in this sample (4.7.2. Chapter 4). The EML response can clearly be distinguished from the PersL emission as an increase in the PersL intensity at 105 and 54s respectively. This effect was caused by a diametral compression of 140 MPa being applied for 10s to the samples, no change in ML intensity was visible over this time. In the pelletised sample, which contained a higher content of $Sr_2Si_3O_8$ crystals, a slightly larger EML response can be seen, suggesting that the EML response is due to $Sr_2Si_3O_8$ and not secondary phase. After the compression was released, trap depths returned to their normal states, as seen by the PL intensity returning to its previous rate of decay.

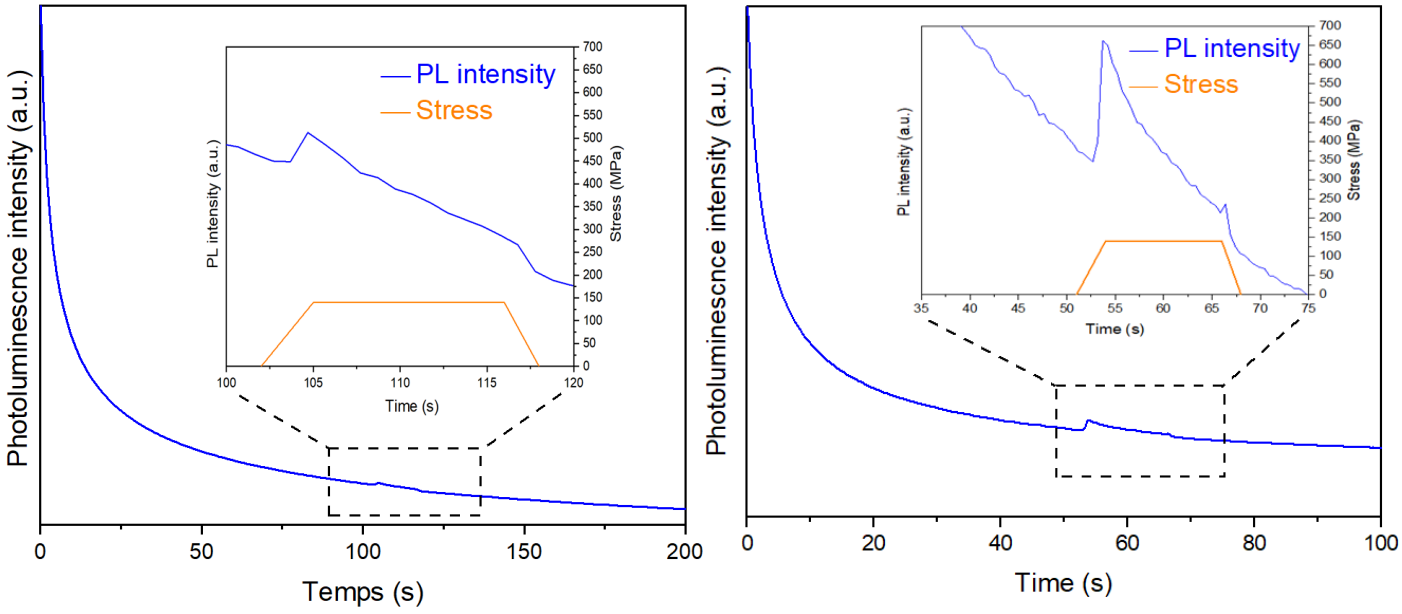

Fig. 3.23. (a) EML response of impure bulk $Sr_2Si_3O_8:Eu^{2+},Dy^{3+}$ glass-ceramic. **(b)** EML response of pelletised $Sr_2Si_3O_8:Eu^{2+},Dy^{3+}$ glass-ceramic.

This highlighted the elastic nature of the EML response in $Sr_2Si_3O_8$; trap depths could be altered through compression and returned to normal when the compression was removed. It is believed that this change in trap depth distribution is what causes the increase in luminescence intensity.

Quantitative comparison of luminescent phenomena is extremely difficult, due to differing quantum yield efficiencies, excitation wavelengths and crystallinities between samples.[46] Qualitatively however, it was noted by eye that the ML intensity of the bulk $Sr_2Si_3O_8:Eu^{2+},Dy^{3+}$ sample was comparable to that of $Ba_4Si_6O_{16}:Eu^{2+},Ho^{3+}$. Therefore, given the room for optimisation of $Sr_2Si_3O_8:Eu^{2+},Dy^{3+}$, e.g. removal of secondary phase, increase crystallinity/crystalline phase fraction and Ln doping concentrations/elements etc. This phase could be a valuable green light ML material for stress sensor applications, although maybe to less of a degree than $Sr_{12}Al_{20}Si_{12}O_{66}$ discussed in Chapter 2, as visually the EML intensity of this phase was much higher.

3.7. Chapter Conclusion & Perspectives

In this chapter the synthesis and optimisation of $Sr_2Si_3O_8$ was investigated by the innovative method GC. The objectives were to synthesise $Sr_2Si_3O_8$ by congruent crystallisation of its binary parent glass $40SrO\text{-}60SiO_2$, the optimisation of the synthesis protocol to produce high quality phase-pure samples, and the functionalisation of the compound to explore possible applications (Eu^{2+}/Ho^{3+} doping for ML, by analogy with $Ba_4Si_6O_{16}$). While the first objective was readily achieved, the second and third objectives were highly challenging due to the intrinsic thermal instability of $Sr_2Si_3O_8$. After structural determination it was realised that the phase could be synthesised from the binary, $40SrO\text{-}60SiO_2$, line. GC from this composition was optimised by *in-situ* VTXRD and DSC measurements. These measurements highlighted the metastability of $Sr_2Si_3O_8$ by showing its decomposition into $SrSiO_3$ ($C2/c$) and SiO_2 (amorphous quartz) at ~1075°C. An optimum GC of 12h at 850°C was found which yielded a homogeneous glass-ceramic with an approximate crystallinity of 89wt.%. Unfortunately, GC from $40SrO\text{-}60SiO_2$ glass caused a shift in certain peak positions, (25° (2, 0, 2) and 28° (3, 1, -2), which could not be modelled by a simple refinement of the unit cell parameters (or by re-indexation). This implied a departure from the average unit cell, which could, for example, be caused by extended defects (stacking faults, shear planes) in the crystal structure. HAADF-STEM measurements were conducted to view and model the cause of this defect, however the instability of $Sr_2Si_3O_8$ under the electron beam prevented the necessary atomic level resolution.

To increase stability, crystalline phase fraction and crystallinity of $Sr_2Si_3O_8$ and permit a properties study, substitutions, Ba^{2+} and Ca^{2+}, and nucleating agents, ZrO_2 and Ag, were investigated. Two different families of behaviour were observed by these substitutions/additions. Family A maintained the same ~250°C synthesis range (between glass crystallisation and thermal decomposition temperatures) but lowered the crystalline phase fraction by ~26wt.% from the 89wt.% achieved by $Sr_2Si_3O_8$. They also increased disorder and lowered

peak resolution resulting in harder to model PXRD patterns. Interestingly, these phases also yielded an un-indexable intermediate phase between 1025-1100°C. Family B lowered both crystalline phase fraction and the stability by, 41wt.% and 50°C on average, respectively. Inversely, these samples drastically improved peak resolution and Rietveld modelling of $Sr_2Si_3O_8$. An ideal zone of $Sr_2Si_3O_8$ synthesis was proposed which combined high crystalline phase fraction with well resolved peaks.

Oxynitride synthesis was the final technique tested to achieve synthesis in this zone. It was found to increase peak resolution, allowing for modelling of $Sr_2Si_3O_8$ with the $P2_1/c$ cell. Eu^{2+} and Dy^{3+} doping was then combined with oxynitride synthesis to study the ML properties of $Sr_2Si_3O_8$:Eu^{2+},Dy^{3+}. However, the dopants introduced secondary phase crystallisation of $Sr_3Ln_2Si_6O_{18}$ ($C2/c$) Ln = Eu^{2+} or Dy^{3+} and $SrSiO_3$ ($C2/c$). These impurities were minimised in bulk and powdered samples so that ML measurements could be conducted. $Sr_2Si_3O_8$ was indeed found to have green emitting ML properties, with a comparable emission to the known $Ba_4Si_6O_{16}$:Eu^{2+},Dy^{3+} phase.

Overall, the results presented here demonstrate that it is challenging to synthesise high quality samples of $Sr_2Si_3O_8$ by glass crystallisation synthesis, but despite these difficulties it is still possible to introduce mechanoluminescence into this system, which remains a rare phenomenon. Future research should be focussed on achieving highly crystalline, pure samples of $Sr_2Si_3O_8$ using the oxynitride synthesis method, as well as potentially solution-based ones which have been used to produce metastable $SrSiO_3$.[47] The removal of secondary phases and an increase in crystallinity would only boost the ML performance of $Sr_2Si_3O_8$. Other Ln dopants (Ho^{3+}, Pr^{3+} and Nd^{3+} for example) should also be investigated as a means to tuning the colour and intensity of the ML emission. Any tuneability of the phase would increase its interest as an EML phase.

3.8. References

[1] C. Collins, M. S. Dyer, M. J. Pitcher, G. F. S. Whitehead, M. Zanella, P. Mandal, J. B. Claridge, G. R. Darling and M. J. Rosseinsky, *Nature*, 2017, **546**, 280–284.

[2] C. Collins, G. R. Darling and M. J. Rosseinsky, *Faraday Discuss.*, 2018, **211**, 117–131.

[3] M. Kimata, 1983, **163**, 295–304.

[4] G. Chiari, M. Calleri, E. Bruno and P. Ribbe, *American Mineralogist*, 1975, **Am. Mineral.**, 111–119.

[5] A. J. Fernandez-Carrion, K. Al Saghir, E. Veron, A. I. Becerro, F. Porcher, W. Wisniewski, G. Matzen, F. Fayon and M. Allix, *Inorg. Chem.*, 2017, **56**, 14446–14458.

[6] E. M. Duncan, A. Ridouard, F. Fayon, E. Veron, C. Genevois, M. Allix, C. M. Collins and M. J. Pitcher, *Chem. Commun.*, 2023, **59**, 10544–10547.

[7] *I: Refinement of the crystal structures of Ba4[Si6O16], Ba5[Si8O21] and Ba6[Si10O26], silicates with triple, quadruple and quintuple chains*, 1980, **153**, 3–17.

[8] K. Momma and F. Izumi, *Journal of Applied Crystallography - J APPL CRYST*, 2008, **41**, 653–658.

[9] J. Deubener, M. Allix, M. J. Davis, A. Duran, T. Höche, T. Honma, T. Komatsu, S. Krüger, I. Mitra, R. Müller, S. Nakane, M. J. Pascual, J. W. P. Schmelzer, E. D. Zanotto and S. Zhou, *Journal of Non-Crystalline Solids*, 2018, **501**, 3–10.

[10] A. Duval, Y. Suffren, M. Benabdesselam, P. Houizot and T. Rouxel, *The Journal of Chemical Physics*, 2023, **159**, 134501.

[11] M. Chen, Z. Xia, M. S. Molokeev and Q. Liu, *J. Mater. Chem. C*, 2015, **3**, 12477–12483.

[12] R. E. Rojas-Hernandez, F. Rubio-Marcos, M. Á. Rodriguez and J. F. Fernandez, *Renewable and Sustainable Energy Reviews*, 2018, **81**, 2759–2770.

[13] S. Tomé-Torquemada, B. Glaser and D. Sichen, *Journal of the European Ceramic Society*, 2018, **38**, 3354–3360.

[14] J. E. Shelby, *Introduction to Glass Science and Technology*, The Royal Society of Chemistry, 2005.

[15] R. E. Marsh and F. H. Herbstein, *Acta Crystallographica Section B*, 1983, **39**, 280–287.

[16] A. Duval, P. Houizot, X. Rocquefelte and T. Rouxel, *Applied Physics Letters*, 2023, **123**, 011905.

[17] H. M. Rietveld, *J Appl Crystallogr*, 1969, **2**, 65–71.

[18] L. B. McCusker, R. B. Von Dreele, D. E. Cox, D. Louër and P. Scardi, *J Appl Crystallogr*, 1999, **32**, 36–50.
[19] T. Runčevski, *Journal of Applied Crystallography*, DOI:10.1107/S1600576719011178.
[20] P. W. Stephens, *Journal of Applied Crystallography*, 1999, **32**, 281–289.
[21] N. Behmanesh, S. Heshmati-Manesh and A. Ataie, *Journal of Alloys and Compounds*, 2008, **450**, 421–425.
[22] X. Fang, V. Castaing, A. Becerro, W. Cao, E. Veron, D. Zanghi, M. Dyer, C. Genevois, M. Allix and M. Pitcher, 2024, preprint, DOI: 10.26434/chemrxiv-2024-1s1wc.
[23] M. Gonon, S. Satha, T. Zanin, H. Satha and S. Abdelouhab, *Ceramics*, 2023, **6**, 1–15.
[24] W. Holand and G. H. Beall, *Glass Ceramic Technology*, Wiley, 2012.
[25] X. Zhi and A. R. West, *Chem. Mater.*, 2023, **35**, 6790–6798.
[26] A. Jabbarzadeh and B. Halfina, *Nanoscale Adv.*, 2019, **1**, 4704–4721.
[27] C. Qin, H. Wang, X. Yuan, T. Xiong, J. Zhang and J. Zhang, *Chemical Engineering Journal*, 2020, **382**, 122977.
[28] U. V. Shah, Z. Wang, D. Olusanmi, A. S. Narang, M. A. Hussain, M. J. Tobyn and J. Y. Y. Heng, *International Journal of Pharmaceutics*, 2015, **495**, 234–240.
[29] C. C. Chou, K. C. Feng, I. P. Raevski, H. Chen, C.-Y. Tsao, P.-Y. Chen, C.-S. Chen, C.-A. Lu and C.-S. Tu, *Materials Research Bulletin*, 2017, **96**, 66–70.
[30] W. Xu, X. Tian, J. Wang, L. Li and J. Han, *Ceramics International*, 2024, **50**, 23150–23156.
[31] E. Kleebusch, C. Patzig, T. Höche and C. Rüssel, *Journal of Materials Science*, 2016, **51**, 10127–10138.
[32] A. Shearer, M. Montazerian, B. Deng, J. J. Sly and J. C. Mauro, *International Journal of Ceramic Engineering & Science*, 2024, **6**, e10200.
[33] J. R. Morones and W. Frey, *Langmuir*, 2007, **23**, 8180–8186.
[34] N. Zulumyan, A. Isahakyan, H. Beglaryan, S. Melikyan and A. Terzyan, *Journal of Thermal Analysis and Calorimetry*, DOI:10.1007/s10973-019-08035-9.
[35] W. L. S. Bragg, Proc. Camb. Phil. Soc., XVII (I), 1912, pp. 43-57.
[36] E. Kleebusch, C. Patzig, T. Höche and C. Rüssel, *Ceramics International*, 2017, **43**, 9769–9777.
[37] E. Kleebusch, C. Patzig, M. Krause, Y. Hu, T. Höche and C. Rüssel, *Scientific Reports*, 2018, **8**, 2929.
[38] E. Kleebusch, C. Patzig, M. Krause, Y. Hu, T. Höche and C. Rüssel, *Scientific Reports*, 2017, **7**, 10869.
[39] J. Zhang, D. Jin, L. Zhao, X. Liu, J. Lian, G. Li and Z. Jiang, *Advanced Powder Technology*, 2011, **22**, 613–616.
[40] C. Thieme, M. Kracker, K. Thieme, C. Patzig, T. Höche and C. Rüssel, *CrystEngComm*, 2019, **21**, 4373–4386.
[41] Alexis Duval. Elaboration, structure and mechanical characterization of oxynitride glasses and mechanoluminescent glass-ceramics from the BaO-SiO_2-Si_3N_4 chemical system. 2023.
[42] A. Duval, P. Houizot and T. Rouxel, *J Am Ceram Soc.*, 2023, **106**, 1611–1637.
[43] M. Dubernet, Y. Gueguen, P. Houizot, F. Célarié, J.-C. Sangleboeuf, H. Orain and T. Rouxel, *Applied Physics Letters*, 2015, **107**, 151906.
[44] A. P. Tyutyunnik, I. I. Leonidov, L. L. Surat, I. F. Berger and V. G. Zubkov, *Journal of Solid State Chemistry*, 2013, **197**, 447–455.
[45] I. P. Sahu, D. P. Bisen, R. K. Tamrakar, K. V. R. Murthy and M. Mohapatra, *Journal of Science: Advanced Materials and Devices*, 2017, **2**, 59–68.
[46] G. Gauglitz, in *Photochromism*, eds. H. Dürr and H. Bouas-Laurent, Elsevier Science, Amsterdam, 2003, pp. 15–63.
[47] A. Ueno, S. Hayashi, K. Okada and N. Ōtsuka, *Journal of Materials Science Letters*, 1991, **10**, 9–12.

General Conclusion & Perspectives

General Conclusion & Perspectives

The principal objective of this PhD work was to further explore the potential for non-equilibrium synthesis methods – notably the crystallisation of glass precursors – for the discovery of new metastable inorganic oxides (glass-ceramics & ceramics) with the potential to be functionalised into useful materials. In particular, the SrO-$AlO_{1.5}$-SiO_2 ternary diagram was investigated for its potential to host such materials, due to its large glass-forming domain and its demonstrated capacity to support interesting optical properties, with examples such as ($SrAl_2O_4$:Eu^{2+},Dy^{3+} and $Sr_{1+x/2}Al_{2+x}Si_{2-x}O_8$) already known to exist within this phase space. For the same reason, optical properties such as persistent luminescence (PersL), and mechanoluminescence (ML) were targeted in the functionalisation of any discovered phases, while the possibility of producing transparent glass-ceramics and ceramics of these compositions means that the volume effect (i.e., light emission and absorption from the full volume of the sample rather than just its surface) offers a route to enhance PersL and ML performance in bulk samples, as well as extend their functional capabilities. Microstructural engineering techniques, such as full and congruent glass crystallisation and the orientation of crystallites, were explored as potential routes to elucidate transparency in systems where it was otherwise challenging.

In the first part of this work, Chapter 2, the synthesis of a previously discovered metastable phase, $SrAl_2SiO_6$ (*Pmc*2_1), was investigated. This phase was identified as the structural 'missing link' between two previously studied solid solutions, ($Sr_{1-X/2}Al_{2-2X}Si_XO_4$ and $Sr_{1+x/2}Al_{2+x}Si_{2-x}O_8$), although its phase-pure synthesis had never been achieved. Developing a phase-pure synthesis protocol for $SrAl_2SiO_6$ became the initial aim of this chapter. This was successfully achieved, through DSC and *in-situ* VTXRD analysis, which revealed a phase-pure powdered ceramic GC synthesis protocol of 1h at 1050°C, subsequently this enabled functionalisation and a properties study to be conducted. Optical properties were targeted in the functionalisation of both powdered and bulk samples, by doping 1mol% Eu^{2+}/ Dy^{3+} into the structure. In the bulk samples, optical properties were enhanced by synthesising a transparent glass-ceramic sample (~15 mm Ø x 2 mm) by partial crystallisation of the samples surface. This sample displayed transparency from the glass as well as luminescent properties from the crystalline layer. The depth of the crystalline layer (11.5 μm) and orientation of the crystallites was examined by SEM, with moderate domain orientation being observed. This led to the belief that transparency could be increased by achieving a higher degree of crystallite orientation on the surface. Once synthesis of the doped samples had been optimised, optical properties (PersL & PL) were qualitatively observed under a UV lamp which inspired quantitative analysis of the properties at the CSIC in Seville.

This promising region of the SrO-$AlO_{1.5}$-SiO_2 diagram, along with the potential existence of $SrAl_2SiO_6$ as part of a solid solution, warranted further investigation, leading to the discovery of a second metastable phase, $Sr_{12}Al_{20}Si_{12}O_{66}$. The phase's novelty was confirmed by PXRD analysis and comparison with the PDF+5

database, as the peak positions and intensities couldn't be indexed to any known phases. Synthesis optimisation and structural determination of $Sr_{12}Al_{20}Si_{12}O_{66}$ formed the second and major aim of this chapter.

The necessary high-resolution diffraction data for structural determination to be conducted was collected on an optimised sample from a non-nominal formula, using NPD and SPD sources. From a combined auto-indexation of these datasets, possible space groups and initial cell parameters were identified, the Pawley method was then used to provide refined cell parameters. A charge-flipping (CF) approach, complemented by Rietveld refinement, was then use to build structural models based on these space groups and cell parameters and find the best solution. From this analysis the nominal formula of $Sr_{12}Al_{20}Si_{12}O_{66}$ was found, which could be described by the $P6_3$ space group. Again, *in-situ* VTXRD and DSC analysis aided in the development of phase-pure (or single crystalline phase) synthesis protocols from this structurally determined formula, with powdered and bulk ceramic synthesis as well as bulk transparent glass-ceramic synthesis all being achieved. Atomic-resolution HAADF-STEM (High angle annular dark field scanning transmission electron microscopy) imaging of a thin foil bulk ceramic sample confirmed the structurally determined model as the unit cell could be perfectly superimposed on the observed images. Despite the 'probe structure' method not being the original inspiration for the discovery of $Sr_{12}Al_{20}Si_{12}O_{66}$, later comparison of the structurally determined formula to the computationally generated heat map found that $Sr_{12}Al_{20}Si_{12}o_{66}$ existed within a local minimum of the diagram. Proving the effectiveness of this method.

From the solved formula, two phase-pure powdered ceramic synthesis protocols were developed. The first, (48h at 1150°C), led to phase purity by giving the crystalline frameworks Al^{3+}/Si^{4+} sites sufficient time to relax to their equilibrium positions. The second (1h at 1150°C) was based on EDS measurements, which revealed a slight excess of Si^{4+} in the impurity phases. When this excess (4mol% Si^{4+}) was removed from the formula, phase-pure powdered ceramic synthesis was achieved by a much shorter annealing time.

Topological analysis of the phase then revealed it to be structurally analogous with a known phase, ($Ba_{13}Al_{22}Si_{10}O_{66}$). This raised questions about $Sr_{12}Al_{20}Si_{12}o_{66}$ existing as part of a solid solution and its structural flexibility to Ba^{2+} and Ca^{2+} substitutions. These questions were successfully answered, with three solid solutions being discovered, according to the formulae $Sr_{12+x}Al_{20+2x}Si_{12-2x}O_{66}$ ($0\leq x\leq 1.0$), $Sr_{12-x}Ba_xAl_{20+2x}Si_{12-2x}O_{66}$ ($0\leq x\leq 12.0$) and $Sr_{12-x}Ca_xAl_{20}Si_{12}O_{66}$ ($0\leq x\leq 2.4$). The end members of the first two solutions, $Sr_{13}Al_{22}Si_{10}O_{66}$ and $Ba_{12}Al_{20}Si_{12}O_{66}$, were previously only theorised, proving the effectiveness of a non-equilibrium synthesis techniques (GC)in novel phase discovery.

The two phase-pure synthesis protocols, developed on powdered ceramic samples, led to the belief that Al^{3+}/Si^{4+} ordering could be observed in $Sr_{12}Al_{20}Si_{12}O_{66}$. This theory was investigated by ^{29}Si MAS and ^{27}Al MQMAS NMR measurements and subsequent comparison of theoretical NMR spectra (GIPAW-DFT) generated from prospective models which had been built in supercell and optimised by DFT computations. The results from these experiments identified two plausible models which strongly suggested a mixed occupancy of at least the T5 site, as both models permitted mixed occupancy of this site.

The Si-deficient formula (P4-$Sr_{12}Al_{20}Si_{12}O_{66}$) was selected for bulk sample synthesis on glasses of size ~15 mm length x ~12 mm width x ~3 mm thickness. This led to the development of a bulk fully crystallised ceramic protocol and two bulk glass-ceramic protocols, using the full and partial crystallisation from a bulk glass technique. Two levels of transparency were achieved in the glass-ceramic samples (transparent and opaque) depending on the depth of crystallisation achieved (68 μm, and 349 μm respectively). Again, a doping level of 1mol% Eu^{2+} and Dy^{3+} was employed for optical functionalisation of the bulk and powdered samples. Qualitatively, deep blue PL and PersL emission and solar charging was observed with this doping level which warranted quantitative analysis of the phase at the CSIC in Seville, along with the doped $SrAl_2SiO_6$ phase.

This information as well as the solid solutions became the basis of property tuning once the PersL and ML of the nominal phase had been studied.

Optical measurements, PL and PersL, performed on powdered and bulk samples of $SrAl_2SiO_6:Eu^{2+},Dy^{3+}$ found the phase to have green emitting PL properties, centred in the 485 nm range, with maximum emission intensity observed under 270 nm light excitation. A lifetime of over 1 hour was observed for PersL emission when the sample was excited for 30s, again, with 270 nm light. The PL and PersL measurements of bulk and powdered $Sr_{12}Al_{20}Si_{12}O_{66}:Eu^{2+},Dy^{3+}$ revealed intense blue emission centred in the 420 nm range and three separate maximum excitation wavelengths, 270, 300, and 325 nm. Excitation for 30s with 300 nm light led to an impressive PersL lifetime, with light still detectable after 12 hours.

The solid solutions and substitutions of the cation and/or anion sites were then investigated as routes to tuning the emission. Unfortunately, these efforts failed to tune the properties of $Sr_{12}Al_{20}Si_{12}O_{66}:Eu^{2+},Dy^{3+}$, however they did show the compositional flexibility of the framework, permitting many different substitutions. A sample substituted with 30mol% Ga^{3+} was perhaps the most interesting, as despite producing a highly crystalline, almost phase-pure sample, no optical properties were observed.

Finally, the polar space group of $Sr_{12}Al_{20}Si_{12}O_{66}$ suggested that ML properties may be observable and so a bulk sample of size 4(width) × 4(depth) × 4.5(height) mm^3, was prepared and analysed, in collaboration with the University of Rennes. A doping level of 1%Eu^{2+} and 1.5%Dy^{3+} was used, and after a 30s excitation with 365 nm light and a compression force of 60 MPa, (applied after 1500s of excitation ending), a strong ML response was observed in the PersL spectra. This response indicated elastic-ML (EML) behaviour with the PersL intensity returning to baseline levels after the compression force was released. Visually, this EML response was found to be on a par with the EML response observed for $SrAl_2O_4:Eu^{2+},Dy^{3+}$, the current market leader for ML materials. The novelty and high-performing PersL and EML properties of $Sr_{12}Al_{20}Si_{12}O_{66}$ led to a patent application being filed on the material.

In the second part of this work, Chapter 3, the phase-pure synthesis and functionalisation of a recently discovered metastable phase, $Sr_2Si_3O_8$ ($P2_1/c$), was investigated. This phase had been found previously by C. Collins and M. Pitcher through GC exploration of a low energy zone in the SrO-$AlO_{1.5}$-SiO_2 ternary diagram.

Therefore, it embodied the pure essence of this project's aims and highlighted the relevance of the combined innovative synthesis and 'probe structure' prediction methodology developed here.

Originally, the phase was discovered as a pseudoternary composition, ($Sr_2Si_3O_8$:Al), however through, NMR, DSC and *in-situ* VTXRD analysis, it was realised that the phase could be made from the binary $Sr_2Si_3O_8$ formula. Synthesis optimisation at this composition revealed a phase-pure glass-ceramic synthesis protocol of 12 hours at 850°C, giving a crystalline phase fraction of almost 90% and answering the first research question of the chapter ("Can $Sr_2Si_3O_8$ glass-ceramics be synthesised by a GC of $40SrO–60SiO_2$ glass, (i.e. without the presence of Al)?").

Increasing the crystalline phase fraction, while retaining phase purity, was important for a properties study to be performed on $Sr_2Si_3O_8$, however, achieving this was challenging. Synthesis from the binary $Sr_2Si_3O_8$ composition appeared to introduce a structural defect which was not present in the original $Sr_2Si_3O_8$:Al composition, and could not be modelled by the $P2_1/c$ space group. This was observed by a shifting of the (2, 0, 2) and (3, 1, -2) peaks, a shoulder appearing on the (3, 0, -4) peak, and a Stephens monoclinic macro for strain broadening being required to improve the refinement. The low thermal stability of $Sr_2Si_3O_8$ prevented a microstructural study by HAADF-STEM to determine the origin of the defect. Under a high-voltage electron beam (200keV), necessary for atomic-level resolution, the sample decomposed meaning only the thermodynamic products, crystalline $SrSiO_3$ ($C2/c$) and amorphous SiO_2, were observed. Instead only low-voltage TEM and compositional EDS measurements were able to be performed, which confirmed the glass-ceramic nature of this material by showing crystals embedded in a glassy matrix, and confirming the structurally refined formula of $Sr_2Si_3O_8$.

A range of options were investigated for increasing both the crystalline phase fraction, crystallinity and thermal stability of $Sr_2Si_3O_8$, with the aim of preventing the defect from forming or allowing its visualisation and modelling. Initially, alternative non-equilibrium synthesis routes such as high-energy milling (HEM) and aerodynamic levitation (ADL) were investigated, however these further reduced crystallinity and the crystalline phase fraction. Next, substitutions, (Ba^{2+}, Ca^{2+}) and nucleating agents, (ZrO_2, Ag and Au) were explored. Two families of behaviour, A and B, were noticed during these experiments. Family A contained the substituents as well as the nucleating agents, Ag and Au. This family, reduced crystallinity, leading to a worse fit of the shoulder at (3, 0, -4) and a reduction in the overall crystalline phase fraction. An interesting point observed in these samples was that they appeared to stabilise a potentially new intermediate phase, which formed between the decomposition of $Sr_2Si_3O_8$ and formation of $SrSiO_3$. Family B, which contained the nucleating agents ZrO_2 as well as the original Al containing sample, improved crystallinity and allowed the shoulder to be modelled by the $P2_1/c$ model alone. However, the crystalline phase fraction suffered even more than in family A. Therefore, none of the alternative synthesis methods or nucleating agents/ substitutions tested succeeded in increasing the crystalline phase fraction or allowing the defect to be

modelled, which prevented a properties study from being conducted on a sample prepared from a pure GC approach.

A final method, partial nitridation of the glass, was devised in collaboration with the University of Rennes to functionalise $Sr_2Si_3O_8$. This technique had previously been used to improve the crystallisation and EML response of the analogous, $Ba_4Si_6O_{16}$, phase. Phase-pure undoped bulk and powdered glass-ceramic samples of $Sr_2Si_3O_8$ were able to be synthesised by this method. However, when these samples were doped with 1mol%Eu^{2+} and 1.5%Dy^{3+}, for their EML properties to be studied, the optimised synthesis protocol, 12h 800°C, no longer yielded single-phase samples. Minor secondary phases of $SrSiO_3$ (*C*2/*c*) and $Sr_3Ln_2Si_6O_{18}$ (*C*2/*c*) now formed. Two samples of $Sr_2Si_3O_8$:EU^{2+},Dy^{3+}, were therefore prepared, one which contained highly crystalline $Sr_2Si_3O_8$:Eu^{2+},Dy^{3+} as well as the impurities, and another which contained a higher glass content but less impurities. It was hypothesised that by comparing the EML response of both, the specific contribution from $Sr_2Si_3O_8$:Eu^{2+},Dy^{3+} could be estimated. After 30s of excitation with 354 nm UV light, both samples were subjected to a compression force of 140 MPa. The same EML response was observed in both samples, with it even being slightly more intense in the lower impurity sample, and so it was concluded that $Sr_2Si_3O_8$:Eu^{2+},Dy^{3+} had green emitting EML properties, which answered the third research question of this chapter, ("Can optimised $Sr_2Si_3O_8$ be functionalised to have persistent luminescent or mechanoluminescent properties, e.g. through doping with lanthanides such as Eu^{2+}, Dy^{3+}, and Cr^{3+} etc?).

In conclusion, this PhD work succeeded in developing a novel approach for the targeted discovery of new metastable inorganic oxides in the form of ceramics or glass-ceramics. The discovery and functionalisation of $Sr_{12}Al_{210}Si_{12}O_{66}$, as well as the phase-pure synthesis and functionalisation of $SrAl_2SiO_6$ and $Sr_2Si_3O_8$, exemplified this. In particular, the intense EML and long lasting PersL properties of $Sr_{12}Al_{20}Si_{12}O_{66}$, showed that targeted discovery of new materials can lead to step change improvements in property limits. As it was noted visually that the PersL and EML response of $Sr_{12}Al_{20}Si_{12}O_{66}$ was on a par with $SrAl_2O_4$:Eu^{2+},Dy^{3+}, a mature state-of-the-art material that is widely commercialised. On the other hand, the property optimisation of $Sr_{12}Al_{20}Si_{12}O_{66}$ has only just begun, with doping level concentrations/elements, substitutions, effect of the specific Al^{3+}/Si^{4+} ordering, and alternative non-equilibrium synthesis methods all still needing to be investigated. The transparency of the phase also has room for optimisation, through improved control of the crystallisation process a higher degree of crystallite orientation and lower degree of defects (cracks, pores etc.) could be achieved, therefore increasing transparency. The ability to be made as a transparent object is one advantage $Sr_{12}Al_{20}Si_{12}O_{66}$ already has over $SrAl_2O_4$:Eu^{2+},Dy^{3+}, as to date this phase has not been made as a transparent material without first doping it. A synthesis method which could lead to fully crystallised transparent bulk pieces of $Sr_{12}Al_{20}Si_{12}O_{66}$, is molten-glass pressing, which can rapidly produce micrometre thin samples. Meaning that if the same crystalline depth layer of approximately 350 μm is achieved, with highly orientated crystallites then a transparent fully crystalline sample may be achievable, with long lasting PersL properties. Future work should also consider the tuning of colour and intensity of the light emission

from $Sr_{12}Al_{20}Si_{12}O_{66}$. Optimisation of the 30mol% Ga substituted sample appears to be a good starting point, the formation of the correct crystalline phase but lack of optical properties suggests that the coordination environment has changed to such a degree that different optical dopants are now required to induce a response. It is likely, therefore, that if a response is achieved it will be of a different colour and/or intensity to the measured sample.

In a similar vein, the properties of $SrAl_2SiO_6:Eu^{2+},Dy^{3+}$ can be further optimised, through control of crystallite orientation and volume of crystalline phase. It is believed that through this, a more intense PersL response would be observed. For the $Sr_2Si_3O_8$ composition, achieving highly crystalline phase-pure samples should be the top priority of future work. Additional solution-based non-equilibrium techniques such as sol-gel, could be employed to solve this problem. However, the partial nitridation approach also holds promise, if further optimisation of the technique succeeds in removing the impurity phases and allowing highly crystalline samples to be synthesised.

Finally, the methodology laid out in this manuscript is not limited to the $SrO\text{-}AlO_{1.5}\text{-}SiO_2$ phase diagram, or in fact, ternary diagrams in general. In principle, the 'probe structure' method can be performed on almost any chemical system, (e.g. calculations of the $CaO\text{-}AlO_{1.5}\text{-}SiO_2$ diagram have already been performed). Substitutions of one, or two axes of the predicted diagram can also be explored, for example changing SiO_2 for GeO_2, or $AlO_{1.5}$ for $BO_{1.5}$ or $GaO_{1.5}$. The wide variety of non-equilibrium synthesis techniques available, can then allow for their targeted exploration, even in systems where glass synthesis is not possible. Additionally, this approach can be used to target specific properties, such as energy storage, and not just the optical ones discussed in this work. Therefore, it is believed that through use of the combined approach outlined in this thesis a wide range of metastable phases with high-performing properties, necessary to answer the growing demand for new functional materials, can be discovered. With only a motivated researcher being required to conduct the experiments.

Chapter 4: Experimental Methods & Characterisation Techniques

Contents Page

4.1. Synthesis Methods

4.1.1. The Glass Crystallisation Method

Step 1 – Glass Formation

Glass-crystallisation (GC) involves two steps, the formation of glass and its subsequent crystallisation. To prepare reactant mixtures for glass formation, first high-purity oxide or carbonate precursors (99.98+%) were dried at 100°C, to remove any moisture. These powders were then weighed according to the desired molar ratio and thoroughly ground in an agate mortar until fine, homogeneous reactant mixtures were achieved, in certain cases ethanol was added to aid in mixing. Once homogenised, powder mixtures were melted in Pt crucibles by a muffle-quenching furnace, at temperatures at least 50°C above their respective melting points, as determined from literature or differential scanning calorimetry (DSC). Samples were equilibrated at this temperature for ~1.5 hours, to permit atomic-level homogenisation, before the crucible was quenched in water. For bulk glass samples an additional annealing step of 15 mins at the melting temperature was added, to relax internal stresses and therefore reduce cracking (loss of transparency) during the crystallisation step.[1] Afterwards, the formation of glass was qualitatively determined by the observation of a transparent sample, and quantitatively determined by powder X-ray diffraction (PXRD).

Step 2 – Crystallisation

Once glass formation had been confirmed, the material was prepared for subsequent annealing, as shown in Fig. 4.1. This involved hand-grinding the glass to form a fine powder, which was then uniaxially pressed into pellets (~50mg, 5mm ϕ, 1mm thick). Pellets were sintered in Pt crucibles which were placed inside muffle furnaces. Temperatures of crystallisation were experimentally determined by *in-situ* variable temperature X-ray diffraction (*in-situ* VTXRD) and DSC. The specific times and temperatures used for each respective annealing protocol are discussed in the relevant sections of the manuscript. Crystallisations were also conducted on bulk glass pieces. Typically, these experiments required longer sintering times due to their reduced surface area compared to powdered samples, which limited the kinetics of the surface-based crystallisation mechanisms observed in these materials.

For the sintering of glasses doped with Eu^{3+}, a tube furnace was used, allowing crystallisation under a controlled atmosphere, specifically nitrogen-hydrogen N_2:H_2 (94%:6%), which reduced Eu^{3+} to Eu^{2+}. A temperature plateau at 500°C for 3h was included in these procedures to promote the complete reduction of Eu^{3+} ions.

Fig. 4.1. Schematic of the glass crystallisation approach utilised in this work.

While the classic melt-quenching method has many advantages for glass formation, namely its ease of use, scalability and 'activation' of precursors, it also has its drawbacks.

(i) Slow cooling rates facilitate crystallisation in systems where glass formation is challenging.

(ii) Nucleation sites & impurities occurring from contact with the Pt crucible.

(iii) Only forms glass in readily vitrifiable systems.

Where necessary these problems were overcome through the use of alternative synthesis techniques, such as the solid-state method, high energy milling (HEM), and aerodynamic levitation (ADL) coupled to two CO_2 lasers. Oxynitride synthesis was also employed, specifically in Chapter 3 (Section 3.4.1.), as a method to increase the crystalline phase fraction of the sample and enhance certain properties of the crystalline phase.

4.1.2. The Solid-State Method

The classic route used for metal oxide synthesis is the solid-state reaction.[2] At the laboratory scale, this process involved weighing out precursor powders according to the desired stoichiometric ratio, followed by grinding them together (either by hand, in a mortar or mechanically with a mill) until a homogeneous mixture was achieved. This process results in a reduction of the average grain size, which enhances the reaction rate. Typically, the reaction mixtures are then formed into pellets, by uniaxial pressing, increasing the surface contact area between grains where reaction takes place. The precursor pellet was then placed in an inert crucible, (typically Al_2O_3, perhaps lined with inert foil such as Pt), and heated to high temperatures (900-1700°C) for several hours. The cycle of – grinding, pelletising, firing – can be repeated multiple times or until the reaction reaches completion. While this technique has the advantages of simplicity and adaptability to a wide range of compositions, the disadvantage is that due to long reaction times and high temperatures, typically only formation of the most thermodynamically stable products is favoured.

4.1.3. Preparation & Crystallisation of Partially-Nitrided Glasses

In collaboration with Patrick Houizot at the University of Rennes, partially-nitrided glasses were prepared for subsequent crystallisation.[3] The partial nitridation, or more generally oxy-nitride, strategy employed in this work involved the mixing of the desired oxide powders, with Si_3N_4, which provided nitrogen and silicon (along with SiO_2) to the reaction. This was followed by their melt-quenching in a specialised furnace capable of producing glass under atmosphere, specifically N_2:H_2 (94:6). The content of nitrogen added to the glass was calculated by the following equation:

$$eq.\%N = \frac{3N^{*}100}{3N + 2O} \qquad \textbf{(Eq. 4.1)}$$

Where eq.%N, represents the equivalent percentage of nitrogen added and N, O are the molar concentrations of nitrogen and oxygen respectively.

It was necessary for partial nitridation of the glasses to take place in an oxygen free, N_2:H_2, atmosphere, to limit the loss of nitride from the melt. A specialised glove box was therefore used which permitted precursor melting and glass annealing to take place in a controlled atmosphere, as shown in Fig. 4.2. The muffle furnace connected on top was used for precursor melting, while the smaller furnace inside was used for glass annealing. Boron nitride (BN) crucibles were used for glass formation and glass relaxations as Pt-ones had been shown to form alloys when heated in reducing atmospheres.[4]

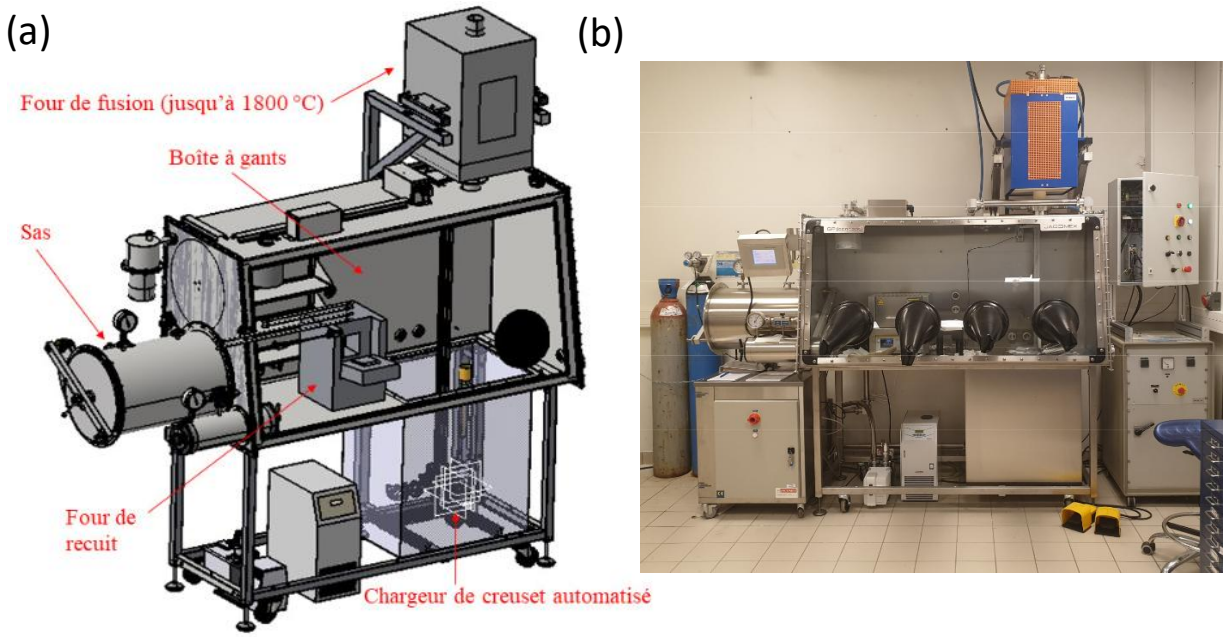

Fig. 4.2. **(a)** Labelled schematic of the oxy-nitride glass synthesis chamber. **(b)** Photograph of the real oxy-nitride glass synthesis chamber used in this work. Setup housed at the university of Rennes. Images taken from [5].

4.1.4. Mechanical Activation of Precursors by High Energy Milling

In this work, high energy milling (HEM) was considered as a route to full crystallisation, or at least increasing the crystalline phase fraction, of systems where this otherwise proved challenging ($Sr_2Si_3O_8$ in Chapter 3).[6] This was achieved through the complete homogenisation of the glass and a reduction in its particle size. Investigations into literature found that by reducing particle size and thereby increasing surface area, crystallisation kinetics could be improved in systems which demonstrated surface-based mechanisms.[7,8] This method therefore, permitted lower synthesis temperatures and times to be used, which helped target metastable phase synthesis.

A Retsch high energy ball-mill E_{max} was used for these experiments, as shown in Fig. 4.3.(a). This machine rotates the milling jars in an elliptical, rather than circular motion, meaning that the glass powders are in a constant state of acceleration or deceleration. This increases particle collision rates, leading to a higher

degree of homogenisation and smaller particle sizes. Three diameters of ZrO_2 beads, 10mm, 5mm and 1mm, were used for milling in 125ml reaction jars. These jars were filled according to the following approximate volume fractions: 1/3 glass powder + beads, 1/3 iso-propanol and 1/3 free space.

For the results presented in Chapter 3 (Section 3.4.1.), all three bead sizes were used consecutively, with the following programs: 2 x 30 min at the highest rpm available for the bead (1200 rpm for 10mm beads, and 2000 rpm for the 5mm and 1mm beads). At the largest bead size (10mm) particle size reduction is facilitated by a collision-based mechanism, whereas the 5mm and 1mm beads utilise a friction-based one, as demonstrated in Fig. 4.3(b)(c). Resultant particle sizes were analysed by a Partica LA-960V2 particle size distribution analyser from HORIBA. This device uses the Fraunhofer scattering model to relate the degree by which a particle scatters light to its size.[9] It is a high precision machine capable of measuring standards up to 0.6% of specification. Samples can be measured either wet or dry, for this work they were all measured wet using either deionised water or isopropanol as the liquid. A camera imaging system also allowed confirmation of the results observed by the particle size distribution graph.

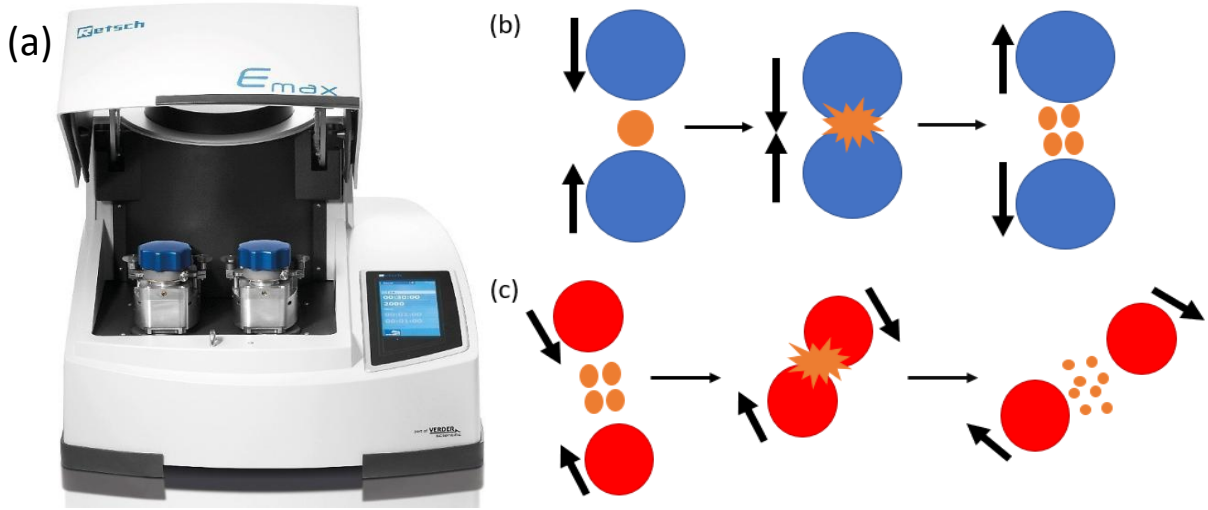

Fig. 4.3. (a) Picture of the Retsch high energy ball-mill E_{max} used in this work. **(b)** Diagram showing the collision-based mechanism for particle size reduction. **(c)** Diagram showing the friction-based mechanism for particle size reduction.

4.1.5. Aerodynamic Levitation Coupled to Two CO_2 Lasers

This technique employs the same precursor preparation steps - weighing, grinding, and pelletising – as described in Section 4.1.1. However, following this, pellets are fragmented and small pieces placed inside copper nozzles. An adjustable gas flow of Ar, O_2, He, or a dual mixture, then levitates the sample, while it is heated (max. 3000°C) from above and below, to ensure uniform heating, by a pair of 10.6 μm CO_2 lasers (Fig. 4.4.). Once molten, samples form spherical beads, whose temperatures can be monitored by pyrometers, which permits fine control and optimisation of the heating and quenching process. Contactless levitation of the bead means that once the lasers are shut off the sample rapidly cools. Typically, a cooling rate of 500°C/s is observed, however by changing the gas type/flow or mass of the pellet piece this rate can be tailored,

(between 300-1000°C/s). The fast cooling rates and contactless nature of this technique enables glass to be formed in otherwise non-vitrifiable systems.[10] In all cases, the formation of glass was confirmed by visual inspection and PXRD analysis. Formed glass was either sintered directly as a bulk bead or crushed and pelletised before annealing, similar to the melt-quenching GC approach.

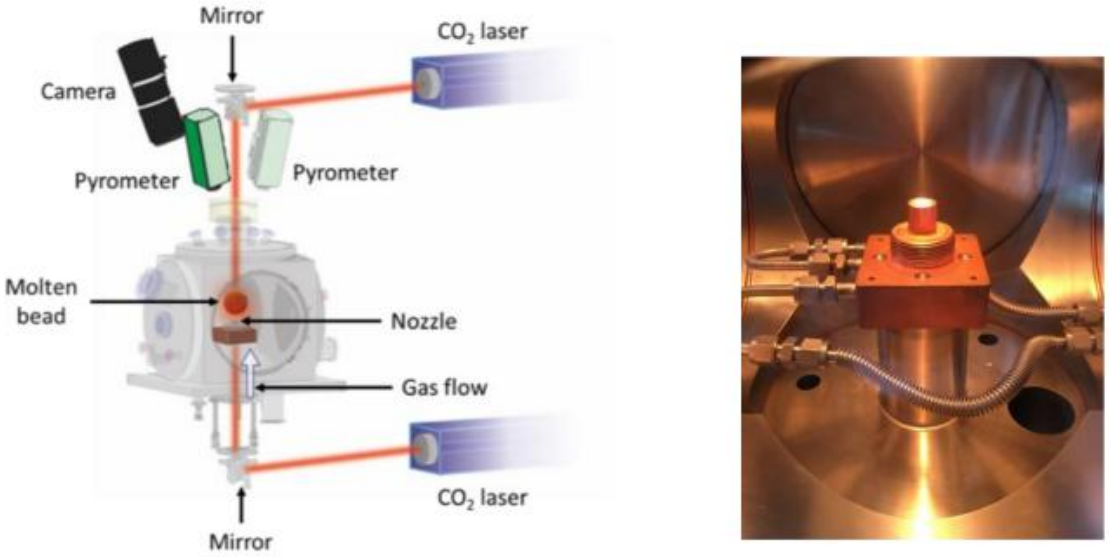

Fig. 4.4. A schematic representation of the ADL setup and an image of the actual setup used in this work are shown.

4.2. Characterisation Techniques

4.1. Differential Scanning Calorimetry Analysis

DSC was typically, the first characterisation technique carried out after glass synthesis. It determined the glass transition temperature (T_g), the temperature of crystallisation (T_c), the temperature of decomposition (T_d), and the temperature of melting (T_m). Which are extremely useful parameters in the optimisation of synthesis conditions.

Experiments were conducted using a double chambered Setaram MULTI HTC 1600 instrument, on powdered glass samples, 150–200 mg. Samples were heated to 1600°C, under an Ar atmosphere, using a heating rate of 10°C min^{-1}.

Experimentally, DSC subjects a reference and sample chamber to the same heating program and then monitors the difference in heat flow. As the sample goes through phase changes (e.g. solid to liquid) or structural changes (e.g. crystallisation, phase transition, fusion etc.) more energy is required to maintain equal temperatures between the chambers. This energy flow is observed as an endothermic or exothermic peak in the trace, demonstrated in Fig 4.5. When combined with PXRD and *in-situ* VTXRD these events can be linked to specific phase transitions (for example glass to ceramic). DSC experiments were conducted by Sandra Ory (CEMHTI).

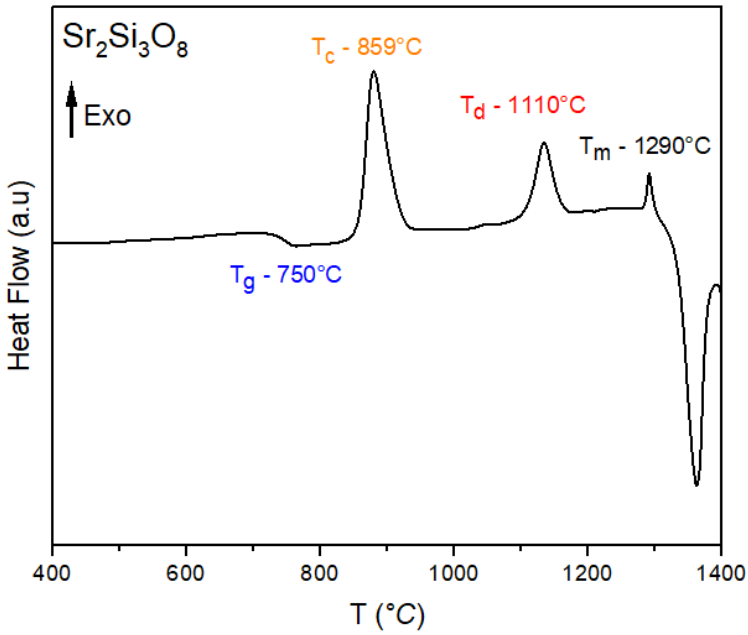

Fig. 4.5. Example of a DSC trace from Chapter 3, with the T_g, T_c, T_d and T_m events shown.

4.3. Average Structure Determination

4.3.1. Ambient Temperature Powder X-Ray Diffraction

PXRD measurements were performed on a Bruker D8 Advance (Cu $K\alpha_{1,2}$ radiation) instrument combined with a LynxEye XE detector operating in a Bragg Brentano (θ-θ) geometry. This method fixes the sample in a horizontal position but allows the source and detector to move in equal but opposing directions. X-rays were generated in an X-ray tube, by the firing of electrons at a Copper target (anode) which released, superimposed on the Bremsstrahlung, characteristic $K\alpha_1$, $K\alpha_2$ and Kβ radiations. The Kβ emission was removed by a Ni filter before the beam passed over the sample.

The resultant PXRD diffraction patterns permitted useful micro(structural) information to be determined. The widths, intensities, and positions of the peaks made it possible for the unit cell, crystallite size and/or structural parameters such as atomic positions to be defined.[11] Moreover, through combined use with software, such as EVA, PXRD becomes a powerful phase identification tool capable of comparing experimental patterns to listed structures in the ICDD databases.[12] As the database is exhaustive an un-indexed pattern can signal the synthesis of a novel phase.

In this project, samples were prepared for PXRD analysis by either dispersing powder on a silicon wafer with the help of ethanol or compacting them in a silicon holder with a small cavity. To ensure better powder averaging, samples were finely crushed before analysis. [13] Measurements were also typically, conducted on rotating sample holders to provide better statistics (more crystallites under the beam).[14,15]

As shown in Fig. 4.6.(a), the incident X-ray beam is scattered as it strikes the electrons of the crystal lattice, in a process known as elastic scattering. This scattering occurs in specific directions due to the regular array of the crystal lattice, in some directions scattered waves cancel out due to destructive interference and in others they are amplified, constructive interference, as determined by Bragg's law.[16]

$$2d_{h,k,l}\, sin\theta = n\lambda \qquad \textbf{(Eq. 4.2)}$$

Where:

- $d_{h,k,l}$ is the interplanar distance between the planes family (*h, k, l*)
- Θ is the incident angle
- n is an integer
- λ is the beam wavelength, hence X-rays as these are of the same magnitude as the *d*-spacings of crystal planes (1–100*Å*)

Detection of the scattered beam as function of diffraction angels, allows a diffractogram to be plotted, example shown in Fig. 4.6.(b), with the x-axis representing the diffraction angle, in 2Θ(°), and the y-axis representing the number of photons detected (intensity). The nature of crystals (cell, chemical composition) allowed their specific patterns to be used as a 'finger print' in their identification. Combined with the Rietveld method, discussed in Section 4.4.3., structural parameters such as the unit cell, atomic positions, bond lengths, angles and potentially orderings within the crystalline phase can be explored. The parameters used for PXRD measurement are discussed in the relevant sections of each chapter.

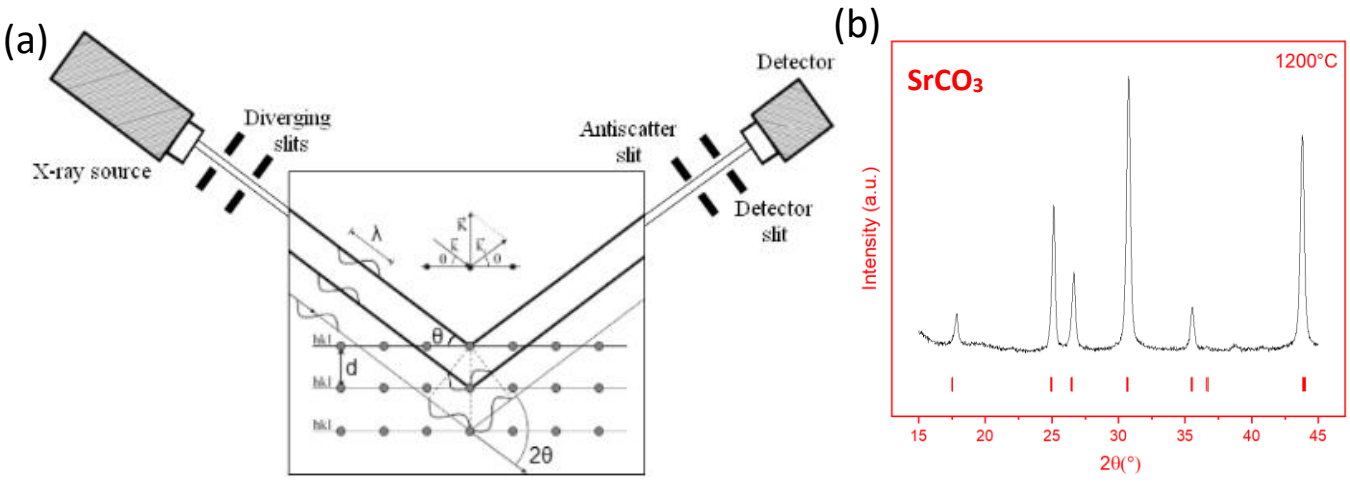

Fig. 4.6. (a) Principles of X-ray diffraction. **(b)** Example of a PXRD pattern with the phase indexation (Bragg peaks) shown.

4.3.2. *In-Situ* Variable Temperature X-Ray Diffraction

It was also possible to monitor the progress of crystallisation as a function of temperature, by using *in-situ* VTXRD. Similar to DSC, this method allowed phase changes or crystallisation events to be visualised by heating the sample while simultaneously recording PXRD diagrams. This facilitated thermal optimisation of the crystallisation mechanism (thermal stability of phase domains, decomposition, phase transition etc.). It was also an indication of metastability as phase decompositions or changes could also be observed. These experiments were conducted on a Bruker D8 Advance laboratory diffractometer with Cu $K\alpha_{1,2}$ radiation, in Bragg–Brentano Θ-Θ geometry. A linear Vantec detector was used for photon detection, while an Anton Paar HTK12 or HTK16 furnace was used for the heating to 1200°C and 1600°C, respectively (max heating rate 5°C/s). Experiments were conducted between 700-1200°C or 700-1600°C, with measurements every 20°C or 25°C, angular range of 5-50°, time per step of 0.6s and increment of 0.0164°. Experiments were prepared by depositing finely powdered sample onto a platinum disk in an alumina crucible. The temperature behaviour and the thermal expansion of the setup had previously been calibrated using a corundum reference.

4.3.3. Synchrotron Powder Diffraction

Synchrotron X-ray diffraction (SPD) is another diffraction-based analysis technique, operating from the principles of Bragg's law. This technique can produce X-ray beams up to one million times more intense than typical lab-based sources. Which, combined with highly sensitive detectors, permits high-resolution PXRD patterns to be collected with low background signal. The high-resolution and low signal to noise ratio enables the visualisation of peaks that may have been missed by lab based XRD instruments. This in turn leads to better peak indexation and therefore, structure solution of unknown phases.

For SPD and sometimes XRD, Debye-Scherrer geometry is used, which requires the beam to penetrate the sample, meaning factors such as absorption from the sample holder (capillary) are important (<~1muR).[17] The main difference between PXRD and SPD is the methods by which the X-rays are generated. In SPD, X-rays are generated by accelerating electrons within a storage ring, through the use of magnetic fields perpendicular to the beam line, (Fig. 4.7.). This generates a beam with energies ranging from 5–30 keV, depending on experiment requirements (e.g. sample/capillary absorption), and an energy resolution of $\frac{\triangle E}{E} \sim 10^{-4}$. Bendable mirrors and monochromators are then used to direct the beam towards the sample and make it single wavelength.

The data sets presented in this work were collected at two sites. The first was the SOLEIL synchrotron source, using the CRISTAL beamline. Experiments were conducted, over the period of one hour on samples held within 1mm ϕ borosilicate capillaries. An incident wavelength of 0.5904 *Å* was used which allowed for a wide Q ($Å^{-1}$) range to be investigated. Finally, an angular range of 0.5-60° and step size of 0.004° was used to ensure

that high-resolution was achieved. The second synchrotron source used was the 11BM beamline, housed at the Argonne National Laboratory, U.S.A. Data was collected at room temperature from a spinning sample holder (60 Hz, 0.8mm Kapton capillary) over a 0.5−60° 2Θ range with a 0.001° step size and an incident wavelength of 0.413978 *Å*.

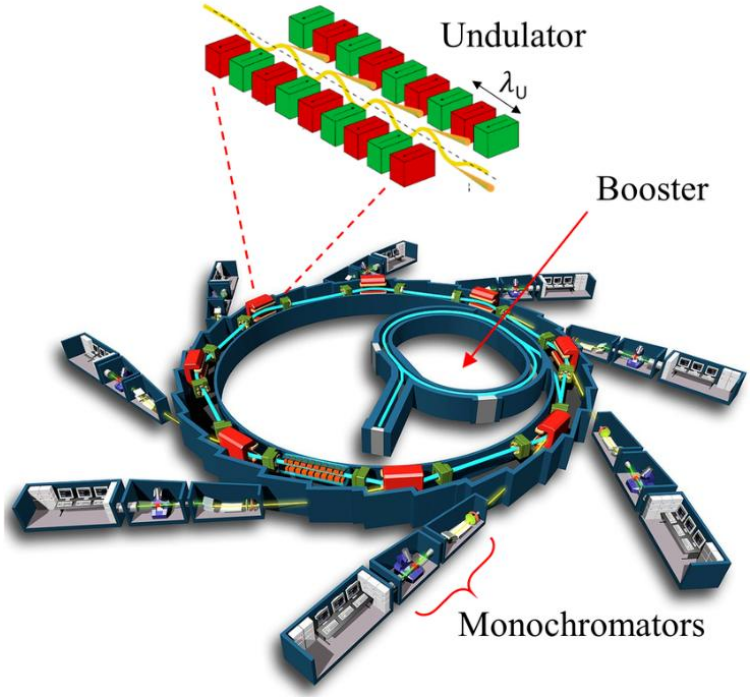

Fig. 4.7. Illustration of a synchrotron source. From [18].

4.3.4. Neutron Powder Diffraction

Another complementary technique to PXRD is neutron powder diffraction (NPD). As neutrons and atomic nuclei are the source of interactions in this technique it permits elements with small (e.g. O^{2-}) or similar (e.g. Si^{4+} and Al^{3+}) electron densities to be distinguished. Clearly, for the structural determination of aluminosilicates this is extremely useful as the precise location and occupation of Si^{4+} and Al^{3+} within a crystal structure may have an impact on its properties.[19] Equally, for accurate structure and property determination, it is necessary to know the O^{2-} positions within a crystal lattice. Another advantage NPD has over PXRD and SPD, is that due to the independent relationship between diffraction angle and scattering power, NPD doesn't show a decay of peak intensity at high angle, with loss of intensity being solely due to thermal motion of the atoms.[20] However, it should be mentioned that due to relatively low power of the neutron beam and the smaller space occupied by nuclei compared to electron orbitals, a large quantity of powder, approximately 4g in this work, is required to keep acquisition times low. This explains why NPD is mainly used as a complementary technique to XRD.

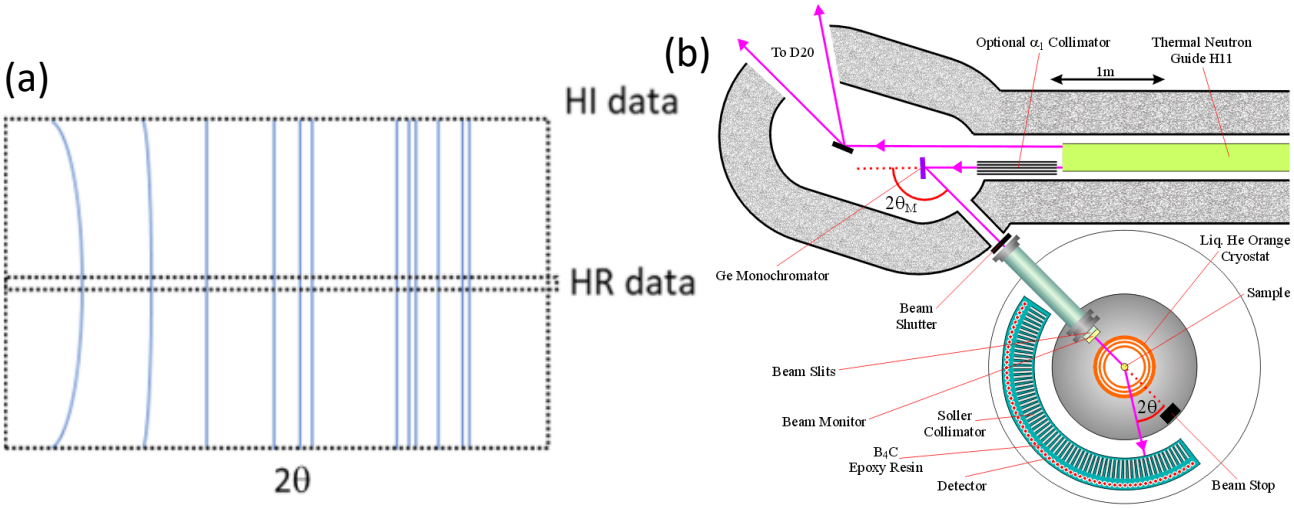

Fig. 4.8. (a) Visualisation of the neutron detector when being integrated for HI and HR data. **(b)** NPD source and detector in HR mode.

For the NPD data collection of the materials in Chapter 2, the D2B line at the ILL laboratory in France was used. Two experiments were conducted, with incident wavelengths of 1.594 *Å* and 2.398 *Å*, respectively, and angular ranges of 0.5–160°. A Step size of 0.05° was used in both experiments.

For structural solution of $Sr_{12}Al_{20}Si_{12}O_{66}$ in Chapter 2, the 2.398 *Å* data was used as it helped resolve the peaks of the large, low symmetry cell. However, this did come at the cost of cutting off the peaks at lower *d*-spacings. Cylindrical sample holders (5–16 mm in diameter) made of vanadium were used due to its low neutron scattering length.

Two data sets were received from the D2B line, high-intensity (HI) and high-resolution (HR), as shown in Fig. 4.8. The HI data is integrated over the whole 2D pattern which means that the intensity of the peaks is much higher, this is useful in the detection of low intensity peaks. However, the downside is that peaks are also broader, especially at low angle, due to asymmetric peak broadening induced by the curvature of the Scherrer cones. This effect can be minimised by solely integrating a central strip of the 2D pattern, HR data, which overall results in lower intensities but much better peak resolutions.

4.4. Structural Refinement of Synthesised Materials

Two main challenges are presented by PXRD data for structural determination, the phase problem and the compression of 3D information down to a 1D scale. The phase problem is common in both powder and single crystal PXRD: for each *h,k,l* the form factor can be positive or negative however only F^2 is observed experimentally (and so only positive values are recorded), making it hard to model data accurately. The PXRD 3D to 1D compression means that *h,k,l* markers with the same *d*-spacings can't be resolved (eg. Cubic 001, 010, and 001 overlap perfectly by PXRD). This problem is not encountered in single crystal PXRD. These

problems are particularly apparent in low symmetry and/or large crystal lattices which give rise to many diffracted spots.[14,21]

In this thesis, these problems were tackled for structural determination through the use of high-resolution data collection sources (SPD and NPD), and the use of *ab-initio* (first principle) methods. Namely, charge-flipping (CF) was used to generate structural models which were then refined with the Pawley and Rietveld method.[22]

4.4.1. Peak Indexation

The first step in the creation of structural models for refinement was peak indexation. This was carried out using the DICVOL software as implemented in WinPlotR from the FullProf program.[23] Based on the indexed peaks and their respective intensities, these programs produce a list of cell parameters which match the indexation. Then combined with SUPERFLIP, implemented in JANA2006 software, the cell parameters and indexed peaks was used to generate a list of space groups. From this list, the best solutions were selected based on their associated figures of merit.[24] The Pawley method, implemented in JANA2006 and TOPASV7, tested these generated space groups and identified the most plausible solutions that can fit the whole diffraction pattern.[25] Crucially, Pawley refinement gave initial lattice parameter values and reflection intensities which are mandatory prerequisites for the charge-flipping method to be used.

4.4.2. The Pawley Method

The Pawley method assumes that powder diffraction data can be fitted with just, the intensity of each reflection with *h,k,l* indices, instrument corrections, and unit cell and peak shape parameters, through the nonlinear least squares refinement of them.[25] From this a computed pattern is generated, enabling comparison with the experimental data. The method, essentially, requires the following equations to be solved:

$$y_{calc,0} = \sum_{s} (I_s \,.\, \phi_{s,0}) + Bkg_1 \qquad \textbf{(Eq. 4.3)}$$

$$y_{calc,1} = \sum_{s} (I_s \,.\, \phi_{s,1}) + Bkg_2 \qquad \textbf{(Eq. 4.4)}$$

...

$$y_{calc,N-1} = \sum_{s} (I_s \,.\, \phi_{s,N-1}) + Bkg_N \qquad \textbf{(Eq. 4.5)}$$

Where $y_{calc,i}$ is the calculated scan intensity at position *i* in the diffraction pattern and I_s, is the intensity of reflection **s**. The value of the normalised peak shape function of reflection **s** at position I ∈ [0…N – 1] in the diffraction is represented by $\phi_{s,i}$. The reflection positions are determined by the unit cell parameters and the zero-point error (which accounts for instrument corrections). The background curve can be either predetermined or modelled by a polynomial function.

The method differs slightly from the Le Bail method, which doesn't refine peak intensities but instead gives them arbitrary values, I_{obs}.[26] At the time (1988) this reduced computation power and times, which enabled more researchers to utilise the method. Today however, these issues have been addressed by improvements in computation technology.

The advantage and disadvantage of the Pawley method is that it refines the pattern as a whole, giving information on the unit cell dimensions and profile parameters but no information on the atomic positions. This means that it can be a very quick method to test a structural model/space group. Thereby giving the 'ideal' refinement quality achievable when a more rigorous method, such as Rietveld refinement, is used. Conversely however, as atomic positions are disregarded, this method cannot be used to generate a real structural model from the data and so ultimately for structure determination it must be used in combination with other methods.

4.4.3. *Ab-intio* Structure Determination by Charge-Flipping

The disadvantages of the Pawley method were addressed by a CF approach, which was used to assign atomic positions and build a real structural model. An electron density map was generated from the given cell parameters, initial reflection intensities, and PXRD data. Based on a given space group (or *P*1 model if the space group isn't known) atoms assigned to positions within this map based on a CF approach, (SUPERFLIP) conducted in JANA2006 software.[27,28] This approach, reverses the sign (+/-) of any pixel in the electron density map below a threshold. It then performs a series of Fourier transformations on the data, switching between real and reciprocal space. This iterative loop is repeated until the electron density map is well matched and a chemically sensible structure is found. By flipping signs during iterations, CF encourages convergence towards correct electron density solutions and minimises local minima problems. Typically, the heaviest atoms are assigned first as they have the strongest scattering contributions; lighter atoms can then be assigned based on the remaining electron density. Due to its simplicity, this algorithm has been used to identify quite complex structures relatively quickly.[29,30]

Other approaches which use real-space methods, such as simulated annealing (SA), can also be used.[31] These methods can build structural models based on lower quality data, when compared to CF, by imposing certain chemical assumptions. For example, in Chapter 3, the structure of $Sr_2Si_3O_8$ was solved by SA and the

assumption that all Si atoms were found in SiO_4 tetrahedra, with the Sr atoms sitting somewhere between them.

4.4.4. The Rietveld Method

To make full use of PXRD, SPD and NPD data the Rietveld method can be used.[32] This method employs a minimisation algorithm, based on least squares refinement. A good starting model is therefore vital, to ensure the global minimum (i.e. the correct structure) is found and not a local one. The Rietveld method involves the calculation of Bragg peak intensities (y_{calc}), from a starting (approximate) structural model which is then refined against the recorded diffraction intensities (y_{obs}) to generate a new structural model which matches the observed scattering. Therefore, based on agreement of the real and simulated patterns an idea of the quality of the predicted model is gained. It is sometimes coupled to a provisional Pawley refinement, as the lattice parameters and peak profile refined by the Pawley method can be used as a starting point for Rietveld refinement.

The first step of the Rietveld method involves simulating the intensity of a given atomic position from the theoretical model at a given *2Θ* angle, called *i* here, using the following formula:

$$Y_{calc\,i} = \sum_{\phi}^{N} S_k \sum_{k=k1}^{k2} J_{\phi k} \,.\, Lp_{\phi k} \,.\, O_{\phi k} \,.\, M \,.\, \left[F_{\phi k}\right]^2 .\, \Omega_{i\phi k} + Y_{back\,i} \qquad \textbf{(Eq. 4.6)}$$

Where:

- $Y_{Calc\,i}$: Calculated intensity of a given 2θ position
- $Y_{back\,i}$: Calculated background intensity of the i^{th} position, in 2θ
- S_ϕ: Scale factor term proportional to the number of scattering unit cells divided by the unit cell volume
- $J_{\phi k}$: Multiplicity factor of the k^{th} reflection
- $L_{p\phi k}$: Lorentz-polarisation factor
- $O_{\phi k}$: Factor to correct for preferred orientation
- M: Beam correction function
- $[F_{\phi k}]$: Structural factor which translates peak position to XYZ coordinate
- $\Omega_{i\phi k}$: Profile function

Like the Pawley method, the background can either be predetermined or defined through refinement of a polynomial function such as Chebyshev or Legendre. For the peaks themselves there are two problems to tackle; matching the peak position and matching the peak intensity. To solve these problems in powder diffraction, a pseudo-Voigt profile function is commonly used as it combines both the Gaussian (from the instrument) and Lorentzian (from the sample, microstructure and strain) contributions. For this work, a

Thompson-Cox-Hastings pseudo-Voigt, *TCHZ,* profile function was used with the *U, V, W* and *Y* parameters being refined, while *X* and *Z* were set to zero (no size contribution). The *pku, pkv, pkw* and *pkz* contributions described the $2\Theta_0$ dependence of the gaussian contribution. However, the effect of *pkz* can be described in terms of a combination of *pku and pkw* and therefore, when additional constraints are not used, as in this case, should not be refined. The *pkx* and *pky* contributions describe the $2\Theta_0$ dependence of the Lorentzian contribution, in this work refinement of just *pky* proved sufficient.

An important term in Eq. 4.6. is the structure factor, [$F_{\phi k}$] or more simply F(**s**):

$$F(\boldsymbol{s}) = \sum_j t_j f_j(s) e^{2\pi i s.x_j} \qquad \textbf{(Eq. 4.7)}$$

Calculation of this term allows peak positions to be the translated into XYZ vector coordinates. The $f_j(s)$ specifically relates atomic position/reflection (*s*) to observed intensity (*f*). Therefore, it is crucial for structural solution by turning the diffracted pattern into a 'real' crystalline structure.

The Rietveld method can be extremely useful, however as mentioned, its use of least square's refinement enables it to fall into local minima's rather than the global one. Leading to improper fitting of the data. To avoid this, figures of merit are calculated to judge the quality of the Rietveld refinement. The first parameter often checked is the difference curve, calculated from ($Y_{obs\,i} - Y_{calc\,i}$), the smoother this curve is the better the agreement is between the model and data. Reliability factors (R_p, R_{wp}, R_{exp} and χ^2 or gof) are also calculated after each refinement cycle, essentially, the lower they are the better the fit is. These factors are calculated from the following formulas:

- R-profile: $R_p = 100.\frac{\sum_i |Y_{obs\,i} - Y_{calc\,i}|}{\sum_i Y_{obs\,i}}$ **(Eq. 4.8)**

- R-weighted profile: $R_{wp} = 100.\sqrt{\frac{\sum_i W_i |Y_{obs\,i} - Y_{calc\,i}|^2}{\sum_i W_i Y_{obs\,i}^2}}$ **(Eq. 4.9)**

- Experimental statistic factor: $R_{exp} = \sqrt{\frac{(N-P+C}{\sum_i W_i Y_{obs\,i}^2}}$ **(Eq. 4.10)**

Where N, P and C represent the number of measured points, refined parameters and used constraints respectively.

- Goodness of fit (gof): $\chi^2 = \left(\frac{R_{wp}}{R_{exp}}\right)^2$ **(Eq. 4.11)**

The powdered diffraction problems tackled in this thesis were mainly done using TOPAS academic (V7), with some structural solution done using SUPERFLIP in JANA2006 software.

4.4.5. Crystalline wt.% Determination

Determining the crystalline wt.%, and hence the amorphous wt.%, of samples played an important role in the optimisation of synthesis procedures during this thesis. Particularly, in samples where qualitatively differentiating between their PXRD patterns was difficult. It was also useful in low symmetry systems that produced many diffracted peaks and hid the amorphous bump typically seen for incomplete crystallisations. NMR and sometimes SEM are the common methods used for accurate crystalline wt.% determination, however, a faster method was developed here, which utilised lab-PXRD data.

Using $Sr_{1.8}Ba_{0.2}Si_3O_8$ as an example to better explain the procedure. A known amount of well crystallised standard (Al_2O_3) was thoroughly ground with the sample ($Sr_{1.8}Ba_{0.2}Si_3O_8$), giving the total weight, the exact weights of the Al_2O_3 and $Sr_{1.8}Ba_{0.2}Si_3O_8$ were carefully noted, (measured weight in mg). Before weighing, powders were dried at 100°C overnight, to remove any moisture. Al_2O_3 (99.995% Alfa), was chosen as the standard, due to its well resolved peaks which didn't overlap with the samples being analysed. A 3:1 ratio of sample to standard was approximately aimed for when weighing, as this kept the Al_2O_3 peaks at a similar intensity to the sample. Measured weights were converted into measured wt.% by:

$$Measured\ wt.\%\ (Sr_{1.8}Ba_{0.2}Si_3O_8) = 100.\frac{Measured\ weight}{Total\ weight} = 100.\frac{217}{289} = 75wt.\% \qquad \textbf{(Eq. 4.12)}$$

PXRD data was then collected on the mixture; a deep sample holder was used which gave better powder statistics. The data was then Rietveld fitted using TOPASV7 software, an example fit is shown in Fig. 4.9. An angular range of 6-90°, time per step of 2s and increment of 0.0164° was used for these PXRD scans.

A multiphase refinement file was created with the relevant sample's refinement parameters and those of Al_2O_3 (SG. *R-3cH, a/b = 4.76 and c = 12.99 Å*), which gave the refined wt.% of each phase. A ratio of these two values was then used to find the amorphous, crystalline sample ($Sr_{1.8}Ba_{0.2}Si_3O_8$) and Al_2O_3 contributions (the mixture wt.%). Al_2O_3 was assumed to be 100% crystalline, therefore its measured wt.% was also its mixture wt.%, the sample and amorphous contributions were calculated based on this. From this, the amorphous and crystalline sample (cry. $Sr_{1.8}Ba_{0.2}Si_3O_8$) contributions to the sample wt.% were found by:

$$Sample\ wt.\%(\mathrm{cry.}\ Sr_{1.8}Ba_{0.2}Si_3O_8) = 100.\frac{Mixture\ wt.\%}{Total\ mixture\ wt.\% - Al_2O_3} = 100.\frac{46.6}{75} = 62wt.\% \qquad \textbf{(Eq. 4.13)}$$

Inputting the sample and amorphous mixture wt.%, gave the crystalline wt.% and the amorphous wt.%, respectively.

This technique was used to compare the samples synthesised in Chapter 3. The calculated values allowed reliable comparison between the crystallinity of samples, however, they were never treated as absolute values and merely served as a way of quickly comparing the success of heat treatments, substitutions or nucleating agents on the crystalline phase fraction.

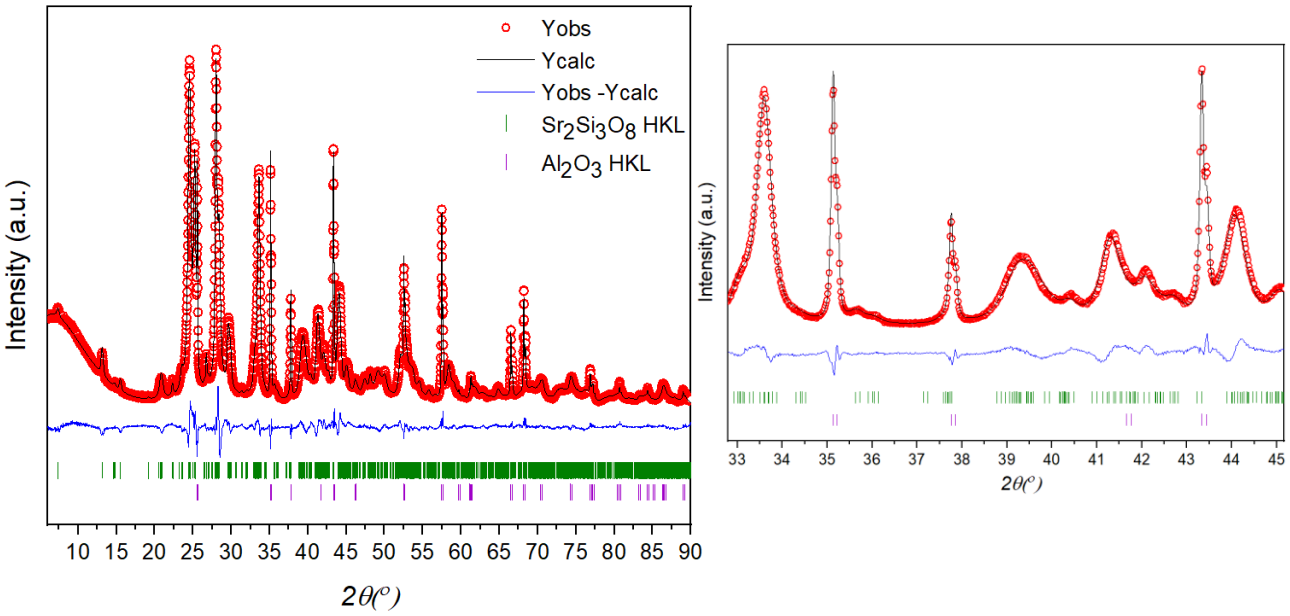

Fig. 4.9. Example of the Rietveld refinement of a sample being analysed for its crystalline wt.%, with a zoom of the fit to show the relative match of scattering contribution.

4.5. Local Structure Determination

4.5.1. ^{29}Si MAS & ^{27}Al MQMAS Nuclear Magnetic Resonance

The effectiveness of powder diffraction-based analysis methods, which provide information on the average structure, can be enhanced through complementary techniques such as nuclear magnetic resonance (NMR). This analysis provides insights regarding the local environment (1-2 bonds) of atoms and any orderings or vacancies which may be present. This information can be extremely important for accurate structural and property determination, as these features often give rise to thermal or electrical conduction properties as well as energy storage.[33] NMR can also be used to distinguish between isoelectronic (Z value) atoms which are indistinguishable by PXRD methods. This fact was of particular importance in this work as the SrO-$AlO_{1.5}$-SiO_2 diagram was being investigated. Through the study of the ^{29}Si and ^{27}Al isotopes found within materials, information on the chemical formula, glass content, and Al^{3+}/Si^{4+} orderings are gained.

The principle of NMR is based on the Zeeman effect, which refers to the splitting of energy levels into several distinct sublevels, when an external magnetic field is applied.[34] A higher magnetic field means a larger Zeeman splitting and better peak resolution. This method requires that probe nuclei have a nuclear spin I ≠ 0, and consequently a magnetic moment, μ. In solid-state NMR, which was used here, the sample is spun at the magic spinning angle (MAS) of 54.7° with respect to the magnetic field.[35] By applying an external magnetic field, B_0, to these nuclei their spins can be split into orientations corresponding to the formula 2I+I, where I equals and which are separated by Larmor frequency (ν0):

$$v_0 = \frac{\gamma B_0}{2\pi} \quad \textbf{(Eq. 4.14)}$$

The magnetic field of a nucleus is influenced by the electron cloud of neighbouring nuclei, which causes different types of interactions, for example chemical shift, j coupling, and dipole-dipole interactions. Therefore, through the study of these interactions and how they influence the Zeeman effect, information on the local environment of the investigated isotope is gained.

^{29}Si magic angle spinning (MAS) NMR experiments were conducted on a Bruker Avance III spectrometers operating at a magnetic field of 9.4 T (^{29}Si Larmor frequency of 79.5 MHz) using 4 mm rotors spinning at a frequency of 10 kHz. Quantitative ^{29}Si MAS spectra were recorded using a 10° flip angle (pulse duration of 0.6µs) and a recycle delay of 22.5 s. ^{27}Al MAS NMR experiments were carried out on a Bruker Neo spectrometer operating at a magnetic field of 20.0 T (^{27}Al Larmor frequency of 221.5 MHz) using 2.5 mm rotors spinning at a frequency of 30 kHz. ^{27}Al quantitative MAS spectra were recorded using a flip angle of π/18 (pulse duration of 0.4 µs) and a recycling delay of 1s. Two-dimensional ^{27}Al MQMAS spectra were recorded at a spinning rate of 30 kHz using the Z-filter sequence.[36] Pulse durations for the excitation and reconversion of triple quantum coherences were 2.6 and 0.8 µs with a nutation frequency of 140 kHz. 80 rotor-synchronized t_1 increments were recorded with 624 transients each and a recycle delay of 0.5 s. ^{29}Si and ^{27}Al chemical shifts were referenced at 0 ppm towards external neat TMS and an 1M aqueous solution of $Al(NO_3)_3$, respectively.[37]

4.5.2. Density Functional Theory in Combination with NMR

To fully utilise solid-state NMR in structural determination, the electron densities of prospective models, generated by the supercell code in this case, must be computed.[38] This permits the experimental data to be linked back to the local crystalline structure that it arose from, as NMR parameters are influenced by the electron cloud surrounding a nucleus. However, in practice this can be challenging as, in all but the simplest of systems, no analytical method exists for determining electron densities. Approximate electron densities area therefore computed, with plane wave based density functional theory (DFT) being one such method.

DFT is fundamentally based on the theorems of Hohenberg and Kohn.[39] These theorems state that the average value of a parameter can be entirely determined by the electron density n(**r**). Meaning, the total energy of the system can be defined as:

with:

$$E^{HK}[n] = F[n] + \int V_{ext}(\boldsymbol{r})n(\boldsymbol{r})d\boldsymbol{r} \quad \textbf{(Eq. 4.15)}$$

$$F[n] = T[n] + V_{ee}[n] \quad \textbf{(Eq. 4.16)}$$

Where, *T[n],* is the kinetic energy and, $V_{ee}[n]$, is the electron repulsion energy. In complex cases, no analytical solution is known for *T[n]* and $V_{ee}[n]$.

A key to accurate DFT calculations is therefore, how these values are approximately calculated. The simplest method is the local density approximation (LDA) approach.[40] With this method, the energy of an infinitesimal volume is related directly to the electron density at that point, and is proportional to the energy of an electron gas of the same density.

In this work, DFT computations, with periodic boundary conditions of ^{29}Si and ^{27}Al NMR parameters, were performed using the CASTEP code.[41,42] Models were built from a (1x1x1) cells and *P*1 space group, with cell parameters that adhered to the experimentally observed values. Additionally, all equivalent configurations were merged together. The Perdew–Burke–Ernzerhof (PBE) functional was used to describe the exchange-correlation effects.[43] The core–valence interactions were described by ultrasoft pseudopotentials[4-5] (USPPs) implemented in Materials Studio 20.0.[44,45] The USPPs were generated using the on-the-fly generator (OTF_USPP) included in CASTEP. An energy cut off of 600 eV was used for the plane-wave basis set expansion and the Brillouin zone was sampled using a Monkhorst-Pack grid spacing of 0.04 $Å^{-1}$. These computational parameters were used for both geometry optimization and calculations of NMR parameters.

4.5.3. Relating DFT Calculations to NMR Parameters

Once calculated by the supercell code and relaxed by the DFT method, generated models were translated into a set of NMR parameters, so that their theoretical spectra could be compared against the observed data. For this, the electron field gradient (EFG) and NMR chemical-shielding tensors must be calculated respectively. In this work, the gauge-including projector augmented wavefunction (GIPAW) method was used.[46,47] This approach, allows the NMR parameters, chemical shifts, of periodic systems to be calculated:

$$\delta_{iso}^{calc} = \frac{-(\sigma_{iso}^{calc} - \sigma_{ref})}{1 - \sigma_{ref}} \approx -(\sigma_{iso}^{calc} - \sigma_{ref}) \qquad \textbf{(Eq. 4.17)}$$

σ_{ref} is a reference magnetic shielding, calculated from a series of reference compounds.

The work in Chapter 2, Section 2.5., used GIPAW-DFT calculations to identify plausible models which accounted for the Al^{3+}/Si^{4+} ordering observed in the material. Through comparison of the observed ^{29}Si MAS and ^{27}Al MQMAS NMR patterns and the theoretically generated ones, models could be discarded or kept and further refined.

4.6. Microstructure Analysis Techniques

4.6.1. Scanning Electron Microscopy

For the study of a samples surface morphology, chemical composition/ homogeneity, and grain size, scanning electron microscopy (SEM) analysis can be used. It is a non-destructive technique that proved to be a useful complementary tool in structural solution. SEM experiments were conducted using an IT800SHL JEOL scanning electron microscope (FEG SEM), equipped with an SSD Ultim Max 100mm2 detector (EDS Oxford system) (Fig. 4.10.(a)). Condenser lenses focus an intense beam of electrons (5 to 50 keV) onto the samples surface, leading to three separate types of analysis:

- Secondary electrons (SE): The incident beam causes valence electrons to be ejected as it strikes the surface. Detection of these electrons gives insight into the topology and morphology of the surface.
- Backscattered electrons (BSE): Elastic interaction between the sample's nuclei and incident beam makes some electrons bounce back to the detector. Detection of these electrons gives information on the chemical homogeneity (phase contrast) of a sample as atoms produce a specific number of BSE based on their Z number. Brighter regions indicate phases containing heavier atoms, when viewed in imaging mode.
- Energy dispersive X-ray spectroscopy (EDS): X-rays are generated by the inelastic interaction between core electrons and the incident beam. Each element has a specific energy transition for this interaction, meaning that collection of these X-rays allows the chemical composition of a sample to be quantified.

Sample preparation consisted of encasing a bulk or powdered sample in epoxy resin, a 90/10 wt.% ratio of resin to hardener was used ("EPOFIX resin Struers" bisphenol-A-diglycidylether/"Epofix hardener Struers" triethylenetetramine).

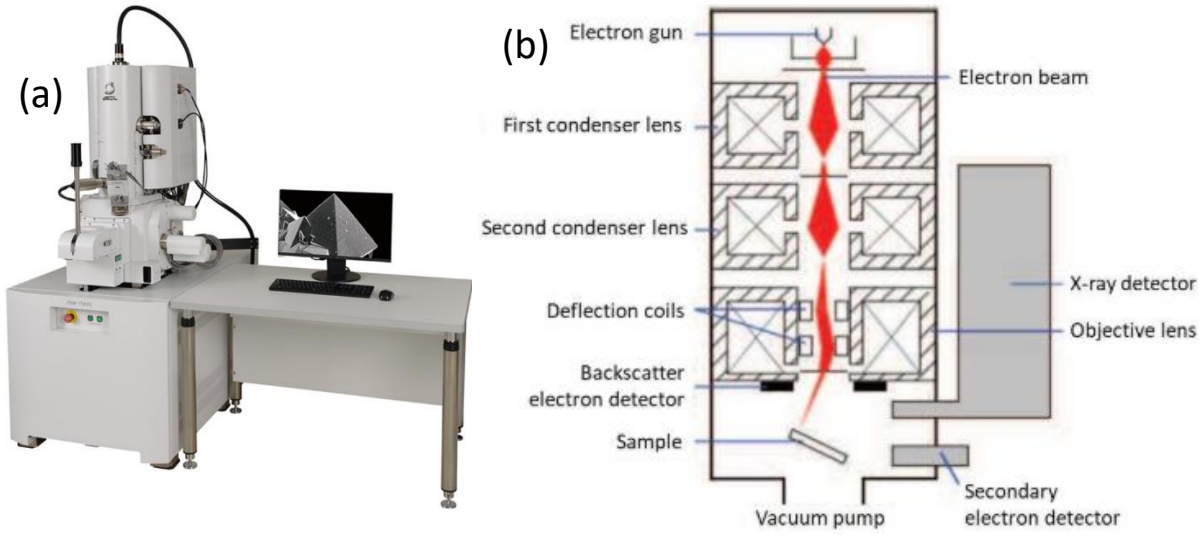

Fig. 4.10. (a) Image of the JEOL microscope. **(b)** General schematic representation of an SEM setup.

The surface of the resultant resin cylinder was then carefully polished, a crucial step in achieving high-resolution imaging. Prior to analysis, samples were carbon coated (15-20 nm) under vacuum. SEM experiments were conducted with the help of Dr. Emmanuel Veron (CEMHTI).

4.6.2. Transmission Electron Microscopy

For nanometric and even atomic scale, imaging of a sample, transmission electron microscopy (TEM) was used. This powerful technique was again an extremely useful complementary tool for verifying structural models. Samples were analysed using a CM20 transmission electron microscope operating at 200kV or a JEOL ARM200F (JEOL Ltd.) Cold FEG corrected TEM. Both were equipped with a double-tilt holder which allowed the crystals to be orientated, to examine specific orientations or zone axis. Atomic-level resolution was achieved by high angle annular dark field - scanning transmission electron Microscopy (HAADF-STEM) imaging mod, performed on the double Cs corrected JEOL ARM200F (JEOL Ltd.) Cold FEG TEM instrument.

Three imaging modes are possible in TEM mode: bright field, dark field and electron diffraction, as shown in Fig. 4.11. In bright field TEM, the aperture is tuned to only select electron intensity from the transmitted beam (000). Meaning, areas which absorb or diffract electrons will appear dark and areas which transmit electrons will appear light. In dark field mode, the aperture selects a diffracted spot, resulting in an inverted image contrast compared to the bright field mode. The brightest part of the image is at the origin of the selected diffracted spot, while the rest of the image appears darker. This mode can enhance the contrast when imagining small crystal features such as defects or stacking faults.

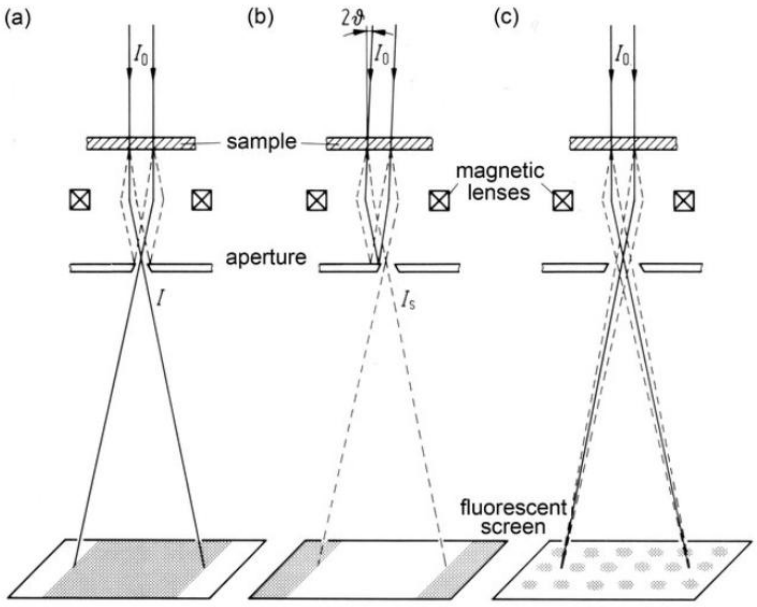

Fig. 4.11. Diagram of the different imaging modes available by TEM **(a)** Bright field **(b)** Dark field **(c)** Electron diffraction. Figure from [48].

In selected area electron diffraction mode (SAED), each *h,k,l* peak is individually viewed as diffracted spots, making it possible to determine if the sample is polyphasic. By assigning the Miller indices and examining the allowed and forbidden reflections, the crystals space group and lattice parameters can be determined, making it a powerful mode for structural determination. EDS is also possible to provide information on the chemical composition of a crystal.

Only powdered samples were analysed by TEM. For this, samples were finely ground in an agate mortar, dispersed in ethanol and then a droplet was deposited on a copper grid lined with a holey, amorphous carbon matrix. This matrix is invisible to SAED measurements and highly contrasted in the other imaging modes making it easy to differentiate the crystallites and the grid. The high number of grains within powdered samples made it possible to retrieve and identify each target *h,k,l* peak allowing for phase identification, however, sometimes problems with resolution arose due to uneven thicknesses and phase stability under the beam.

The atomic-resolution HAADF-STEM images in Chapter 2 (Section 2.4.3.), were obtained on a bulk crystallised thin foil sample. Initially, the sample was polished, using a tripod and inlaid diamond discs, to a thickness of 50µm. Then the thickness was reduced to 15-20nm by argon ion milling (PIPS GATAN), the incident beam voltage was gradually reduced to remove beam induced amorphisation. In HAADF-STEM imaging mode, a 68-174.5 mrad inner – outer collection angle and a 0.1nm probe size were used. The intensity of the acquired images is proportional to the thickness (e), the density (ρ) and the average atomic number (Z): $I \propto e\rho Z^n$ where n is in the range 1.6-2. The uniform thickness and extreme thinness of the sample permitted high-resolution atomic-level images to be obtained, which was used to confirm the Rietveld generated structural model of $Sr_{12}Al_{20}Si_{12}O_{66}$ by direct viewing of the crystalline structure. TEM and HAADF-STEM imaging was carried out by Dr. Cécile Genevois (CEMHTI).

4.7. Optical Property Measurements

4.7.1. Photoluminescence & Persistent Luminescence

Photoluminescence (PL) is the phenomenon by which a sample emits light when excited by photons. The electrons of luminescent centres (Eu^{2+}, Dy^{3+}, Cr^{3+} etc…) present in the sample absorb incoming photons and are excited out of the valence band. This transition, leaves behind an electron hole with a positive charge, (h+). Upon the release of thermal energy, electrons relax back down to these holes, releasing photons in the process. If this electronic transition is spin allowed ($\triangle S=0$), the process is called fluorescence, however, if it is spin forbidden (typically $\triangle S=1$) it is called phosphorescence. In PL, decay times are extremely short, 10^{-11} s to 10^{-8} s, meaning luminescence essentially ends when the excitation source is removed. The charge carrier responsible for the emittance of light can either be the electron or the hole. The wavelength of light produced

is dependent on the energy difference between the ground state, highest occupied molecular orbital (HOMO), and the excited state, lowest unoccupied molecular orbital (LUMO).[49]

The same principles apply to persistent luminescence (PersL), but, through the trapping of electrons, emission can last for several hours after excitation stops. As of today, no general mechanism exists to describe the afterglow effect, however, several have been suggested. The latest model is accepted here which states that photoexcitation of 4f7-5d0 to 4f6-5d1 leads to a reduction of Dy^{3+} into Dy^{2+} while the hole is kept on the Eu site, oxidising Eu^{2+} into Eu^{3+}.[50,51]

PL and PersL measurements are broken up into two parts; excitation (PLE) and emission (PL). For PLE measurements a varying high energy beam is fired at the sample while monitoring the characteristic emission peak at a fixed wavelength. PL measurements can then be conducted by fixing the incident beam at the optimum excitation wavelength, determined from the PLE measurement, and scanning the emission intensity. For PersL measurements, the sample is irradiated for a certain period of time (typically a few minutes) at the optimum PersL excitation wavelength. The PersL curve is then recorded, as a function of time, at the characteristic PersL emission wavelength.

PL, PLE and PersL measurements were conducted at room temperature on bulk and powdered samples held in quartz sample holders. An FLS1000 photoluminescence spectrometer (Edinburgh Instruments) equipped with a 450 W ozone free xenon arc lamp for excitation, was used. The arc lamp covered broadband excitation (200-1000nm) while a laser was used for specific excitation wavelengths. PersL experiments were conducted in the dark and in between measurements, samples were heated to empty all of the traps and bring any luminescence down to baseline levels. PL and PerL data were collected in collaboration with Dr. Victor Castaing and Dr. Ana I. Becerro (CSIC, Seville, Spain).

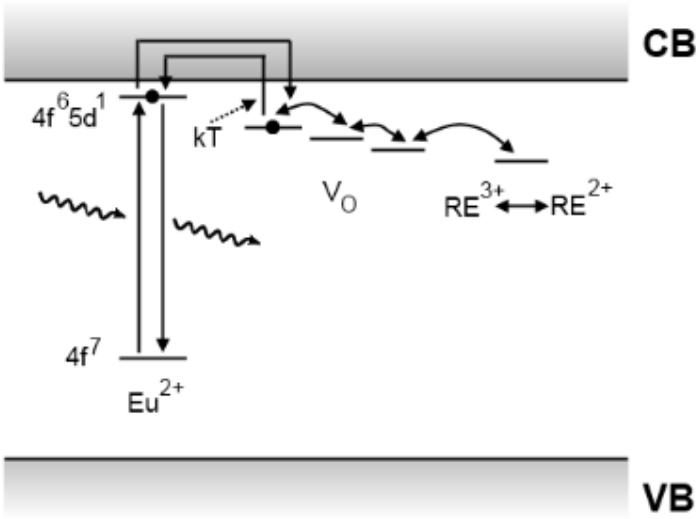

Fig. 4.12. One of the most recent PersL mechanism, proposed by Aitasalo *et al.* in 2006 for $CaAl_2O_4:Eu^{2+},Dy^{3+}$ [52] Image taken from [53].

4.7.2. Mechanoluminescence Measurements

ML is the phenomena of light emission, induced by mechanical loading.[54–56] ML measurement is a spectroscopic technique used to study the difference in PL intensity caused by this loading (compression, friction, strain etc.). PL emission is caused by the electronic transitions of absorbed electrons from discrete energy levels, as already discussed. In ML materials, mechanical loading can disrupt these energy levels causing a change in the wavelength and/or intensity of the light. Here, elastico ML (EML) in particular was examined, where light is produced through elastic deformation of the material, (Fig. 4.13.).

The exact mechanism of EML is not clearly understood, therefore the proposed mechanism for $SrAl_2O_4:Eu^{2+},Dy^{3+}$ crystals, the current best-in-class, is accepted here.[57] UV illumination induces excitation of the Eu^{2+} ions and trapping of some carriers (electrons) in deep traps. Mechanical loading then eases the de-trapping of the carriers in the traps, returning them to the excited state. The de-excitation of these electrons is what produces photon emission.

For ML measurement to be conducted, specimens were first exposed to UV light (365 nm) for 30 s prior to mechanical testing, with the loading cycle starting 50, 100 or 1000 seconds later (depending on PL intensity of the sample, the phosphorescence background emission needed to become negligible in comparison with the EML intensity). Uniaxial compression tests were carried out on 4(width) × 4(depth) × 4.5(height) mm^3 parallelepiped sample specimens (Fig. 4.14.(a)), which allowed an even force to be applied across the surface. A Schimadzu-AGS-X testing machine equipped with a 10 kN load cell and a SiC pusher, was used for compression (Fig. 4.14.(b)(c)). The luminescence intensity was measured using a Zyla 5.5 sCMOS Andor Technology high sensitivity camera.

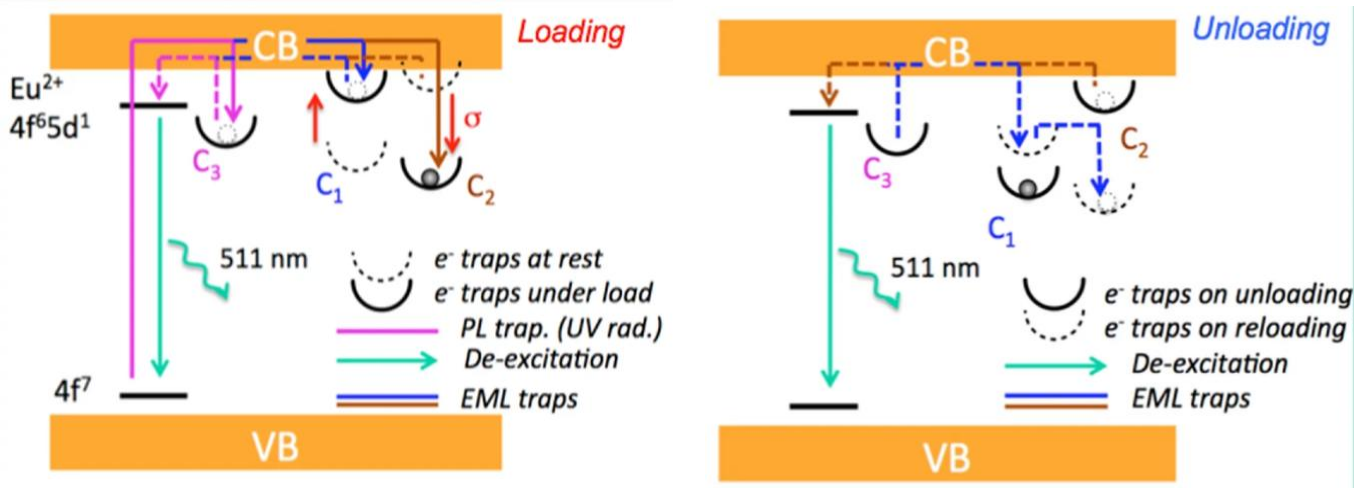

Fig. 4.13. Proposed mechanism of EML for a general system with Eu^{2+} as the doped RE. From [58].

The stress, σ, created in all the samples, was calculated according to the following formula:

$$\sigma = \frac{F}{S} \qquad \textbf{(Eq. 4.18)}$$

Where σ is calculated in Pascals (Pa), by the strength, F, in Newtons (N) and the surface, S, in m^2.

The effect of mechanical loading was then made clear by plotting the luminescence as a function of time and stress applied. ML measurements were conducted by Patrick Houizot at the university of Rennes.

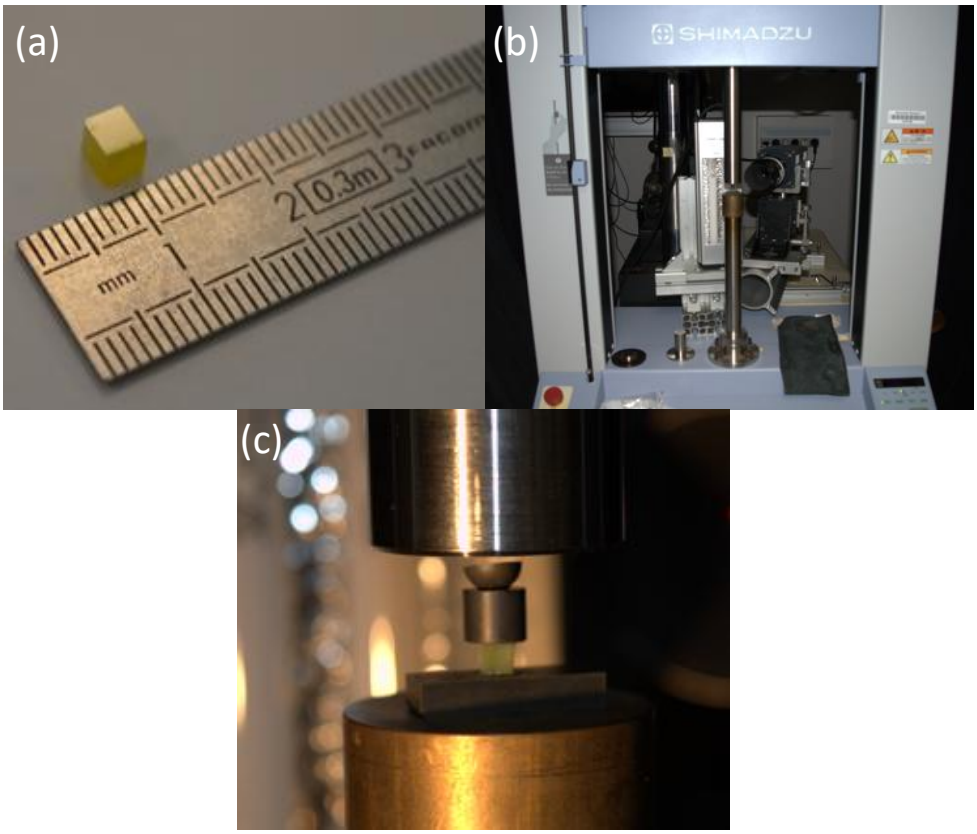

Fig. 4.14. (a) Image of the Sr2Si3O8 (Chapter 3) sample prepared for ML measurement. **(b)** Shimadzu machine used to apply stress on the materials. **(c)** Image of the same sample about to be compressed for ML measurement.

A.8. References

[1] S. Musikant, in *Encyclopedia of Physical Science and Technology (Third Edition)*, ed. R. A. Meyers, Academic Press, New York, 2003, pp. 781–806.

[2] K. G. Webber, O. Clemens, V. Buscaglia, B. Malič, R. K. Bordia, T. Fey and U. Eckstein, *Journal of the European Ceramic Society*, 2024, **44**, 116780.

[3] A. Duval, P. Houizot and T. Rouxel, *J Am Ceram Soc.*, 2023, **106**, 1611–1637.

[4] M. Min, J. Cho, K. Cho and H. Kim, *Electrochimica Acta*, 2000, **45**, 4211–4217.

[5] Alexis Duval. Elaboration, structure and mechanical characterization of oxynitride glasses and mechanoluminescent glass-ceramics from the BaO-SiO_2-Si_3N_4 chemical system. 2023.

[6] R. Iordanova, M. Gancheva, I. Koseva, P. Tzvetkov and P. Ivanov, *Materials*, DOI:10.3390/ma17153724.

[7] X. Zhi and A. R. West, *Chem. Mater.*, 2023, **35**, 6790–6798.

[8] A. Jabbarzadeh and B. Halfina, *Nanoscale Adv.*, 2019, **1**, 4704–4721.

[9] W. Nai-Ning, Z. Hong-Jian and Y. Xian-Huang, *Advanced Powder Technology*, 1992, **3**, 7–14.

[10] X. Fang, V. Castaing, A. Becerro, W. Cao, E. Veron, D. Zanghi, M. Dyer, C. Genevois, M. Allix and M. Pitcher, 2024, preprint, DOI: 10.26434/chemrxiv-2024-1s1wc.

[11] S. Garcia-Granda and J. M. Montejo-Bernardo, in *Reference Module in Chemistry, Molecular Sciences and Chemical Engineering*, Elsevier, 2013.
[12] C. Gilmore, G. Barr and W. Dong, .
[13] W. Pitschke, H. Hermann and N. Mattern, *Powder Diffraction*, 1993, **8**, 74–83.
[14] J. A. Kaduk, S. J. L. Billinge, R. E. Dinnebier, N. Henderson, I. Madsen, R. Černý, M. Leoni, L. Lutterotti, S. Thakral and D. Chateigner, *Nature Reviews Methods Primers*, 2021, **1**, 77.
[15] H. Dittrich and A. Bieniok, in *Encyclopedia of Electrochemical Power Sources*, ed. J. Garche, Elsevier, Amsterdam, 2009, pp. 718–737.
[16] W. L. S. Bragg, Proc. Camb. Phil. Soc., XVII (I), 1912, pp. 43-57. .
[17] U. Holzwarth and N. Gibson, *Nature Nanotechnology*, 2011, **6**, 534–534.
[18] Nilforoushan, Niloufar. (2018). Out-of-equilibrium electron dynamics of Dirac semimetals and strongly correlated materials.
[19] A. J. Fernandez-Carrion, K. Al Saghir, E. Veron, A. I. Becerro, F. Porcher, W. Wisniewski, G. Matzen, F. Fayon and M. Allix, *Inorg. Chem.*, 2017, **56**, 14446–14458.
[20] Y. Xiao and Z. Fu, in *Encyclopedia of Nanomaterials (First Edition)*, eds. Y. Yin, Y. Lu and Y. Xia, Elsevier, Oxford, 2023, pp. 65–86.
[21] H A Hauptman, *Reports on Progress in Physics*, 1991, **54**, 1427.
[22] G. Oszlányi and A. Süto, *Acta Crystallographica Section A*, 2004, **60**, 134–141.
[23] D. Louër and A. Boultif, in *Prague, September 2-5, 2004*, Oldenbourg Wissenschaftsverlag, 2006, pp. 225–230.
[24] B. O'Connor and D. Li, D.Li, Influence of Refinement Strategies on Rietveld Phase Composition Determinations, 2000, https://api.semanticscholar.org/CorpusID:18260240.
[25] G. S. Pawley, *Journal of Applied Crystallography*, 1981, **14**, 357–361.
[26] A. Le Bail, H. Duroy and J. L. Fourquet, *Materials Research Bulletin*, 1988, **23**, 447–452.
[27] L. Palatinus and G. Chapuis, *Journal of Applied Crystallography*, DOI:10.1107/S0021889807029238.
[28] V. Petrícek, M. Dusek and L. Palatinus, *Zeitschrift für Kristallographie - Crystalline Materials*, DOI:10.1515/zkri-2014-1737.
[29] L. Palatinus, *NATO Science for Peace and Security Series B: Physics and Biophysics*, 2012, 105.
[30] J. Wu, K. Leinenweber, J. C. H. Spence and M. O'Keeffe, *Nature Materials*, 2006, **5**, 647–652.
[31] D. Delahaye, S. Chaimatanan and M. Mongeau, in *Handbook of Metaheuristics*, eds. M. Gendreau and J.-Y. Potvin, Springer International Publishing, Cham, 2019, pp. 1–35.
[32] H. M. Rietveld, *Physica Scripta*, 2014, **89**, 098002.
[33] K. Siegert, F. Lange, R. Sittner, H. Volker, C. Schlockermann and M. Wuttig, *Reports on progress in physics. Physical Society (Great Britain)*, 2014, **78**, 013001.
[34] R. P. Ozerov and A. A. Vorobyev, in *Physics for Chemists*, eds. R. P. Ozerov and A. A. Vorobyev, Elsevier, Amsterdam, 2007, pp. 423–496.
[35] B. Reif, S. E. Ashbrook, L. Emsley and M. Hong, *Nature Reviews Methods Primers*, 2021, **1**, 2.
[36] J.-P. Amoureux, C. Fernandez and S. Steuernagel, *Journal of magnetic resonance. Series A*, 1996, **123 1**, 116–8.
[37] R. Harris, E. Becker, S. Menezes, P. Granger, R. Hoffman and K. Zilm, *Magnetic resonance in chemistry : MRC*, 2008, **46**, 582–98.
[38] K. Okhotnikov, T. Charpentier and S. Cadars, *Journal of Cheminformatics*, 2016, **8**, 17.
[39] P. Hohenberg and W. Kohn, *Phys. Rev.*, 1964, **136**, B864–B871.
[40] D. M. Ceperley and B. J. Alder, *Phys. Rev. Lett.*, 1980, **45**, 566–569.
[41] S. Clark, M. Segall, C. Pickard, P. Hasnip, M. Probert, K. Refson and M. Payne, *Zeitschrift für Kristallographie*, DOI:10.1524/zkri.220.5.567.65075.
[42] M. Segall, P. Lindan, M. Probert, C. Pickard, P. Hasnip, S. Clark and M. Payne, *Journal of Physics: Condensed Matter*, 2002, **14**, 2717.
[43] J. P. Perdew, K. Burke and M. Ernzerhof, *Phys. Rev. Lett.*, 1996, **77**, 3865–3868.
[44] D. Vanderbilt, *Phys. Rev. B*, 1990, **41**, 7892–7895.
[45] J. R. Yates, C. J. Pickard and F. Mauri, *Phys. Rev. B*, 2007, **76**, 024401.
[46] A. R. Ferreira, *J. Phys. Chem. C*, 2019, **123**, 9371–9381.
[47] C. J. Pickard and F. Mauri, *Phys. Rev. B*, 2001, **63**, 245101.
[48] Wiese, Nils. Coupling phenomena and scalability of CoFeB/Ru/CoFeB sandwiches.
[49] A. C. Sparavigna, *International Journal of Sciences*, DOI:10.18483/ijSci.593.
[50] D. Van der Heggen, J. J. Joos, A. Feng, V. Fritz, T. Delgado, N. Gartmann, B. Walfort, D. Rytz, H. Hagemann, D. Poelman, B. Viana and P. F. Smet, *Advanced Functional Materials*, 2022, **32**, 2208809.
[51] J. J. Joos, K. Korthout, L. Amidani, P. Glatzel, D. Poelman and P. F. Smet, *Phys. Rev. Lett.*, 2020, **125**, 033001.
[52] T. Aitasalo, J. Hölsä, H. Jungner, M. Lastusaari and J. Niittykoski, *J. Phys. Chem. B*, 2006, **110**, 4589–4598.
[53] K. Van Den Eeckhout, P. F. Smet and D. Poelman, *Materials*, 2010, **3**, 2536–2566.
[54] B. P. Chandra, in *Luminescence of Solids*, ed. D. R. Vij, Springer US, Boston, MA, 1998, pp. 361–389.
[55] J.-C. Zhang, X. Wang, G. Marriott and C.-N. Xu, *Progress in Materials Science*, 2019, **103**, 678–742.
[56] A. Feng and P. F. Smet, *Materials*, DOI:10.3390/ma11040484.
[57] P. Jha and B. P. Chandra, *Journal of Luminescence*, 2013, **143**, 280–287.
[58] M. Dubernet, E. Bruyer, Y. Gueguen, P. Houizot, J. C. Hameline, X. Rocquefelte and T. Rouxel, *Scientific Reports*, 2020, **10**, 19495.

Annexes I, II, & III to the Main Text

Annex I – Introduction of Extended Defects in Rietveld Models of $Sr_2Si_3O_8$

The observed shift of the peaks at 25° (2, 0, 2) and 28° (3, 1, -2) when the $Sr_2Si_3O_8$:Al and $Sr_2Si_3O_8$ PXRD patterns were compared, (Fig. 3.18.(b)), suggested the presence of a structural defect. However, the instability of $Sr_2Si_3O_8$ to atomic-resolution analysis techniques such as HAADF-STEM prevented a study of the defect's origin. This lack of data hindered the Rietveld methods ability to model it, however, attempts were made regardless.

Through structural comparison of $Sr_2Si_3O_8$ and its Ba analogue $Ba_4Si_6O_{16}$, a common structural motif was found; $[Si_6O_{16}]^{4-}$ ribbons stacked in an antiparallel configuration. However, in $Sr_2Si_3O_8$ the arrangement is checkerboard-like, whereas in $Ba_4Si_6O_{16}$ a stripe-like arrangement is observed (Fig. 1.). This change in stacking arrangement could explain the origin of the defect and the shoulder on the peak at 28°. To tests this a theoretical *P*1 unit cell was created which had a +(1/18) displacement shift of each consecutive layer along the *a*- axis, which permitted the $[Si_6O_{16}]^{4-}$ ribbons to stack in a similar way as $Ba_4Si_6O_{16}$, i.e. a stripe-like stacking fault, using the supercell approach implemented in TOPASV7. In this approach the structure is constructed from modules which are stacked along one axis, with the length of the stack (number of modules) defined by the user. Extended defects (stacking faults, shear planes) can be introduced by using different modules, or by shifting a module perpendicular to the stacking axis. Each defined defect is assigned a nominal probability of occurring (between 0 and 1), which can be refined against the data. Unlike a classic Rietveld refinement, the atomic coordinates (atom positions within the modules) are typically fixed to limit the number of refined parameters. Rietveld modelling was again attempted, on both the original $Sr_2Si_3O_8$:Al, and optimised $Sr_2Si_3O_8$ PXRD data.

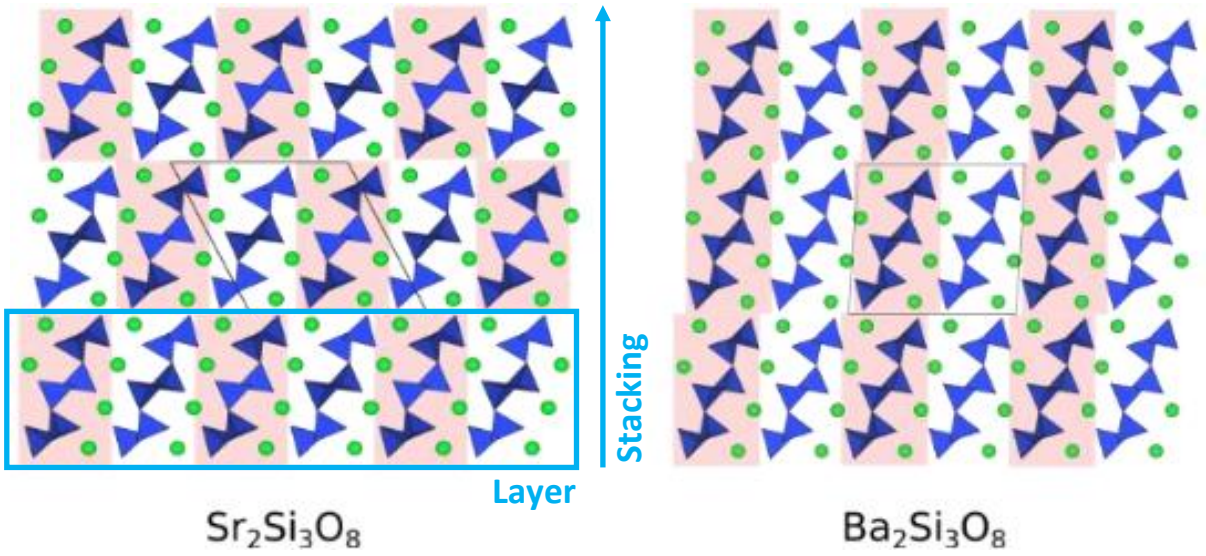

Fig. 1. Comparison of the $[Si_6O_{16}]^{4-}$ ribbon stacking arrangements in $Sr_2Si_3O_8$ and $Ba_2Si_3O_8$. The red boxes show the checkerboard and stripe like packing arrangements, respectively, while the blue rectangle shows the layer displaced to create the theoretical unit cell.

A reasonable R_{wp} of 10.4% was achieved for $Sr_2Si_3O_8$:Al while a much worse R_{wp} of 38.2% was achieved for $Sr_2Si_3O_8$, both refinements are shown in Fig. 2. Clearly, this modification to the $P2_1/c$ model failed to account for the defect and so other models were theorised.

Shear defects in the *a/b*- plane, (using the same +(1/18) layer displacement), rotation about the *c*- axis (i.e. twin fault) and the inclusion of thicker layers along the stacking direction were all attempted. As neither of these simple models provided any hint of improvement to the Rietveld fit, and with no other technique to guide the development of other more plausible microstructural defect models (such as atomic resolution HAADF-STEM), no further progress was made on this analysis.

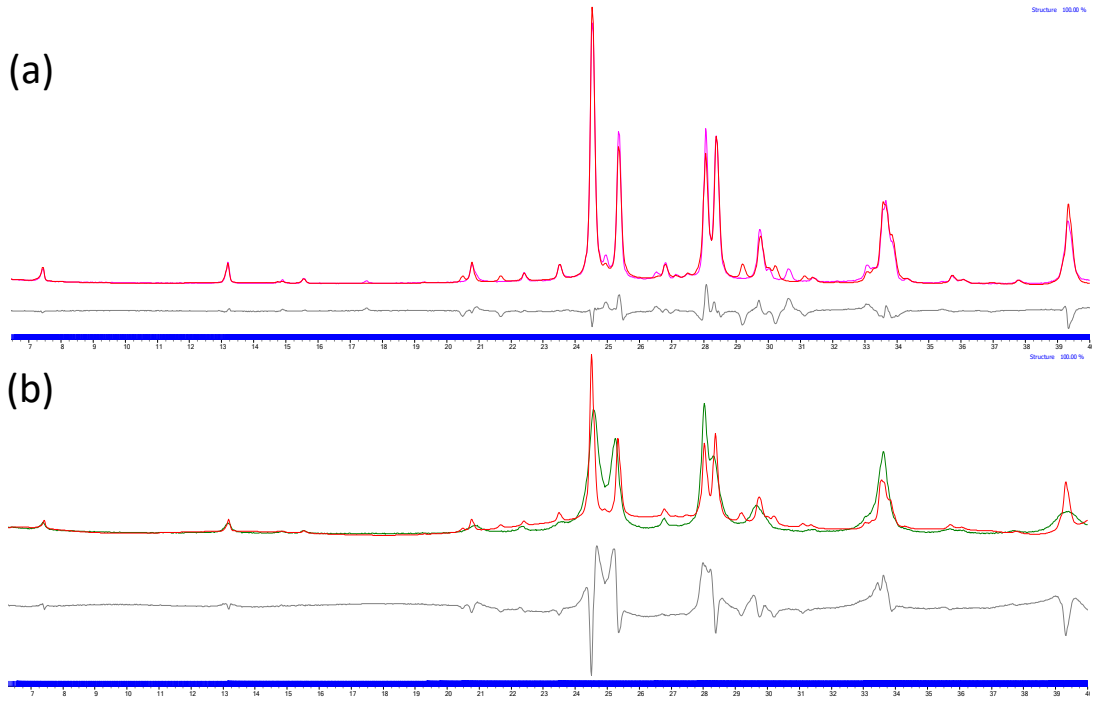

Fig. 2. Rietveld refinement achieved on **(a)** $Sr_2Si_3O_8$:Al (R_{wp} of 10.4%) and **(b)** $Sr_2Si_3O_8$ (R_{wp} of 38.2%), using the *P*1 stacking fault model and Lab-PXRD data.

Annex II – $Sr_2Si_3O_8$ Glass & Glass-Ceramic Formation by Aerodynamic Levitation Coupled to Two CO_2 Lasers

An alternative route to glass formation which was considered in this work was aerodynamic levitation (ADL) coupled to two CO_2 lasers. It was theorised that the faster cooling rates of ADL compared to classic melt-quenching would provide a more homogenised glass and therefore permit a higher crystalline phase fraction of $Sr_2Si_3O_8$. This also aided in determining if GC, via melt-quenching methods, was indeed the optimum synthesis route. The high SiO_2 content of $Sr_2Si_3O_8$, permitted glass beads of varying sizes to be synthesised (Fig. 3.(a)). Two of these glass beads were then crystallised (marked by asterixis in Fig. 3.(a)), while the rest were crushed and sintered as powdered pellets. The optimised annealing protocol of 12h at 850°C was used for these experiments.

The PXRD patterns of the crystallised bulk beads showed broad unresolved peaks and a large amorphous bump, which was reasoned to be due to the reduced surface area of the bulk samples. The PXRD patterns of the powder crystallised samples showed better crystallinity and a flatter backgrounder and so Rietveld refinement was attempted (Fig. 3.(b)), after high-quality lab-PXRD data had been collected. The same refinement file discussed in Section 3.3.1. was used, with a R_{wp} of 11.5% and χ of 2.1 being achieved. These values were higher than those achieved for $Sr_2Si_3O_8$ prepared by melt-quenching methods, R_{wp} = 7.093%. Moreover, the shoulder peak at 28° (3, 1, -2) was still not able to be modelled with additional intensity issues now observed on the main peak. Additionally, although the glass content the sample was not analysed, qualitatively a reasonable amorphous bump could be viewed below the main phase peaks.

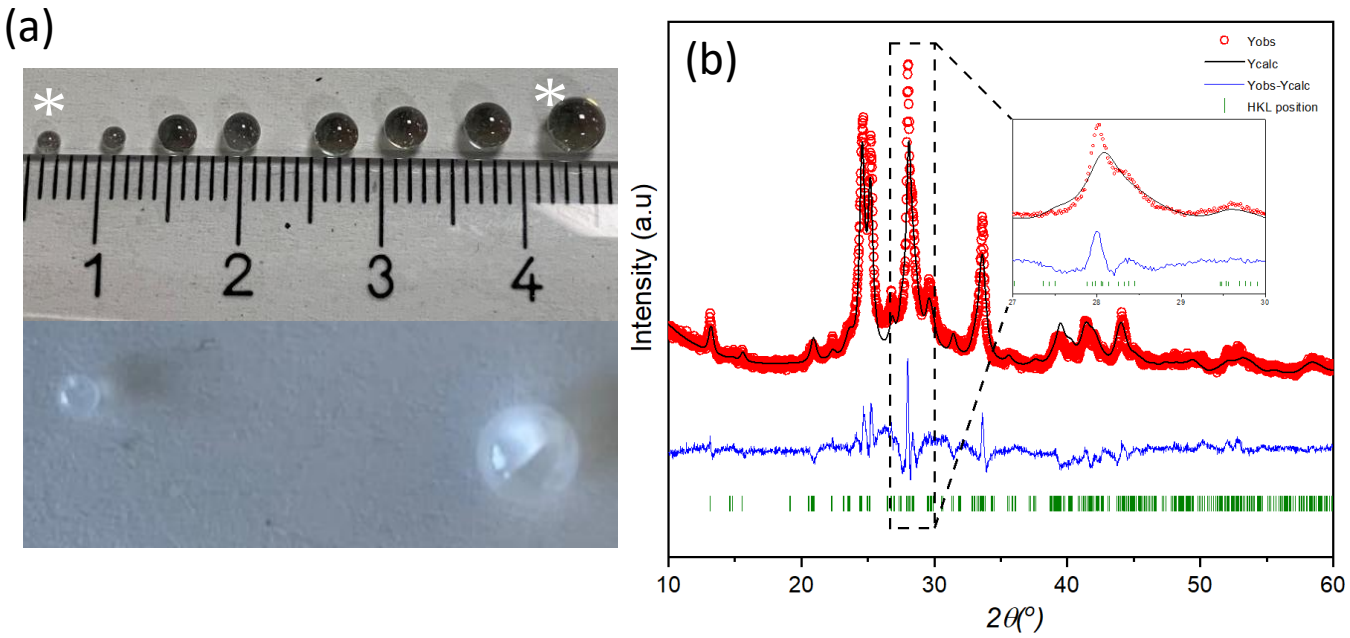

Fig. 3.(a) Transparent beads made by ADL, before and after crystallisation. **(b)** Rietveld refinement of the powder sintered (12h 850°C) $Sr_2Si_3O_8$ glass (R_{wp}=11.5%), which had been prepared by ADL. Inset shows a zoom of the refinement achieved for the 28° (3, 1, -2) shoulder bump.

Crystallisation of $Sr_2Si_3O_8$ directly from the melt was also tried by ADL. It was discovered that when the molten bead was cooled to room temperature from 1600°C, over a relatively long period of time (~7 mins), crystallisation could be induced. This synthesis protocol resulted in opaque beads, however PXRD analysis of these samples revealed that only the thermodynamically stable product $SrSiO_3$ (*C2/c*) had formed. Ultimately, it was concluded that ADL was not the optimum synthesis route for both crystal and glass production of $Sr_2Si_3O_8$. Despite ADL readily forming glass the low scalability of the technique, when compared to melt-quenching methods, prevented its usage for glass formation.

Annex III – The Intermediate Structure of $Sr_{1.9}Ca_{0.1}Si_3O_8$

In the exploration of certain substitutions and nucleating agents, (sub. Ba^{2+} and Ca^{2+}, nuc. agent's Ag and Au) a new or intermediate phase was observed forming. The greatest temperature stability range of this phase was observed by *in-situ* VTXRD of $Sr_{1.9}Ca_{0.1}Si_3O_8$ (yellow zone of Fig. 4.(a)), and so analysis continued on this phase.

Fig. 4.(a), shows that this new intermediate phase forms between 1010-1070°C, with the highest intensity of new phase peaks found at 1020°C. The PXRD pattern at this temperature was isolated, so that phase indexation could be attempted, using EVA software, however no phase was found. Which suggested that either a new phase had formed or that the pattern was not of high enough quality to be indexed. DSC analysis of $Sr_{1.9}Ca_{0.1}Si_3O_8$ was consulted to begin *ex-situ* optimisation of new phase synthesis. It was believed that the small feature at ~1050°C, corresponded to formation of the new phase, which combined with *in-situ* VTXRD gave a synthesis range of 1010-1070°C.

4-hour annealing trials were conducted at 10°C intervals in the temperature range 1010-1070°C, on powdered pelletised samples of $Sr_{1.9}Ca_{0.1}Si_3O_8$. Synthesis at 1020°C was found to yield the highest intensity of new phase peaks (in a mixed phase sample) and so structural determination was attempted on this sample (Fig. 4.(b)). Additionally, it was found, upon comparing the PXRD pattern of this sample to those collected from $Sr_2Si_3O_8$ sintered for 24h at 950°C, the unidentified phase also formed in low concentrations under this thermal treatment. However, again these peaks could not be indexed to any known phase.

To determine if the new peaks represented a phase transition to a new polymorph of $Sr_2Si_3O_8$, rather than an entirely new phase. First the 4h 1020°C PXRD pattern was auto-indexed, focussing solely on the unindexed peaks, to generate new space groups to describe the structure. Through this the space groups, *P*2/*m* (*a*=4.454(1)*Å*, *b*=18.054(4)*Å*, *c*=4.270(1)*Å*, *β*=93.28(2)°) and *Pna*21 (*a*=9.948(5)*Å*, *b*=12.380(3)*Å*, *c*=3.781(1)*Å*, β=90°), were all identified as possible solutions. However, when Pawley refinements were attempted using these space groups and the data collected on 4h 1020°C sintered $Sr_{1.9}Ca_{0.1}Si_3O_8$ a reasonable fit was never achieved. *P*2/*m* provided the best refinement, R_{wp}=10.42%, moreover, its lattice parameters related to those of the *P*21/*c* $Sr_2Si_3O_8$ model (*a*=13.34(1)*Å*, *b*=4.565(5)*Å*, *c*=13.49(1)*Å*, *β*=116.50(2)°), with the *a*- and *c*- axis being ~4x larger and the *b*- axis being ~3x smaller. Making the *P*2/*m* model the most plausible solution discovered so far.

As it was not possible to solve the crystal structure, the question of whether this phase represented an entirely new phase or if it was simply the decomposition of $Sr_2Si_3O_8$ into $SrSiO_3$, (whose (*C*2/*c*) space group also provided a good Pawley refinement). To determine this, Rietveld refinements were attempted on each isolated *in-situ* VTXRD pattern, between 850-1150°C, (Fig. 4.(a)) using a combined refinement file of $Sr_2Si_3O_8$ ($P2_1/c$) and $SrSiO_3$ (*C*2/*c*).

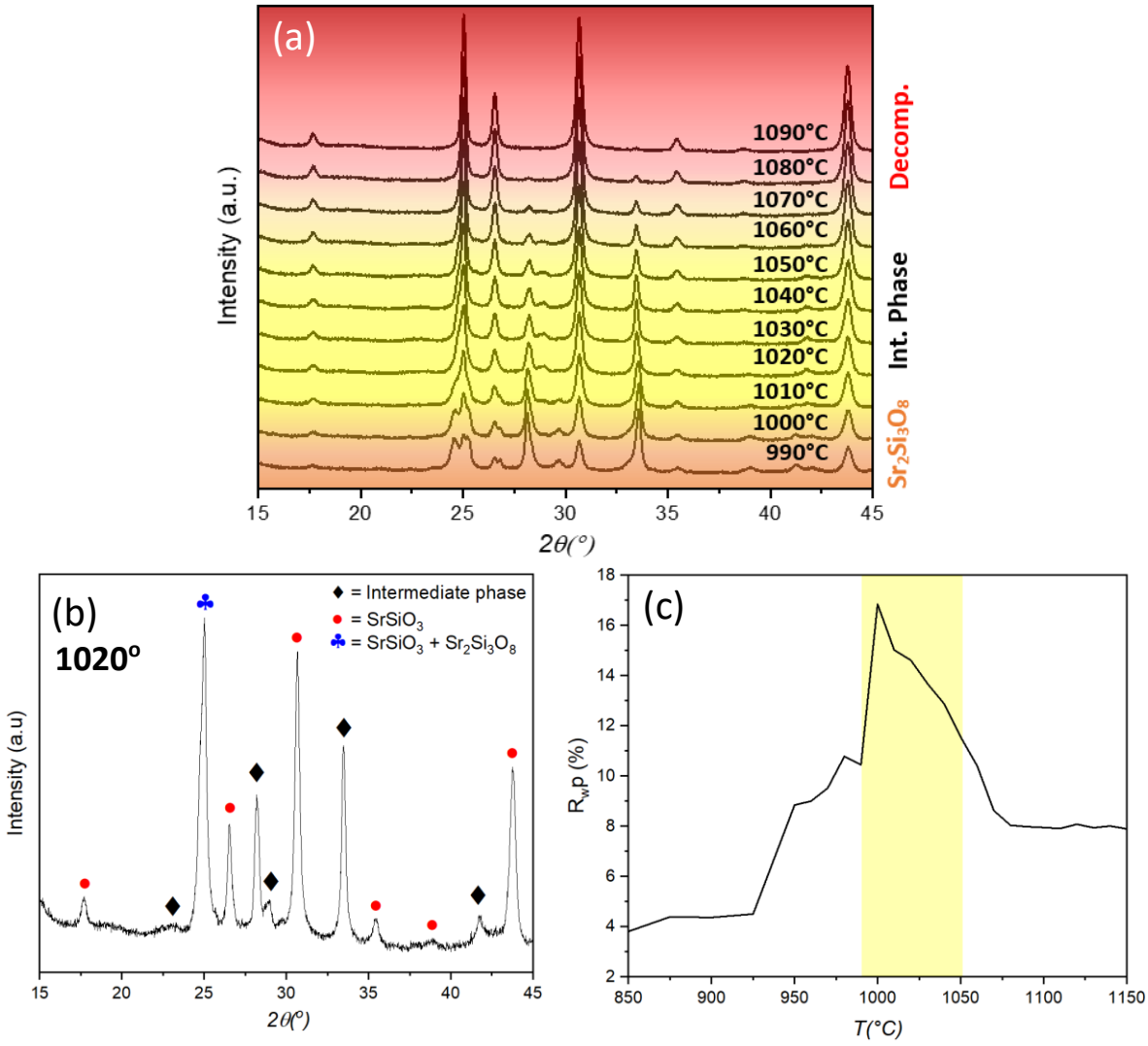

Fig. 4. (a) *In-situ* VTXRD of $Sr_{1.9}Ca_{0.1}Si_3O_8$, conducted on powdered glass between 900-1200°C, with measurements every 10°C. **(b)** Lab-PXRD pattern of *ex-situ* glass crystallised sample, showing the highest intensity of new phase peaks, each phase present is annotated. **(c)** R_{wp} vs. temperature plot, showing the formation and decomposition of the intermediate phase.

At 850°C, the pure $Sr_2Si_3O_8$ ($P2_1/c$) phase is observed, while at 1150°C, the fully decomposed $SrSiO_3$ ($C2/c$) is observed. However, between these temperatures neither space groups fit the data. The R_{wp} values from these fits were plotted against their respective temperatures, (Fig. 4.(c)). Clearly, an increase in R_{wp} values is observed between 950-1050°C, similar to the temperature range identified from *in-situ* VTXRD, which suggests that a new phase is forming. However, this analysis cannot confirm the structural uniqueness of this phase, i.e. whether it is a phase shift to a new polymorph of $SrSiO_3$ or $Sr_2Si_3O_8$ or an entirely new phase. It's small temperature stability range and poorly resolved peaks made finding the solution challenging, meaning future work should focus on expanding the synthesis range and crystalline phase fraction of the unindexed peaks.

Supplementary Information

Appendix 1 – Supplementary Information for Chapter 2

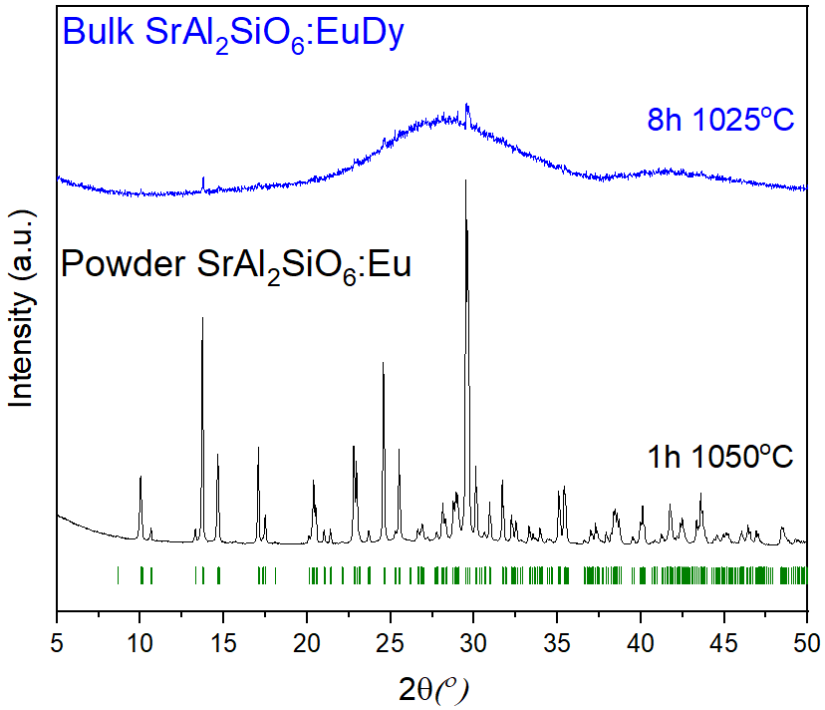

Fig. A.2.1. Comparison of the room temperature lab-PXRD data collected on $SrAl_2SiO_6:Eu^{2+}$ (1h 1050°C) and $SrAl_2SiO_6:Eu^{2+},Dy^{3+}$ (8h 1025°C), prepared as a powdered and bulk sample respectively, the weak reflections of the bulk sample match the main peaks of the powdered sample.

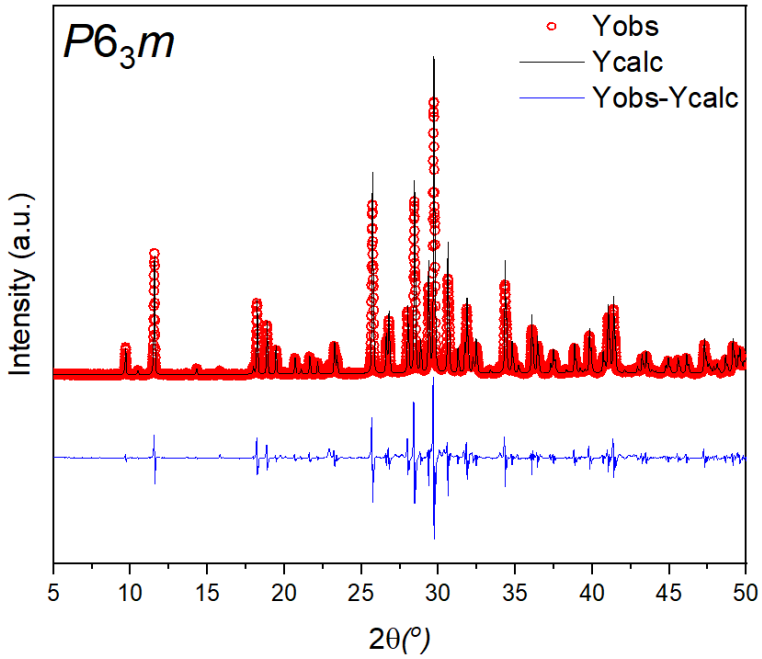

Fig. A.2.2. Pawley refinement of room temperature lab-PXRD data of $Sr_{1.35}Al_{2.7}Si_{1.3}O_8$ (AQ 1h 1075°C) using a $P6_3m$ space group.

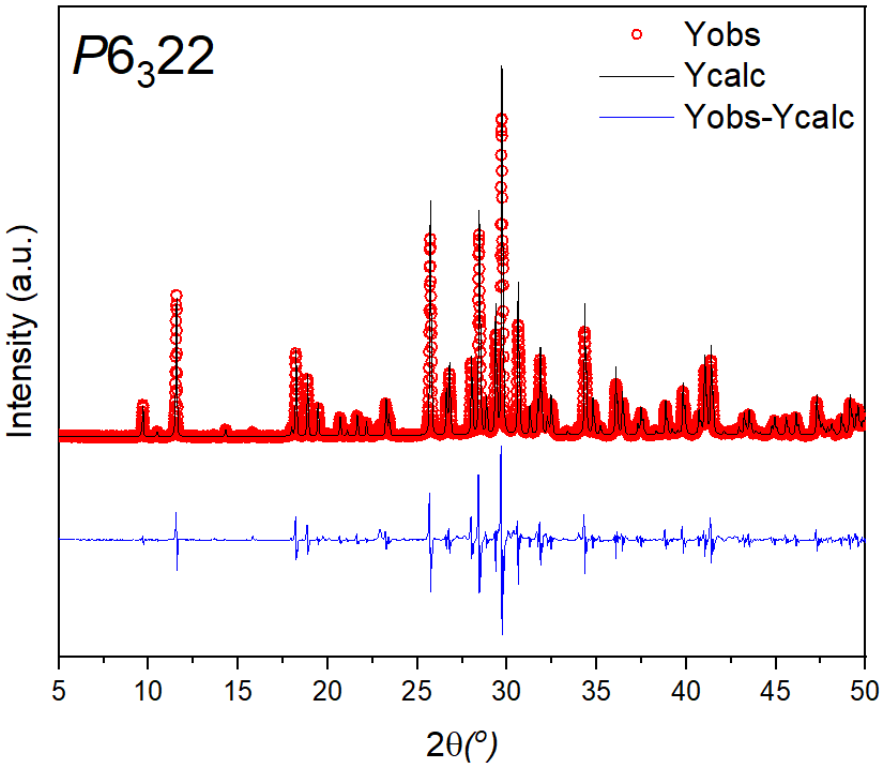

Fig. A.2.3. Pawley refinement achieved on room temperature lab-PXRD data of $Sr_{1.35}Al_{2.7}Si_{1.3}O_8$ (AQ 1h 1075°C) using a *P*6$_3$22 space group.

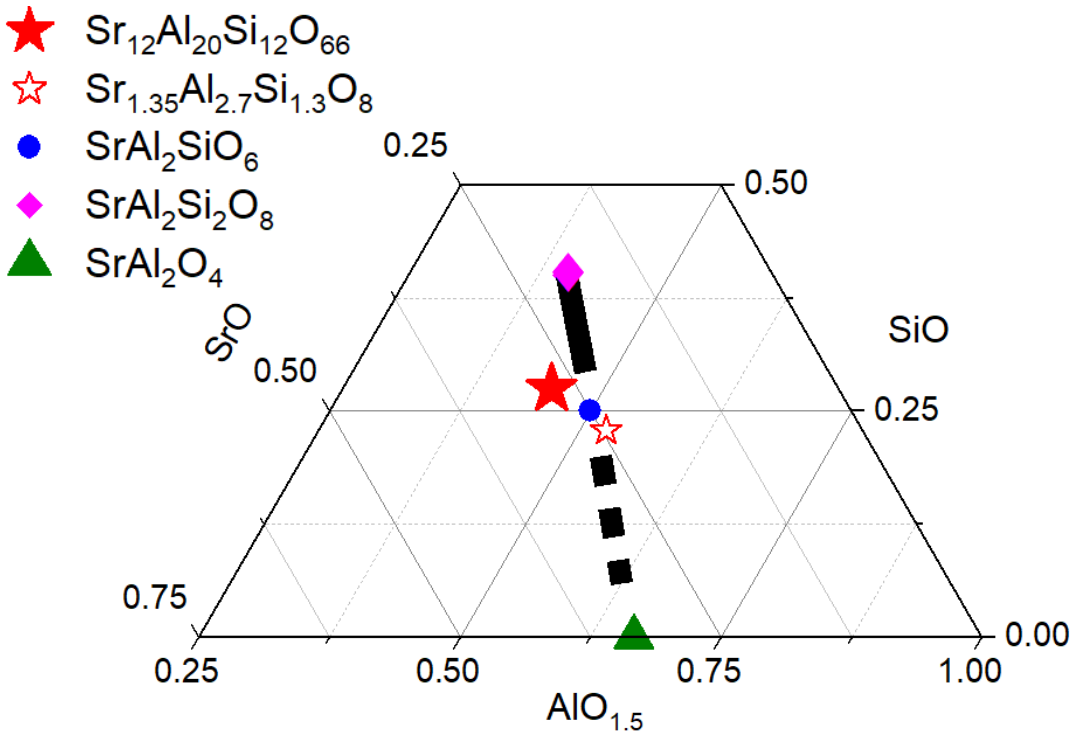

Fig. A.2.4. Zoom of the SrO-$AlO_{1.5}$-SiO_2 ternary diagram showing the positions of the original ($Sr_{1.35}Al_{2.7}Si_{1.3}O_8$, hollow red star) formula and new ($Sr_{12}Al_{20}Si_{12}O_{66}$, filled red star) formula, compared to $SrAl_2SiO_6$ (blue) and the two solid solutions, $Sr_{1-X/2}Al_{2-2X}Si_XO_4$ (dashed black line) and $Sr_{1+x/2}Al_{2+x}Si_{2-x}O_8$ (solid black line).

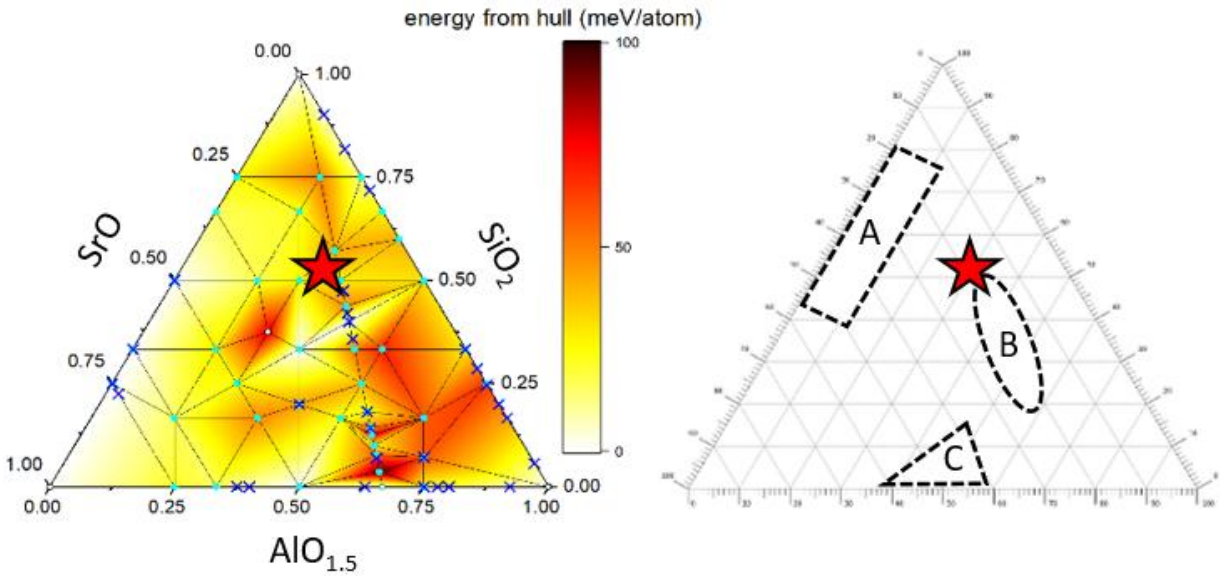

Fig A.2.5. Computationally generated SrO-$AlO_{1.5}$-SiO_2 ternary diagram showing the $Sr_{12}Al_{20}Si_{12}O_{66}$ point, which lay just outside the energy threshold used for investigation. On the right the three zones selected for investigation are shown, with the $Sr_{12}Al_{20}Si_{12}O_{66}$ point lying on the edge of zone B.

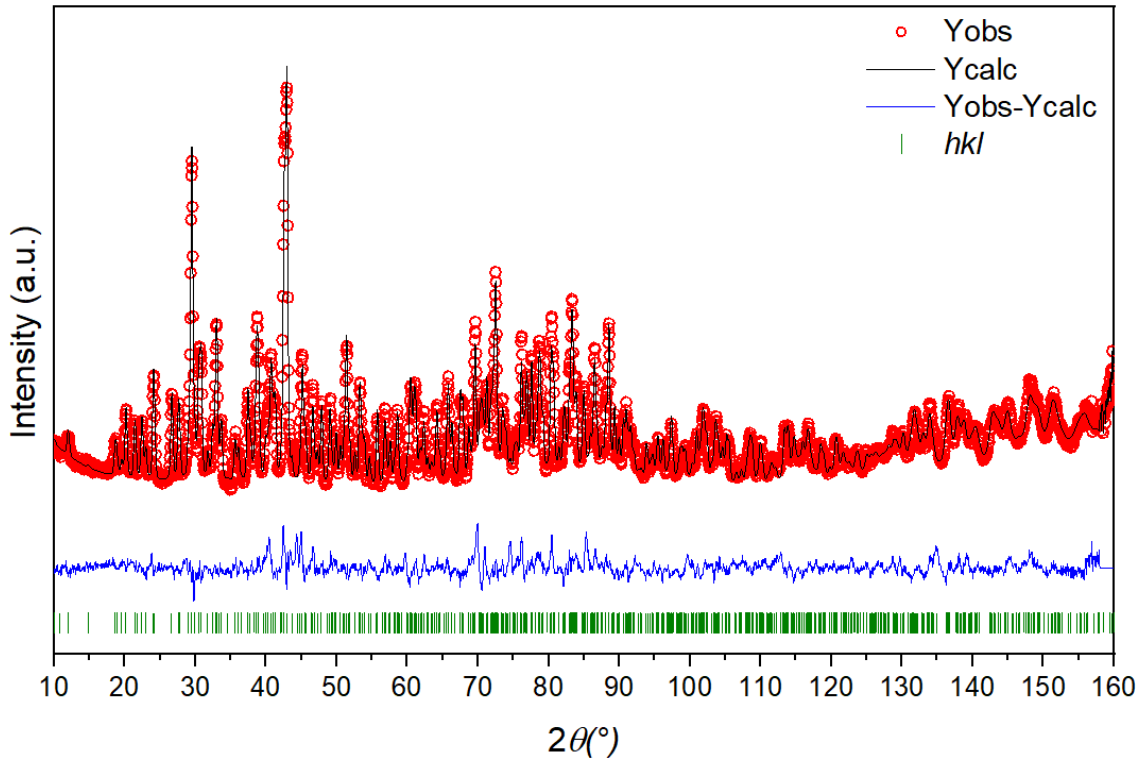

Fig. A.2.6. Rietveld refinement of the NPD data collected on a sample of crystallised optimised AQ $Sr_{1.35}Al_{2.7}Si_{1.3}O_8$ sample. λ=2.3996*Å*.

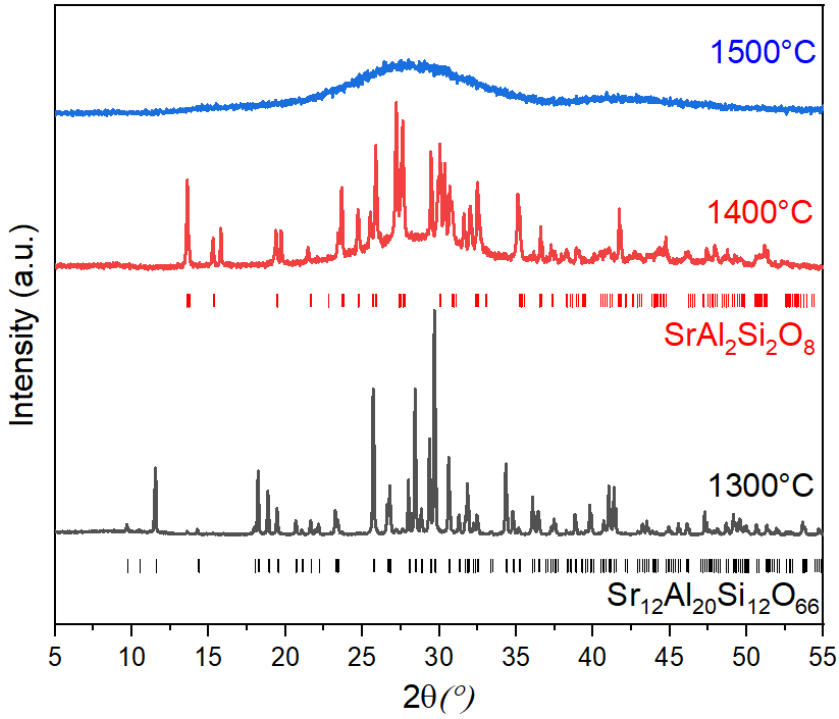

Fig. A.2.7. *Ex-situ* GC's performed on pelletised $Sr_{12}Al_{20}Si_{12}O_{66}$ glass powder, showing the decomposition of the new phase into nominal $SrAl_2Si_2O_8$ (*C2/m*) at 1400°C.

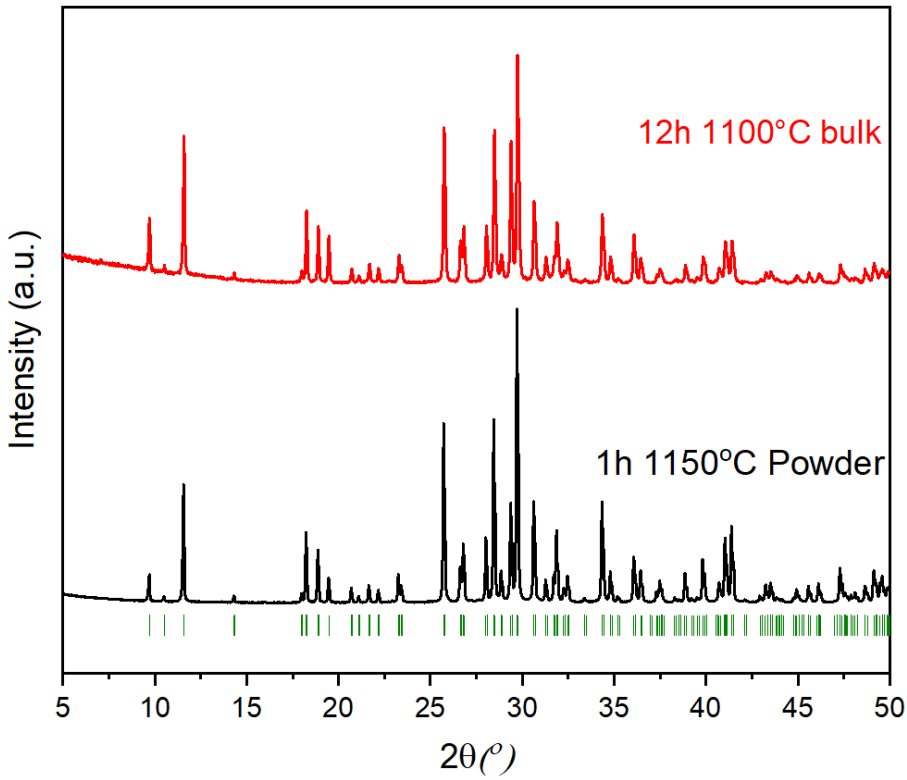

Fig. A.2.8. Comparison of the room temperature lab-PXRD's data collected on crushed samples of - powdered P4-$Sr_{12}Al_{20}Si_{12}O_{66}$ (1h 1150°C) and bulk P4-$Sr_{12}Al_{20}Si_{12}O_{66}$ (12h 1100°C).

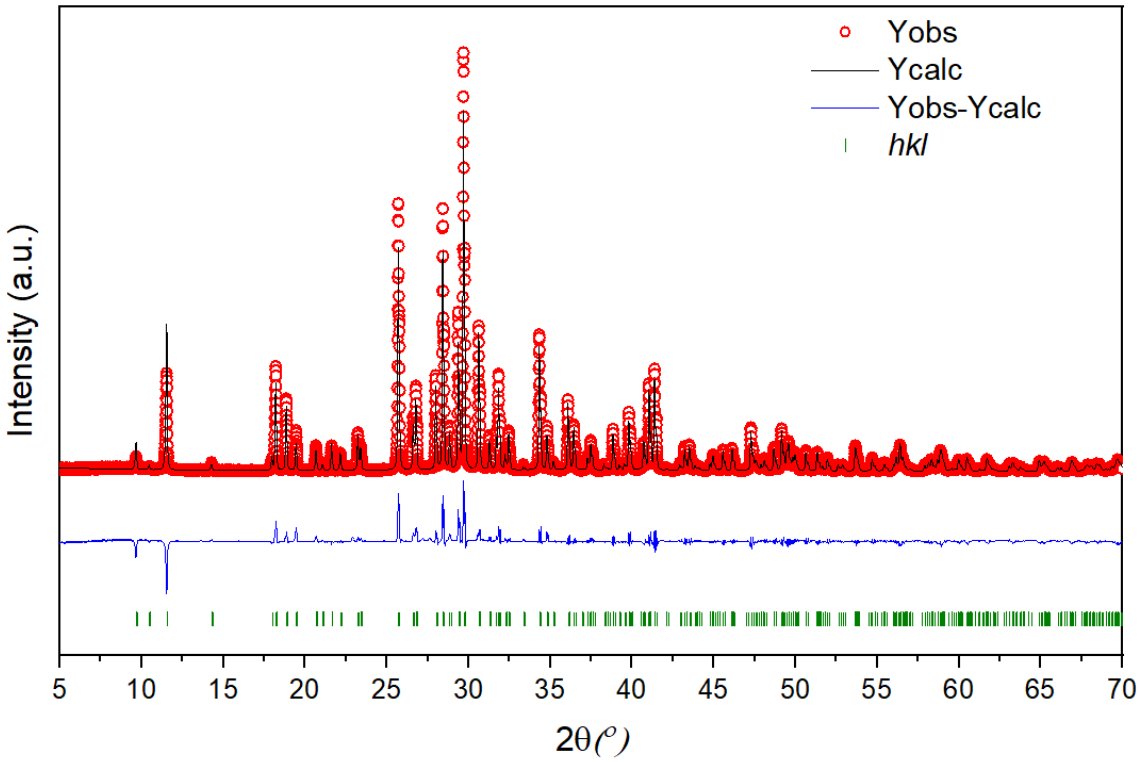

Fig. A.2.9. Rietveld refinement of lab-PXRD data collected at room temperature of $Sr_{12}Al_{20}Si_{12}O_{66}$ sintered for 48h at 1150°C.

Table T.2.1. Occupancies of each model tested to explain the Al^{3+}/Si^{4+} ordering in $Sr_{12}Al_{20}Si_{12}O_{66}$. Based on a (1x1x1) unit cell of $Sr_{12}Al_{20}Si_{12}O_{66}$.

Model (1x1x1)	T1	T2	T3	T4	T5	T6	T7	T8	ΔE	N(Si-O-Si)
m1_00	2Si	6Al2	2Si3	2Al4	6Al5	2Al6	6Si7	4Al8/2Si8	0.85	6
m1_02	2Si	6Al2	2Si3	2Al4	6Al5	2Al6	6Si7	4Al8/2Si8	0.91	6
m2_00	2Si	4Al2/2Si2	2Si3	2Al4	6Al5	2Al6	6Si7	6Al8	0.61	4
m2_02	2Si	4Al2/2Si2	2Si3	2Al4	6Al5	2Al6	6Si7	6Al8	0.71	4
m4_02	2Si	6Al2	2Si3	2Al4	6Al5	2Al6	2Al7/4Si7	2Al8/4Si8	2.21	10
m4_14	2Si	6Al2	2Si3	2Al4	6Al5	2Al6	2Al7/4Si7	2Al8/4Si8	1.46	8
m5_00	2Si	2Al2/4Si2	2Si3	2Al4	6Al5	2Al6	2Al7/4Si7	6Al8	2.22	7
m5_19	2Si	2Al2/4Si2	2Si3	2Al4	6Al5	2Al6	2Al7/4Si7	6Al8	2.42	6
m6_02	2Si	2Al2/4Si2	2Si3	2Al4	6Al5	2Al6	2Al7/4Si7	4Al8/2Si8	2.21	10
m6_14	2Si	2Al2/4Si2	2Si3	2Al4	6Al5	2Al6	2Al7/4Si7	4Al8/2Si8	1.46	8
m7_00	2Si	6Al2	2Si3	2Al4	6Al5	1Al6/1Si6	6Si7	5Al8/1Si8	0.35	6
m7_01	2Si	6Al2	2Si3	2Al4	6Al5	1Al6/1Si6	6Si7	5Al8/1Si8	0.69	6
m8_00	2Si	6Al2	2Si3	2Al4	5Al5/1Si5	1Al6/1Si6	6Si7	6Al8	0.56	3
m8_01	2Si	6Al2	2Si3	2Al4	5Al5/1Si5	1Al6/1Si6	6Si7	6Al8	0.52	3

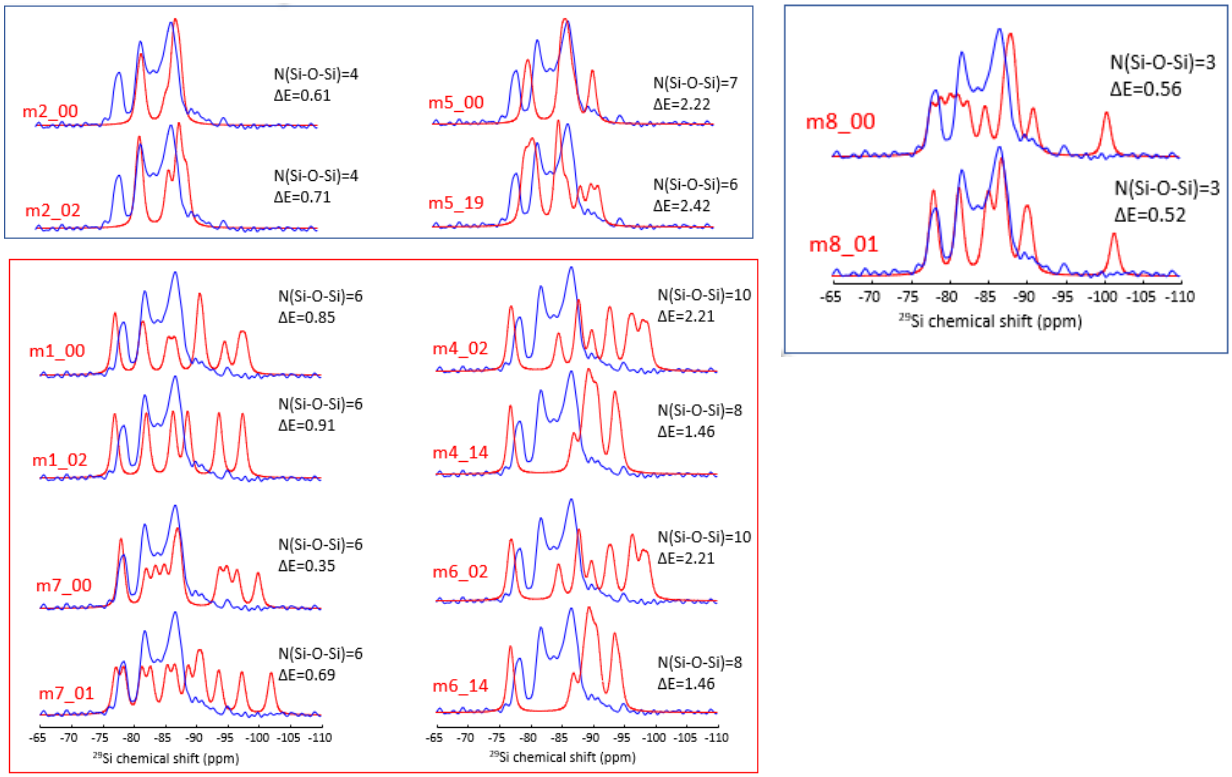

Fig. A.2.10. Comparison of the experimental ^{29}Si MAS NMR spectra, (shown in blue), and the theoretical ^{29}Si MAS NMR spectrums of the generated mixed occupancy models, (shown in red), from the table above. Theoretical spectra were generated using GIPAW-DFT calculations implemented in the Castep code.

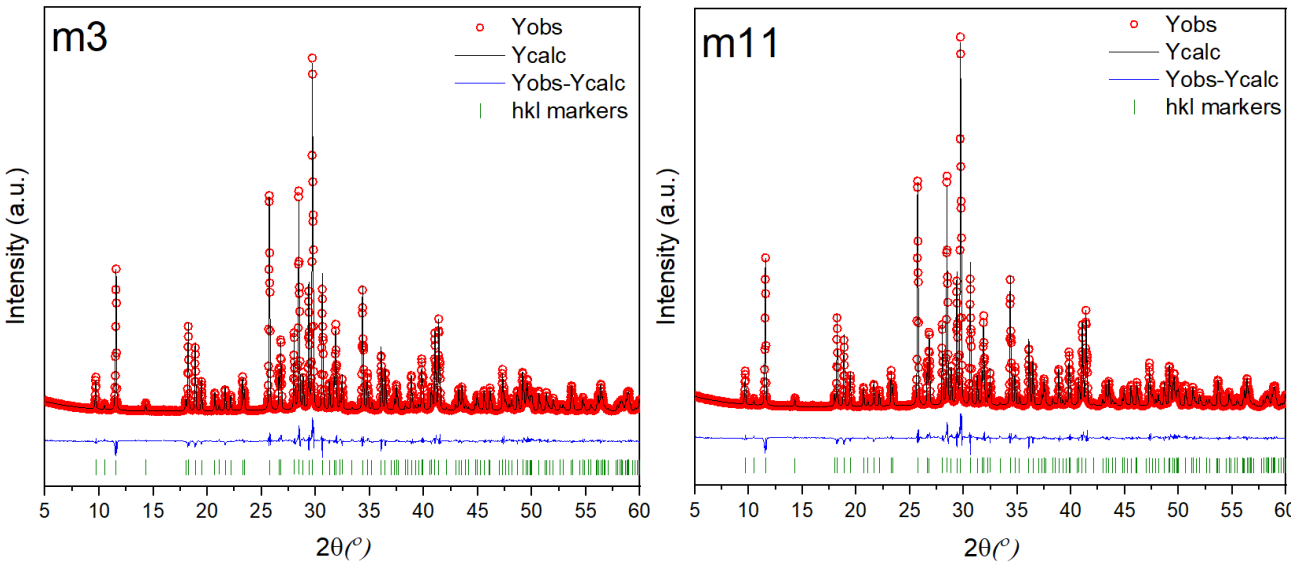

Fig. A.2.11. Rietveld fits achieved using the m3 and m11 models, on room temperature lab-PXRD data collected on a crushed sample of P4-$Sr_{12}Al_{20}Si_{12}O_{66}$. Final R_{wp} values of 7.096% and 7.098 respectively, were observed.

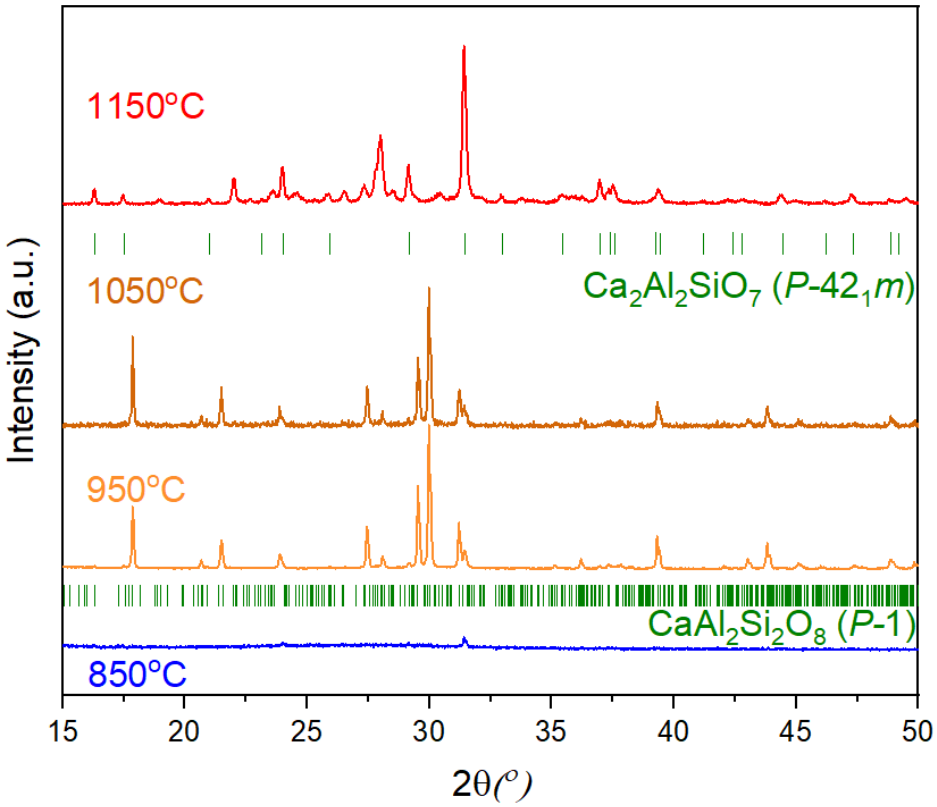

Fig. A.2.12. Sintering trials (1h) attempted in the synthesis of $Ca_{12}Al_{20}Si_{12}O_{66}$, the *h,k,l* markers of the phases which formed instead are shown in green.

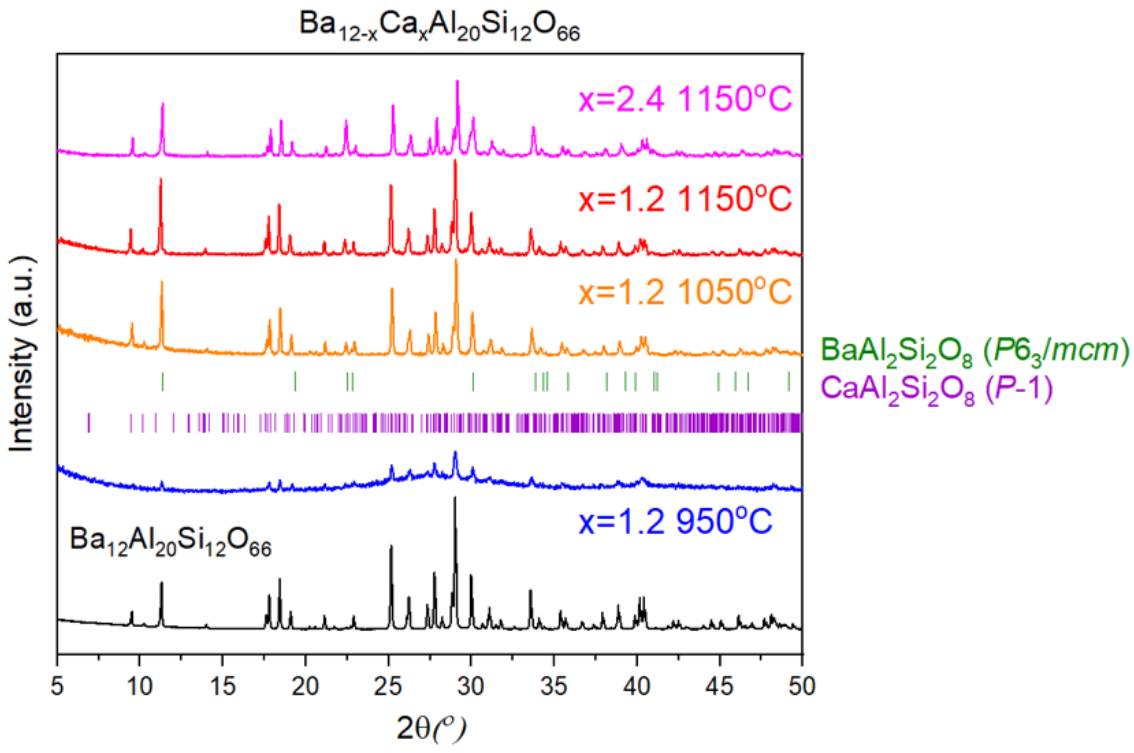

Fig. A.2.13. Sintering trials attempted (1h) in exploration of the $Ba_{12-x}Ca_xAl_{20}Si_{12}O_{66}$ solid solution, the best synthesis achieved was at x=1.2 (1050°C, shown in orange), phase purity was almost reached, with just the peak at 24° belonging to an impurity, $CaAl_2Si_2O_8$ (*P*-1).

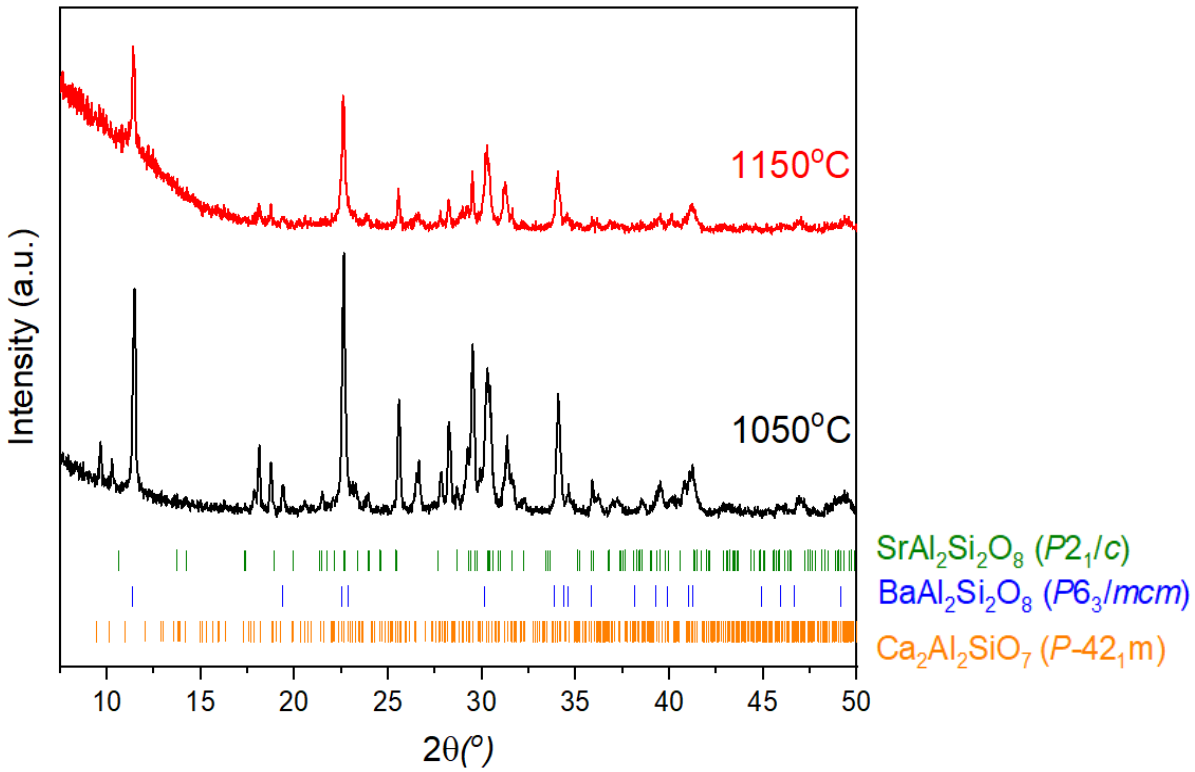

Fig. A.2.14. Annealing temperatures trialled in the synthesis of $(Sr,Ba,Ca)_4Al_{20}Si_{12}O_{66}$, the respective phases which formed instead are shown in green, blue and orange, respectively.

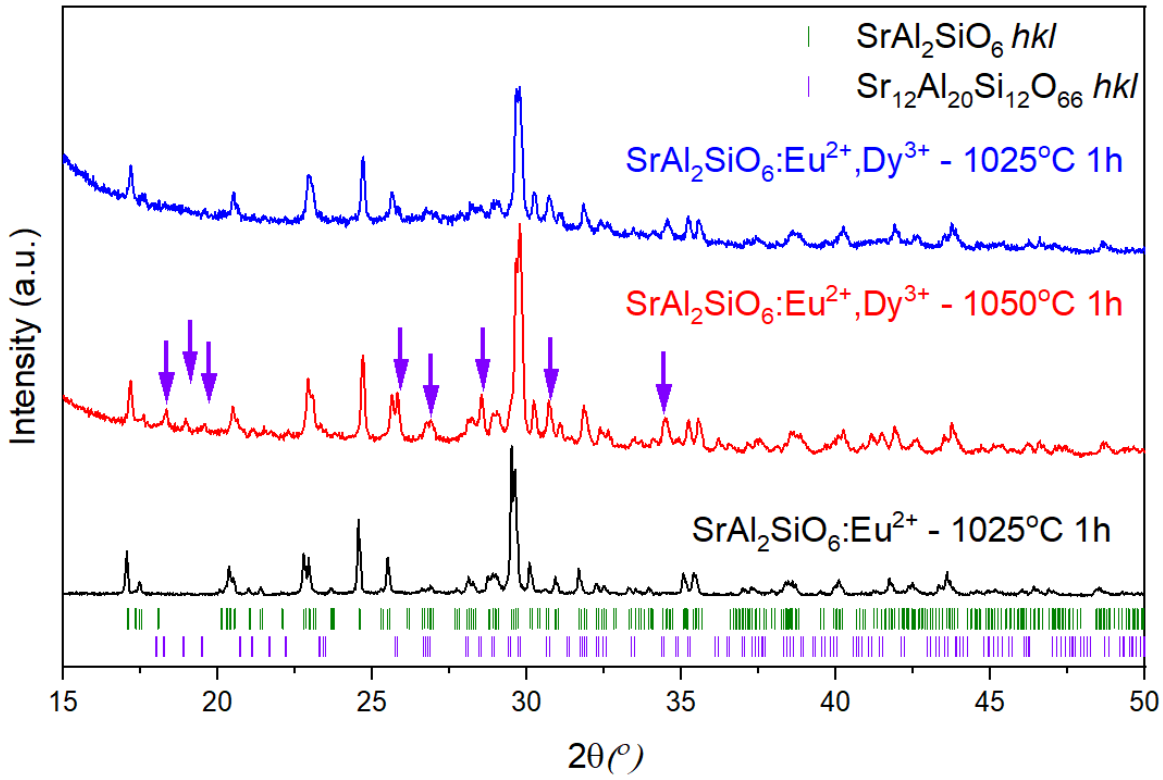

Fig. A.2.15. Comparison of the synthesis trials conducted to make single-phase $SrAl_2SiO_6:Eu^{2+},Dy^{3+}$. The blue line shows single-phase synthesis, however a larger amorphous is also visible. The purple arrows indicate the $Sr_{12}Al_{20}Si_{12}O_{66}$ secondary phase peaks.

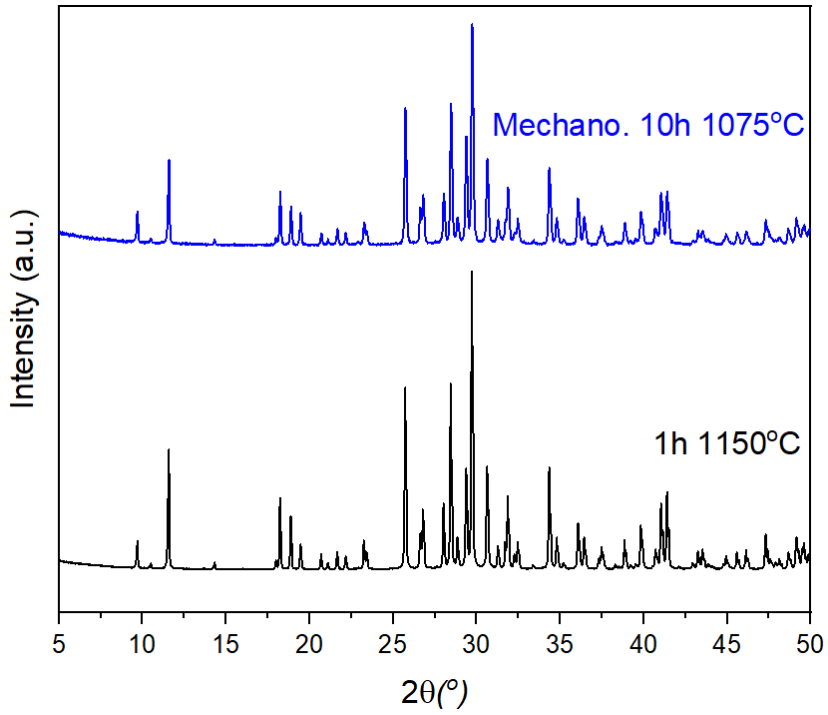

Fig. A.2.16. Comparison of the room temperature lab-PXRD data from phase-pure P4-$Sr_{12}Al_{20}Si_{12}O_{66}$ and the bulk sample tested for mecholuminescent properties.

Appendix 2 – Supplementary Information for Chapter 3

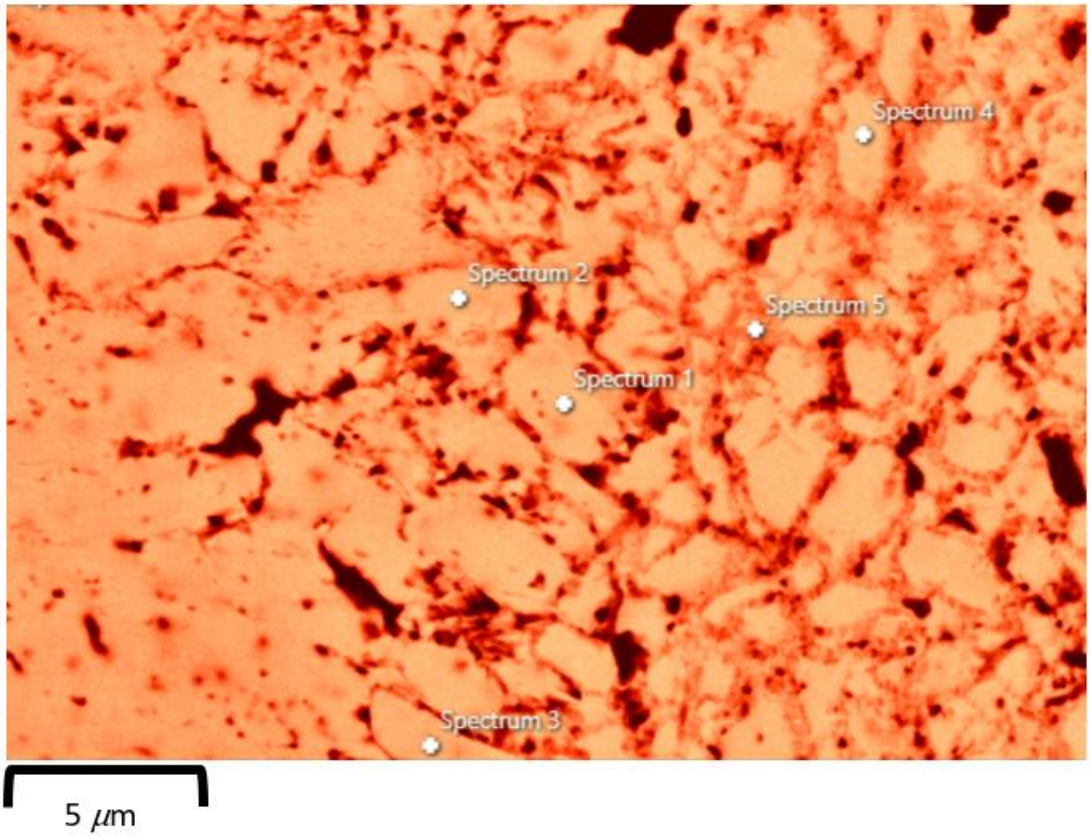

Fig. A.3.17. SEM image of a sintered pellet of $Sr_2Si_3O_8$ (12h 850°C). The uniform colour shows the compositional homogeneity of the sample.

Table T.3.2. Final refined structural parameters obtained from lab-PXRD data, collected at room temperature on a powdered sample of $Sr_2Si_3O_8$ ($P2_1/c$ space group, *a*- = 13.338(1) *Å*, *b*- = 4.5633(5) *Å* and *c*- = 13.486(1) *Å*, *β* = 116.486(3), and volume = 734.7(1) *Å*^{3}).

Atom	Position	x	y	z	Occ	B_{iso}
Sr1	4e	0.6401(3)	0.270(1)	0.0996(3)	1	2.18(6)[a]
Sr2	4e	0.0872(3)	0.207(1)	0.1883(3)	1	2.18(6)[a]
Si1	4e	0.1415(7)	0.301(3)	0.444(7)	1	1.6(1)[b]
Si2	4e	0.2260(7)	0.768(4)	0.5897(7)	1	1.6(1)[b]
Si3	4e	0.4731(8)	0.817(4)	0.1819(8)	1	1.6(1)[b]
O1	4e	0.1268	0.6069	0.4726	1	1
O2	4e	0.1839	0.1246	0.5605	1	1
O3	4e	0.0201	0.1894	0.3441	1	1
O4	4e	0.2405	0.2333	0.3905	1	1
O5	4e	0.3404	0.7259	0.5873	1	1
O6	4e	0.2160	0.6938	0.7001	1	1
O7	4e	0.5399	0.7720	0.0987	1	1
O8	4e	0.5096	0.6630	0.2933	1	1

[a]: Constrained to refine to the same Biso value

[b]: Constrained to refine to the same Biso value

Table T.3.3. Final refined structural parameters obtained from lab-PXRD data, collected at room temperature on a powdered sample of $Sr_2Si_3O_8$:Al ($P2_1/c$ space group, a- = 13.3308(3) Å, b- = 4.5818(1) Å and c- = 13.4664(3) Å, β = 116.643(2), and volume = 735.17(3) $Å^3$).

Atom	Position	x	y	z	Occ	B_{iso}
Sr1	4e	0.6429(2)	0.2740(8)	0.1008(2)	1	2.30(4)[a]
Sr2	4e	0.0856(2)	0.227(1)	0.1874(2)	1	2.30(4)[a]
Si1	4e	0.1425(5)	0.304(2)	0.4396(5)	1	1.7(2)[b]
Si2	4e	0.226(7)	0.746(2)	0.5935(5)	1	1.7(2)[b]
Si3	4e	0.4750(6)	0.836(2)	0.1781(6)	1	1.7(2)[b]
O1	4e	0.1268	0.6069	0.4726	1	1
O2	4e	0.1839	0.1246	0.5605	1	1
O3	4e	0.0201	0.1894	0.3441	1	1
O4	4e	0.2405	0.2333	0.3905	1	1
O5	4e	0.3404	0.7259	0.5873	1	1
O6	4e	0.2160	0.6938	0.7001	1	1
O7	4e	0.5399	0.7720	0.0987	1	1
O8	4e	0.5096	0.6630	0.2933	1	1

[a]: Constrained to refine to the same Biso value

[b]: Constrained to refine to the same Biso value

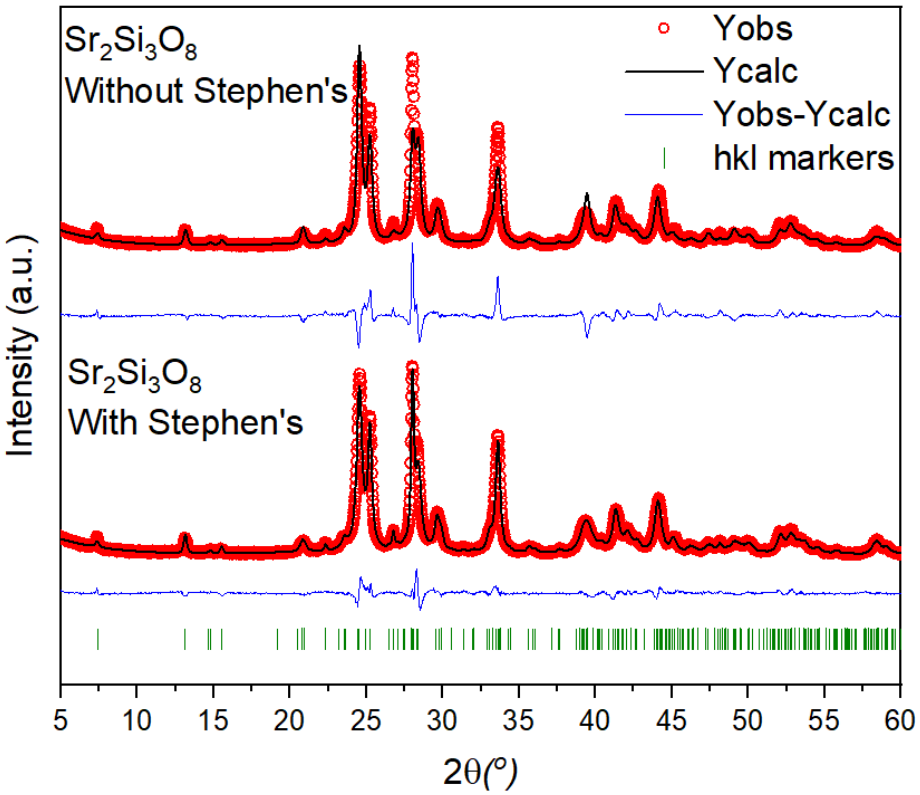

Fig. A.3.18. Comparison of the Rietveld fits achieved on room temperature lab-PXRD data of $Sr_2Si_3O_8$, with and without Stephen's monoclinic macro.

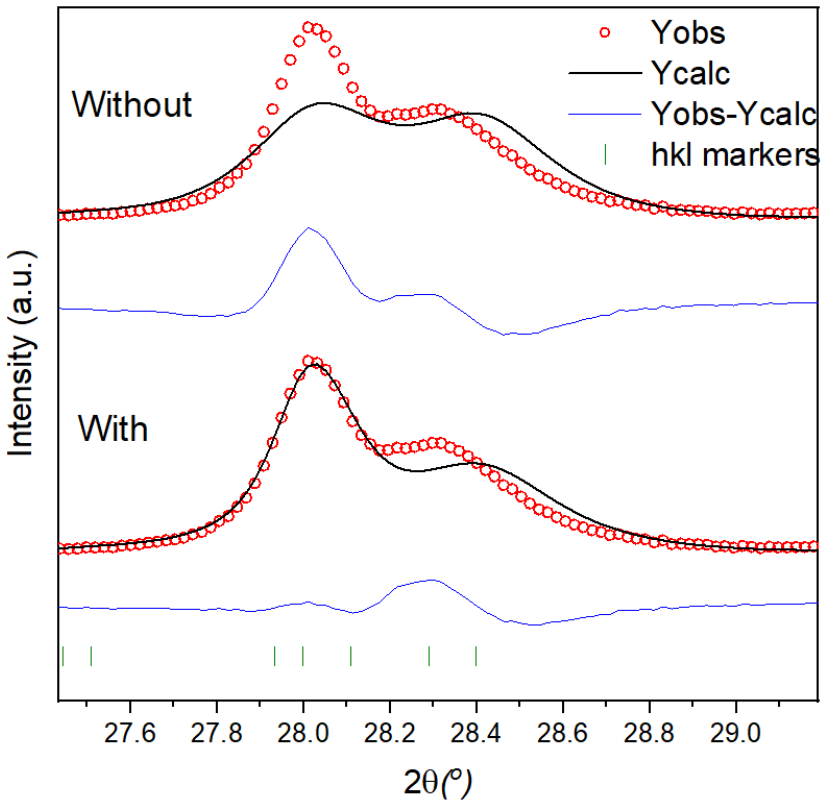

Fig. A.3.19. Zoom of Fig. A.3.18., focussing on the shoulder defect at 28°, showing how it's fitting improves when Stephen's monoclinic macro is used.

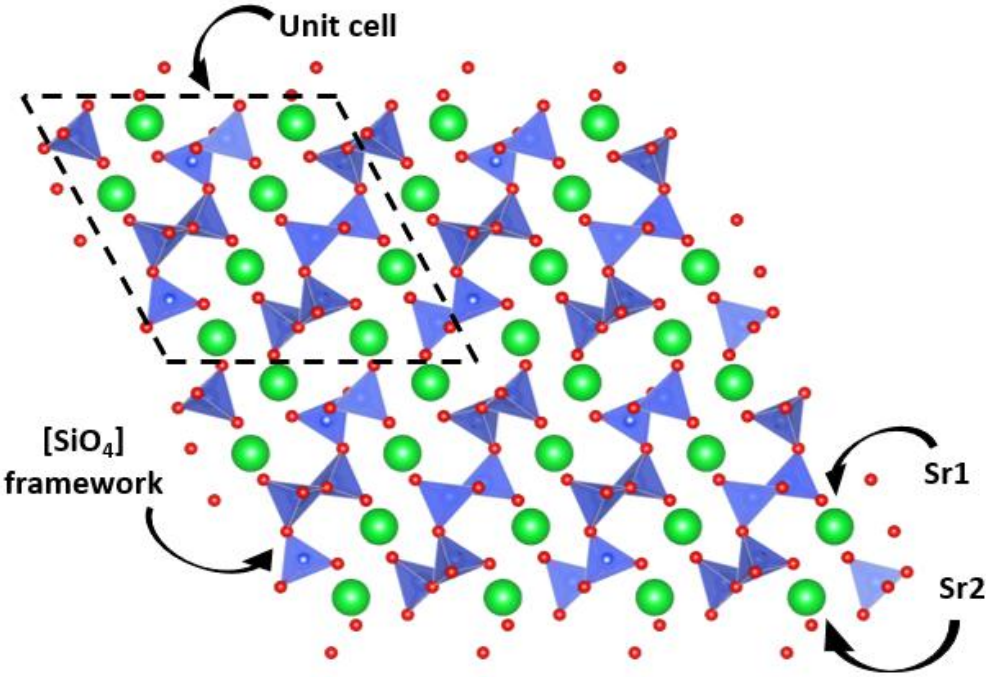

Fig. A.3.20. Expanded unit cell of $Sr_2Si_3O_8$ when viewed down the *c*- axis.

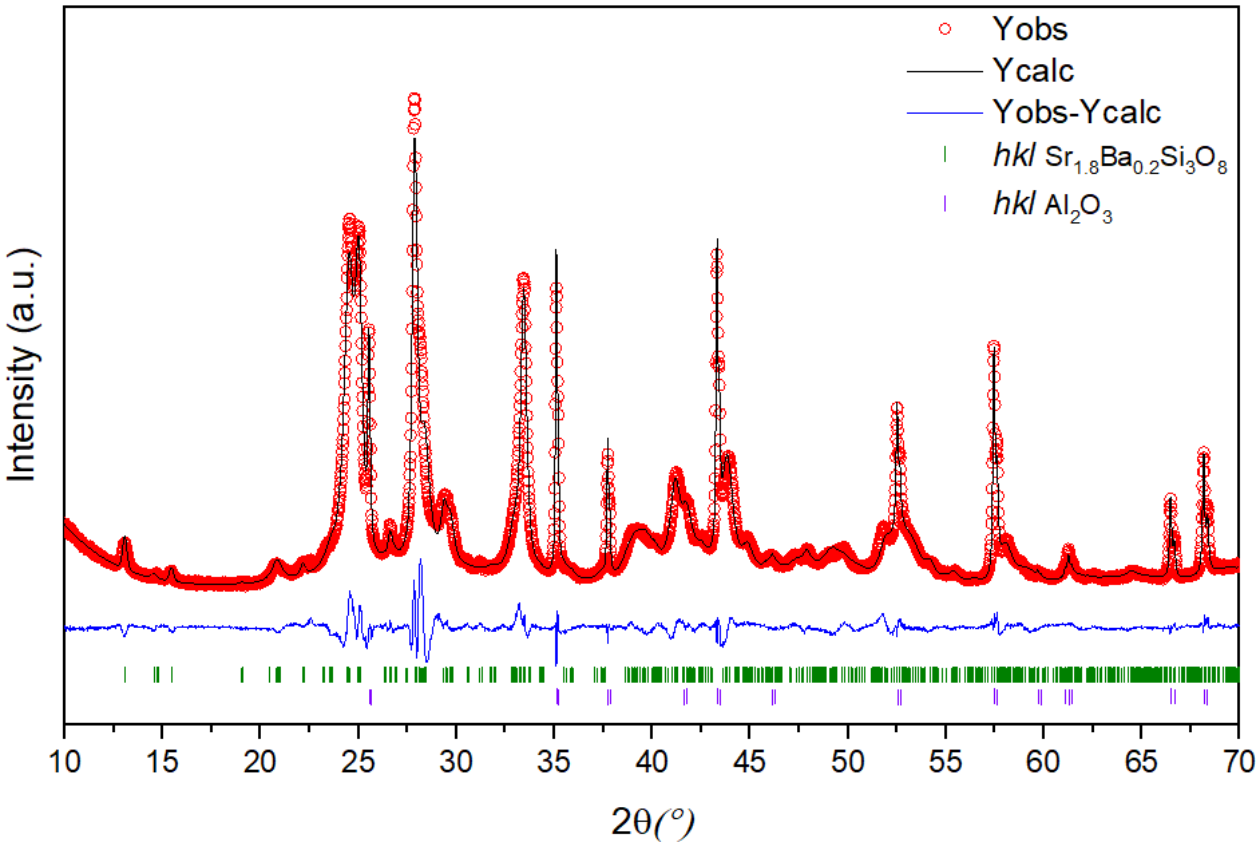

Fig. A.3.21. Rietveld refinement of $Sr_{1.8}Ba_{0.2}Si_3O_8$ mixed with Al_2O_3. This refinement was used to calculate the amorphous and crystalline wt.% of the phase. R_{wp} = 6.35%.

Table T.3.4. Final refined structural parameters obtained from lab-PXRD data, collected at room temperature on a powdered sample of $Sr_{1.8}Ba_{0.2}Si_3O_8$ ($P2_1/c$ space group, *a*- = 13.394(2) *Å*, *b*- = 4.5533(9) *Å* and *c*- = 13.567(2) *Å*, *β* = 116.317(5), and volume = 741.7(2) *Å*^{3}).

Atom	Position	x	y	z	Occ	B_{iso}
Sr1	4e	0.6389(4)	0.265(2)	0.0995(4)	0.9	1.41(8)[a]
Ba1	4e	0.6389(4)	0.265(2)	0.0995(4)	0.1	1.41(8)[a]
Sr2	4e	0.0841(3)	0.201(2)	0.1850(3)	0.9	1.41(8)[a]
Ba2	4e	0.0841(3)	0.201(2)	0.1850(3)	0.1	1.41(8)[a]
Si1	4e	0.1570(4)	0.281(5)	0.450(1)	1	1
Si2	4e	0.233(1)	0.751(6)	0.597(1)	1	1
Si3	4e	0.473(2)	0.878(4)	0.189(1)	1	1
O1	4e	0.1268	0.6069	0.4726	1	1
O2	4e	0.1839	0.1246	0.5605	1	1
O3	4e	0.0201	0.1894	0.3441	1	1
O4	4e	0.2405	0.2333	0.3905	1	1
O5	4e	0.3404	0.7259	0.5873	1	1
O6	4e	0.2160	0.6938	0.7001	1	1
O7	4e	0.5399	0.7720	0.0987	1	1
O8	4e	0.5096	0.6630	0.2933	1	1

[a]: Constrained to refine to the same Biso values

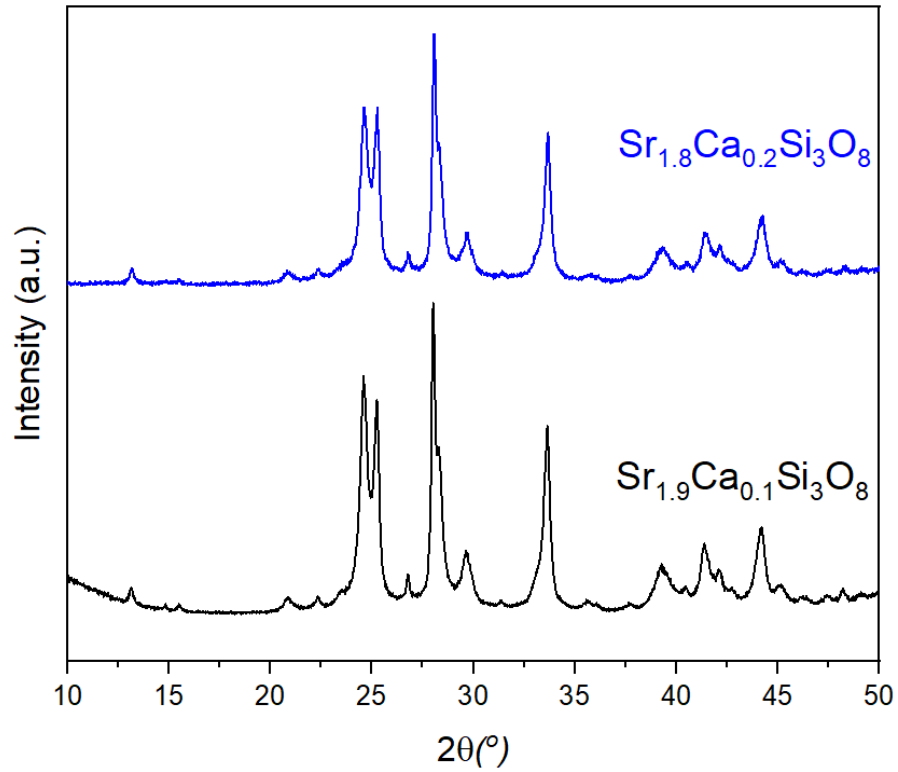

Fig. A.3.22. Comparison of the lab-PXRD patterns collected on $Sr_{1.9}Ca_{0.1}Si_3O_8$ and $Sr_{1.8}Ca_{0.2}Si_3O_8$, showing a marginal improvement in crystallisation for the $Sr_{1.8}Ca_{0.2}Si_3O_8$ sample. Both were sintered at 850°C for 12h.

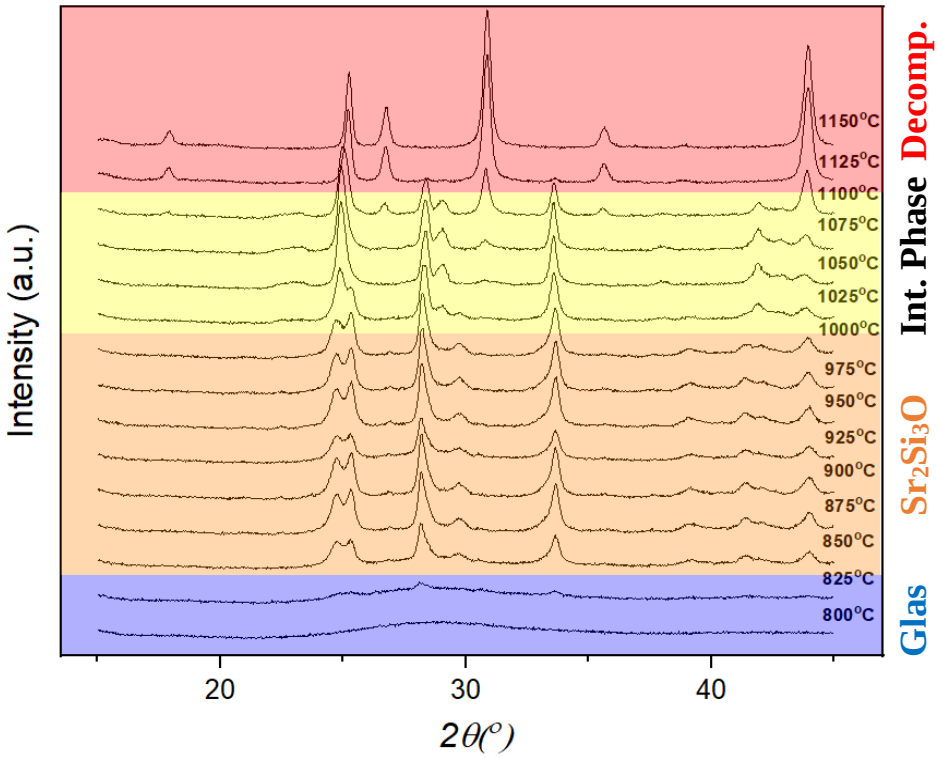

Fig. A.3.23. *In-situ* VTXRD of $Sr_{1.8}Ca_{0.2}Si_3O_8$, collected from glass powder between 600-1200°C.

Table T.3.5. Final refined structural parameters obtained from lab-PXRD data, collected at room temperature on a powdered sample of $Sr_{1.8}Ca_{0.2}Si_3O_8$ ($P2_1/c$ space group, a- = 13.322(2) Å, b- = 4.552(7) Å and c- = 13.479(2) Å, β = 116.391(4), and volume = 732.2(1) Å^3).

Atom	Position	x	y	z	Occ	B_{iso}
Sr1	4e	0.6382(4)	0.2635(2)	0.1006(4)	0.9	1
Ca1	4e	0.6382(4)	0.2635(2)	0.1006(4)	0.1	1
Sr2	4e	0.0867(3)	0.203(2)	0.1874(3)	0.9	1
Ca2	4e	0.0867(3)	0.203(2)	0.1874(3)	0.1	1
Si1	4e	0.1395(9)	0.314(4)	0.4485(9)	1	1
Si2	4e	0.2377(9)	0.820(4)	0.5938(9)	1	1
Si3	4e	0.4723(9)	0.782(6)	0.1823(9)	1	1
O1	4e	0.1268	0.6069	0.4726	1	1
O2	4e	0.1839	0.1246	0.5605	1	1
O3	4e	0.0201	0.1894	0.3441	1	1
O4	4e	0.2405	0.2333	0.3905	1	1
O5	4e	0.3404	0.7259	0.5873	1	1
O6	4e	0.2160	0.6938	0.7001	1	1
O7	4e	0.5399	0.7720	0.0987	1	1
O8	4e	0.5096	0.6630	0.2933	1	1

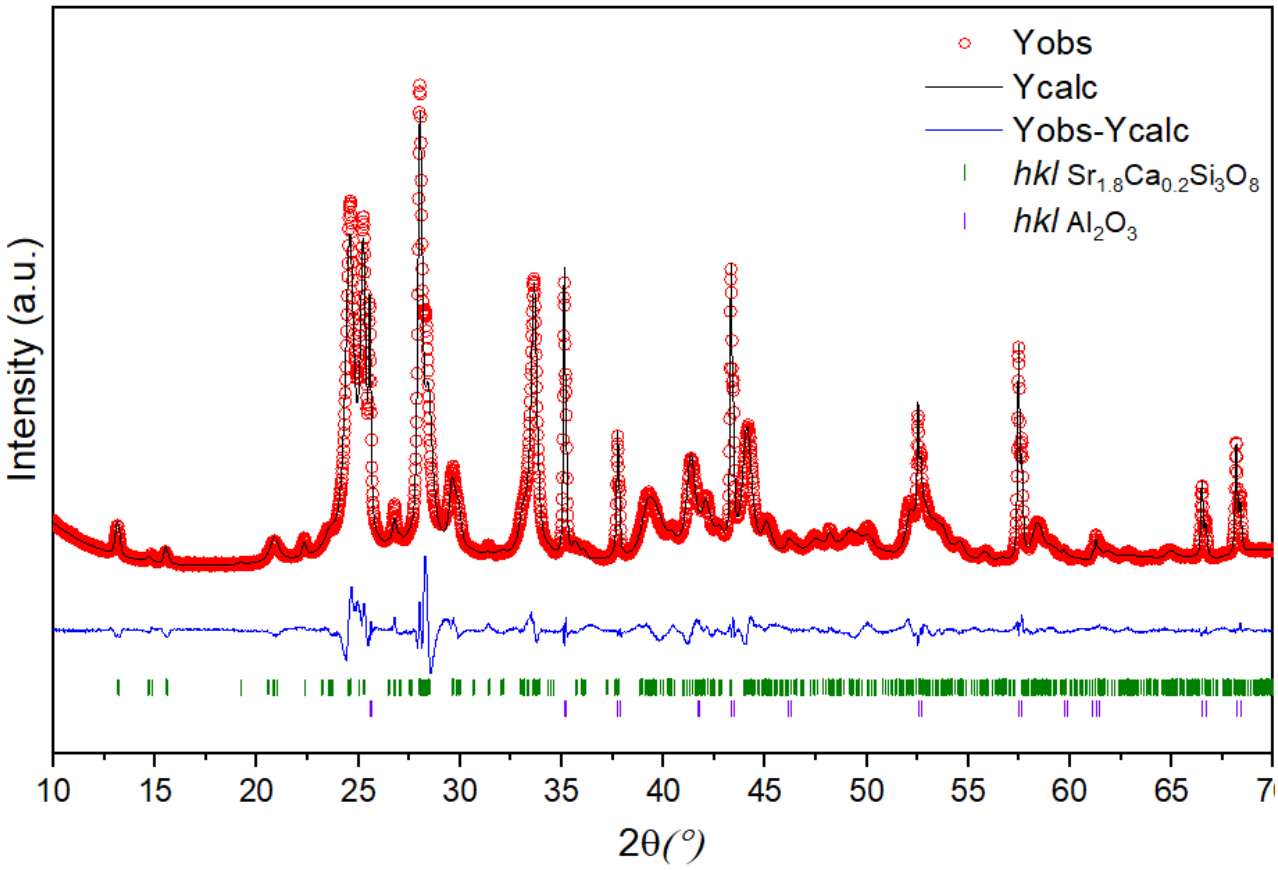

Fig. A.3.24. Rietveld refinement of $Sr_{1.8}Ca_{0.2}Si_3O_8$ mixed with Al_2O_3. This refinement was used to calculate the amorphous and crystalline wt.% of the phase. R_{wp} = 7.24%.

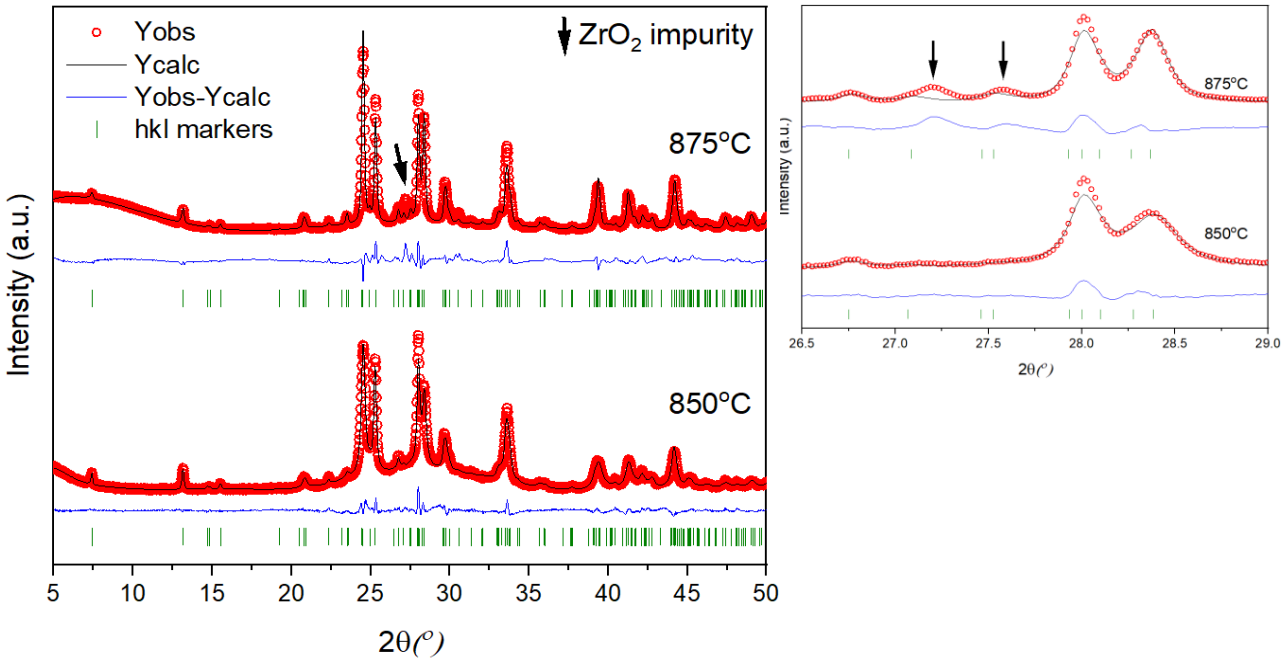

Fig. A.3.25. Comparison of the Rietveld fits achieved on powdered lab-PXRD data of $Sr_2Si_3O_8$:7wt.%ZrO_2 sintered for 12h at 850°C and 875°C, respectively. The ZrO_2 impurity in the 875°C sample is shown by black arrows. For 850°C and R_{wp} of 5.850% was achieved while for 875°C and R_{wp} of 9.722% was observed.

Table T.3.6. Final refined structural parameters obtained from lab-PXRD data, collected at room temperature on a powdered sample of $Sr_2Si_3O_8$:7wt.%ZrO_2 sintered for 12h at 850°C. ($P2_1/c$ space group, *a*- = 13.3359(9) *Å*, *b*- = 4.5749(3) *Å* and *c*- = 13.4733(8) *Å*, *β* = 116.705(3), and volume = 734.33(8) *Å*^{3}).

Atom	Position	x	y	z	Occ	B_{iso}
Sr1	4e	0.6428(3)	0.299(1)	0.0981(3)	1	1
Sr2	4e	0.0843(3)	0.242(1)	0.1852(3)	1	1
Si1	4e	0.1428(8)	0.303(3)	0.4335(7)	1	1
Si2	4e	0.2225(8)	0.777(3)	0.5993(7)	1	1
Si3	4e	0.4738(9)	0.869(2)	0.1874(9)	1	1
O1	4e	0.1268	0.6069	0.4726	1	1
O2	4e	0.1839	0.1246	0.5605	1	1
O3	4e	0.0201	0.1894	0.3441	1	1
O4	4e	0.2405	0.2333	0.3905	1	1
O5	4e	0.3404	0.7259	0.5873	1	1
O6	4e	0.2160	0.6938	0.7001	1	1
O7	4e	0.5399	0.7720	0.0987	1	1
O8	4e	0.5096	0.6630	0.2933	1	1

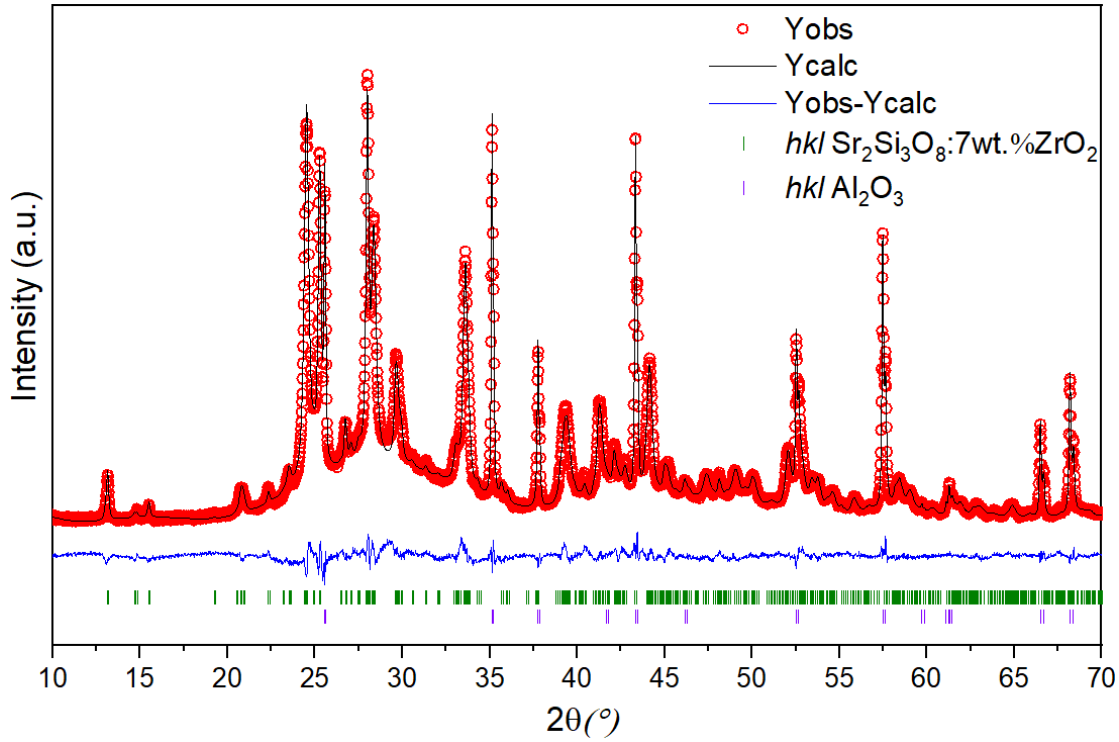

Fig. A.3.26. Rietveld refinement of $Sr_2Si_3O_8$:7wt.%ZrO_2 mixed with Al_2O_3. This refinement was used to calculate the amorphous and crystalline wt.% of the phase. R_{wp} = 4.66%.

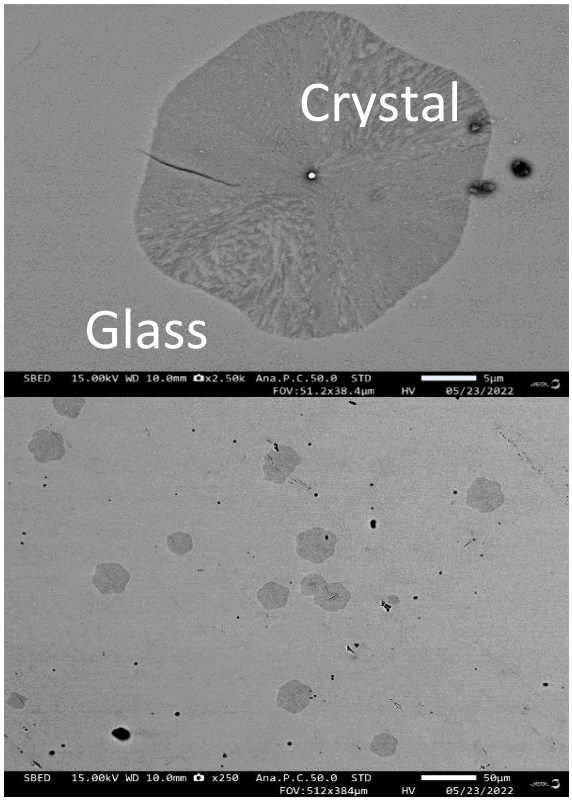

Fig. A.3.27. SEM imaging of bulk crystallised (12h 850°C), ZrO_2 can be seen at the centre of the crystal showing its nucleating abilities. The crack observed in the crystal was due to slight density differences between the glass and the crystal.

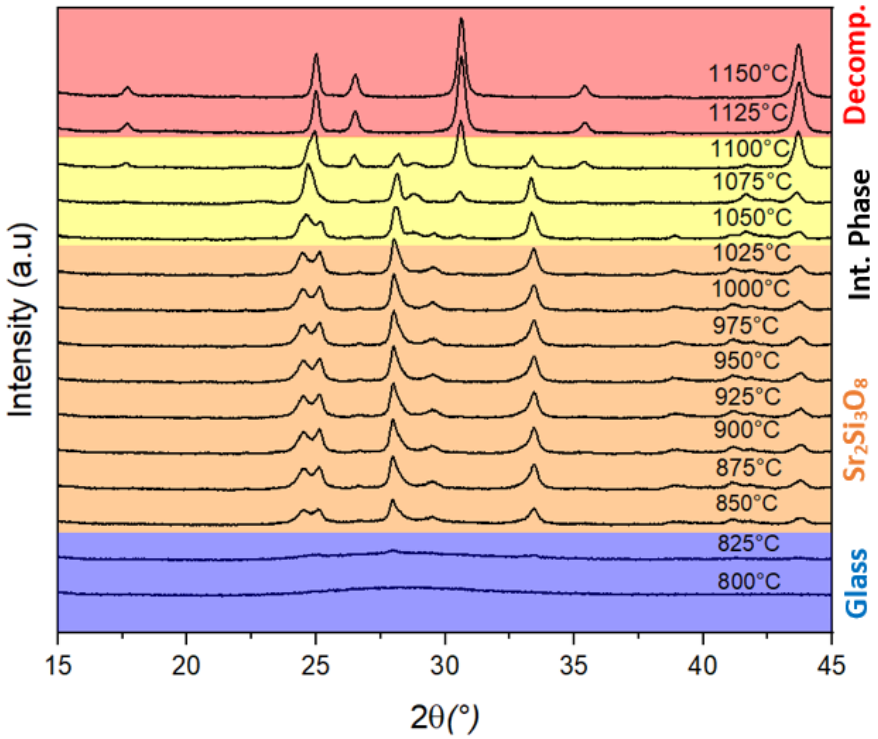

Fig. A.3.28. *In-situ* VTXRD of $Sr_2Si_3O_8$:7wt.%$AgNO_3$, collected from glass powder between 600-1200°C.

Table T.3.7. Final refined structural parameters obtained from lab-PXRD data, collected at room temperature on a powdered sample of $Sr_2Si_3O_8$:7wt.%$AgNO_3$ sintered for 12h at 850°C. ($P2_1/c$ space group, *a*- = 13.346(2) *Å*, *b*- = 4.560(7) *Å* and *c*- = 13.493(1) *Å*, *β* = 116.439(5), and volume = 735.2(2) $Å^3$).

Atom	Position	x	y	z	Occ	B_{iso}
Sr1	4e	0.6498(3)	0.285(2)	0.1051(3)	1	1
Sr2	4e	0.0921(3)	0.235(2)	0.1900(3)	1	1
Si1	4e	0.1500(9)	0.305(5)	0.4493(9)	1	1
Si2	4e	0.2244(9)	0.720(6)	0.5776(8)	1	1
Si3	4e	0.485(1)	0.847(4)	0.1795(9)	1	1
O1	4e	0.1268	0.6069	0.4726	1	1
O2	4e	0.1839	0.1246	0.5605	1	1
O3	4e	0.0201	0.1894	0.3441	1	1
O4	4e	0.2405	0.2333	0.3905	1	1
O5	4e	0.3404	0.7259	0.5873	1	1
O6	4e	0.2160	0.6938	0.7001	1	1
O7	4e	0.5399	0.7720	0.0987	1	1
O8	4e	0.5096	0.6630	0.2933	1	1

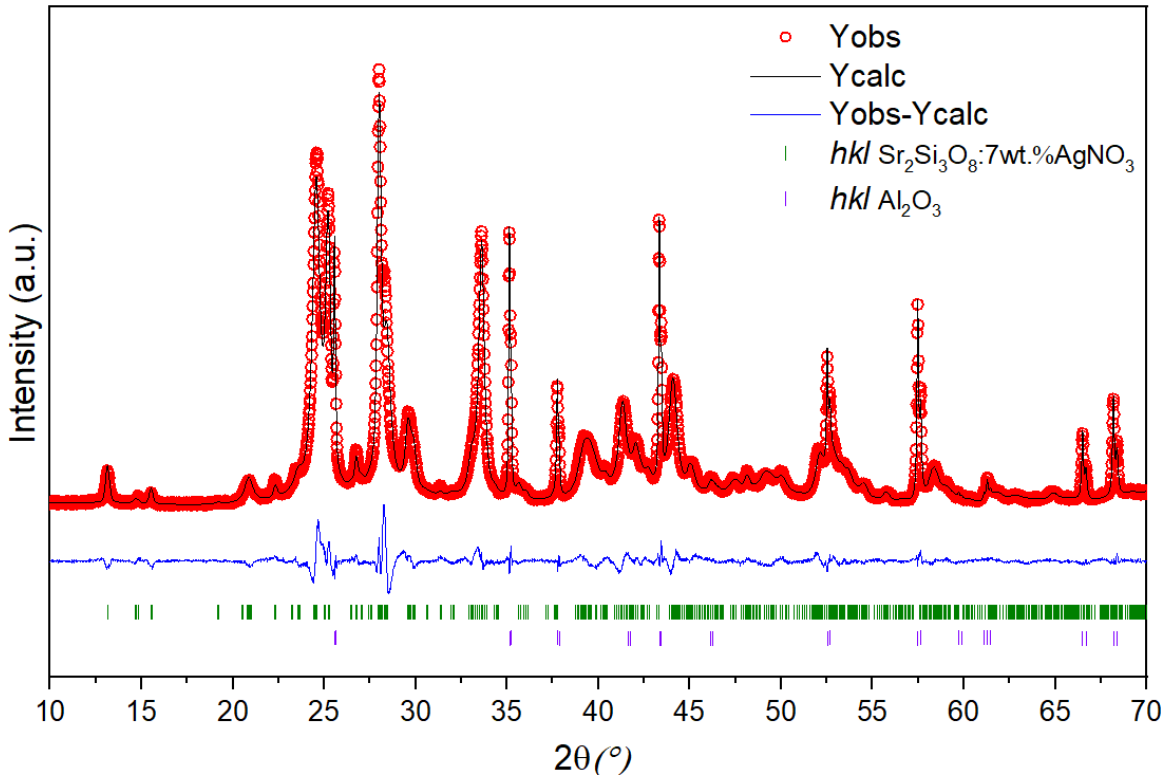

Fig. A.3.29. Rietveld refinement of $Sr_2Si_3O_8$:7wt.%$AgNO_3$ mixed with Al_2O_3. This refinement was used to calculate the amorphous and crystalline wt.% of the phase. R_{wp} = 6.15%.

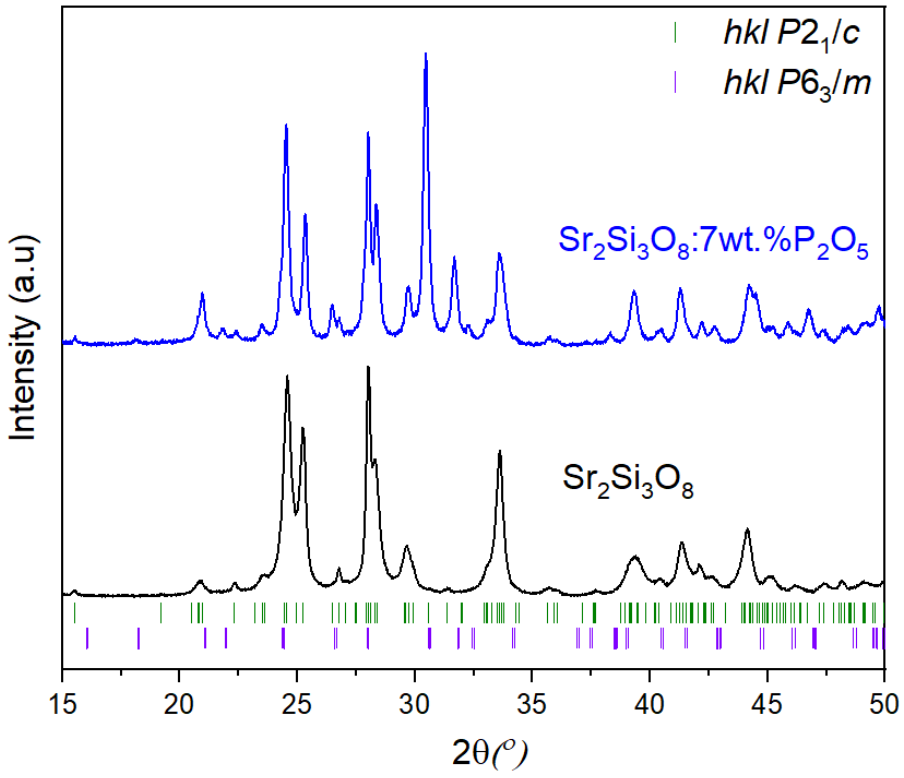

Fig. A.3.30. Comparison of the lab-PXRD data from $Sr_2Si_3O_8$ and $Sr_2Si_3O_8$:7wt.%P_2O_5, showing $Sr_{10}(PO_4)_6$ ($P6_3/m$) as the major crystalline phase in the nucleated sample. Both samples prepared from glass at 850°C for 12h.

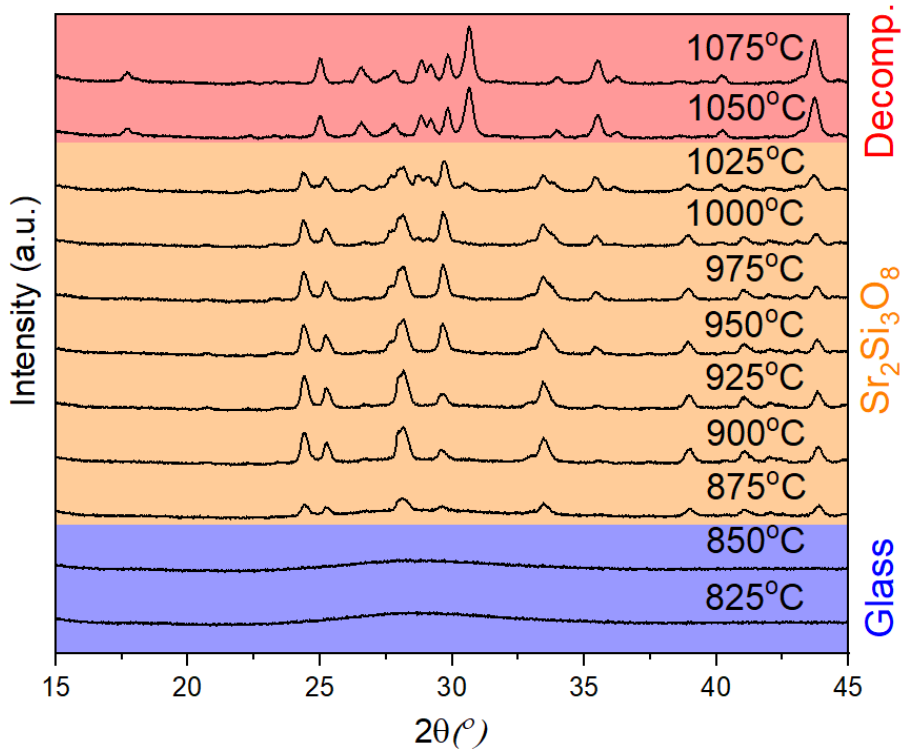

Fig. A.3.31. *In-situ* VTXRD of $Sr_2Si_3O_8$ nucleated by 10wt.% $TiZrO_4$. Collected between 600-1200°C.

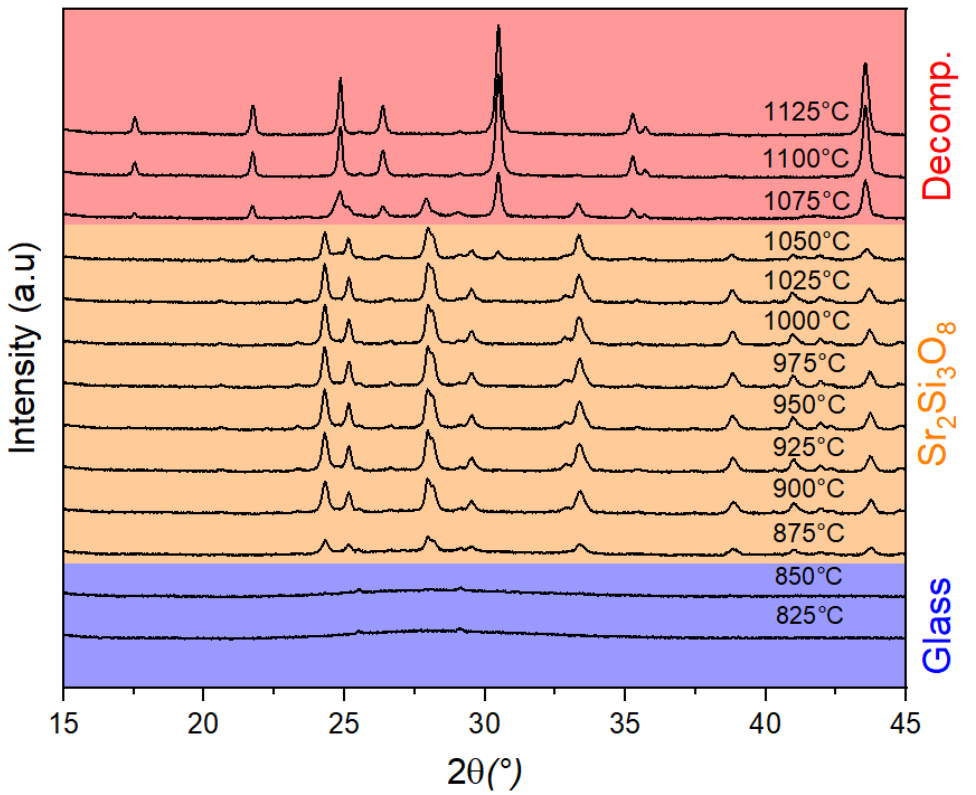

Fig. A3.32. *In-situ* VTXRD of $Sr_2Si_3O_8$:Al, collected between 600-1200°C.

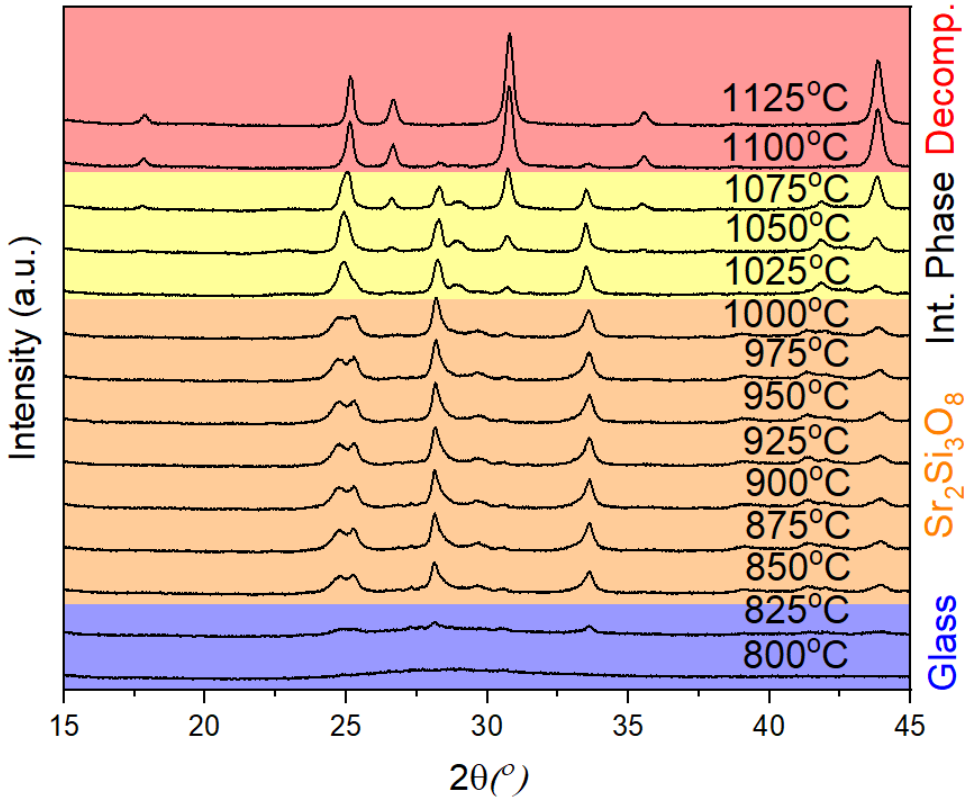

Fig. A.3.33. *In-situ* VTXRD of $Sr_2Si_3O_8$:7wt.%Au, collected between 600-1200°C.

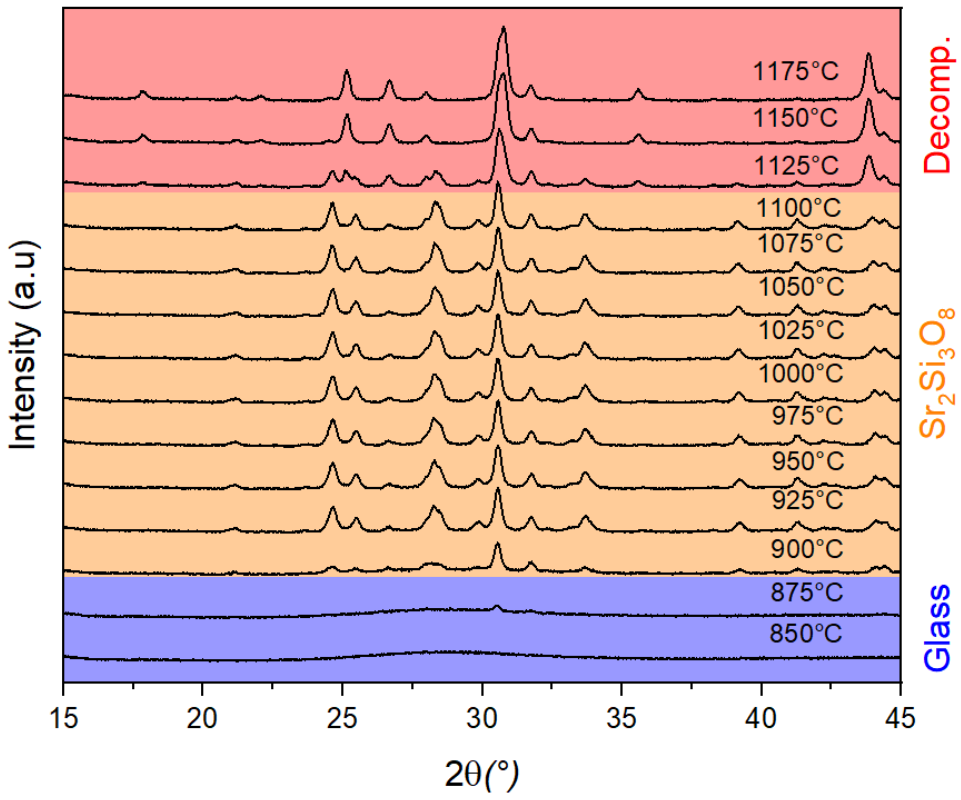

Fig. A.3.34. *In-situ* VTXRD of $Sr_2Si_3O_8$:7wt.%P_2O_5, collected between 600-1200°C.

Table T.3.8. Comparison of the crystallisation and decomposition temperatures of $Sr_2Si_3O_8$ observed from DSC and *in-situ* VTXRD.

Sample	$Sr_2Si_3O_8$ forms (°C)		$Sr_2Si_3O_8$ decomposes (°C)	
	DSC	VTXRD	DSC	VTXRD
$Sr_2Si_3O_8$	859	850	1110	1100
$Sr_2Si_3O_8$:10wt.%$TiZrO_4$	912	900	1083	1050
$Sr_2Si_3O_8$:7wt.%ZrO_2	928	925	1046	1025
$Sr_2Si_3O_8$:Al	886	900	1092	1075
$Sr_2Si_3O_8$:7wt.%$AgNO_3$	838	850	1077	1075
$Sr_2Si_3O_8$:7wt.%Au	845	850	1103	1025
$Sr_{1.8}Ba_{0.2}Si_3O_8$	859	850	1162	1125
$Sr_{1.8}Ca_{0.2}Si_3O_8$	872	850	1118	1100
$Sr_2Si_3O_8$:7wt.%P_2O_5	926	925	1136	1150

Résumé en Français

Résumé du Chapitre 1

Les oxydes inorganiques fonctionnels sont essentiels dans le développement des technologies modernes. Leurs utilisations vont des téléphones portables aux implants dentaires, de la construction aux ustensiles de cuisine, ainsi des lasers et des batteries. Compte tenu du large éventail d'applications fonctionnelles, la demande de nouveaux matériaux inorganiques fonctionnels, dotés de propriétés améliorées (dureté, durabilité, conductivité thermique/électrique, etc.), a augmenté de manière exponentielle. En combinaison avec une tendance générale vers des méthodes de synthèse plus écologiques et plus rentables, un problème se pose : les approches de synthèse conventionnelles seules (les réactions à l'état solide) ne peuvent plus répondre à cette demande. De nouvelles méthodologies sont nécessaires pour cibler spécifiquement la découverte d'oxydes inorganiques de nouvelle génération et les fonctionnaliser afin de dépasser les limites des performances actuelles des leaders actuels du marché.

Malgré une motivation évidente, la découverte de nouveaux matériaux peut s'avérer être une tâche fondamentalement difficile et décourageante. Quelles méthodes de synthèse permettent la formation de nouvelles phases ? Comment sélectionner des compositions cibles stables et intéressantes parmi les possibilités illimitées offertes par le tableau périodique ? Actuellement, ces problèmes sont abordés par deux écoles de pensée : (i) **des approches basées sur la synthèse** - où des méthodes de synthèse innovantes (par exemple, basées sur la synthèse en solution, ou assistées par l'état amorphe fusion/verre) sont employées pour accéder à des phases que les techniques conventionnelles n'ont pas permis d'atteindre. Ces méthodes ne forment cependant principalement que des produits à l'équilibre thermodynamique ; (ii) **des approches basées sur l'efficacité** - elles guident la sélection des compositions cibles par l'exploitation d'outils informatiques (calculs de structure par DFT par exemple), qui ont été développés pour concevoir de nouvelles phases dotées de propriétés à façon. L'assistance informatique améliore donc l'efficacité des recherches en concentrant les efforts de synthèse uniquement sur les compositions intéressantes. Ces méthodologies ne doivent pas être considérées comme distinctes, et souvent des avantages uniques sont obtenus lorsqu'elles sont utilisées de concert. Ce projet présente une approche qui vise à combiner les avantages des méthodes de synthèse innovantes, qui peuvent accéder à des phases typiquement ignorées par les voies conventionnelles, avec l'efficacité de l'orientation informatique. Nous visons à sélectionner de nouveaux oxydes fonctionnels, avec le potentiel d'héberger des propriétés fonctionnelles, et donc, de surmonter les limitations de propriétés des matériaux actuels.

Les céramiques vitreuses métastables du diagramme ternaire SrO-$AlO_{1.5}$ -SiO_2 ont été spécifiquement ciblées. La nature fondamentalement instable des phases métastables signifie qu'elles ne sont généralement pas prises en compte par les méthodes de synthèse classiques. Par conséquent, même dans les diagrammes de phase historiquement bien étudiés, il peut exister de nombreuses phases métastables non découvertes jusqu'alors. D'autre part, les vitrocéramiques constituent une classe de matériaux diversifiée et étudiée depuis longtemps. Leur capacité à combiner les propriétés mécaniques du verre avec les applications fonctionnelles des cristaux leur a permis, dans certains cas, de rivaliser avec leurs homologues céramiques, tout en conservant des propriétés uniques telles que la transparence. La nature inexploitée de la découverte des phases métastables, en plus des applications réelles des vitrocéramiques, a le potentiel de produire des matériaux très intéressants.

La cristallisation du verre (CG) est la principale technique de synthèse utilisée pour cibler les vitrocéramiques métastables. En utilisant la cristallisation à partir d'un état de la matière intrinsèquement hors équilibre, ici le verre, cette technique favorise la formation de produits hors équilibre (métastables). L'approche GC s'aligne également sur la formation de vitrocéramiques, en fournissant la matrice vitreuse initiale dans laquelle la cristallisation se produit. La cristallisation à partir d'un état hors équilibre réduit l'énergie nécessaire au démarrage de la réaction, ce qui fait de la GC une voie de synthèse moins énergivore et donc plus respectueuse de l'environnement que les voies conventionnelles. Outre la GC, d'autres techniques de synthèse hors d'équilibre ont également été explorées, telles que le broyage à haute énergie (HEM), la lévitation aérodynamique (ADL) et la synthèse d'oxynitrures.

Pour compléter les éléments de synthèse de ce produit, une méthode prédictive de structure a été utilisée, en collaboration avec l'Université de Liverpool. L'utilisation de cette approche a guidé la sélection des compositions cibles en identifiant rapidement les "zones d'intérêt" à faible énergie dans le diagramme ternaire SrO-$AlO_{1.5}$ -SiO_2. Ces zones abritent les potentielles nouvelles phases et leur exploration ciblée par GC a permis de réduire les ressources et les temps de travail.

Des recherches dans la littérature ont révélé une multitude de matériaux optiques importants et intéressants dans le diagramme de phase SrO-$AlO_{1.5}$ –SiO_2. Les propriétés optiques ont donc été recherchées dans la fonctionnalisation de toutes les compositions découvertes. En particulier, les propriétés optiques de luminescence persistante et/ou de mécanoluminescence ont été ciblées car elles sont utiles pour diverses applications (bijouterie, signalisation de sécurité et construction) et qu'il existe relativement peu d'exemples de céramiques élaborées par cristallisation complète du verre. En outre, des techniques d'ingénierie de la microstructure ont été employées pour développer la transparence dans les matériaux découverts, et donc pour bénéficier d'effets de volume en luminescence, ce qui élargit encore les possibilités d'applications.

La combinaison de méthodes de synthèse innovantes (GC) et de la prédiction de nouvelles phases cristallines a permis de développer une nouvelle approche de découverte de matériaux. Cette approche a permis de produire et de fonctionnaliser trois nouvelles céramiques métastables élaborées par cristallisation du verre et présentant des propriétés de luminescence persistante et de mécanoluminescence performantes.

Résumé des Résultats du Chapitre 2

Dans ce chapitre, deux nouvelles céramiques métastables, $SrAl_2SiO_6$ et $Sr_{12}Al_{20}Si_{12}O_{66}$, sont examinées. L'objectif initial était de synthétiser $SrAl_2SiO_6$ monophasique, en poudre et en massif, pour permettre une étude de ses propriétés, PL et PerL. Cetravail a cependant permis de découvrir une nouvelle phase, $Sr_{12}Si_{20}Si_{12}O_{66}$, qui a rempli les objectifs principaux de ce chapitre : la détermination structurale, l'optimisation de la synthèse et la fonctionnalisation de la phase cristalline. La fonctionnalisation (PL, PerL et ML) a été ciblée pour les échantillons en poudre et les échantillons transparents massifs, par dopage avec Eu^{2+} et Dy^{3+}. Cette méthode s'était en effet avérée fructueuse pour d'autres aluminosilicates ($Ba_{13}Al_{20}Si_{10}O_{66}$ - PL et PerL, $SrAl_2O_4$ - PL, PerL et ML).

Les objectifs ont été atteints avec succès dans le cas de $SrAl_2SiO_6$, grâce à une approche GC et à une étape de frittage d'une durée de 1 heure à 1050°C. Le protocole de synthèse a été optimisé par des mesures DSC et VTXRD *in-situ*. L'utilisation d'une approche GC combinée à une cristallisation partielle de l'échantillon massif a facilité la synthèse de larges morceaux devitro- céramiques transparentes (échelle centimétrique), ce qui a élargi le potentiel d'application de ce matériau.

Le dopage des échantillons en poudre et massifs avec 1 mol% d'Eu^{2+} et de Dy^{3+} a permis d'observer des émissions PL et PerL. Cependant, il a été noté que leur ajout rendait plus difficile l'obtention d'échantillons cristallisés monophasiques. Ces propriétés ont ensuite été quantifiées, à la fois pour les échantillons en poudre et massifs, au laboratoire CSIC de Séville. Une émission PL verte intense, émission à 485 nm, et une durée de vie modérée, PerL de 1 heure, ont été observées expérimentalement.

L'optimisation de $SrAl_2SiO_6$ a conduit à la découverte de la nouvelle phase cristalline $Sr_{12}Al_{20}Si_{12}O_{66}$ et d'atteindre les principaux objectifs de ce chapitre. La structure de ce nouveau matériau a été résolue et la composition affinée grâce à une approche combinée d'indexation de phase à partir de données SPD/NPD de haute qualité, d'analyse SAED et de charge-flipping. Une fois encore, l'optimisation de la synthèse a été réalisée dans le cas des échantillons poudre et massifs. La cristallisation partielle du verre massif a permis d'obtenir trois degrés de transparence (totalement transparent, partiellement transparent et opaque), tout en conservant un matériau monophasique. L'épaisseur de la couche cristalline (cristallisation de surface) a été analysée par MEB, ce qui a permis d'établir un lien entre l'orientation des cristallites, l'épaissuer de la couche et la transparence de l'échantillon. La structure résolue a été confirmée par analyse Rietveld et imagerie STEM-HAADF à résolution atomique réalisée sur un préparé sous forme de lame mince. Une étude structurale locale des sites Al^{3+}/Si^{4+} spécifiques et de leur mise en ordre potentielle a été réalisée par ^{29}Si MAS et ^{27}Al MQMAS NMR. Ces études ont permis de proposer deux modèles probables avec une occupation mixte complexe des sites T_5 et T_4.

$Sr_{12}Al_{20}Si_{12}O_{66}$ a été trouvé (par comparaison avec $Ba_{13}Al_{22}Si_{10}O_{66}$) comme faisant partie de trois solutions solides avec des limites variables, $Sr_{12-x}Al_{20+2x}Si_{12-2x}O_{66}$ et $Sr_{12-x}(Ba/Ca)_xAl_{20+2x}Si_{12-2x}O_6$. Une solution solide étendue a été déterminée pour les ajouts de Sr^{2+} et Ba^{2+}, révélant les seules compositions proposées précédemment dans la littérature, $Sr_{13}Al_{22}Si_{10}O_{66}$ et $Ba_{12}Al_{20}Si_{12}O_{66}$.

Au CSIC de Séville, les propriétés PL et PerL de $Sr_{12}Al_{20}Si_{12}O_{66}$ ont à nouveau été étudiées. Des propriétés PL et PerL bleues extrêmement intenses et durables ont été observées autour de 420 nm, la lumière étant encore détectable 12 heures après coupure de l'excitation. Les tentatives de modification de la couleur et de l'intensité de l'émission en jouant sur la composition de l'hôte ont malheureusement échoué. Néanmoins, la substitution réussie des sites A et B a prouvé l'impressionnante flexibilité structurale de $Sr_{12}Al_{20}Si_{12}O_{66}$. A l'IPR de Rennes, les propriétés ML d'un échantillon massif partiellement cristallisé ont été quantifiées pour un niveau de dopage RE de 1 %Eu^{2+} et 1,5 %Dy^{3+}. Une réponse EML intense a été observée et s'est avérée équivalente à celle du produit commercial de référence, $SrAl_2O_4:Eu^{2+},Dy^{3+}$.

Associées à la transparence, les impressionnantes propriétés PL, PerL et ML observées dans $Sr_{12}Al_{20}Si_{12}O_{66}$, offrent un large éventail d'applications fonctionnelles, surtout si l'on considère que ces propriétés peuvent être optimisées. La transparence peut être améliorée grâce à une orientation maitrisée des cristallites, des échantillons transparents entièrement cristallisés pouvant être obtenus s'ils sont suffisamment fins et sans impuretés. La modification de la couleur et de l'intensité de PerL peut être obtenue en modifiant l'élément dopant/la concentration ou la composition de l'hôte. L'absence d'émission dans l'échantillon substitué par Ga ($Sr_{11.76}Eu_{0.12}Dy_{0.12}Al_{14}Ga_6Si_{12}O_{66}$) est particulièrement intéressante car sa structure cristalline similaire au pur aluminosilicate suggère que des propriétés optiques différentes seront observées avec des terres rares différentes. Enfin, il est possible d'améliorer les propriétés ML par une cristallisation complète de l'échantillon massif. Même l'ordre probable observé par RMN offre la possibilité d'ajuster les propriétés en faisant varier le rapport Al^{3+}/Si^{4+}.

Résumé des Résultats du Chapitre 3

Dans ce chapitre, la synthèse et l'optimisation de $Sr_2Si_3O_8$ ont été étudiées par la méthode innovante GC. Les objectifs étaient de synthétiser $Sr_2Si_3O_8$ par cristallisation congruente et complète du verre parent binaire 40SrO-60SiO_2, optimiser le protocole de synthèse et produire des échantillons monophasiques de haute qualité, puis fonctionnaliser le composé pour explorer les applications possibles (dopage Eu/Dy pour ML, par analogie avec $Ba_4Si_6O_8$). Si le premier objectif a été facilement atteint, les deuxième et troisième objectifs ont été très difficiles à atteindre en raison de l'instabilité thermique de $Sr_2Si_3O_8$. Après détermination de la structure, il s'est avéré que la phase pouvait être synthétisée à partir de la ligne binaire 40SrO-60SiO_2 (sans Al_2O_3 comme initialement reporté). La GC à partir de cette composition a été optimisée par des mesures VTXRD et DSC *in-situ*. Ces mesures ont mis en évidence la métastabilité de $Sr_2Si_3O_8$ en montrant sa décomposition en $SrSiO_3$ (*C2/c*) et SiO_2 à ~1075°C. Une étape de cristallisation optimale de 12h à 850°C a été déterminée, ce qui a permis d'obtenir une vitrocéramique homogène avec une cristallinité approximative de 89%. Malheureusement, la cristallisation à partir du verre 40SrO-60SiO_2 a provoqué un déplacement de certaines positions de pics, qui n'ont pas pu être ajustées par un simple affinement des paramètres de la maille unitaire (ou par une ré-indexation). Cela implique un écart par rapport à la maille unitaire moyenne, qui pourrait, par exemple, être causé par des défauts étendus (défauts d'empilement, plans de cisaillement)

dans la structure cristalline. Des mesures STEM et MEB ont été effectuées pour visualiser et modéliser la cause de ce défaut, mais l'instabilité de $Sr_2Si_3O_8$ sous le faisceau électronique a empêché d'obtenir la résolution au niveau atomique nécessaire pour visualiser ces effets.

Pour augmenter la stabilité, la fraction de phase cristalline et la cristallinité de $Sr_2Si_3O_8$ et permettre une étude des propriétés, des substitutions, Ba^{2+} et Ca^{2+}, et l'utilisation d'agents nucléants, ZrO_2 et Ag, ont été étudiés. Ces substitutions/additions ont permis d'observer deux familles de comportement différentes. La famille A a conservé la même plage de température de synthèse de ~250°C mais a réduit la fraction de phase cristalline de 26% en moyenne. Elles ont également augmenté le désordre et réduit la résolution des pics, ce qui a entraîné des modèles PXRD plus difficiles à modéliser. Il est intéressant de noter que ces phases ont également stabilisé une phase intermédiaire non indexable entre 1025 et 1100°C. La famille B a réduit la cristallinité et la stabilité de 41% et 50°C en moyenne respectivement. Inversement, ces échantillons ont considérablement amélioré la résolution des pics et la modélisation Rietveld de $Sr_2Si_3O_8$. Une zone idéale de la synthèse de Sr_2 Si O_{38} a été théorisée, combinant une cristallinité élevée et des pics bien résolus.

La synthèse d'oxynitrures a été la dernière voie testée pour réaliser la synthèse dans cette zone. On a constaté qu'elle augmentait la résolution des pics, ce qui a permis de modéliser $Sr_2Si_3O_8$ avec la cellule $P2_1$ *c.* Le dopage Eu^{2+} et Dy^{3+} a ensuite été combiné à la synthèse d'oxynitrures pour étudier les propriétés ML de $Sr_2Si_3O_8$. Cependant, les dopants ont introduit une cristallisation de la phase secondaire $Sr_3RE_2Si_6O_{18}$ *(C2/c)* RE = Eu^{2+} ou Dy^{3+} et $SrSiO_3$ (*C2/c*). Ces impuretés ont été minimisées dans les échantillons massifs et en poudre afin de pouvoir effectuer des mesures ML. Il s'est avéré que $Sr_2Si_3O_8$ avait des propriétés de ML émettant dans le vert, avec une émission comparable à la phase connue $Ba_4Si_6O_{16}$:Eu^{2+},Dy^{3+}.

Les recherches futures devraient se concentrer sur l'obtention d'échantillons monophasiques et hautement cristallins de $Sr_2Si_3O_8$ en utilisant la méthode de synthèse utilisant l'oxynitrure, ainsi que d'autres méthodes potentiellement basées sur de la chimie en solution. L'élimination des phases secondaires et l'augmentation de la cristallinité ne feraient qu'améliorer les performances ML du $Sr_2Si_3O_8$. D'autres dopants RE (Ho^{3+}, Pr^{3+} et Nd^{3+} par exemple) devraient également être étudiés comme moyen de varier la couleur et l'intensité de l'émission ML. Toute possibilité de modification de la structure cristalline augmenterait son intérêt en tant que phase EML.

Résumé des Résultats du Chapitre 4

Synthèse par Cristallisation du Verre Étape 1 - Formation du Verre

La cristallisation du verre (GC) implique deux étapes, la formation du verre et sa cristallisation ultérieure. Pour préparer les mélanges de réactifs pour la formation du verre, des précurseurs d'oxydes ou de carbonates de haute pureté (>99,98%) ont d'abord été séchés à 100° C, afin d'éliminer toute humidité, puis pesés dans les rapports molaires souhaités. Les poudres ont ensuite été soigneusement broyées dans un mortier en agate, avec l'aide d'éthanol si nécessaire, jusqu'à l'obtention de poudres fines et homogènes. Les

mélanges de réactifs ont été fondus dans un creuset en platine dans un four de trempe à moufle, à des températures supérieures d'au moins 50° C à leurs points de fusion respectifs, tels que déterminés dans la littérature ou par calorimétrie différentielle à balayage (DSC). Les échantillons ont été laissés à cette température pendant ~1.5 heures, pour permettre une homogénéisation au niveau atomique, avant que le creuset ne soit trempé dans l'eau. Pour les échantillons de verre massifs, une étape supplémentaire de recuit de 15 minutes à la température de fusion a été ajoutée, afin de relaxer les contraintes internes et donc de réduire la fissuration (perte de transparence) au cours de l'étape de cristallisation. La confirmation de l'état vitreux a été déterminée qualitativement par l'obtention d'un échantillon transparent et quantitativement par diffraction des rayons X sur poudre (PXRD).

Étape 2 - Cristallisation

Une fois le verre formé, il a ensuite été cristallisé au cours d'une deuxième étape de recuit, comme le montre la figure A.1.1. Cette étape a consisté à broyer le verre (broyage manuel mortier/pilon) pour obtenir une poudre fine, qui a ensuite été pastillée (~50mg, 5mm ϕ, 1mm d'épaisseur), par pressage uniaxial. Les pastilles ont été placées dans un creuset en Pt et placées à l'intérieur d'un four à moufle. Les températures de cristallisation ont été déterminées par diffraction des rayons X à température variable *in-situ* (VTXRD *in-situ*) et par DSC. Les durées et températures spécifiques utilisées pour les étapes de cristallisation sont discutées dans les sections correspondantes. Des cristallisations ont également été réalisées sur des morceaux de verre massifs. Généralement, ces expériences nécessitent des temps de frittage plus longs en raison de leur surface réduite par rapport aux échantillons en poudre, ce qui limite la vitesse des mécanismes de cristallisation basés sur la surface observée dans ces matériaux.

Pour les frittages effectués sur les verres dopés à l'Eu^{3+}, un four tubulaire a été utilisé, ce qui a permis une cristallisation sous atmosphère contrôlée, en l'occurrence azote-hydrogène N_2:H_2 (94%:6%), réduisant Eu^{3+} en l'Eu^{2+}. Un plateau de température à 500° C pendant 3h a été ajouté à la procédure pour ces expériences, afin d'encourager la réduction complète des ions Eu^{3+}.

Si la trempe depuis l'état fondu présente de nombreux avantages pour la formation du verre, à savoir une facilité d'utilisation, son évolutivité et "l'activation" des précurseurs, elle présente également des inconvénients.

(i) Les vitesses de refroidissement lentes ont facilité la cristallisation dans les systèmes où la formation de verre n'était pas favorable.

(ii) Sites de nucléation et impuretés provenant du contact avec le creuset de Pt.

(iii) Formation de verre seulement dans les systèmes facilement vitrifiables

Le cas échéant, ces inconvénients ont été surmontés par l'utilisation de techniques de synthèse alternatives, telles que la méthode à l'état solide, le broyage à haute énergie (HEM) et la lévitation aérodynamique (ADL). La synthèse d'oxynitrure a également été utilisée, en particulier au chapitre 3, comme moyen d'obtenir une cristallisation complète et d'améliorer les propriétés de la phase cristallisée.

Fig. A.1. Schéma de l'approche de la cristallisation du verre utilisée dans ce travail.

A computationally-guided non-equilibrium synthesis approach to materials discovery in the SrO-Al_2O_3-SiO_2 phase field

Euan M. Duncan,[a] Amandine Ridouard,[a] Franck Fayon,[a] Emmanuel Veron,[a] Cécile Genevois,[a] Mathieu Allix,[a] Christopher M. Collins,*[b] and Michael J. Pitcher*[a]

[a] *CEMHTI, CNRS UPR3079, 1d Ave. de la Recherche Scientifique, 45071 Orléans, France.*
[b] *Department of Chemistry, Materials Innovation Factory, University of Liverpool, Liverpool L7 3NY, U.K.*

*Correspondence: c.m.collins@liverpool.ac.uk, michael.pitcher@cnrs-orleans.fr

Abstract

Glass-crystallisation synthesis is coupled to probe structure prediction for the guided discovery of new metastable oxides in the SrO-Al_2O_3-SiO_2 phase field, yielding a new ternary ribbon-silicate, $Sr_2Si_3O_8$. In principle, this methodology can be applied to a wide range of oxide chemistries by selecting an appropriate non-equilibrium synthesis route.

The discovery of inorganic oxides with new compositions and crystal structures is a key challenge in materials chemistry, with many domains in which new functional materials are required to enable advances in performance, cost or sustainability. When searching for new complex (ternary or higher) oxides, two important limiting factors are the intrinsic tendency of high-temperature ceramic synthesis to promote formation of the most thermodynamically stable phases, and the vast number of potential compositions for exploration. Together, these factors complicate attempts to identify and isolate new metastable materials, and render exhaustive searches impractical even for fairly limited phase fields.[1] Solutions to these problems have focused on alternative synthesis approaches that operate under conditions that are more amenable to the formation of non-equilibrium phases (e.g. chimie douce,[2] molten salt,[3] co-metathesis[4] or diverse solution-based processes[5]), on rapid automated characterisation,[6] and increasingly on materials-by-design approaches based on crystal structure prediction[7] and machine learning[8] that allow synthetic efforts to be concentrated on a manageable number of targets. Predictive and non-equilibrium synthesis methods are commonly applied in isolation, but the possibility of combining their respective advantages can enable new types of problems to be approached, such as the guided synthesis of new metastable oxide polymorphs,[9] which have so far received less attention.

Here, we tackle the metastability and combinatorial problems together by combining the probe structure (PS) compositional prediction approach[10,11] with glass-crystallisation (GC) as a non-equilibrium synthesis technique, for the guided discovery of new metastable compounds in the previously well-explored SrO-Al_2O_3-SiO_2 phase field. The PS approach aids the synthetic exploration of complex phase diagrams by mapping the most energetically-favourable regions for crystalline phase formation, and has previously been harnessed to conventional ceramic synthesis methods.[10] It is also suited to the discovery of metastable materials, which exist in local energy minima that are close to the convex hull,[12] as demonstrated recently by the isolation of the aperiodic titanate $Ba_{10}Y_6Ti_4O_{27}$ by careful optimisation of a ceramic synthesis protocol.[13] However, PS calculations have not previously been harnessed to a non-equilibrium synthesis route to target metastable compounds intentionally. Such an approach is expected to raise the energy threshold above the convex hull at which synthesisable compounds might be attainable, increasing the probability of new compounds being accessible in a given phase field.

GC is a non-equilibrium synthesis method that can yield metastable oxides with extraordinary compositions[14] or entirely new structure types.[15] Its capability is enhanced by the use of containerless synthesis methods[16] that allow a wide range of compositions to be vitrified, including highly atypical glass-formers,[17–19] which can then be crystallised at moderate temperatures. GC is complementary to other non-equilibrium methods, which can provide alternative routes to the same metastable phases.[20,21] By selecting a phase field with a broad glass-forming region, GC can be coupled effectively to the PS approach in a systematic search for new compounds. In this context, the SrO-Al_2O_3-SiO_2 phase field is an ideal test case: most of the phase space can be vitrified,[22] and it is known to host functional materials such as luminescence phosphor hosts[23–25] and transparent ceramics.[26,27] Furthermore, the possibility of isolating new metastable compounds in this system has been demonstrated by the GC synthesis of $SrAl_2SiO_6$, which exists in the solid solution gap between two transparent ceramic tectosilicate families on the $SrAl_2O_4$ – SiO_2 tie-line, and adopts a unique structure type.[28]

Encouraged by the realisation of such new and complex oxides in the SrO-Al_2O_3-SiO_2 phase field by GC, we conducted a probe-structure analysis using FUSE[11] to identify other fertile regions for exploration. Probe structure calculations were performed on the whole SrO-Al_2O_3-SiO_2 phase field, for a total of 42

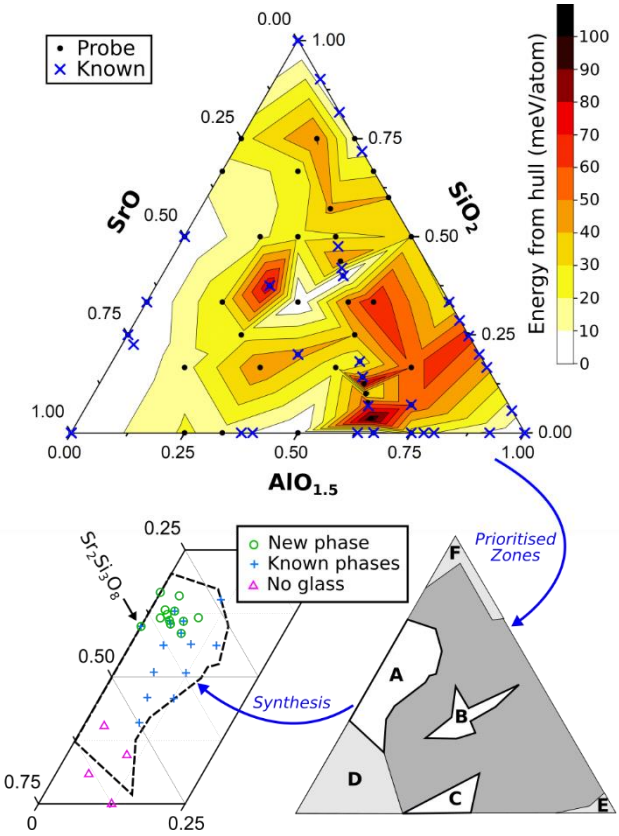

Fig. 1 *Convex hull calculated for the phase field SrO-$AlO_{1.5}$-SiO_2. The 42 probe structure compositions are plotted as black points, and blue crosses indicate known compounds from the equilibrium phase diagram and/or ICSD. Where two points coincide, the lower energy structure (probe or ICSD) was taken for the convex hull calculation. A full list of probe structures is available in Table S1. The lowest energy regions A-C were prioritised for exploration by glass-crystallisation synthesis, whilst other low energy regions D-F were not explored synthetically. Region A yielded a new phase which could not be indexed to a known compound (green circles).*

compositions. The calculations included 15 compositions on the $SrAl_2O_4$ – SiO_2 line, which is known to host a range of metastable cation-disordered crystalline phases:[25,26,28] their inclusion in the convex hull construction allows a threshold energy to be estimated for the formation of new metastable phases in this system. The resulting $SrAl_2O_4$ – SiO_2 energy profile is plotted in Figure S1 alongside its constituent probe structures, which all contain chemically-plausible corner-sharing tetrahedral aluminosilicate frameworks (consistent with the known structural chemistry of such materials) and reasonable coordination numbers for Sr^{2+} (see Figure S2). The ability of FUSE to generate plausible structures at these compositions is highlighted at 40% SiO_2 ($SrAl_2Si_2O_8$), where the probe structure corresponds to a cation-ordered variant of the experimentally-obtained hexacelsian structure.[26] From the energy profile it can be seen that almost all of the known compounds on the $SrAl_2O_4$ – SiO_2 line lie within 50 meV/atom of the convex hull. The region 25 – 30% SiO_2, which hosts metastable $SrAl_2SiO_6$, lies approximately 40 meV/atom above the convex hull.

The calculated convex hull for the whole phase diagram is plotted in Figure 1. The energy surface exhibits several low-energy regions which cover a substantial fraction of the phase diagram: the application of a 35 meV/atom threshold for exploration (an arbitrary value used previously for stable oxides[10,11]) would entail an excessively broad experimental search (see Figure S3). In order to focus only on the most promising regions for experimental exploration, six candidate regions **A** – **F** were identified, corresponding only to the lowest calculated energies (< 20 meV/atom) as shown in Figure

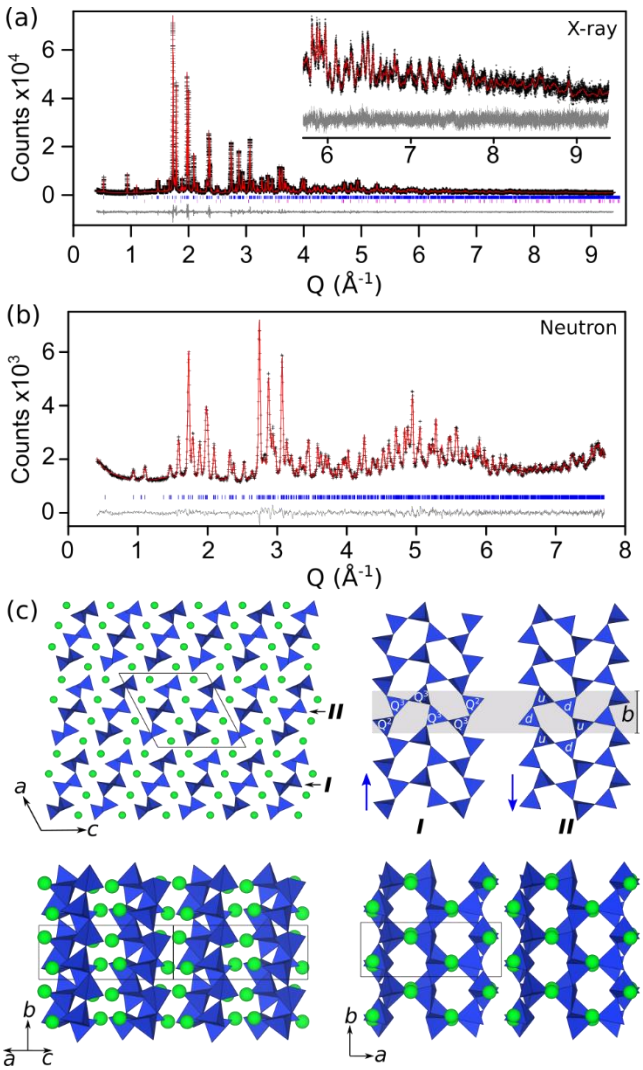

Fig. 2 *Crystal structure of $Sr_2Si_3O_8$, obtained by crystallisation of $Sr_{0.344}Al_{0.033}Si_{0.623}O_{1.64}$ glass at 900°C. Rietveld refinement against (a) SXRD data (λ = 0.45808 Å, R_{wp} = 7.34 %, χ^2 = 1.35) and (b) neutron diffraction data (λ = 1.5936 Å, R_{wp} = 3.00 %, χ^2 = 1.72). (c) Projections of the SXRD-refined structure showing an antiparallel arrangement of $[Si_6O_{16}]^{8-}$ ribbons, where **I** and **II** represent "up" and "down" orientations. Atoms = Sr^{2+}, tetrahedra = $[SiO_4]$.*

1. Regions **A – C** encompass compositions which are far from the vertices of the phase diagram, far from other known pseudo-ternaries, and amenable to glass formation, and these were selected for systematic synthesis trials. Conversely, the regions **D, E** and **F** were not explored experimentally due to the difficulty in vitrifying compositions close to SrO (**D**) and Al_2O_3 (**E**), and difficulty in crystallising SiO_2-rich compositions (**F**) at moderate temperatures.

To enable a consistent synthetic approach to the experimental phase search, standard synthesis conditions were defined for each region **A – C** by preparing 1 or 2 reference glasses from the centre of each region. These were then crushed into powder and their crystallisation temperatures (T_C) obtained by in-situ PXRD (the reference compositions and their crystallisation temperatures are shown in Figure S4). A spread of trial glass compositions was then synthesised according to these conditions, with crystallisations performed ex-situ for 1 hour (see Methods). In regions **B** and **C**, glass synthesis was successful for all trial compositions, but the crystallisation steps produced only mixtures of known compounds: **B** compositions crystallised predominantly into mixtures of $Sr_2Al_2SiO_7$ and feldspar-type $SrAl_2Si_2O_8$, whilst **C** compositions were dominated by a stuffed-tridymite phase resembling the nearby

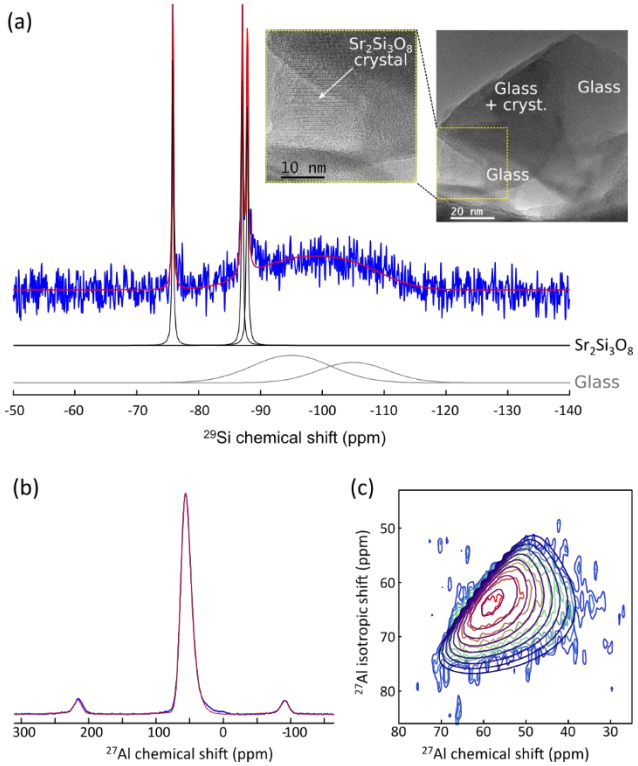

Fig. 3 *MAS-NMR spectra of $Sr_2Si_3O_8$, crystallised from $Sr_{0.344}Al_{0.033}Si_{0.623}O_{1.64}$ glass. (a) ^{29}Si spectrum showing sharp resonances from three inequivalent Si atoms in the $Sr_2Si_3O_8$ structure, with a Q^2/Q^3 ratio that agrees closely with the Rietveld model, and a broad resonance from amorphous Si in Q^3 and Q^4 configuration accounting for 58 % of the Si nuclei. Inset is a TEM image of a $Sr_2Si_3O_8$ crystal embedded in a glassy matrix, consistent with the NMR data. (b,c) 1D and 2D-MQMAS ^{27}Al NMR showing only a single broad resonance typical of an amorphous phase.*

$Sr_{0.9}Al_{1.8}Si_{0.2}O_4$[25] (see Figure S5). In contrast, initial exploration of region **A** yielded several samples whose multi-component PXRD patterns, generally dominated by $SrSiO_3$, contained a new pattern that could not be indexed to a known phase. By refining the target composition systematically, this new PXRD pattern was eventually isolated as the only crystalline phase at six different nominal compositions, as shown in Figure 1.

One of these compositions, $Sr_{0.344}Al_{0.033}Si_{0.623}O_{1.64}$, was crystallised at 900°C (see DSC, Figure S6) and selected for *ab initio* crystal structure solution due to its sharp Bragg peaks and the absence of secondary crystalline phases. High resolution SXRD data were collected at ambient temperature and indexed to a primitive monoclinic unit cell of dimensions a = 13.327 Å, b = 4.582 Å, c = 13.464 Å and β = 116.7° in space group $P2_1/c$. Using the same data set, the structure was then solved *ab initio* by simulated annealing of Sr^{2+} ions and $[SiO_4]^{4-}$ rigid tetrahedra (see Supplementary Information). The resulting model provided excellent Rietveld fits to both SXRD (Figure 2a, Table S2) and neutron diffraction data (Figure 2b, Table S3). It is a one-dimensional structure whose main feature is a $[Si_6O_{16}]^{8-}$ ribbon, formed by three zweier chains that are linked into 6-membered rings of tetrahedra in *ududud* orientation. This generates two Q^2 (2-connected) and four Q^3 (3-connected) tetrahedra, as indicated in Figure 2c. The ribbon is polar along its propagation direction, but an antiparallel checkerboard-type packing arrangement produces a non-polar structure overall, as indicated by the blue arrows on ribbons ***I*** and ***II*** in Figure 2. Adjacent ribbons are separated by columns of Sr^{2+} in 7-fold coordination. The structure is closely related to that of $Ba_2Si_3O_8$,[29] which features similar $[Si_6O_{16}]^{8-}$ ribbons. The two structure types differ in terms of their antiparallel ribbon packing modes, and by a significant ribbon

distortion in $Sr_2Si_3O_8$ corresponding to a large cooperative twist of the two external zweier chains (see Supplementary Information, section E).

The structural model has a different composition from the parent glass ($Sr_{0.344}Al_{0.033}Si_{0.623}O_{1.64}$), and offers no obvious mechanism for incorporating Al^{3+}. ^{29}Si and ^{27}Al MAS-NMR were used to confirm the crystal structure, and to investigate the fate of the Al^{3+}. Here, distinct narrow peaks at ^{29}Si isotropic chemical shifts of -75.9, -87.1 and -87.9 ppm with relative intensities in a 1:1:1 ratio indicate the presence of one Q^2 and two inequivalent Q^3 Si sites with the same multiplicities (Figure 3 and Figure S7), as expected from the structural model. Furthermore, the observed isotropic and anisotropic chemical shifts were very close to GIPAW-calculated values from the refined structure (Table S4), confirming the accuracy of the refined atomic positions. The ^{29}Si spectrum also features a broad resonance corresponding to an amorphous phase, whose chemical shift range is typical of Q^3 and Q^4 species found in silicate glasses, accounting for 58 % of the Si nuclei. At the same time, 1D and MQMAS ^{27}Al MAS-NMR spectra show line shapes typical of disordered Al^{3+} in tetrahedral coordination, with no quadrupolar splitting, indicating that Al^{3+} is present only in the amorphous phase. These conclusions are supported by TEM imaging and EDS (Figure 3(a) inset, and Table S5) showing $Sr_2Si_3O_8$ crystals embedded in a SiO_2-enriched glassy matrix.

In addition to heterogeneous crystallisation of alumina-containing precursor glasses, $Sr_2Si_3O_8$ can also be obtained directly by crystallisation of 0.40 SrO – 0.60 SiO_2 glass in the range 825 - 1050°C. Above 1050 °C, it decomposes rapidly to the equilibrium phases $SrSiO_3$ and SiO_2, illustrating its metastability (see *in situ* PXRD, Figure S8). This homogeneous crystallisation route yields samples of relatively low crystallinity with a substantial residual glass fraction, as shown by PXRD and ^{29}Si NMR (Figures S9 and S10). Attempts to improve the crystallinity by optimising temperature and annealing time had no significant effect on the PXRD peak widths, and tended to promote thermal decomposition (Figures S11 and S12). This difficulty in isolating fully-crystallised ceramic samples of $Sr_2Si_3O_8$ directly is surprising, given its apparent ease of crystallisation from alumina-containing precursor glasses, and may require an improved understanding of the crystallisation process before it can be overcome.

Probe structure prediction has been combined with a non-equilibrium synthesis method for the first time. In principle, this allows access to a greater range of new compounds than would be possible by exploring with a conventional ceramic synthesis method. The approach is validated by the discovery of $Sr_2Si_3O_8$, the first ambient-pressure example of a ternary strontium silicate with a polymerised [SiO_4] framework. $Sr_2Si_3O_8$ forms readily by heterogeneous crystallisation of alumina-containing glass precursors, yielding glass-ceramics of sufficient crystalline quality for *ab initio* structure solution. It can also be prepared with lower crystalline quality by homogeneous crystallisation of 0.40 SrO – 0.60 SiO_2 glass. $Sr_2Si_3O_8$ may be of interest for scintillation or luminescence properties,[30,31] but an improved synthesis protocol is required to obtain fully-crystallised samples suitable for functionalisation. The experimental focus on very low calculated energy regions (< 20meV/atom) in this study is non-exhaustive and may leave scope for the discovery of other metastable compounds at higher energy thresholds (e.g. < 50meV/atom). The PS-GC methodology can be applied directly to other glass-forming phase fields, and can be extended to non-glass-forming systems by using alternative non-equilibrium synthesis routes.

Conflicts of interest

There are no conflicts to declare.

Acknowledgements

Funding was provided by the ANR (grant 20-CE08-0007), EPSRC (grant EP/N004884), and PHC-ALLIANCE (grant 44791ZG). DSC data were collected by Sandra Ory (CEMHTI). Neutron data were collected by Dr. Stanislav Savvin (ILL, Grenoble, France). Use of the Advanced Photon Source at Argonne National Laboratory was supported by the U. S. Department of Energy, Office of Science, Office of Basic Energy Sciences, under Contract No. DE-AC02-06CH11357. Computing resources were provided by the University of Liverpool.

Notes and references

1 D. W. Davies, K. T. Butler, A. J. Jackson, A. Morris, J. M. Frost, J. M. Skelton and A. Walsh, *Chem*, 2016, **1**, 617–627.
2 J. Gopalakrishnan, *Chem. Mater.*, 1995, **7**, 1265–1275.
3 D. Portehault, S. Delacroix, G. Gouget, R. Grosjean and T. H. C. Chan-Chang, *Acc. Chem. Res.*, 2018, **51**, 930–939.
4 P. K. Todd and J. R. Neilson, *J. Am. Chem. Soc.*, 2019, **141**, 1191–1195.
5 D. L. M. Cordova and D. C. Johnson, *ChemPhysChem*, 2020, **21**, 1345–1368.
6 J. Li, C. Lin, Y. Min, Y. Yuan, G. Li, S. Yang, P. Manuel, J. Lin and J. Sun, *J. Am. Chem. Soc.*, 2019, **141**, 4990–4996.
7 A. R. Oganov, C. J. Pickard, Q. Zhu and R. J. Needs, *Nat. Rev. Mater.*, 2019, **4**, 331–348.
8 J. Schmidt, M. R. G. Marques, S. Botti and M. A. L. Marques, *npj Comput. Mater.*, 2019, **5**, 1–36.
9 A. Parija, G. R. Waetzig, J. L. Andrews and S. Banerjee, *J. Phys. Chem. C*, 2018, **122**, 25709–25728.
10 C. Collins, M. S. Dyer, M. J. Pitcher, G. F. S. Whitehead, M. Zanella, P. Mandal, J. B. Claridge, G. R. Darling and M. J. Rosseinsky, *Nature*, 2017, **546**, 280–284.
11 C. Collins, G. R. Darling and M. J. Rosseinsky, *Faraday Discuss.*, 2018, **211**, 117–131.
12 M. Aykol, S. S. Dwaraknath, W. Sun and K. A. Persson, *Sci. Adv.*, 2018, **4**, eaaq0148.
13 C. M. Collins, L. M. Daniels, Q. Gibson, M. W. Gaultois, M. Moran, R. Feetham, M. J. Pitcher, M. S. Dyer, C. Delacotte, M. Zanella, C. A. Murray, G. Glodan, O. Pérez, D. Pelloquin, T. D. Manning, J. Alaria, G. R. Darling, J. B. Claridge and M. J. Rosseinsky, *Angew. Chem., Int. Ed.*, 2021, **60**, 16457–16465.
14 W. Cao, A. I. Becerro, V. Castaing, X. Fang, P. Florian, F. Fayon, D. Zanghi, E. Veron, A. Zandonà, C. Genevois, M. J. Pitcher and M. Allix, *Adv. Funct. Mater.*, 2023, **33**, 2213418.
15 M. Allix, S. Alahrache, F. Fayon, M. Suchomel, F. Porcher, T. Cardinal and G. Matzen, *Adv. Mater.*, 2012, **24**, 5570–5575.
16 C. J. Benmore and J. K. R. Weber, *Advances in Physics: X*, 2017, **2**, 717–736.
17 K. Yoshimoto, A. Masuno, H. Inoue and Y. Watanabe, *J. Am. Ceram. Soc.*, 2012, **95**, 3501–3504.
18 J. Yu, Y. Arai, T. Masaki, T. Ishikawa, S. Yoda, S. Kohara, H. Taniguchi, M. Itoh and Y. Kuroiwa, *Chem. Mater.*, 2006, **18**, 2169–2173.
19 A. Masuno, S. Kohara, A. C. Hannon, E. Bychkov and H. Inoue, *Chem. Mater.*, 2013, **25**, 3056–3061.
20 J. Fan, V. Sarou-Kanian, X. Yang, M. Diaz-Lopez, F. Fayon, X. Kuang, M. J. Pitcher and M. Allix, *Chemistry of Materials*, 2020, **32**, 9016–9025.
21 Y. Zhang, L. Zhao, Z. Ye and Y. Zeng, *J. Adv. Ceram.*, 2022, **11**, 1613–1625.
22 D. Bahat, *J. Mater. Sci.*, 1969, **4**, 855–860.
23 S. Kubota, H. Yamane and M. Shimada, *Chem. Mater.*, 2002, **14**, 4015–4016.
24 S. Ye, Z.-S. Liu, X.-T. Wang, J.-G. Wang, L.-X. Wang and X.-P. Jing, *J. Lumin.*, 2009, **129**, 50–54.
25 A. J. Fernandez-Carrion, K. Al Saghir, E. Veron, A. I. Becerro, F. Porcher, W. Wisniewski, G. Matzen, F. Fayon and M. Allix, *Inorg. Chem.*, 2017, **56**, 14446–14458.
26 K. Al Saghir, S. Chenu, E. Veron, F. Fayon, M. Suchomel, C. Genevois, F. Porcher, G. Matzen, D. Massiot and M. Allix, *Chem. Mater.*, 2015, **27**, 508–514.

27 V. Castaing, C. Monteiro, A. D. Sontakke, K. Asami, J. Xu, A. J. Fernández-Carrión, M. G. Brik, S. Tanabe, M. Allix and B. Viana, *Dalton Trans.*, 2020, **49**, 16849–16859.
28 W. Wisniewski, A. J. Fernández-Carrión, P. Schöppe, C. Rüssel and M. Allix, *CrystEngComm*, 2018, **20**, 3455–3466.
29 K. F. Hesse and F. Liebau, *Z. Kristallogr. - New Cryst. Struct.*, 1980, **153**, 3–17.
30 Y. Eagleman, E. Bourret-Courchesne and S. E. Derenzo, *IEEE Trans. Nucl. Sci.*, 2012, **59**, 479–486.
31 M. Chen, Z. Xia, M. S. Molokeev and Q. Liu, *J. Mater. Chem. C*, 2015, **3**, 12477–12483.

Euan Duncan

Nouveaux oxydes fonctionnels par cristallisation de précurseurs vitreux

Résumé :

Ce travail de thèse à découvrir de nouveaux composés fonctionnels à base d'oxydes, en utilisant la cristallisation du verre comme moyen de synthèse original. Ces recherches sont nécessaires pour répondre au besoin croissant de nouvelles phases cristallines à propriétés améliorées, et peut en principe faciliter des évolutions progressives des performances en remplaçant les matériaux actuels. Le diagramme ternaire SrO-Al_2O_3-SiO_2 a été choisi en raison de son large domaine de formation vitreux et de la variété des phases cristallines répertoriées ayant des applications fonctionnelles, en particulier dans le domaine de l'optique. Dans la première partie de ce travail, l'utilisation de la cristallisation de verre provenant de différentes régions du diagramme de phase a conduit à la découverte d'un nouveau composé métastable, $Sr_{12}Al_{20}Si_{12}O_{66}$. La deuxième partie de ce travail concerne les tentatives d'isoler le nouveau silicate $Sr_2Si_3O_8$ (découvert précédemment au CEMHTI par une approche récente utilisant le guidage par calcul prédictif) comme matériau entièrement cristallisé et monophasique, facilitant l'exploration de ses propriétés de mécanoluminescence. Ces composés ont été caractérisés de manière multi-échelle (de la maille unitaire à l'échelle du grain) et en température, par des méthodes de diffraction des rayons X et de neutrons sur poudre et par microscopie électronique en transmission à haute résolution en utilisant des instruments de pointe (résolution atomique STEM-HAADF et spectroscopie EELS). Cette approche a permis de résoudre *ab-initio* la structure du composé $Sr_{12}Al_{20}Si_{12}O_{66}$. Enfin, les arrangements atomiques locaux dans $Sr_{12}Al_{20}Si_{12}O_{66}$ ont été étudiés par spectroscopie RMN du solide à l'angle magique (noyaux ^{27}Al et ^{29}Si) couplée à une modélisation DFT, qui ont révélé un ordre partiel inhabituel entre Al et Si au sein des sites tétraédriques de la structure cristalline, qui n'a pas pu être observé directement par diffraction. Les propriétés de luminescence de ces matériaux ont été explorées (en collaboration avec l'institut CSIC de Séville et l'institut de physique (IPR) de Rennes). Alors que $Sr_2Si_3O_8$ montre une réponse de mécanoluminescence modeste, $Sr_{12}Al_{20}Si_{12}O_{66}$ s'est avéré avoir une émission de luminescence bleue persistante de longue durée, en plus d'une réponse en mécanoluminescence intense. Les performances de ce nouvel aluminosilicate sont comparables à l'état de l'art.

Mots clés : Oxydes, oxydes fonctionnels, vitrocéramiques, métastables, hors équilibre, fondus, amorphes, cristallisation du verre, propriétés optiques, luminescence persistante, mécanoluminescence.

New Functional Oxides by Crystallisation of Glass Precursors

Summary :

This PhD work aimed to discover new metal-oxide compounds, with potential functional applications, by crystallisation of glass precursors. Such approaches are necessary to address the growing need for new phases with enhanced properties, and in principle can facilitate step changes improvements in performance by replacing current materials. The SrO-Al_2O_3-SiO_2 ternary diagram was focussed on due to its broad glass-forming domain, and the variety of known phases with functional (especially optical) applications already found within it. In the first part of this work, glass crystallisation in different regions of the phase diagram led to the discovery of a new metastable compound, $Sr_{12}Al_{20}Si_{12}O_{66}$. The second part of this work concerns attempts to isolate the new ternary silicate $Sr_2Si_3O_8$ (discovered previously at CEMHTI by a recent computationally-guided approach) as a phase-pure fully-crystallised material, facilitating the exploration of its mechanoluminescence properties for the first time. These compounds were characterised at multiple length scales (unit cell to micron scale) and temperatures, through powder X-ray and neutron diffraction methods and high-resolution transmission electron microscopy using state-of-the-art instruments (for diffraction, atomic-resolution STEM-HAADF, and EELS spectroscopy). This permitted *ab-initio* structure solution of $Sr_{12}Al_{20}Si_{12}O_{66}$. Finally, local atomic arrangements in $Sr_{12}Al_{20}Si_{12}O_{66}$ were studied by ^{27}Al and ^{29}Si MAS-NMR coupled to DFT modelling, which revealed an unusual partial ordering of Al and Si over the tetrahedral framework sites of the crystal structure, which could not be resolved directly by diffraction. The luminescent properties of these materials were explored (in collaboration with the CSIC institute in Seville and the Institute de Physique (IPR) in Rennes). Whilst $Sr_2Si_3O_8$ was found to have a modest mechanoluminescence response, $Sr_{12}Al_{20}Si_{12}O_{66}$ was found to have bright long-lasting blue persistent luminescence emission in addition to an intense mechanoluminescence response, with the performance of both properties comparable to current state-of-the-art materials.

Key words: Oxides, functional oxides, glass-ceramics, metastable, out-of-equilibrium, molten, amorphous, glass-crystallisation, optical properties, persistent luminescence, mechanoluminescence.

CEMHTI-CNRS UPR3079
1D Avenue de la Recherche Scientifique
45071 Orléans Cedex 2